Dissertation

submitted to the

Combined Faculties for the Natural Sciences and for Mathematics

of the Ruperto–Carola University of Heidelberg, Germany

for the degree of

Doctor of Natural Sciences

presented by

Diplom-Physiker Martin Göbel

born in: Rottweil (Germany)

Oral examination: 12.11.2008

Low-Dimensional Traps for Bose-Fermi Mixtures

Referees: Prof. Dr. Jörg Schmiedmayer
Prof. Dr. Jian-Wei Pan

Zusammenfassung

Niedrigdimensionale Fallen für Bose-Fermi-Mischungen

Diese Arbeit beschreibt den Entwurf und die Realisierung eines neuartigen Experimentaufbaus zur Untersuchung von ultrakalten Bose-Fermi Mischungen. Der neue Aufbau kombiniert ein Experiment für die Mischung aus ^{87}Rb und ^{40}K mit eindimensionalen Fallen, wie sie in den miniaturisierten Drahtfallen eines Atomchips erreichbar sind. Durch die zusätzliche Kopplung der internen Zuständen der magnetisch gefangenen Atome mit Radio-Frequenz (RF) Feldern, können vielseitige Potentiale erzeugt werden, die zustands- und speziesabhängig sind. Ein Spezialfall dieser Potentiale ist die Überführung einer eindimensionalen Falle in eine neuartige zweidimensionale Geometrie, in der die Atome auf die Wände einer geraden Röhre eingeschränkt sind. Diese Fallengeometrie wurde experimentell und in numerischen Simulationen ausführlich mit dem Ziel untersucht, die Variationen im Fallenpotential zu minimieren. Dies führte zu einer neuen verbesserten Anordnung der Drähte, die die RF Felder erzeugen. Diese optimierte Anordung der Drähte wurde im neuen Experimentaufbau implementiert und wird die erste Realisierung einer solchen zweidimensionalen Fallenkonfiguration mit periodischen Randbedingungen ermöglichen. In Experimenten, die mit einer vereinfachten Anordnung der RF Drähte durchgeführt wurden, wurde das zweidimensionale Regime mit thermischen Atomen erreicht.

Abstract

Low-Dimensional Traps for Bose-Fermi Mixtures

This thesis describes the design and realization of a novel experimental setup for the investigation of ultracold Bose-Fermi mixtures. The new setup combines a mixture experiment of ^{40}K and ^{87}Rb with one-dimensional trapping geometries that are accessible in the miniaturized wire traps of an atom chip. By additionally coupling the internal states of magnetically trapped atoms with radio-frequency (rf) fields, versatile state-selective and species-selective potentials can be created. One special case is the deformation of the static one-dimensional trap to a novel two-dimensional geometry in which the atoms are confined to the walls of a straight tube. An extensive numerical and experimental analysis of this trapping geometry with the aim of minimizing the variations in the trapping potential was performed. This leads to a new improved spatial arrangement for the wires that create the rf fields. The optimized wire layout was implemented in the new experimental setup and will allow the first realization of such a two-dimensional trap configuration with periodic boundary conditions. Results of experiments performed with a simplified arrangement of the rf wires allowed the observation of the two-dimensional regime with thermal atoms.

Contents

Abstract i

Contents iii

List of Figures vii

1. Introduction 1

2. Static Traps for Neutral Atoms 5
2.1. Static Magnetic Fields . . . 5
2.2. Basic Trapping Geometries . . . 6
2.2.1. Quadrupole Trap . . . 6
2.2.2. Ioffe-Pritchard Trap . . . 7
2.3. Wire Traps . . . 7
2.3.1. Typical Configurations . . . 8
2.3.2. Finite Size Effects . . . 9
2.3.3. Gravitational Sag . . . 10
2.4. Atom Chips . . . 11

3. Radio-Frequency Adiabatic Potentials 15
3.1. Dressed-State Hamiltonian . . . 16
3.2. Possible Trapping Configurations . . . 18
3.2.1. One Linear RF Field . . . 19
3.2.2. Two Linear RF Fields . . . 20
3.2.3. Toroidal Trap . . . 21
3.2.4. Details on the Effective Coupling . . . 22
3.3. Real-World Effects . . . 22
3.3.1. Gravity . . . 22
3.3.2. Real Wires . . . 23
3.4. Feasibility of a Two-Dimensional Toroidal Trap . . . 25

3.4.1. Two-Wire Setup . . . 25
3.4.2. Four-Wire Setup . . . 27
3.5. Numerical Calculations in Three Dimensions . . . 31
3.5.1. Beam Splitter . . . 31
3.6. State-Selective & Species-Selective Traps . . . 32

4. Cold Bosons & Fermions **37**
4.1. Statistics . . . 37
4.1.1. Fermions . . . 39
4.1.2. Bose-Einstein Condensation . . . 39
4.1.3. Interacting Bosons . . . 40
4.2. Density Distributions . . . 42
4.2.1. Fermions at T=0 . . . 43
4.2.2. Bosons at T=0 . . . 43
4.3. Expansion & Thermometry . . . 44
4.3.1. Thermal Atoms . . . 44
4.3.2. Fermions . . . 45
4.3.3. Bosons . . . 46
4.4. Bosons in Two Dimensions . . . 47
4.4.1. Experimental Approaches . . . 49

5. Bose-Fermi Mixtures **51**
5.1. Sympathetic Cooling . . . 52
5.1.1. Inelastic Collisions . . . 52
5.1.2. Elastic Collisions and Thermalization . . . 53
5.1.3. Thermalization in the Degenerate Regime . . . 54
5.1.4. Influence of High Confinement . . . 54
5.2. Attractive Interaction . . . 55
5.2.1. Collapse . . . 56
5.2.2. Modification of a Double-Well Potential . . . 57

6. Setup for the New Mixture Experiment **61**
6.1. History . . . 61
6.2. Design Goals . . . 62
6.3. Optics . . . 63
6.3.1. Lasers . . . 63
6.3.2. Optical Table . . . 65
6.4. A New Vacuum Chamber . . . 68
6.4.1. The Window Issue . . . 69
6.4.2. Double-MOT . . . 70
6.4.3. External Coils . . . 72
6.4.4. Compensation Coils . . . 74
6.5. Chip Mounting . . . 75
6.5.1. Ceramic Structures . . . 75
6.5.2. Copper Structures . . . 77
6.5.3. Thermal Management . . . 78
6.5.4. Foil for Additional RF Wires . . . 80

6.6. Atom Chip . . . 80
6.6.1. Fabrication . . . 80
6.6.2. Coating . . . 81
6.6.3. Layout . . . 82
6.6.4. Imaging . . . 84

7. First Measurements at the K-Rb Experiment **87**
7.1. Optimization of the MOT Parameters . . . 87
7.1.1. Population of the Different ^{40}K-Levels . . . 88
7.2. Current Status & Next Steps . . . 90

8. Two-Dimensional Toroidal Trap **93**
8.1. Experimental Apparatus . . . 93
8.1.1. Imaging . . . 94
8.1.2. Double-Layer Chip . . . 94
8.1.3. RF Setup . . . 98
8.1.4. Experimental Cycle . . . 99
8.2. Experimental Methods . . . 100
8.2.1. Oscillations . . . 100
8.2.2. RF Spectroscopy . . . 102
8.3. Characterization of the Setup . . . 103
8.3.1. Magnification of the Imaging Systems . . . 103
8.3.2. Height Calibration . . . 104
8.3.3. Absolute RF Amplitude . . . 104
8.4. Experimental Realization of a Toroidal Trap . . . 106
8.4.1. Adiabatic Loading of the RF Trap . . . 107
8.4.2. Balancing the RF Fields . . . 109
8.4.3. Oscillation Frequencies of the Toroidal Trap . . . 111
8.4.4. Crossover to Two Dimensions . . . 112
8.4.5. Cooling in the Adiabatic Trap . . . 115
8.4.6. Lifetime & Heating . . . 116

9. Summary & Outlook **119**

A. Atomic Data for ^{87}Rb and ^{40}K **123**
A.1. Atomic Parameters . . . 123
A.2. Level Schemes . . . 124

B. Magnetic Fields of Extended Wires **125**

C. Technical Drawings of the Mounting **127**

Acknowledgments **147**

References **149**

List of Figures

2.1. Basic Side Guide 7
2.2. Three-Dimensional Trapping 9
2.3. Optimizing a U-Trap by Rotating the Bias Field 10
2.4. B Field of Wires With Finite Dimensions 11
2.5. Gravitational Sag for ^{40}K and ^{87}Rb. 12

3.1. Coupled Two-Level System 17
3.2. Transversal Field in Ioffe Configuration 18
3.3. RF Double-Well 20
3.4. Coupling Term for Different Detunings 21
3.5. Layout of the RF Wires in the K-Rb Experiment 23
3.6. Simple Toroidal Trap 24
3.7. Effect of the Phase on the Geometry of the Trap 26
3.8. Compensating Inhomogeneities by Changing the Relative Phase 27
3.9. Compensated Toroidal Four-Wire Trap 28
3.10. Optimized Torus 29
3.11. Optimized Torus II 29
3.12. Displaced Ring Trap 30
3.13. Changing the Ratio Between the RF Amplitudes 30
3.14. Toriodal Potential in Three Dimensions 31
3.15. Real Space Interferometer for Positive Detuning 33
3.16. Real Space Interferometer for Negative Detuning 34
3.17. Zeeman Splitting 35

4.1. Chemical Potential for Fermions and Bosons 39
4.2. In Situ Density Distributions 42
4.3. Thermal Cloud Expanded 45
4.4. Expansion of a BEC 46

5.1. In Situ Distribution for Bosons and Fermions With Attractive Interaction . . 56

5.2. Stability Diagram for Different Radial Confinements 57
5.3. Modified Double-Well I 58
5.4. Modified Double-Well II 59

6.1. Spectroscopy for ^{39}K and the Potassium Laser Locking Scheme 65
6.2. Optical Table of the K-Rb Experiment 66
6.3. Science Chamber 68
6.4. Broken Window 69
6.5. Lower MOT Chamber 71
6.6. Magnetic Coils 72
6.7. CAD Rendering of the K-Rb Setup 74
6.8. Mounting 76
6.9. Trap Volume of the Copper Structures 78
6.10. Simulation: Temperature Rise in the Small Copper Z-structure 79
6.11. Alignment of the Atom Chip and the Kapton Foil 80
6.12. Atom Chip Under the Microscope 81
6.13. Central Region of the Chip 82
6.14. Longitudinal Trapping 83
6.15. Schematics of the Transveral Imaging 85
6.16. Overview of the Chip Layout 86

7.1. Determination of the Atom Number in a MOT 88
7.2. Atom Number of ^{87}Rb for Different Intensities and Detunings 89
7.3. Loading rate of ^{87}Rb for Different Detunings 89
7.4. Level Population for ^{40}K as a Function of the Intensity 90

8.1. Central Region of the RbII Chip 95
8.2. Height Variations in the Central Part of the RbII Chip 96
8.3. In Situ Density Distribution for Weak Longitudinal Confinement 97
8.4. RF Setup 98
8.5. Phase-Space Density in the Copper Z-Structure 99
8.6. Damped Longitudinal Oscillation 100
8.7. Parametric Heating 101
8.8. Trap Bottom of the Static Trap 102
8.9. Calibration of the Longitudinal Imaging 103
8.10. Height Calibration 104
8.11. Calibration of the RF Amplitudes 105
8.12. Toroidal Trap, Schematic 106
8.13. Experimental Sequence to Load the Adiabatic Trap 107
8.14. Horizontal Double-Well, In Situ 108
8.15. Adiabaticity of the Transfer 109
8.16. Balancing of the RF Fields 110
8.17. Oscillation Frequencies of a Toroidal Trap 111
8.18. Expansion From a Toroidal Trap: Measurement and Simulation 114
8.19. Ratio Between Horizontal and Vertical Temperatures 115
8.20. Cooling in the Adiabatic Trap I 116
8.21. Cooling in the Adiabatic Trap II 117

8.22. Heating in the Static Trap 118

A.1. Level Schemes for ^{87}Rb and ^{40}K 124

C.1. Technical Drawing: Copper U-Structure 128
C.2. Technical Drawing: Wide Z-Structure I 129
C.3. Technical Drawing: Wide Z-Structure II 130
C.4. Technical Drawing: h-Structure I 131
C.5. Technical Drawing: h-Structure II 132
C.6. Technical Drawing: Shapal I 133
C.7. Technical Drawing: Shapal II 134
C.8. Technical Drawing: Shapal III 135
C.9. Technical Drawing: Shapal III 136
C.10. Technical Drawing: Support Structure 137
C.11. Technical Drawing: Base of the Support Structure 138
C.12. Technical Drawing: Flange 139
C.13. Technical Drawing: Isolators I 140
C.14. Technical Drawing: Isolators II 140
C.15. Technical Drawing: Isolators III 141
C.16. Technical Drawing: Isolators IV 141
C.17. Technical Drawing: Copper Clamps 142
C.18. Technical Drawing: Copper Clamps II 142
C.19. Technical Drawing: Copper Block 143
C.20. Technical Drawing: Copper-Berylium Pins 143
C.21. Technical Drawing: Copper Rods 144
C.22. Technical Drawing: Star-Shaped Chamber 145
C.23. Technical Drawing: Helicoflex-CF Adaptor 146

1 Introduction

After the first experimental realization of Bose-Einstein condensation in 1995 [1, 2, 3], the interest in ultracold dilute atomic gases has grown rapidly. On the experimental side, a whole variety of tools and methods was developed to manipulate and probe the atomic samples. Initial experiments were motivated by the fact that the weak interactions between the atoms is extremely well understood and that these systems are theoretically easily accessible. Many phenomena such as interference, superfluidity and collective excitations could be studied in a very well controlled experimental environment.

The next step was to go beyond mean-field physics to strong interactions and correlations in the system. Strong interactions were accessible with the advent of magnetic Feshbach resonances [4], a tool that allows the controllable tuning of the interaction strength in the atomic gas. However, the regime of strong interactions between bosons always has the drawback of strong inelastic losses in the sample [5, 6].

Parallel to the work on Bose gases, fermions were also brought to lower and lower temperatures, and in 1999 the first ultracold gas of fermions with $T < T_{Fermi}$ was created in ^{40}K [7]. The cooling of fermions turned out to be experimentally more challenging than the cooling of bosons. Evaporative cooling of spin-polarized fermionic samples is, due to the Pauli principle, highly ineffective at low temperatures. The interest in fermions was driven by the notion that fermionic quantum gases are the ideal model system for many physics questions, since they are the elementary constituent of all visible matter. Ultracold fermionic gases might lead to a better understanding of the behavior of electrons in metals, neutron stars, nuclei or the mechanisms of superconductivity.

Using Feshbach resonances in spin mixtures of fermions, surprisingly long lived molecules could be created [8]. Late in 2003, the pairing of fermionic atoms with equal and opposite momenta led to the creation of superfluid condensates of molecules [9, 10]. Since then, much experimental and theoretical work was done to study the exact nature of the crossover point between correlated pairs of fermions on the BCS side and a BEC of diatomic molecules (for a recent overview on this field see [11]). An impressive direct indication of superfluidity was the observation of quantized vortices in both regimes [12].

With Bose-Fermi mixtures a completely new field of ultracold quantum gases is available. For example, composite fermions might be accessible in the periodic potentials of optical

lattices [13]. The bosons were initially only used to sympathetically cool the fermionic sample, and the bosonic component was removed after the cooling. The main focus was on the investigation of the properties of the non-interacting Fermi gas, like the size of the trapped cloud [14] and effects like Pauli blocking [15].

However, starting in 2002, the interspecies scattering properties especially of the mixture ^{40}K-^{87}Rb were investigated in several experiments [16, 17, 18]. The scattering length was changed using heteronuclear Feshbach resonances [19, 20]. Since then, the interaction strength has been, similar to the homonuclear case, tunable, and highly excited heteronuclear molecules could be produced and were investigated [21]. At the same time, mixture experiments in optical lattices made it possible to study the effect of fermions on the transport and localization of bosons [22] and of bosons on the transport of fermions [23].

Besides Feshbach resonances, there is a second way to create strong correlations in a bosonic sample: in highly-confined situations and therefore in lower-dimensional geometries, the atom-atom interactions become increasingly important [24, 25]. Such high confinements can be reached either in deep optical lattices or in wire traps. In optical lattices, this already enabled the observation of strong correlations in a gas of one-dimensional bosons [26, 27].

In magnetic traps, phase fluctuations were investigated in the weakly interacting regime for the equilibrium [28] and for the non-equilibrium case [29]. In two-dimensional systems the main focus was on the exact nature of the superfluid transition [30, 31]. However, the crossover from the three-dimensional to the one-dimensional regime [32, 33] has still to be studied experimentally.

Over the years, the technical development of simple wire traps towards highly integrated atom chips evolved quickly. Nowadays, the guiding and trapping of atoms in highly anisotropic traps and the condensation to BEC in atom chips are standard methods [34, 35]. Furthermore, the detection of a few atoms using fully integrated optical elements is possible [36]. The small size of the atom chip opens the route for very stable miniaturized setups, with potential applications like the precise mapping of magnetic fields [37, 38] or interferometric sensors. Additionally, these setups are candidates for quantum information processing devices [39]. Even portable battery-powered setups are feasible [40].

The versatility of the wire trap approach to low-dimensional traps was enhanced greatly with the implementation of adiabatic radio-frequency (rf) traps on an atom chip. These potentials were first suggested in [41]. Subsequently M. Andersson, then a member of our group, realized that the vector character of the rf field allowed much more elaborate trapping configurations such as the splitting of a cylindrical static trap into a double-well potential [42, 43]. Within the last few years, a whole list of other groups started working on bosons in adiabatic rf traps on atom chips [44, 45, 46, 47], making this a very active field of research.

Aim of this Project

When starting this project in 2004, the main goal was the achievement of a cold gas of fermions in an atom chip experiment and the investigation of a mixture of bosons and fermions in low-dimensional traps. At this time, no experiment existed that combined these technologies and fields. Such a setup allows the study of novel quantum phases and their behavior in different model potentials, e.g. periodic potentials, waveguides, disordered potentials and quantum-point contacts [48].

In an initial attempt in Heidelberg, an existing setup was extended to a mixture experiment of ^{6}Li-^{87}Rb and this mixture was cooled. However, the focus of my work was on the

construction of a new setup in Vienna. Therefore, the design, planning, commissioning and build-up of a new mixture apparatus and preliminary experiments constitute the main part of this thesis work.

The new setup combines a Bose-Fermi mixture experiment with an atom chip and with adiabatic potentials. During the time of this project, the Thywissen group has succeeded in combining all these different parts in one single setup [47].

Within this thesis, the application of an adiabatic trap as a two-dimensional trapping geometry is investigated theoretically and experimentally. Adiabatic traps make a smooth crossover between a one-dimensional geometry and a two-dimensional trap experimentally accessible. A similar method was implemented previously for a thermal gas [49], but there is no realization for a BEC yet. In addition, the novel trapping geometry suggested in chapter 3 of this thesis allows the first implementation of a two-dimensional trap with periodic boundary conditions. This toroidal trap is a geometry in which the atoms are confined to the wall of a straight tube. The spatial dependence of the rf fields that are applied was optimized, leading to a novel four-wire design with negligible variations of the trapping potential across the torus. Exactly this optimized wire geometry was integrated in the new mixture setup. First experiments on a two-dimensional adiabatic trap and the cooling of thermal samples in such a geometry were performed at a two-wire rf setup at one of the experiments in our group.

Structure of this Thesis

- The first two chapters, chapter 2 and 3 introduce the different trapping concepts for neutral atoms that are employed in the experiments of this thesis. Chapter 2 is devoted to static trapping concepts, whereas chapter 3 deals with the adiabatic trapping geometries that are accessible once a radio-frequency (rf) field is added to the static trap. Within this chapter, the feasibility of a two-dimensional trap with periodic boundary conditions is discussed. Numerical simulations in two and three dimensions are presented which show that with an optimized wire geometry the creation of such a two-dimensional trap is indeed possible.

- In chapter 4 the different statistical considerations for bosons and fermions are reviewed, leading to the well-known results of Bose-Einstein condensation and the requirements for the ultracold regime in a Fermi gas. As the novel trapping geometry introduced in the previous chapter allows the creation of a two-dimensional system, results are presented for this geometry as well.

- Interaction and scattering between the two species is introduced in chapter 5, where the sympathetic cooling mechanism and the modification of the trapping potential due to the mean-field attraction will be discussed. As an example the change of an adiabatic double-well potential is described in more detail.

- The new experimental apparatus for the mixture of ^{40}K-^{87}Rb is introduced in chapter 6. Starting with an empty lab and some components from a previous experiment, a novel mixture experiment was developed and realized. All parts of the experimental setup are described in detail, hopefully guiding the following generations of PhD students through their first time with the setup. In the subsequent chapter 7, first measurements that characterize the performance of the collection MOT are presented.

- A piloting experiment on the implementation of the toroidal trapping geometry was carried out at a different experimental setup within the group. The loading and cooling of thermal gases and BECs in a two-dimensional trap were studied. Results were obtained for different settings of the rf fields and cooling ramps. These results can be found in chapter 8.
- In chapter 9 the results of the measurements are summarized and an outlook on different experiments that are feasible with the new setup is given.

2 Static Traps for Neutral Atoms

The following chapter shall serve as a reminder of the basic concepts of trapping neutral atoms in static magnetic traps. This was first demonstrated in the beginning of the 1980s [50] and was one of the key techniques on the way to cool dilute atomic alkali gases to quantum degeneracy [1, 2, 3]. For more detailed discussions the reader is pointed to textbooks like [51] and reviews like [52].

The underlying physical mechanism is the coupling of the internal magnetic moment of the atom to a spatially varying magnetic field. In section 2.1, the derivation of the magnetic potential for neutral atoms is outlined, whereas section 2.2 is devoted to the two basic trapping geometries, namely the *Ioffe-Pritchard trap* and the *quadrupole trap*.

In section 2.3, the general trap layouts that can be obtained with planar structures and the scaling behavior of the magnetic gradient and of the trapping frequencies are introduced. To reach high magnetic gradients and high aspect ratios of the traps, it is advantageous to utilize miniaturized structures that are patterned on substrates. In section 2.4, the basic concepts of different experimental realizations are mentioned. The technical details of the fabrication of the miniaturized structures of such an *atom chip* and calculations of the trapping parameters in the new K-Rb setup are postponed to the later section 6.6.

2.1. Static Magnetic Fields

Any particle with total angular momentum $\mathbf{F}$ and therefore an associated magnetic moment $\boldsymbol{\mu} = -g_F \mu_B \mathbf{F}$, experiences in a magnetic field $\mathbf{B}$ the potential of the linear Zeeman effect, as long as the field is not strong enough to decouple the nuclear and electronic spins.

$$U = -\boldsymbol{\mu} \cdot \mathbf{B} = m_F g_F \mu_B |\mathbf{B}|, \tag{2.1}$$

with the usual notations for the Bohr magneton μ_B, the Landé g-factor g_F and the magnetic quantum number m_F. The values for the g-factor of the two species considered in this thesis are $g_{(F=2)} = -1/2$ for ^{87}Rb and for ^{40}K $g_{(F=3/2)} = 2/3$.

In a semi-classical picture, the adiabatic approximation is only valid as long as the spin of the moving atom can adiabatically follow the direction of the external field that defines the quantization axis. The change in the magnetic field has to be slow compared to the

local Larmor frequency ω_L. In this case the eigenvalues of m_F can be treated as spatially independent even when the quantization axis changes its direction as a function of space.

$$\frac{d|\mathbf{B}|}{dt}\frac{1}{|\mathbf{B}|} < \omega_L = \frac{m_F g_F \mu_B B}{\hbar}. \tag{2.2}$$

This inequality does not hold for vanishing magnetic field strengths, making it necessary to use trapping configurations with a finite magnetic field at the trap center.

Based on the sign of the product $m_F g_F$ in equation (2.1), the magnetic states can be grouped in three sets: Atomic states with $m_F g_F > 0$ are attracted to the minimum of the magnetic field (*low-field seekers*), whereas states with $m_F g_F < 0$ are drawn towards regions of high magnetic fields (*high-field seekers*). States with $m_F = 0$ are not affected by the value or gradient of the external magnetic field and are therefore not suitable for magnetic trapping.

As Maxwell's equations do not allow for magnetic field maxima inside a source-free volume (Earnshaw's theorem [53]), there are no stable static trapping configurations for high-field-seeking atomic states in free space. However, as the creation of a minimum in the magnetic field in free space is possible, magnetic traps for atoms in their low-field-seeking magnetic states can be built in which the atoms can be stored and cooled.

Neglecting gravity (see section 2.3.3), the depth of an atom chip trap is roughly given by the magnetic moment of the atom times the external bias fields. Depending on the experimental situation, these bias fields are usually somewhere between 10 and 60 G. As μ_B corresponds to $k_B \cdot 67\,\mu\mathrm{K/G}$ these fields allow the capturing and trapping of atoms once they have temperatures in the 100 µK range. Therefore, optical pre-cooling of the sample in a magneto-optical trap (MOT) [54] and a successive optical molasses stage are necessary.

2.2. Basic Trapping Geometries

There are two basic field configurations for static traps that can be achieved. The main difference between both traps is that they either have a finite magnetic field at the center of the trap or not. An example for the first case is the *Ioffe-Pritchard trap*, the latter one is the so-called *quadrupole trap*.

2.2.1. Quadrupole Trap

The lowest multipole in an expansion of a static B field around a minimum is the quadrupole term. The most straightforward experimental realization is a pair of cirucular coaxial coils with oppositely flowing currents [50]. The gradient along the axis of the pair of coils in anti-Helmholtz configuration is twice the gradient in the radial direction, as their sum is fixed by the Maxwell's equation $\boldsymbol{\nabla} \cdot \mathbf{B} = 0$. The main advantage of the quadrupole configuration is the strong linear magnetic gradient that it offers over a large spatial range, making it ideal for cooling atoms in a magneto-optical trap [55].

However, to purely magnetically trap atoms in such a trap with zero B field at the minimum is experimentally not favorable. Atoms that reach this point will undergo non-adiabatic spin-flips to energetically preferred, but untrapped, magnetic states and are thus lost from the trap. These so-called *Majorana losses* [56] become more important the colder the temperature of the sample gets, as the probability for the atom to be at the minimum of the potential grows.

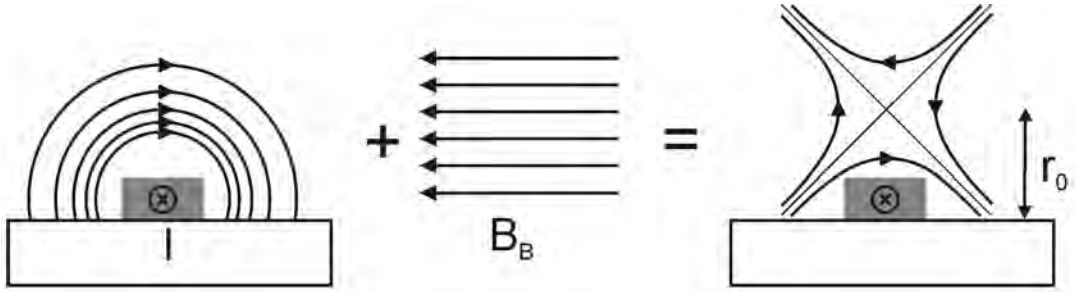

Figure 2.1.: By adding a homogeneous bias field B_B to the magnetic field of a wire with current I (depicted in grey), a minimum of the magnetic field is created in the plane perpendicular to the current flow at a height r_0 above the chip, allowing the trapping and guiding of atoms in low-field-seeking states along the wire.

2.2.2. Ioffe-Pritchard Trap

To overcome the drawbacks of the quadrupole geometry there are different strategies. One possibility is to spatially displace the trap minimum by rotating an external bias field (TOP-trap [57]), another one is to repel the atoms from the trap center using a blue-detuned laser beam [2].

The approach used in the chip trapping geometries originates from the plasma community [58] and was later proposed and demonstrated for neutral atoms by Pritchard [59]. Here an extra field, the Ioffe field B_I, is added to remove the zero magnetic field at the trap minimum and is usually combined with a harmonic confinement along this direction. This leads to a trap in all three spatial directions and is called a *Ioffe-Pritchard trap*.

The rate of non-adiabatic spin-flips that are still present when such a constant Ioffe field B_I is applied can be calculated [60, 61]. For the case of a spin-1 particle in an elongated cylindrical trap with a transversal trapping frequency $\omega_\perp$ at zero temperature one obtains

$$\gamma_{Maj} = 4\pi\omega_\perp \exp\left(-2\frac{\mu_0 B_I}{\hbar\omega_\perp}\right).$$

For a typical case in a miniaturized wire trap with a transversal trapping frequency in the kHz range, this rate is negligible on the timescale of minutes once a Ioffe field above a few 10 mG is applied.

2.3. Wire Traps

Due to the $1/r$ decay of the magnetic field of a wire, it is difficult to reach high magnetic fields or gradients with wires or coils that are several centimeters away from the atomic sample. Over the years, several schemes were developed to overcome these constraints, for example by putting coils inside the vacuum chamber [62], using specially designing reentrant bucket windows [63] or reducing the distance between coils and atomic sample with the help of glass cells [64].

One elegant way that allows for high magnetic gradients without blocking the optical access is to trap atoms close to a single current carrying wire inside the vacuum chamber. This was

first demonstrated in the late 1990s [65] and has successfully evolved into a powerful and versatile tool in the cold atom community to shape static potentials.

2.3.1. Typical Configurations

First, the situation in the plane perpendicular to a single infinitely long and infinitely thin wire is considered. If this wire carries a current I, a radially symmetric magnetic field $\mathbf{B} = \frac{\mu_0}{2\pi} I \mathbf{e}_{\boldsymbol{\varphi}}$ is created around the wire. If this field of the wire is superimposed with a homogeneous bias field $\mathrm{B_B}$ pointing perpendicular to the current flow, then, at a position

$$r_0 = \frac{\mu_0}{2\pi} \frac{I}{B_B} \tag{2.3}$$

away from the wire, the two magnetic field contributions cancel and around this point a quadrupole field in the plane perpendicular to the wire axis is formed. This situation is depicted in figure 2.1. Working with the units G, A and µm for B, I and r, equation (2.3) takes the convenient form $r_0 = 2000\, I/B$.

Around this minimum the B field can be written as

$$\mathbf{B} = \begin{pmatrix} G(y - r_0) \\ Gx \\ 0 \end{pmatrix} \quad \text{with the gradient} \quad G = |\mathbf{B}'| = \frac{2\pi}{\mu_0} \frac{B_B^2}{I} = \frac{B_B}{r_0}. \tag{2.4}$$

Here, the following coordinate system is used that will be used throughout this thesis: The current direction is parallel the z-axis, gravity is pointing toward the positive y-axis, and the bias field is parallel to the x-direction.

This minimum in the B field forms a so-called *side guide* but is not a trap in three dimensions yet. The trapping in the third direction can be obtained by introducing two wires that cross the trapping wire at a right angle and form a H-shaped configuration. Depending on the direction of current flow in these two perpendicular wires, two very different situations can be created:

Z-Trap

If, like in figure 2.2(a), the currents in both wires run in parallel, a harmonic confinement along the trapping wire is obtained, and the field at the trap minimum has a non-zero value. This is a realization of the Ioffe-Pritchard trap mentioned earlier in section 2.2.2. For simplicity, two of the connecting legs can be omitted, and the structure is therefore restricted to a single wire in Z-shape, a so-called *Z-trap*. In the experiments described in this thesis, both a Z-shaped and a H-shaped wire configuration were used.

The perpendicular wires with parallel currents rotate the trap axis a few degrees away from the direction of the trapping wire. This angle depends on the ratio of the width of the wires to the length of the central part of the Z and the distance of the trap center to the trapping wire [66].

Mathematically, the local coordinate system can be found by diagonalizing the Hessian (matrix of the second derivatives) of the potential and such finding the new eigenvectors of the trap. Along the main axis of the trap, the second derivatives of the potential can be expressed in terms of the frequencies of the corresponding potential of a harmonic oscillator:

(a) (b)

Figure 2.2.: The two different possibilities to extend a side guide (red) into a three-dimensional trap by using current in two parallel wires. Depending on the orientation of the current flow, a Ioffe-Pritchard trap (a), or a quadrupole trap (b) is formed. Structure (a) can be reduced to a single Z-shaped wire by omitting the dashed wires, (b) can be reduced to a single U-shaped wire.

$$\omega_i = \sqrt{\frac{1}{m}\frac{d^2U}{dx_i^2}} = \sqrt{\frac{m_F g_F \mu_B}{m}\frac{d^2B}{dx_i^2}} \tag{2.5}$$

with the atomic mass m.

In the case of the infinitely thin wire the transversal trapping frequency evaluates to

$$\omega_\perp = \sqrt{\frac{m_F g_F \mu_B}{m}}\frac{G}{\sqrt{B_I}} = \sqrt{\frac{m_F g_F \mu_B}{m}}\frac{B_B}{\sqrt{B_I} r_0} \tag{2.6}$$

with G the gradient defined in equation (2.4), B_I the non-zero remaining Ioffe field at the trap minimum.

U-Trap

The other possibility, illustrated in figure 2.2(b), is opposite directions for the currents in the crossing leads. The magnetic fields created by the current in these wires then cancel around the minimum point of the potential and give an additional gradient along this trapping direction. As in the example of the Z-trap above, two of the connections can be removed and a single wire bent in a U-shape is obtained, hence the name *U-trap*. This is a typical realization of a quadrupole trap as used in all the experiments of the group to trap and cool atoms in a MOT.

Due to the asymmetry of the magnetic field contributions of the closing wires, the center of the trap is not located above the middle of the central wire of the U-structure, but rotated away to the side where the magnetic flux is lower. This can be seen in figure 2.3. By using an additional orthogonal bias field the trap can be rotated back above the wire, to a position that gives the maximum trapping volume [67].

2.3.2. Finite Size Effects

Equation (2.3) only holds for situations in which the position r_0 is far away from the wire. The relations deduced from the infinite thin wire case help to understand the general scaling and the basic behavior of the resulting trap geometries, but break down once the situation

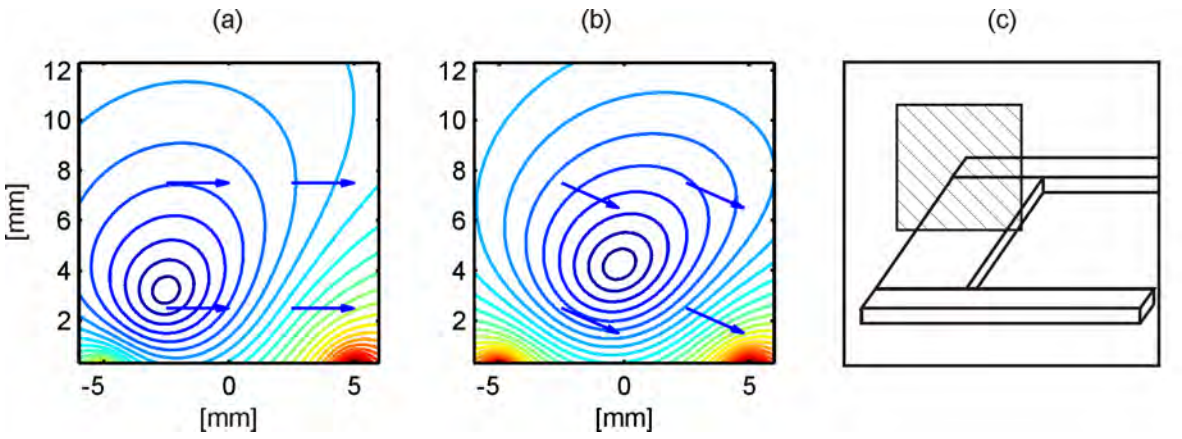

Figure 2.3.: Cut through the B field in the symmetry plane (hatched area in **(c)**) for a 1 cm wide U-shaped trapping structure supplied with 60 A. The arrows indicate the direction of the bias field. **(a)** U-structure with an bias field of $B_x = 20\,\mathrm{G}$. The trap is pushed to the side of the central wire and has not the maximum possible volume. **(b)** By rotating the bias field $B_x = 18.3\,\mathrm{G}$, $B_y = 8\,\mathrm{G}$ the trap moves above the center of the wire and a bigger capture volume for the MOT is available.

close to an extended wire is considered. Nevertheless, B field distributions can be calculated for extended wires analytically by integrating the Biot-Savart equation [68] for different (homogeneous) spacial current densities. The different equations used for the simulations in this thesis can be found in appendix B.

In figure 2.4, the resulting B fields above a infinitely thin wire, a flat sheet-like wire and a bulk wire are compared. Finite size effects are visible once the distance to the wire becomes comparable to the wire width or height. A 5% deviation in the B field from the infinitely thin wire result can be expected for a distance of 1.5 times the width or height of the wire. At a distance of 3.5 times the width or the height of the wire, the error in the B field is smaller than 1%. For a flat wire, the local current density is always lower than in the infinitely thin wire case, such leading to a lower magnetic field close to the wire than in the 1/r case.

2.3.3. Gravitational Sag

In addition to the magnetic potential, there is always the gravitational potential present. This leads to a gradient mg that points in all our experiments away from the chip and therefore tilts the trap in this direction. When a harmonic potential with frequency ω is combined with gravity, the minimum of the potential is displaced by a gravitational sag s:

$$s = \frac{g}{\omega^2}.$$

As shown in equation (2.5), ω will depend on the mass of the trapped species. This is of minor importance in single species experiments, but can play a significant role once working with several species of different masses. Then, the different gravitational sag can lead to a greatly reduced overlap of the two clouds. For two species that are exposed to the same magnetic potential but have different masses m_1, m_2, the ratio of the trapping frequencies scales as $\omega_1^2/\omega_2^2 = m_2/m_1$. Therefore, the difference in the minimum positions evaluates to:

$$\Delta s = \frac{g}{\omega_1^2}\left(1 - \frac{m_2}{m_1}\right) \qquad \text{with } m_2 < m_1.$$

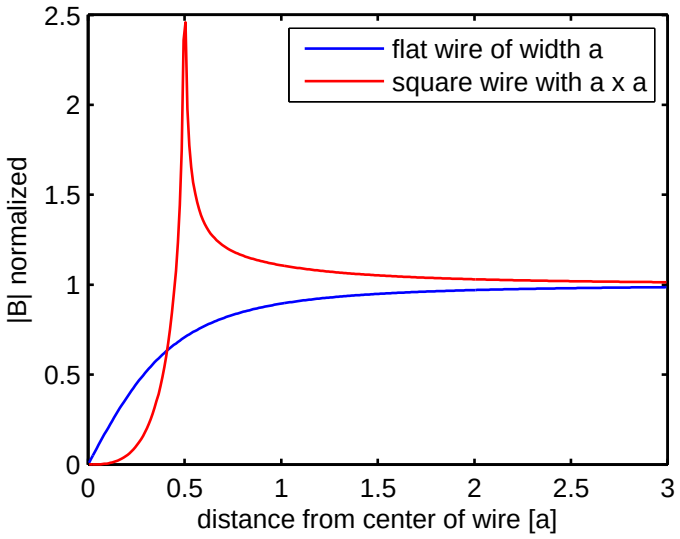

Figure 2.4.: Validity of the infinitely thin wire formula. Visible are the B fields above a flat wire of width a and a square wire with edge length a, both normalized to the result of the infinitely thin wire ($B \propto 1/r$). For distances bigger than 1.5 times the width or the height of the wire the error is smaller than 5%. In the case of the square wire the deviation from the $1/r$ potential is maximal at the surface of the wire.

In figure 2.5, the difference in the gravitational sag for the mixture of ^{87}Rb and ^{40}K is plotted. At very low trapping frequencies the difference in the minimum positions can be in the order of 1 mm. Here, one has to ensure that the size of the ^{87}Rb cloud is big enough so that the ^{40}K cloud is still immersed to allow good thermalization in the sympathetic cooling process.

2.4. Atom Chips

By miniaturizing the current carrying structures, high magnetic field gradients and therefore high trapping frequencies are accessible. From equation (2.4), the general scaling properties are visible: By keeping the current fixed, the gradient scales as $1/r^2$ as long as r is bigger than the dimensions of the wire. As there are technical limits to the current density in the wire and the heat generated, one can only moderately increase both, the current in the wire and the bias field to achieve higher magnetic field gradients at a fixed distance. Therefore, it is advantageous to work as close as possible to a thin wire.

Starting from free-standing wire structures inside vacuum [65, 69], the structures were eventually scaled down [70], requiring a substrate to support the structures and to remove the ohmic heat in these wires. As the technology to fabricate planar structures on the order of 1 to 100 µm originates from the chip fabrication in the semiconductor industry, soon the term *atom chip* [71] was coined for these devices.

The huge variability in patterning wires in planar structures, led to a whole variety of experimental realizations. Only a few examples are mentioned here and shall give a flavor of what is possible in such systems:

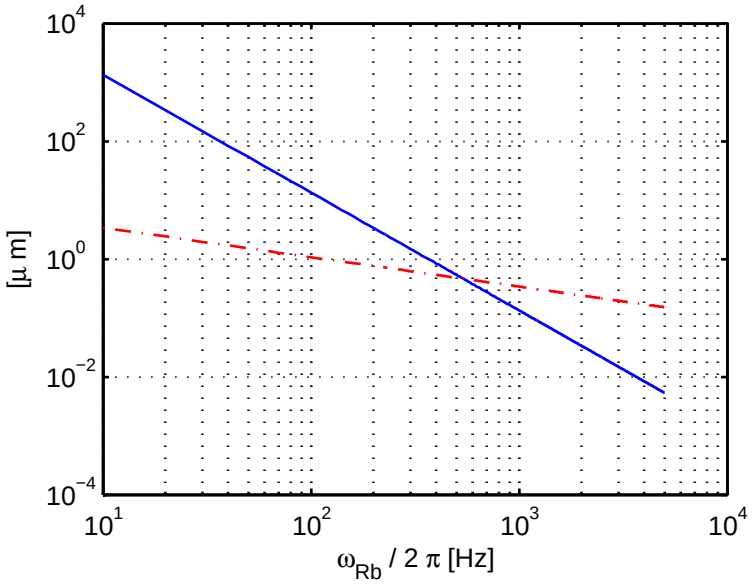

Figure 2.5.: Blue: difference in the gravitational sag for ^{87}Rb and ^{40}K as a function of the trapping frequency, assuming both species to be in their stretched state $|F = 2, m_F = 2\rangle$ and $|9/2, 9/2\rangle$, respectively. As a reference the ground state size $l_0 = \sqrt{\hbar/m\omega}$ for ^{87}Rb in the corresponding potential is depicted in red (dashed). Only for low trapping frequencies below approximately $2\,\pi{\cdot}500\,\mathrm{Hz}$ the gravitational sag can lead to a separation of the two clouds that is bigger than the ground state size. Here special care has to be taken that both clouds are always spatially overlapping to ensure thermalization in the degenerate regime.

- Multi-wire setups that do not require an additional external bias field were demonstrated [72] and led to the development of almost arbitrarily bent waveguides [73].

- Miniaturized interferometers [74] and beam splitters were realized and are still pursued with the possible application of mobile miniaturized sensors for gravitation, rotations and accelerations.

- Atomic clouds were moved along a trapping wire by employing a conveyor belt that is formed by ramping up and down the currents in small U-shaped wires parallel to the trapping wire [75, 76, 77]. This makes it possible to move atoms from a trapping region over several centimeters to an experiment region.

- Positioning an atomic cloud precisely in three dimensions was shown using multilayer chips in which parallel wires on the front side of the substrate are combined with an array of parallel wires on the back side of the chip [78], further allowing the realization of arrays of traps.

- The patterns in the current flow in a polycrystalline gold wire were reconstructed by probing the resulting magnetic potential with cold atoms [38].

- Optical elements such as fiber cavities were integrated on atom chips [79, 80], thereby allowing the detection of very few atoms in a waveguide and the study of their statistics.

- By changing the relative electrical potential on parts of chip surface, electric fields can be created that change the shape of the confining potential [81].
- Coupling microwave radiation to the atomic ensemble, led to the coherent manipulation of the internal state of atoms [82] in a chip trap.
- The richness of possible experiments is even growing when adiabatic potentials are used that are created by rf fields that are added to the static fields [83]. This will be discussed in more detail in the following section.

More details on the field of atom chips can be found in specialized reviews [52, 34, 84, 35].

3 Radio-Frequency Adiabatic Potentials

In the previous chapter, the case of trapping atoms using static magnetic fields was considered. In this chapter, it will be shown that by additionally coupling different Zeeman states by a rapidly oscillating field in the radio-frequency (rf) range, the internal states of the atom are dressed and new eigenstates and eigenenergies of the system can be derived.

The effective potential allows new trapping geometries that go beyond the geometries that are possible following Maxwells equations. The coupling introduced by the rf field is again magnetic. However, due to its vector character, the coupling depends on the relative direction of static field and rf amplitude. By using inhomogeneous static fields or spatially varying rf fields, the spatially dependent coupling term will lead to novel trapping geometries. In section 3.2, the creation of different potential landscapes that are possible by combining a standard Ioffe trap and two linearly polarized rf fields are introduced.

When this scheme is implemented on an atom chip, imperfections in the shape of the adiabatic potential arise that will be discussed in the following sections. Different strategies to avoid field inhomogeneities and to reduce unwanted variations in the trap bottom are shown for the case of a tube-like trap in section 3.4. Such a tube-like trap leads to a two-dimensional trapping configuration if the confinement perpendicular to the tube is high enough to restrict the dynamics of the atoms to movements within the 'wall' of the tube and if the variations within the 'wall' of the tube are small compared to this energy scale.

An advanced realization of such a trap that uses the rf fields of four wires was developed in this thesis and will be presented in section 3.4.2. There, it will be shown that this wire layout allows to reduce the variations in the effective potential to values well below the chemical potential of a typical atomic sample. Therefore, this wire configuration that is implemented in the new Bose-Fermi experiment (introduced in more detail in chapter 6) will allow the realization of a novel two-dimensional trapping configuration with periodic boundary conditions.

Additionally, the three-dimensional nature of the trapping potential is investigated, highlighting the possibility of forming a small scale interferometer in real space using adiabatic rf potentials. As a last point in section 3.5, the species-selective nature of the adiabatic potential is explained and several different possible experiments feasible in the new setup of the K-Rb experiment will be suggested.

3.1. Dressed-State Hamiltonian

Theory presented in this section can be found in more detail in [43, 85]. For the moment the influence of gravity is neglected. In section 3.3.2, it will be shown that gravity can play a significant role in the shape of the trapping potential.

As it was shown in section 2.1, the presence of a B field lifts the degeneracy of the different Zeeman levels in an atom and certain atomic states can be trapped at a magnetic field minimum. The Hamiltonian of the system is then defined as

$$H = \frac{\mathbf{p}^2}{2m} + g_F \mu_B \mathbf{F} \cdot \mathbf{B}(\mathbf{r}, t)$$

with $\mathbf{F}$ being the total angular momentum operator of the atom. $\mathbf{B}(\mathbf{r}, t)$ being composed of a static part $\mathbf{B}_S(\mathbf{r})$ and a rapidly oscillating term $\mathbf{B}_{RF}(\mathbf{r}, t)$ that itself can be composed of several different rf fields with phase shifts δ_n

$$\mathbf{B}_{RF}(\mathbf{r}, t) = \sum_n \mathbf{B}_{RF,n}(\mathbf{r}) \cos(\omega t - \delta_n).$$

The static part of the magnetic field shall be such that it traps the atoms spatially, and the local direction of $\mathbf{B}_S(\mathbf{r})$ is chosen to be the local quantization axis. By employing a unitary transformation $U_S(\mathbf{r})$, the interaction with the static field $\mathbf{B}_S(\mathbf{r})$ is transformed into a diagonal form:

$$U_S^\dagger(\mathbf{r}) \mathbf{B}_S(\mathbf{r}) U_S(\mathbf{r}) \cdot \mathbf{F} = F_z |\mathbf{B}_S(\mathbf{r})|.$$

F_z being a diagonal matrix with the entries m_F with $-F < m_F < F$. This transformation splits the time-dependent part $\mathbf{B}_{RF}(\mathbf{r}, t)$ into a part $\widetilde{B}_{RF,z}(\mathbf{r}, t)$ parallel to the local direction of the static field (the z-axis) and a part $\widetilde{B}_{RF,\perp}(\mathbf{r}, t) = \sqrt{\widetilde{B}_{RF,x}(\mathbf{r}, t)^2 + \widetilde{B}_{RF,y}(\mathbf{r}, t)^2}$ that is perpendicular to this axis. Here and for the rest of this section, $\widetilde{B}_i$ denotes the magnetic fields in the new rotated coordinate system with its z-axis along the direction of the static field.

The rotation leads to the new Hamiltonian

$$\begin{aligned} H' &= \frac{1}{2m}[\mathbf{p} + \mathbf{A}(\mathbf{r}, t)]^2 + g_F \mu_B |\mathbf{B}_S(\mathbf{r})| F_z + g_F \mu_B \widetilde{B}_{RF,z}(\mathbf{r}, t) F_z \\ &+ g_F \mu_B \widetilde{B}_{RF,x}(\mathbf{r}, t) F_x + g_F \mu_B \widetilde{B}_{RF,y}(\mathbf{r}, t) F_y, \end{aligned} \tag{3.1}$$

with the gauge term $\mathbf{A}(\mathbf{r}, t)$ that arises in the new coordinate system.

To remove the time dependencies in equation(3.1), one can go to a frame that rotates with ω around the local z-axis by using the unitary transformation $U_R = \exp[-i \frac{g_F}{|g_F|} F_z \omega t]$. After some algebra [85], the Hamiltonian can be split into time-dependent and time-independent terms and several approximations can be made:

The first assumption is that the dynamics in the $\widetilde{e}_x$-$\widetilde{e}_y$-plane is dominated by the rf frequency ω. The Larmor frequency that is due to the projection of the amplitude of the n-th rf field on the static field has to be is small compared to the rf frequency:

$$\omega \gg w_{Larmor,||} = |\frac{g_F \mu_B \widetilde{B}_{RF,n,z}}{\hbar}|.$$

Then the part of the rf field that is parallel to the static field can be neglected.

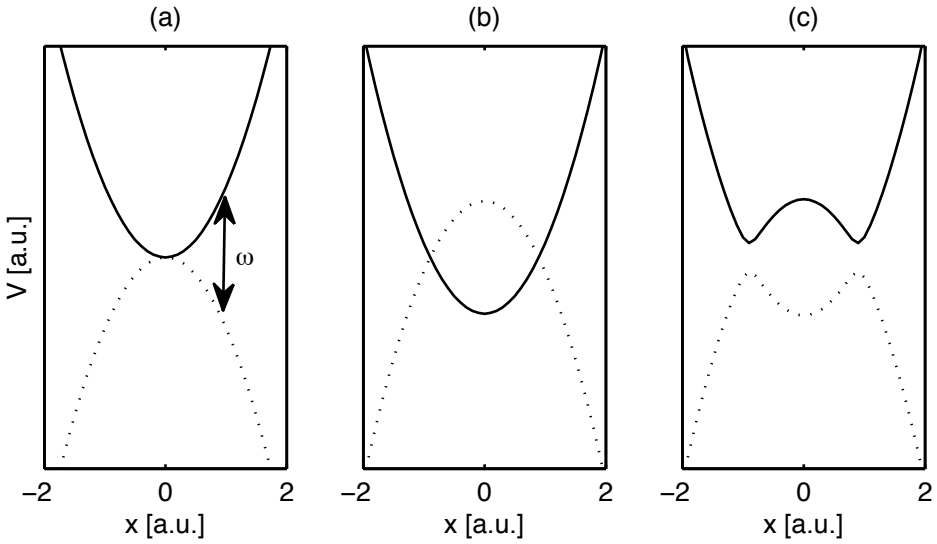

Figure 3.1.: **(a)** One-dimensional example of a two-level system coupled by a rf photon with frequency ω. **(b)** Through the coupling, the levels are shifted and intersect if the frequency ω is bigger than the energy difference between the two levels at the trap center. **(c)** The coupling term Ω leads to an avoided crossing and a level repulsion of the two dressed states.

In a second step, the so-called rotating wave approximation (RWA) is applied, similar to the formalism developed in the description of the dressing of atomic states in the optical regime. This is done by neglecting terms that in the rotating reference frame are now oscillating with $2\,\omega$ and leads to the simplified Hamiltonian:

$$H_{\mathrm{RWA}} = \frac{1}{2m}[\mathbf{p} + \mathbf{A}'(\mathbf{r},t)]^2 + \left[g_F \mu_B |\mathbf{B}_s(\mathbf{r})| - \frac{g_F}{|g_F|}\hbar\omega\right] F_z + g_F \mu_B \left(B_{\mathrm{eff},x} F_x + B_{\mathrm{eff},y} F_y\right)$$

with the effective fields

$$\begin{aligned} B_{\mathrm{eff},x}(\mathbf{r}) &= \frac{1}{2}\sum_n \left(\cos(\gamma_n), -\sin(\gamma_n), 0\right) \cdot \widetilde{\mathbf{B}}_{RF,n}(\mathbf{r}) \\ B_{\mathrm{eff},y}(\mathbf{r}) &= \frac{1}{2}\sum_n \left(\sin(\gamma_n), \cos(\gamma_n), 0\right) \cdot \widetilde{\mathbf{B}}_{RF,n}(\mathbf{r}) \\ B_{\mathrm{eff},z}(\mathbf{r}) &= |\mathbf{B}_s(\mathbf{r})| - \frac{\hbar\omega}{|g_F|\mu_B} \end{aligned} \tag{3.2}$$

and the angle $\gamma_n = -\frac{g_F}{|g_F|}\delta_n$, describing a rotation around the axis of the static field.

Again this Hamiltonian can be diagonalized and, in the adiabatic approximation, the gauge term is omitted. Therefore, one arrives at the final Hamiltonian

$$H_{ad} = \frac{\mathbf{p}^2}{2m} + g_F \mu_B |\mathbf{B}_{\mathrm{eff}}(\mathbf{r})| F_z = \frac{\mathbf{p}^2}{2m} + V_{ad}(\mathbf{r})$$

with the adiabatic potential

$$V_{ad}(\mathbf{r}) = \tilde{m}_F g_F \mu_B \sqrt{\Delta(\mathbf{r})^2 + \Omega(\mathbf{r},\delta)^2}, \tag{3.3}$$

where the new $\tilde{m}_F$ are now defined along $B_{\mathrm{eff},z}(\mathbf{r})$.

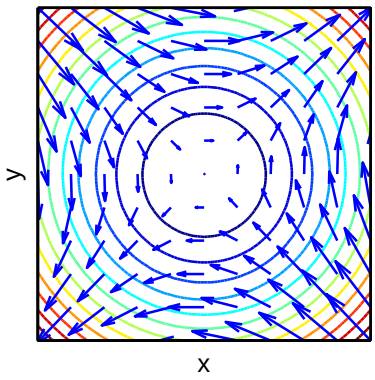

Figure 3.2: Transversal cut through the magnetic field configuration of a Ioffe trap. Visible are the equipotential lines of $|\mathbf{B}_s|$ as contours, showing the rotational symmetry of the absolute value and the direction of the magnetic field in the x-y plane.

In equation (3.3), the two terms can be identified as follows:

- The detuning term $\Delta(\mathbf{r}) = B_s(\mathbf{r}) - \frac{\hbar\omega}{|g_F|\mu_B}$ describes the energy difference between the energy of the rf photon $\hbar\omega$ and the space-dependent energy splitting between adjacent Zeeman states in the static field $\mathbf{B}_s(\mathbf{r})$.
- the coupling term $\Omega(\mathbf{r}) = \sqrt{B^2_{\mathrm{eff},x}(\mathbf{r}) + B^2_{\mathrm{eff},y}(\mathbf{r})}$ is a measure of the local coupling between the levels that are connected by the rf frequency. In the case, where the detuning term Δ vanishes locally, this term is responsible for the avoided crossing and the level repulsion, as sketched in figure 3.1. In this situation, the coupling term acts as an effective Ioffe field preventing Majorana flips. It is important to stress that only rf amplitudes that are perpendicular to the static field give a contribution to the coupling.

3.2. Possible Trapping Configurations

All experiments in this thesis are performed with atoms that are trapped in a static trap that has a Ioffe-Pritchard geometry and usually a high aspect ratio. In this section, the situation perpendicular to the trapping wire in such a trapping geometry is described in more detail, neglecting the z-dependence of the Ioffe field. The three-dimensional nature of the rf potential is discussed in detail in section 3.5.

As seen in the previous chapter, the static field of a Ioffe trap can be defined as

$$\mathbf{B}_s(\mathbf{r}) = Gy\mathbf{e}_x + Gx\mathbf{e}_y + B_I\mathbf{e}_z \tag{3.4}$$

with G being the gradient. In figure 3.2, a cut through the quadrupole geometry in the $\mathbf{e}_x, \mathbf{e}_y$-plane of the field defined in equation (3.4) is depicted.

Defining polar coordinates in this plane, the static B field is for any point (ρ, φ) with $\rho = \sqrt{x^2 + y^2}$ and $\tan\varphi = y/x$ given by

$$\mathbf{B}_S(\rho, \varphi) = |B_s(\rho)|\mathbf{e}_{\pi/2-\varphi}.$$

As the magnitude B_s is rotationally invariant, the detuning term Δ in equation (3.3) will again be rotationally symmetric.

Depending on the ratio of the rf frequency ω compared to the Ioffe field B_I two cases arise:

- if $\hbar\omega < |g_F|\mu_B B_I$, the detuning term $\Delta(\rho)$ reflects the shape of $|B(\rho)|$, only its magnitude is reduced by $\frac{\hbar\omega}{|g_F|\mu_B}$
- if $\hbar\omega > |g_F|\mu_B B_I$, neighboring Zeeman levels intersect, and the detuning Δ equals zero on a circle with radius $\rho = \frac{1}{G}\sqrt{\left(\frac{\hbar\omega}{|g_F|\mu_B}\right)^2 - B_I^2}$. Along this radius the only contribution to the effective potential is due to the coupling term Ω.

In any of these cases, the shape of the potential as a function of the polar angle is only determined by the coupling term Ω. The different trapping geometries in the x-y plane that are possible by changing the spatial dependency of the coupling term will be discussed in the rest of this section.

3.2.1. One Linear RF Field

First, the case of the static trap configuration defined in equation (3.4) and a homogeneous rf field of amplitude B_{RF} that has an angle α with the x-axis is considered:

$$\mathbf{B}_{RF} = (\cos\alpha, \sin\alpha, 0)\cos(\omega t).$$

With this rf field, the coupling term defined in (3.3) evaluates to

$$\Omega^2(\mathbf{r}) = \frac{B_{RF}^2}{4B_s^2(r)}\left(G^2(x\cos(\alpha) - y\sin(\alpha))^2 + B_I^2\right).$$

Using cylindrical coordinates (r, φ) for x and y this coupling term simplifies to

$$\Omega^2(\mathbf{r}) = \frac{B_{RF}^2}{4B_s^2(r)}\left(G^2 r^2\cos^2(\alpha+\varphi) + B_I^2\right). \tag{3.5}$$

Depending on the angle α of the rf field with the x-axis, the positions of minimal coupling are found to be at the polar angles $\varphi = -\alpha \pm \pi/2$.

Looking at the vector character of the both fields $\mathbf{B}_{RF}$ and $\mathbf{B}_s$, or more formally, at the physical content of equation (3.1), it is clear that for minima in the Rabi frequency the perpendicular contribution of $\mathbf{B}_{RF}$ to $\mathbf{B}_s$ has to be minimal. This is the case at locations where both vectors $\mathbf{B}_{RF}$ and $\mathbf{B}_s$ are parallel or anti-parallel in the x-y plane. A typical double-well configuration that arises in the case of a linear rf field can be seen in figure 3.3.

Along the same lines, the angular positions where the coupling to the rf field are maximal, are found at the angles $-\alpha$ and $-\alpha+\pi$ where $\mathbf{B}_s$ and $\mathbf{B}_{RF}$ are perpendicular. The adiabatic potential along the axis of the minima calculates as

$$V_{ad}(r) = \tilde{m}_F g_F \mu_B \sqrt{\left(B_s(r) - \frac{\hbar\omega_{RF}}{|g_F|\mu_B}\right)^2 + \frac{B_{RF}^2 B_I^2}{4B_s^2(r)}}.$$

For the case of a negative detuning term Δ there will always be a double-well structure. For the opposite case of a positive detuning, $\Delta = B_s - \hbar\omega/|g_F|\mu_B$, there will be a splitting in a double-well once a critical amplitude B_C of the rf field is exceeded. This critical field evaluates to

$$B_C = 2\sqrt{B_I\Delta}.$$

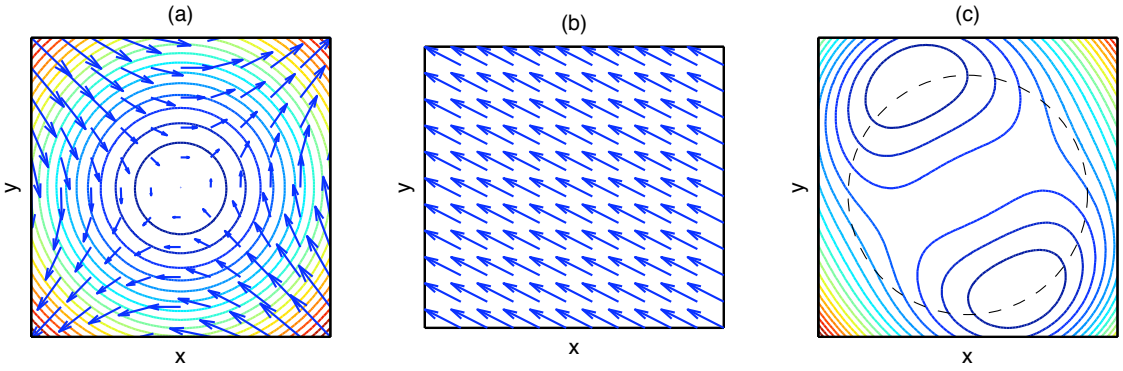

Figure 3.3.: **(a)** Magnitude and direction of the static trapping field. **(b)** Direction of the additionally applied linear rf field. **(c)** The resulting adiabatic potential. Minima are located at positions where the vectors of the static and the rf field are parallel. The dashed circle indicates the region where the resonance condition $\Delta = 0$ is fulfilled.

3.2.2. Two Linear RF Fields

By adding a second homogeneous rf field, two more degrees of freedom in the realization of complex trapping potentials are accessible: the relative amplitude of the two fields, and the relative phase of the two rf fields. First, the case of two orthogonal rf fields in the x-y plane with identical amplitudes $B_{RF}/\sqrt{2}$ and a relative phase shift of δ is discussed.

$$\mathbf{B}_{RF1} = \frac{B_{RF}}{2}(\mathbf{e}_x + \mathbf{e}_y)\cos(\omega t) \qquad \mathbf{B}_{RF2} = \frac{B_{RF}}{2}(\mathbf{e}_x - \mathbf{e}_y)\cos(\omega t + \delta)$$

With the same static Ioffe trap configuration as defined in equation (3.4), and again the replacement $\gamma = -\frac{g_F}{|g_F|}\delta$, the coupling term Ω evaluates to

$$\Omega^2(\mathbf{r}) = \frac{B_{RF}^2}{8B_s^2(\rho)}\left(B_I^2 + B_s^2(\rho) + 2B_I B_s(\rho)\sin\gamma - G^2\rho^2\cos\gamma\cos(2\varphi)\right). \tag{3.6}$$

For $\gamma = \pi$ it reproduces the result from equation (3.5) with $\alpha = 0$. Similarly, for the angle $\gamma = 0$ the corresponding result for $\alpha = \pi/2$ is recovered. This reflects the fact that the superposition of two orthogonally polarized linear fields leads for a relative phase $\delta = 0$ or π again to a linear field. This situation is depicted in figure 3.4(a) and (c).

For $\gamma = \pi/2$ and $\gamma = -\pi/2$ the last term in equation (3.6) vanishes and such the Rabi frequency Ω becomes independent of the polar angle φ. These two situations are visible in figure 3.4(b) and (d) and are discussed in more detail in the following section.

For phase shifts apart from $\gamma = n\pi$ the more general case of an elliptically polarized rf field is present. The angular position of the minima and maxima of the potential does not change for $\gamma \in]-\pi/2, \pi/2[$ from the value for $\gamma = 0$. Only the modulation depth decreases once going away from $\gamma = 0$. Similar the position of the extrema for $\gamma \in]\pi/2, 3\pi/2[$ is given by the positions for $\gamma = \pi$.

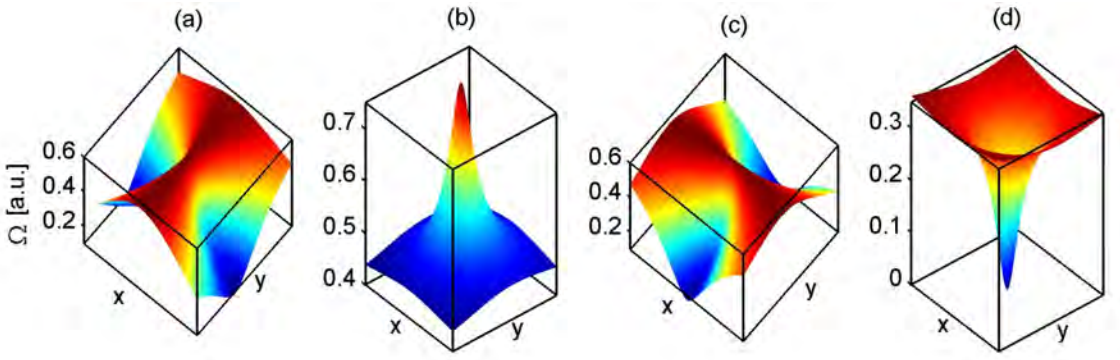

Figure 3.4.: Coupling term Ω for two perpendicular rf fields with different relative phases $\delta = -g_F/|g_F|\gamma$. The static field of figure 3.2 is applied. **(a)** and **(c)**: For $\gamma = 0(\pi)$ a linear polarization parallel to the $y(x)$-axis leads to a double-well aligned with the $x(y)$-axis. **(b)**: For a circular polarized rf field with $\gamma = \pi/2$, the coupling is maximum at the origin. **(d)**: For circular rf field with $\gamma = -\pi/2$ the coupling is zero at the center and grows with the distance. For (b) and (d) the coupling is rotational symmetric.

3.2.3. Toroidal Trap

For the rotational symmetric case of $\gamma = \pm\pi/2$ equation (3.6) can be simplified and the coupling term Ω expresses as:

$$\Omega(\rho) = \frac{B_{RF}}{2\sqrt{2}B_s(\rho)} \left(B_I \pm B_s(\rho)\right), \tag{3.7}$$

where the sign in the last term depends on the phase shift γ as defined earlier. The positive sign in equation (3.7) is valid for $\gamma = \pi/2$, the negative sign for $\gamma = -\pi/2$. Therefore, the coupling depends on a combination of the helicity of the rf field and the sign of g_F. This type of coupling is a prominent candidate for the realization of a state-dependent or species-dependent potential, as will be shown in section 3.6.

In the case of $\gamma = \pi/2$, Ω has a maximum of $B_{RF}/\sqrt{2}$ at $\rho = 0$ and asymptotically decays to $B_{RF}/2\sqrt{2}$ for large radii. In the opposite case of a negative sign, Ω vanishes at the origin and reaches the same value of $B_{RF}/2\sqrt{2}$ for large ρ.

Including the detuning term Δ, the total adiabatic potential defined in equation (3.3) reads:

$$V_{ad}(\mathbf{r}) = \tilde{m}_F g_F \mu_B \sqrt{\left(B_s(\rho) - \frac{\hbar\omega_{RF}}{|g_F|\mu_B}\right)^2 + \frac{B_{RF}^2}{8B_s^2(\rho)}\left(B_I \pm B_s(\rho)\right)^2}.$$

Similar to the case of linear rf polarization, it has to be distinguished between the resulting potential for a positive detuning term $\Delta > 0$ and for a negative detuning term $\Delta < 0$:

For $\Delta < 0$ the potential has always a minimum on a ring that has a slightly different radius than $\rho^2 = \frac{1}{G^2}\left(\left(\frac{\hbar\omega}{|g_F|\mu_B}\right)^2 - B_I^2\right)$. For the case of $\gamma = -\pi/2$ the radius is slightly reduced as the coupling term Ω has a minimum at the origin and for the case $\gamma = \pi/2$ the radius is slightly larger.

For $\Delta > 0$ the situation depends on the helicity of the rf field: For a phase shift of $\gamma = -\pi/2$, no toroidal trap is formed. In the case of opposite helicity with $\gamma = \pi/2$, there will be a splitting in a ring once a critical field amplitude B_C is exceeded. This critical field amplitude is defined as in the case of the double-well.

3.2.4. Details on the Effective Coupling

From equation (3.2) it can be seen that the vector of the effective B field $\mathbf{B}_{\text{eff}}(\mathbf{r})$ is always tilted away from the direction of the static field vector $\mathbf{B}_s$ by an angle α that is determined by the ratio

$$\tan\alpha = \frac{|\Omega_{RF}(\mathbf{r})|}{|\Delta(\mathbf{r})|}.$$

For large detunings the angle α tends to zero and the effective field is aligned parallel to the static trapping potential. On resonance ($\Delta = 0$) and for high coupling strength the angle α is 90°, and the vector of the effective field is completely perpendicular to the static field direction. For a single linear polarized rf field the vector of the effective field always lies in the plane that is defined by $\mathbf{B}_{RF}$ and $\mathbf{B}_s$.

For the case of multiple rf fields with relative phases δ_n, the situation is not as intuitive any more. As visible in equation (3.2), first a rotation of the single components of $\mathbf{B}_{RF}$ by an angle that depends on their individual phases δ_n has to be performed and subsequently a summation. Therefore, the direction and magnitude of $\mathbf{B}_{\text{eff},\perp}$ in the plane perpendicular to z does not usually coincide with the direction and magnitude of the perpendicular component of $\mathbf{B}_{RF}$.

3.3. Real-World Effects

When the rf fields are implemented in a real setup, the situation is quite different to the ideal case discussed in section 3.2.2. The two main effects, namely gravity and the spatial inhomogeneity of the applied rf fields, will be discussed for the case of a toroidal trap formed by two perpendicular rf fields with a relative phase of $\gamma = \pi/2$ as introduced in section 3.2.3. There the inhomogeneities change the rotational symmetry of the trap and introduce a variation of the trap bottom going along the torus.

The motivation for more elaborate studies of this potential was the fact that such a trapping geometry allows the realization of a novel two-dimensional trap with periodic boundary conditions if the variations in the trap bottom of the potential can be suppressed to values well below the transversal confinement.

For all numerical simulations in this and the following sections, the layout of the new K-Rb experiment is chosen. On the chip surface the new atom chip has two rf wires that are 150 µm apart. The layout will be introduced in more detail in chapter 6.2. In figure 3.5, the setup of the corresponding rf wires is shown. The labeling A to D of rf wires in figure 3.5 will be used where necessary throughout the next two sections.

3.3.1. Gravity

In all experiments in our group, the current-carrying structures are mounted in a way that the static trap is formed below the structure; therefore, gravity points away from the chip surface. To incorporate gravity in the description of the adiabatic rf potentials, the gravitational potential has to be added to the adiabatic potential in the same way as in section 2.3.3. If the axis of gravity is labeled as y-axis, one obtains:

$$V_{tot} = V_{ad} + mg\,y\,\mathbf{e}_y.$$

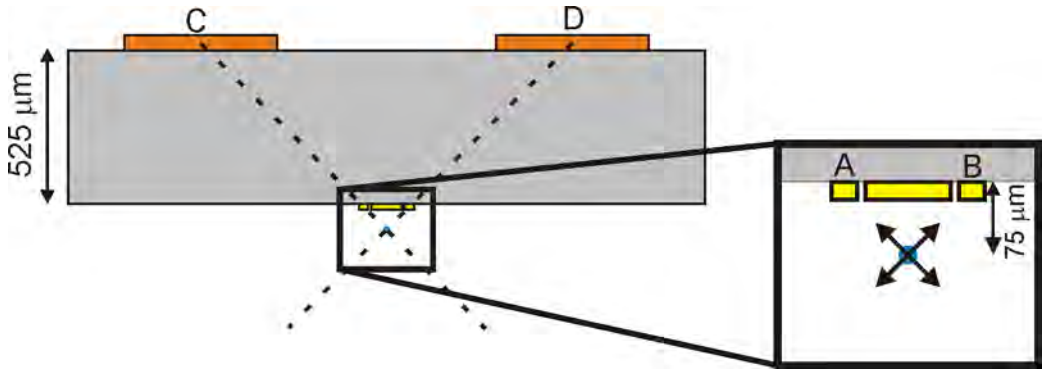

Figure 3.5.: Layout of the four rf wires in the K-Rb experiment: The atoms are statically trapped in the field of the central 100 µm gold wire visible in the inset. At a distance of 75 µm above the chip the two rf wires A and B provide two perpendicular rf fields. Two additional rf wires C and D on the back side of the 525 µm thick substrate can be used to reduce the inhomogeneities of the resulting rf field. They are aligned such that their fields at the position of the atoms are parallel to the fields originating from A and B. The height of the wires is not to scale.

For the case of a ring potential in the x-y plane, as discussed in section 3.2.3 with a radius ρ, the polar oscillation frequency along this ring can be calculate around the minimum of the combined potential V_{tot}.

In the small-angle approximation the corresponding frequency around the minimum is $\omega = \sqrt{g/\rho}$, the frequency of a pendulum of length ρ. In the case of a ring with 5 µm diameter this frequency evaluates to $2\pi \cdot 315\,\mathrm{Hz}$.

3.3.2. Real Wires

Until now, it was always assumed that the rf fields are homogeneous over the area that the atoms explore in the x-y plane perpendicular to the trapping wire. In both experimental realizations that are considered in this thesis, the situation is quite different, as in both cases the rf fields are created by single wires. The rf fields of these wires have spatially the same $1/r$-dependence as the corresponding static fields.

As an example, the static fields of the two main rf wires in the K-Rb experiment are shown in the first two panels of figure 3.6. Over a distance of 5 µm (a diameter of a typical ring trap), the field of the single rf wires varies about 10 mG that is 6 % of the total value; a fact that will be reflected in the coupling strength. As the coupling term gets larger for increasing rf amplitudes, the trap is always tilted away from the wires; therefore, this effect adds to the tilt due to gravity.

A rather small effect for the trap geometries considered here is due to the arrangement of the wires. The angle between the fields of the two wires is not perpendicular over the whole area explored by the torus. For the case of the geometry depicted in figure 3.5 and again a ring of diameter 5 µm the angle between the two rf sources varies by $\pm 2°$ around the perfect perpendicular orientation.

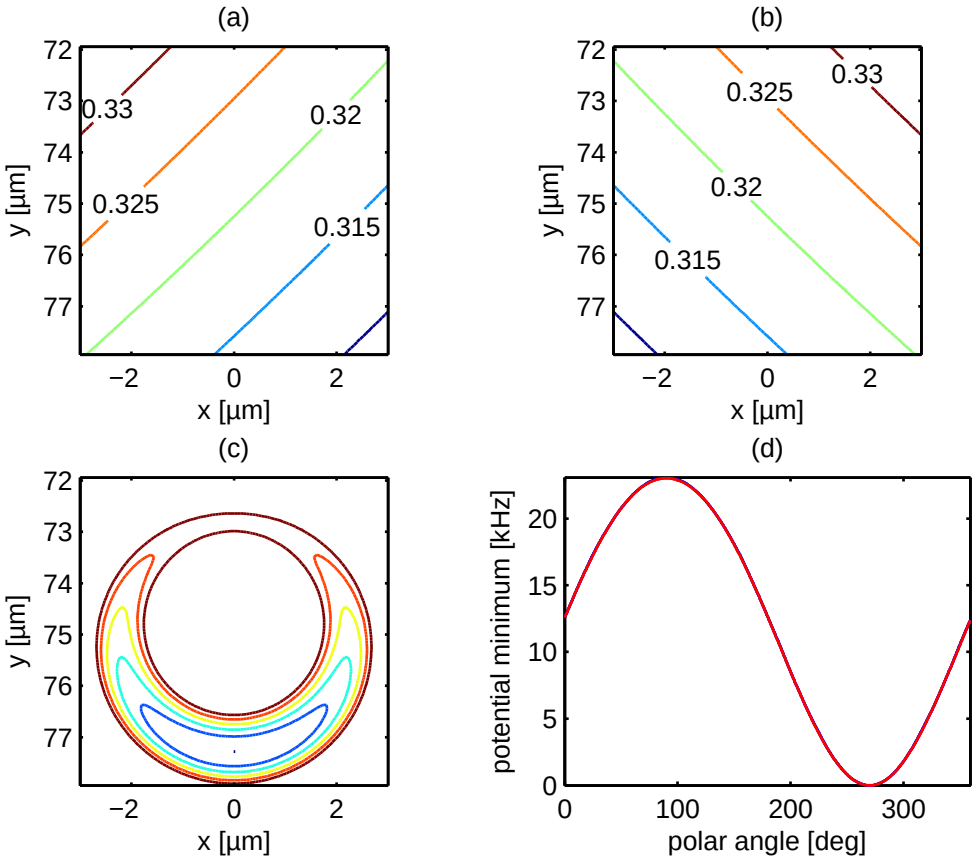

Figure 3.6.: **(a)** and **(b)**: Magnitude of the static fields created by the two rf wires A, B in G. **(c)** Equipotential lines for V_{tot} in the case of circular polarization of the rf field. The spacing of the lines is $h \cdot 5\,\mathrm{kHz}$. **(d)** Variation of trap bottom going along the ring. The polar trapping frequency around the minimum position is $2\pi{\cdot}530\,\mathrm{Hz}$. The radial trapping frequency, transversally to the torus, is $2\pi{\cdot}3.8\,\mathrm{kHz}$. Parameters used: 1 A in trapping wire, 23.5 G bias field, 0.7 G Ioffe field, $\nu_{RF} = 600\,\mathrm{kHz}$, $\delta = 0.5\,\pi$.

3.4. Feasibility of a Two-Dimensional Toroidal Trap

One of the goals of this project was the realization of a two-dimensional system using adiabatic potentials. Extending a toroidal trap as presented in section 3.2.3 in the third direction, the z-direction, a tube-like trap is obtained.

The trap can be characterized around the minimum by three distinct frequencies. The longitudinal oscillation frequency along the z direction, a transversal oscillation frequency along the radial direction in the x-y plane and a polar oscillation frequency along the ring in the x-y plane. In the case of homogeneous rf fields and a rotational symmetric trap, the polar frequency is zero.

As long as this trap has a much higher confinement in the radial direction than in polar or z direction, this trap can serve as a two-dimensional system or quasi-two-dimensional system with periodic boundary conditions.

In this section, the limiting factors for the variations of the ring potential in the x-y plane will be discussed, using the layout of the rf wires implemented in the K-Rb experiment. In the previous section, the two main mechanisms were introduced that destroy the prefect ring geometry and limit both, the minimal variations of the trap bottom going along the ring and the polar oscillation frequency around the minimum of the trap. A typical case for these variations of the trap bottom is visible in the last panel of figure 3.6.

To achieve a two-dimensional trap, the variations of the trap bottom going along the ring have to be reduced below the chemical potential of a typical atomic sample (a few kHz). In this case the atoms explore the whole volume of the tube and a two-dimensional system with periodic boundary conditions can be achieved.

To be in a two-dimensional or quasi-two-dimensional situation, the radial frequency has to be much greater than the longitudinal and polar frequency, and the chemical potential of the sample has to be below the energy scale given by the radial frequency. The system is then quenched to the lowest radial energy state, but is still free to move in the bent toroidal surface.

As will be shown in this chapter, by changing the relative phase of the two rf fields or by adding more rf fields the variations of the trap bottom in the x-y planes can be reduced greatly. A situation can be obtained that fulfills the above criteria that are necessary for a quasi-two-dimensional system.

All simulations in this section were carried out with a wire arrangement that corresponds to the layout of the K-Rb experiment that was introduced in figure 3.5.

3.4.1. Two-Wire Setup

Changing the Phase

In section 3.2.2, it was mentioned that for an elliptical polarization of the rf field the angular positions of the minima of the resulting double-well are fixed to polar angles $\varphi = n\pi/2$. Incorporating gravity and the gradient due to the inhomogeneous magnetic fields, the angular position of the two minima will depend on the relative phase between the two rf fields. In the case of a horizontal splitting, the two minima are pulled downwards to the position on the ring that is the furthest away from the chip. The closer the phase gets to the case of circular polarized rf, the closer the two minima of the double-well move together.

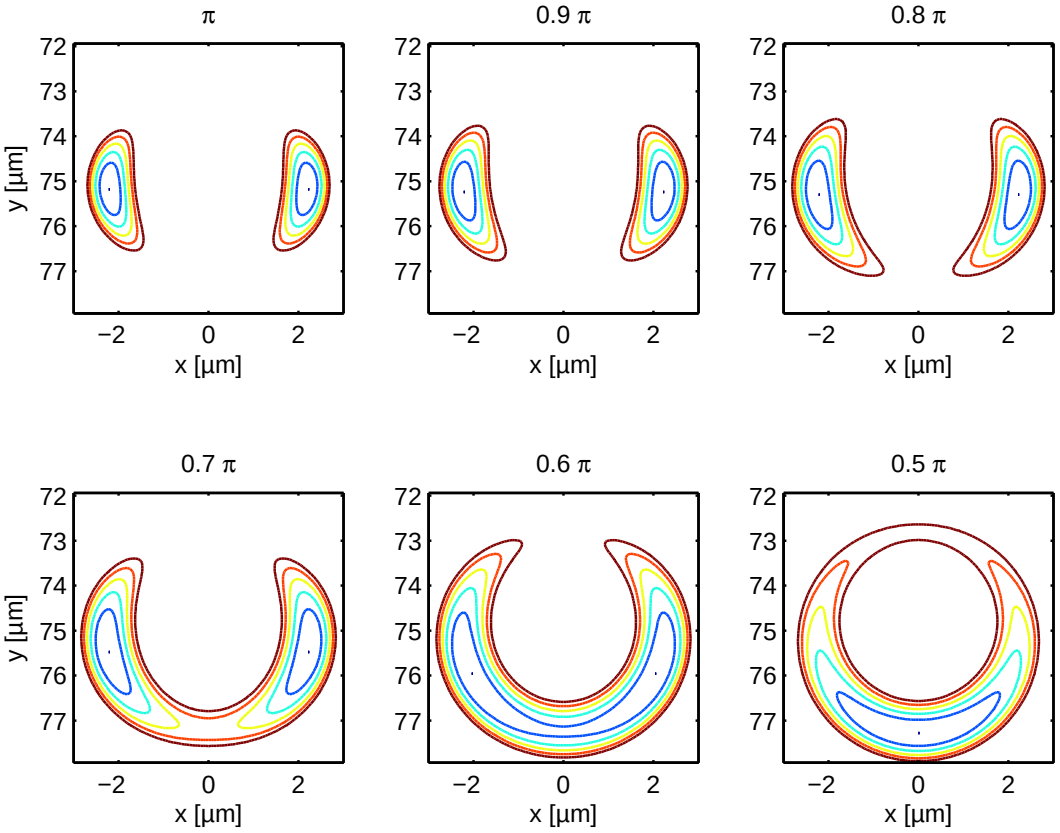

Figure 3.7.: Adiabatic potential for different phases between the two rf wires. The spacing of the lines is $h \cdot 5\,\mathrm{kHz}$. Due to the inhomogeneities in the wire potential and due to gravity the double-well structure opens downwards and joins at the position furthest away from the chip. At a phase shift between $0.5\,\pi$ and $0.6\,\pi$ there is a point where the curvature around the minimum of the potential along the polar direction is minimal.

In figure 3.7, the resulting adiabatic potentials are plotted for different relative phases of the rf fields. Between the case of a single well at the position the furthest away from the chip and a clear double-well, there is an intermediate region in which the gradient created by gravity and the inhomogeneous magnetic fields is compensated by the spatially varying coupling of the rf field. At this intermediate point the polar frequency is minimal.

This is visible by comparing figure 3.8 with figure 3.6. The only parameter changed between both simulations is the phase between the two rf wires leading to a reduction of the polar trapping frequency almost by a factor of four. Unfortunately, this strategy cannot remove the large variations in the trap bottom of more than $h \cdot 20\,\mathrm{kHz}$ along the radius of the trap. This is still much larger than the transversal trapping frequency of the trap. Therefore, the realization of a bent two-dimensional trap is feasible, but the atoms will not explore the whole volume of the torus and the surface will not be closed.

Changing the Position of the Static Trap

A second approach with the same effect as changing the phase of the rf fields, is to move the atoms closer to the chip, whilst keeping the relative phase between the rf fields fixed. As the

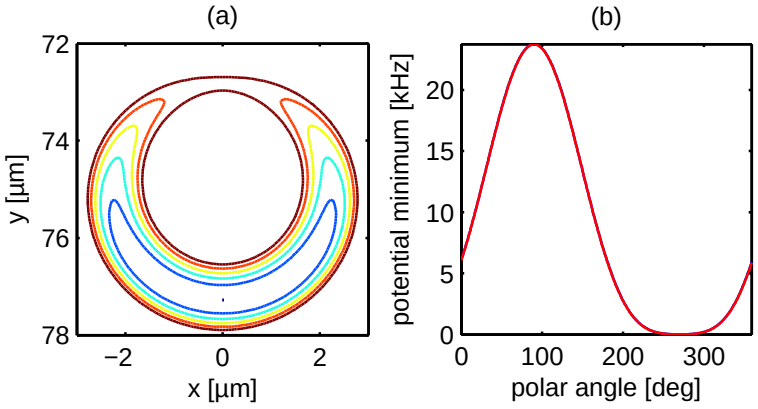

Figure 3.8: Adiabatic potential and variation of the trap bottom for a phase δ between the two rf wires of $0.544\,\pi$. All other parameters of the simulation are the same as in figure 3.6. The polar trapping frequency is reduced by more than 70 % to $2\pi{\cdot}148$ Hz.

geometric angle of the two rf sources changes, this has the identical effect as changing the phase between the rf sources as long as the two rf amplitudes are identical.

Similar to the previous example, the polar frequency is reduced to around $2\pi{\cdot}150$ Hz if the bias field is increased by 10 % compared to the values used in figure 3.6. Nevertheless, big variations in the trap bottom of $h{\cdot}20$ kHz remain along the radius of the trap.

3.4.2. Four-Wire Setup

An even more homogeneous case can be achieved if the field of each of the rf wires is created by a combination of two wires that have current flowing in opposite direction. The field of one wire of current I at a position $\mathbf{r_0}$ away from the trap position can be replaced by a different current I_1 in the same wire and an additional wire at position $(r_0+r_1)\frac{\mathbf{r_0}}{r_0}$ that has the current I_2 running in the opposite direction.

Having an additional degree of freedom, the gradient of the B field at the position of the trap can be removed by the appropriate choice of the currents I_1 and I_2:

$$\begin{aligned} B = \frac{I}{r_0} \quad &\rightarrow \quad \frac{I_1}{r_0} + \frac{I_2}{r_0+r_1} = \frac{I}{r_0} \\ \frac{dB}{dr}_{|r=r_0} = 0 \quad &\rightarrow \quad \frac{I_1}{r_0^2} + \frac{I_2}{(r_0+r_1)^2} = 0 \end{aligned}$$

$$\text{with the solutions } I_1 = -I\frac{r_0}{r_1}, \quad \text{and} \quad I_2 = I\frac{(r_0+r_1)^2}{r_0 r_1}.$$

If this technique is applied to both of the rf wires on the chip surface, one ends up with an arrangement of four wires that create the rf field for the adiabatic potential. This four-wire layout was integrated in the chip design of the new K-Rb setup that is visible in figure 3.5. The wires C and D on the backside of the chip are positioned such that their fields are parallel to the ones created by the wires A and B respectively. More details on the actual implementation of these wires on the back side of the chip can be found in section 6.5.4.

The effect of these wires on the trap geometry is visible in figure 3.9(c). If the current in the two wires on the backside of the chip is out of phase to the current in the respective wire on the front side, the large variations of the trap bottom going along the ring are suppressed by almost one order of magnitude compared to the optimized two wire trap.

As in the previous section with two wires, the potential can be made even smoother by either changing the position of the static trap, by changing the phase shift between the both

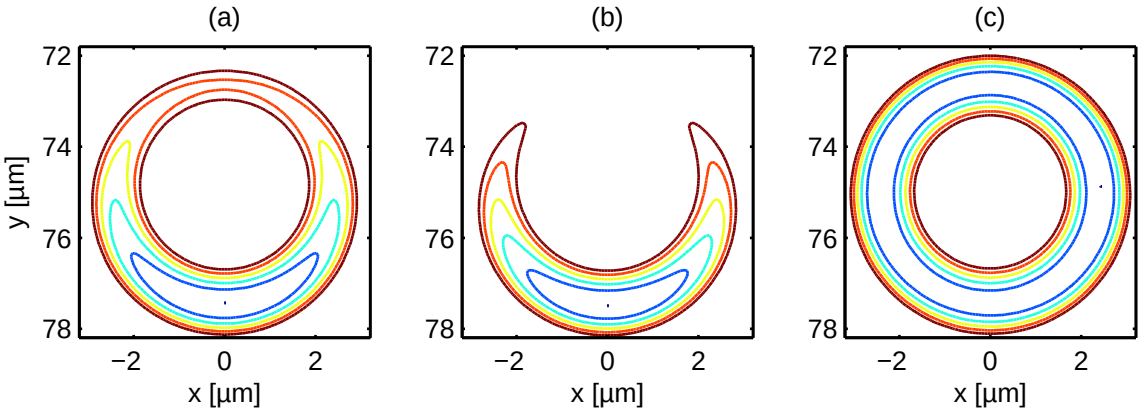

Figure 3.9.: Equipotential lines at energies 0 to 25 kHz·h, step size $h \cdot 5$ kHz for different settings of a toroidal trap. **(a)** only the two wires A, B on the front side of the chip apply a rf field. The trap is inhomogeneous due to the 1/r decay of the B fields of the rf wires. **(b)** same as (a) but additionally gravity points downwards **(c)** compensating the inhomogeneities by additionally using two more rf wires on the back side of the chip (C, D) whose currents are π out of phase with these in the rf wires A and B. Parameters used: B_I=0.8 G I_{trap}=1 A, B_B=23.5 G, ω_{RF}=2π·600 kHz, $I_{A,B}$=23 mA in (a) and (b), 17 mA in (c), $I_{C,D}$= 370 mA.

wires on the front side of the chip (A, B), or by changing the phase shift between the two wires on the back side of the chip (C, D) slightly from the value 0.5 π.

In figure 3.10, the maximum variation in trap bottom and the polar oscillation frequency around the minimum are plotted as a function of both, the current in the wires C and D and their relative phase. There is a clear minimum in both variation and oscillation frequency. For the parameters of this optimal point the variation of the trap bottom is plotted separately in figure 3.11(b) and stays below h·250 Hz. At the same time the polar oscillation frequency around the single minimum is around 2π·60 Hz.

Compared to the optimized case of a toroidal potential created by two wires as in the example of figure 3.8, this is a suppression of the variation in the trap bottom by a factor of 8. With these settings for the individual rf wires, it will be possible to create a two-dimensional trap with periodic boundary conditions in the new setup of the K-Rb experiment, as the variations are more than an order of magnitude smaller than energy scale of $h \cdot 3.8$ kHz of the radial confinement of the torus.

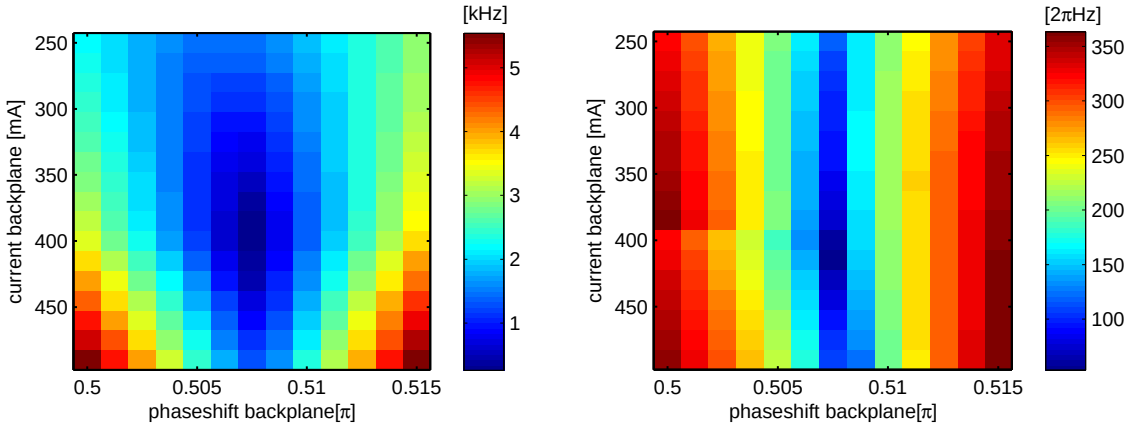

(a) Maximum variation of the trap bottom going along the ring.

(b) Polar oscillation frequency around the minimum position of the potential.

Figure 3.10.: Optimizing the smoothness of the torus by changing the current and the relative phase of the two wires on the backplane, i.e. the two wires furthest away from the atom cloud.

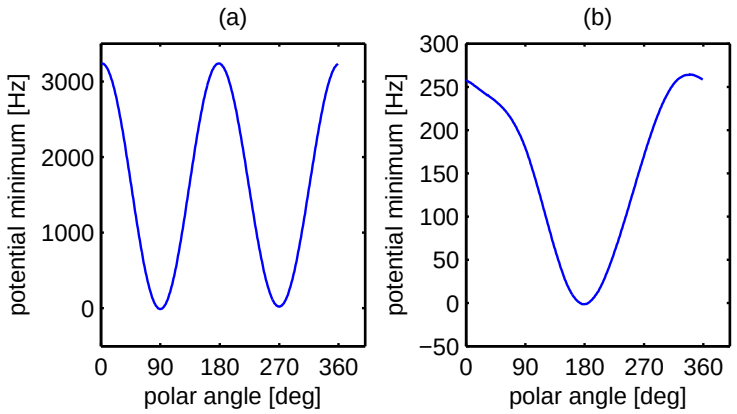

Figure 3.11: Variation in trap bottom along ring in the case of the four-wire rf setup with $I_{C,D}$=395 mA **(a)** with relative phase 0.5 π between the wires C and D **(b)** by choosing 0.5075 π the variations are suppressed by one order of magnitude. The minimum position moves to a polar angle of π. Other parameters of the simulation as before. The polar oscillation frequency in this single well is $2\pi{\cdot}60$ Hz, the transverse confinement $2\pi{\cdot}3.5$ kHz.

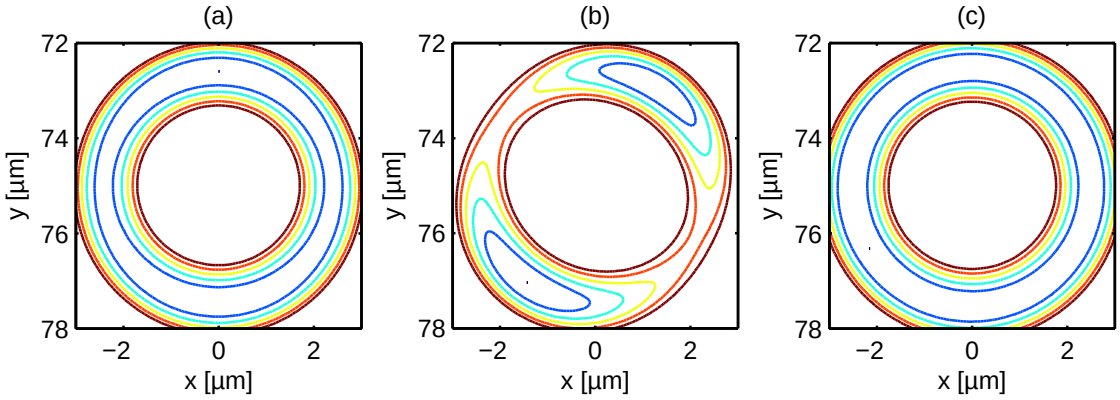

Figure 3.12.: **(a)** Same setting as in figure 3.9(c). **(b)** Backplane with wires C and D displaced by 100 µm horizontally **(c)** again a horizontal displacement of 100 µm, but now with a ratio 0.85 in the amplitudes of C and D and a phase shift 0.51 π between C and D.

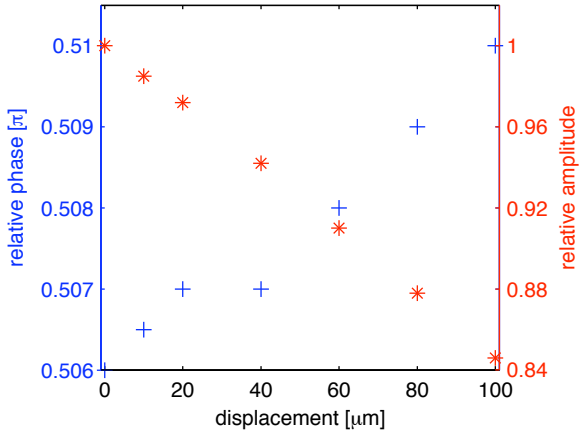

Figure 3.13: By changing the ratio of the currents in the wires C and D and their relative phase it is possible to keep the polar trapping frequency below $2\pi \cdot 100$ Hz for different horizontal displacements of the wires C, D relative to the wires A, B.

Relative Displacement of the Wires

In the case of a four-wire setup, it is technically challenging to align the pair of wires C, D on the back side of the chip substrate with the two wires A, B on the front side perfectly so that the fields of the wires A and C and of the wires B and D are parallel. A small horizontal displacement in the order of several 10 µm is hard to avoid, as will be shown in section 6.5.4.

Therefore, simulations of the trapping potential had to answer the question, whether such a misplacement in the wire positions has any effect on the resulting trap geometry and whether these effects can be compensated for by optimizing the wire currents and phases.

As an example, the resulting potential for a displacement of 100 µm and an optimal setting of the currents and the phase between C and D are visible in figure 3.12. Trying to find optimized parameters for different horizontal displacements, it can be seen that for every position, settings for the balance between the wires C and D and for their relative phase can be found with which the polar trapping frequency can be kept below $2\pi \cdot 100$ Hz.

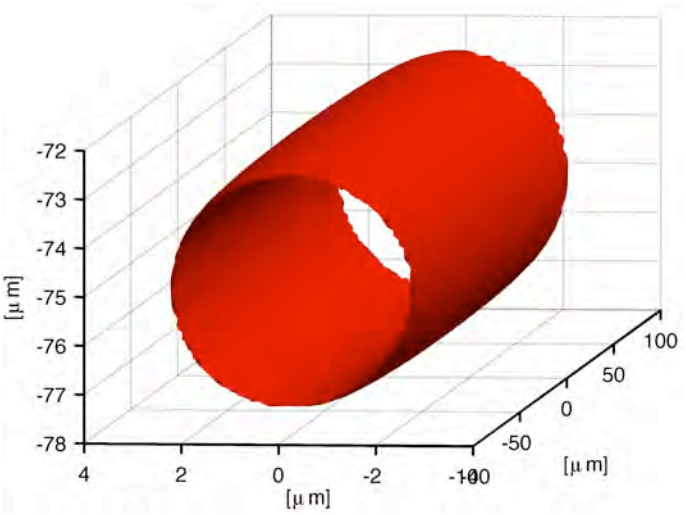

Figure 3.14: Isosurface for an energy of $h{\cdot}2\,\mathrm{kHz}$ for the optimized four-wire rf trap, as introduced in section 3.4.2, extended by a harmonic trapping potential with frequency $2\pi{\cdot}15\,\mathrm{Hz}$ along the z-direction.

3.5. Numerical Calculations in Three Dimensions

Until now, only the situation perpendicular to the direction of the trapping wire was considered, and it was assumed that the static field has no dependence on the third, the z-direction. In all trapping configurations presented in this theses, the static trapping along this direction can be described by an harmonic confinement $B_z \propto \omega_z^2 z^2$. This changes the direction of the static field $\mathbf{B}_s$ as a function of the z-coordinate. Therefore, the coupling to the rf field and the detuning between static trap and rf field will vary along this direction, ensuring that the trap is closed in this direction as well. A typical example for the three-dimensional nature of the trapping geometry is visible in figure 3.14. Here the trapping potential of the optimized four-wire geometry of section 3.4.2 is extended by a harmonic confinement along the z-direction of $2\pi{\cdot}15\,\mathrm{Hz}$.

A second effect that is visible in all numerical simulations of the employed trapping geometries, is the small rotation of the trap in the x-z-plane away from the direction z of the current flow. This is due to field inhomogeneities that are introduced through the closing wires, and was already mentioned in section 2.3.1. All simulations in this section were carried out assuming the wire configuration used in the RbII experiment (introduced in chapter 8), where the longitudinal confinement is provided by two wires that are each 500 µm wide and are 2 mm apart. In chapter 8, the distances and sizes of the single wires of the corresponding chip layout are given.

3.5.1. Beam Splitter

In section 3.1, it was shown that the splitting of a double-well depends strongly on the ratio between the absolute value of the static field and the frequency of the rf field. By changing the Ioffe field in space, a real-space beam splitter can be created on an atom chip. Such miniaturized small scale interferometers are of great interest as they allow unprecedented stability for example in metrology.

The usual realization of a Y-beam splitter with static fields has some drawbacks: Usually the outgoing waveguides have much different trapping frequencies than the input path, the

trap bottom changes suddenly at the splitting point and, due to topological reasons, there will always be a fourth waveguide pointing towards the chip surface [34].

This is not a problem in the case of rf adiabatic potentials. Here the effective magnetic field does not have to fulfill Maxwell's equations any more. A true Y-beam splitter is possible that has a smooth transition in the trap bottom and the symmetry of the splitting process can be controlled with great precision. Such a beam splitter can be realized either temporal (by deforming a single well into a double-well) [42] or spatially (by taking advantage of the three-dimensional nature of the rf coupling).

There are two slightly different cases of a spatial beam splitter possible in our setups that are visible in figures 3.15 and 3.16. Both take advantage of the modulation of the absolute field along the trap due to the longitudinal trapping.

For the first case, an rf field is applied that has a slightly lower frequency than the splitting between the neighboring Zeeman levels at the minimum of the potential. This is the case of a positive detuning term Δ. The strength of the rf field is chosen such that it exceeds the critical value B_C (see section 3.2) at the center of the trap. Moving along the trapping wire the detuning Δ grows. As $B_C \propto \Delta$, the double-well will at a certain distance smoothly merge into a single trap.

Experimentally, one could proceed as follows: first excite longitudinal oscillations in the static potential, then at the turning point of the motion switch on the rf fields. During their motion in the longitudinal potential, the atoms see a potential that is then given by the z-dependent trap bottom of the adiabatic potential. This adiabatic potential is depicted in figure 3.15 (b).

For the second case, the approach is a little different. If an rf field is added that has a slightly higher frequency than the absolute trap bottom, the trap will show again a double-well at the central position. Going away from this point along the trap, the detuning grows again and at a distance z_0 with $B_s(z_0) = \hbar\omega_{RF}$ the detuning Δ changes sign.

As long as the applied rf amplitudes stays below the critical field B_c, the double-well merges into one minimum again. For these settings, the change in the transversal oscillation frequencies is much higher than in the setting for an interferometer with the rf below the trap bottom as described previously. So, from an experimental point of view, where one tries to avoid excitations during the splitting of the cloud and where one would like to split the cloud coherently, the first situation is preferable. The experimental realization of a beam splitter with a rf frequency above the level-splitting was published just recently by the van Druten group [45].

As visible in the panels (b) of figures 3.15 and 3.16, the rf field has in both cases still an effect on the trapping geometry far away from the splitting region. Mainly the local trap bottom and such the longitudinal trapping frequency is reduced due to the coupling.

3.6. State-Selective & Species-Selective Traps

One big advantage of the adiabatic rf potentials is the fact that they allow for species-selective potentials if both species have different g_F factors. If both atoms are in their maximally stretched state, they will experience exactly the same static magnetic potential. But still situations can be created in which the atomic cloud of one species is split without a splitting of the other atomic cloud. This is for example possible in the K-Rb experiment where the two elements ^{40}K in $F = 9/2$ and ^{87}Rb with $F = 2$ have $g_F = 2/9$ and $g_F = 1/2$ respectively.

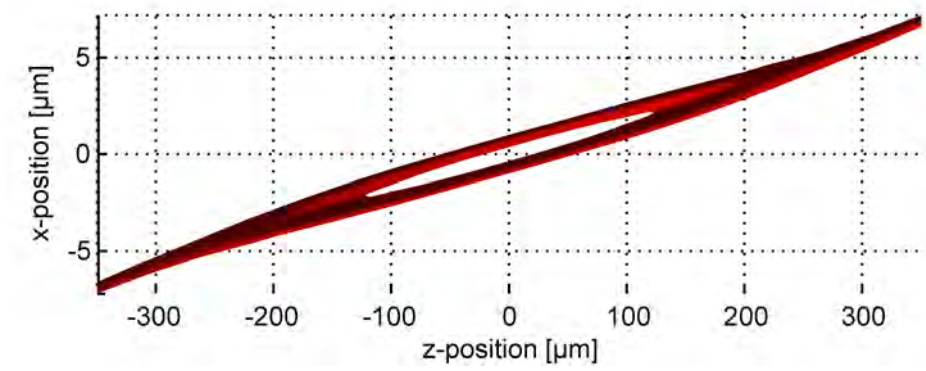

(a)

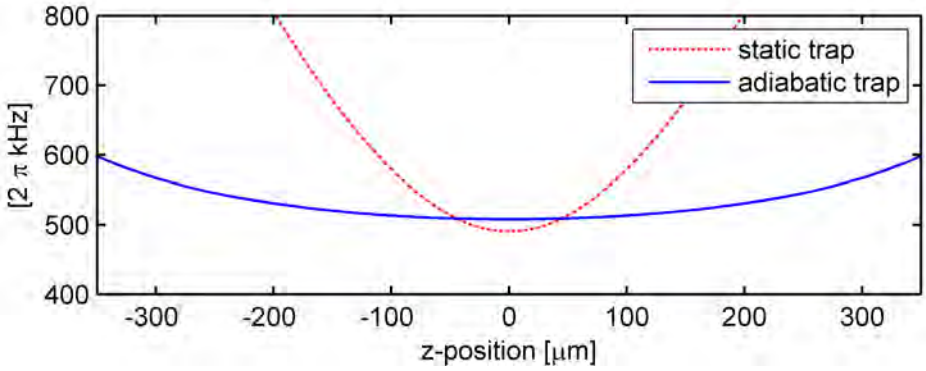

(b)

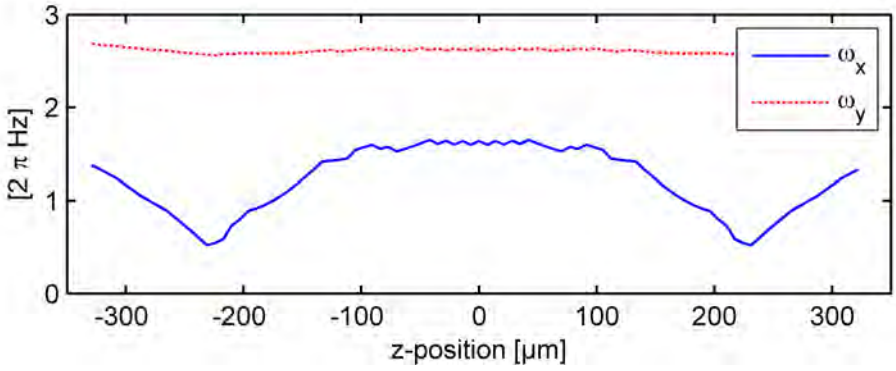

(c)

Figure 3.15.: Real space interferometer realized by tuning the rf frequency below the level spacing at the minimum Ioffe field and by making the rf amplitude high enough so that the critical field for splitting is exceeded in the central region. **(a)** Isoenergy surface $2\pi\cdot 1$ kHz for the adiabatic potential after subtracting for each z-position the corresponding trap bottom. This is the potential locally seen by atoms at the corresponding z-position. The slight rotation of the static trap is due to the fields of the closing wires. **(b)** Trap bottom for the adiabatic and static trap. **(c)** Horizontal and vertical transverse trapping frequencies. At the point of the Y-junction the horizontal trapping frequency is greatly reduced. Parameters used: I_{trap}=0.5 A, B_{Bias}=17 G, longitudinal confinement by two wires 2 mm apart, each with 1 A, I_{RF}=20 mA, $\delta=\pi$, ν_{RF}=365 kHz, trap bottom of static trap 0.7 G.

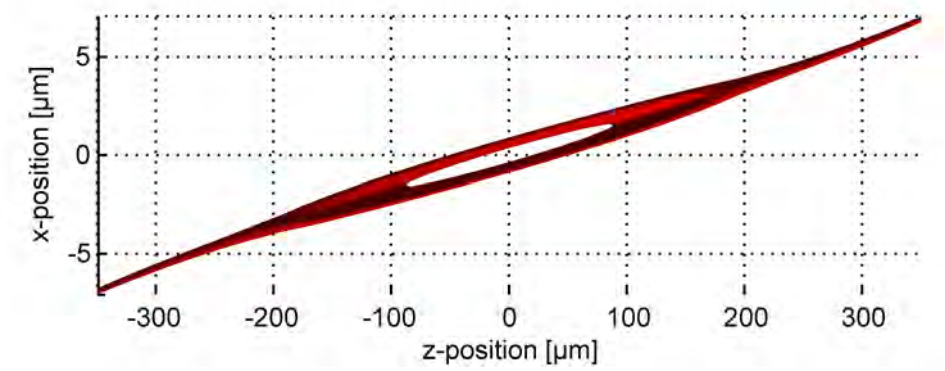

(a)

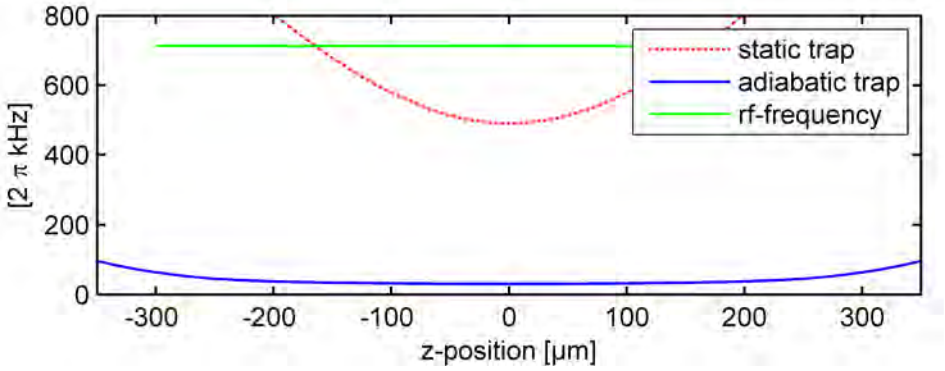

(b)

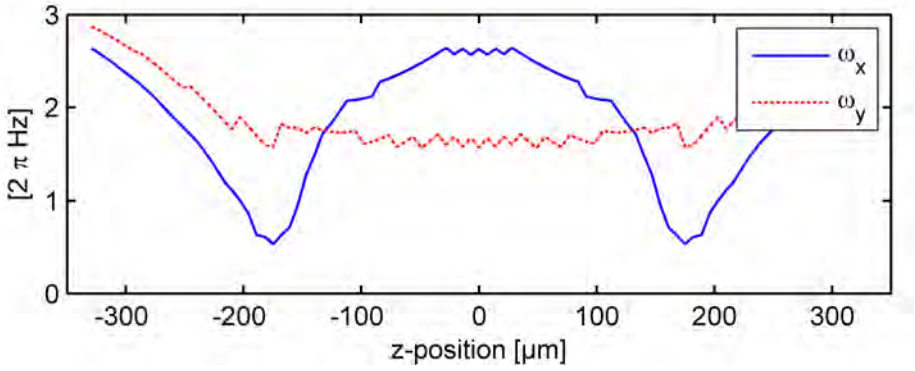

(c)

Figure 3.16.: Beam splitter by using a rf frequency that is bigger than the minimum level spacing introduced by the static field. Compared to the previous picture these settings have the drawback that the trap bottom of the adiabatic trap in **(b)** is rather small and in **(c)** the change in the transversal trapping frequencies is much bigger than for the case of the interferometer in fig. 3.15. In **(b)** additionally the rf frequency is plotted as reference. Splitting occurs once the rf frequency is bigger than the trap bottom of the static trap. The wiggles visible in the plots for the trapping frequencies have no physical origin: They are due to the finite grid used for the calculations. Parameters used: I_{RF}=5 mA, ν_{RF}=500 kHz, other parameters as in the previous figure.

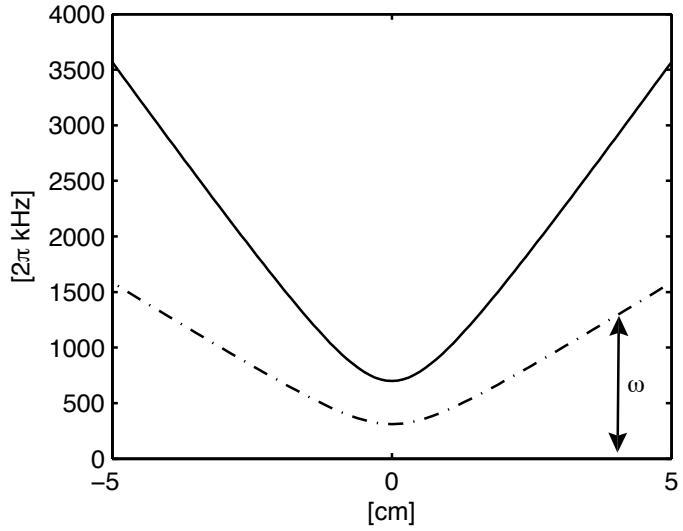

Figure 3.17: Zeeman splitting between two neighboring m_F-states for ^{87}Rb (solid) and ^{40}K(dashed) in a potential of 1 G Ioffe field and a gradient of 1 G/cm. Depending on the applied rf frequency ω only one of the potentials is split in a double-well.

Species-selective traps between bosons and fermions allow truly new experiments, for example by looking at the coupling between bosons that is mediated by fermions. By splitting a quasi one-dimensional BEC into a double-well and having an unsplit fermionic cloud sitting right between the two BECs, a situation can be created in which the fermionic cloud has an overlap with both bosonic clouds, whilst the barrier between the BECs is high enough so that there is no other coupling between them. In section 5.2.2, this situation will be studied in more detail.

For simplicity, only the one-dimensional case with the formation of a double-well is considered in the following. Nevertheless, the same arguments still hold for a ring trap or a double-well in two dimensions perpendicular to the current-carrying wire.

Due to the different g_F factors, the Zeeman splitting is different for both species. For clarity, the splitting between neighboring Zeeman levels in the case of ^{40}K and ^{87}Rb is plotted in figure 3.17.

Depending on the frequency of the rf field used, there are two different scenarios possible:

- If the rf frequency is chosen such that it is above the trap bottom for ^{40}K, but still below the trap bottom of ^{87}Rb, the potassium cloud will be split in a double-well or ring, whilst the Rb atoms are, in a first approximation, still experiencing their static trap. By increasing the frequency of the rf field, the minima of the double well for potassium move further away from each other. This is due to the fact that the resonance condition, where the rf frequency and the splitting between the hyperfine levels are resonant, is fulfilled at larger and larger distances from the minimum of the trap.

  At a certain frequency, close to the resonance condition between the trap bottom of the Rb atoms and the rf field, their trap will be split as well, but the distance of the minima of the Rb potential will always be smaller than the distance of the minima for the ^{40}K cloud.

- To create the opposite situation of a split bosonic Rb cloud with a fermionic K cloud still experiencing the initial static trap, a rf frequency ω_{RF} can be chosen that is slightly below the trap bottom for Rb. For a Ioffe field of 1 Gauss, the trap bottom is resonant with an rf frequency of $2\pi\cdot700\,\mathrm{kHz}$. Therefore, the rf is $2\pi\cdot389\,\mathrm{kHz}$ detuned from the transition frequency between the undressed states of the potassium potential. The hyperfine transitions with $\Delta m_F = 2$ or 3 in ^{40}K are closer to the rubidium frequency, but forbidden due to selection rules. On the potential for ^{40}K this rf frequency acts like a rf knife opening the potential at high energy values, so only for sufficiently cold samples they are not influenced by this frequency. If now the rf frequency is swept to higher values, the Rb cloud will be split to larger and larger distances, leaving the potassium cloud unchanged.

For the case of a circular polarization of the rf field, there is another possibility for rotational symmetric species-dependent potentials. Working with states whose g_F factors have the opposing sign, for example the combination of ^{87}Rb in $F = 1$ with $g_F = -1/2$ in combination with the same species in $F = 2$, or the combination ^{87}Rb in F=1 with ^{40}K in $F = 9/2$, the phase shift $\gamma = -\frac{g_F}{|g_F|}\delta$ has the opposite sign for both species. So it can be chosen to be π for one species and $-\pi$ for the other. Therefore, one cloud experiences a toroidal trap potential in two dimensions, whereas the other one is still at the position of the static trap and even more strongly confined. This could actually be a way to store these mixtures in the same magnetic trap for longer times, as due to the reduced spatial overlap of both clouds, the inelastic scattering processes (see section 5.1.1 for more details) that are dominant in these mixtures are greatly reduced.

4 Cold Bosons & Fermions

In this chapter, the basic concepts of degenerate quantum gases will be reviewed. The statistical approach followed in section 4.1 is valid for non-interacting particles like identical spin-polarized fermions and is a reasonably good approximation for thermal clouds of bosons. This leads to a good estimate for the transition temperature to a Bose-Einstein condensate.

To gain more insight in the properties of the ground state of the bosonic system, the interactions between the atoms have to be taken into account, and in section 4.1.3 it will be shown that even if the atomic cloud is dilute, interactions dominate in most situations the behavior of the condensed phase.

In section 4.2, the density distributions for fermionic and bosonic systems at T=0 will be studied in more detail. Furthermore, in section 4.3 it will be explained that the density and momentum distribution of dilute atomic gases can be derived for arbitrary temperatures and expansion times. Therefore, the measurement of the shape of an expanded cloud of atoms is a good thermometer for these samples.

For more details on the description of cold bosons the reader is directed at textbooks, e.g. [51], and reviews like [86]. The properties of a harmonically trapped Fermi gases at low temperatures can, for example, be found in [87, 88] and are nicely described in the thesis of DeMarco [15].

4.1. Statistics

First, the situation of a trapped many particle system with discrete single-particle eigenstates ϵ_n is considered. From a statistical viewpoint the difference between bosons and fermions manifests in the mean occupation number of the single-particle eigenstates that show their difference especially in the limit of low temperatures.

By introducing a parameter $a = 0, \pm 1$, the distribution function can be treated in the same formalism, independent of the underlying statistics. ϵ_n denotes the energy of the single particle state for the particular trapping potential considered. Then, the distribution function can be written as

$$f(\epsilon_n) = \frac{1}{\exp[\beta(\epsilon_n - \mu)] + a} \tag{4.1}$$

with the abbreviation $\beta = 1/k_B T$ and the chemical potential μ. The constant a takes the values $a = -1$ for Bose-Einstein statistics and $a = +1$ for Fermi-Dirac statistics. At high temperatures, the effects of quantum statistics become negligible, and the classical Maxwell-Boltzmann distribution is recovered. In equation (4.1) this limit is reproduced by going to $a = 0$. For the following calculations, it is mathematically favorable to introduce the fugacity $\mathfrak{z}$, defined as $\mathfrak{z} = \exp[\beta\mu]$.

The main differences between bosons and fermions is already visible from equation (4.1): for Fermi-Dirac statistics the occupation number of the single energy levels is always less or equal one, for bosons the occupation number can diverge, a fact that is related to the macroscopical occupation of a single state at low temperatures.

For the distribution functions in equation (4.1), the chemical potential μ and such the fugacity $\mathfrak{z}$ are for a given temperature fixed by the normalization condition that the summation over all energy levels has to reproduce the atom number:

$$\sum f(\epsilon_n) = N.$$

To go from a discrete summation over energy levels to an integration, the density of states that corresponds to the respective trapping configuration has to be calculated. Considering the typical case of a harmonic trap in three dimensions

$$V(r) = \frac{1}{2} m(\omega_1 x_1^2 + \omega_2 x_2^2 + \omega_3 x_3^2), \tag{4.2}$$

the density of states can be calculated to

$$g(\epsilon) = \frac{\epsilon^2}{2(\hbar\bar{\omega})^3}$$

with the mean trapping frequency $\bar{\omega}^3 = \omega_1\omega_2\omega_3$.

In the limit of a large number of atoms N, the energy difference between the single states becomes small, and the number of excited atoms that have an energy other than the ground state can then for the cases $a = \pm 1$ be calculated by an integration over the distribution function:

$$N_{ex} = \int_0^\infty f(\epsilon) g(\epsilon)\, d\epsilon = -a \left(\frac{k_B T}{\hbar\bar{\omega}}\right)^3 Li_3(-a\mathfrak{z}). \tag{4.3}$$

The function $Li_n(x)$ appears often in the context of harmonically trapped quantum gases and is the so-called polylogarithm that is defined as

$$Li_n(x) = \sum_{l=1}^{\infty} \frac{x^l}{l^n}.$$

It converges for real valued x with $x \leq 1$. In physics, $-aLi_n(-a\mathfrak{z})$ is sometimes called either Fermi-Dirac integral, or Bose-Einstein integral, depending on the sign of a. For the argument $x = 1$, $Li_n(x)$ can be identified with the Riemann Zeta function $\zeta(n)$.

In figure 4.1, the chemical potential is plotted as a function of the temperature for all three statistics considered. In all cases, the chemical potential is less than zero at high temperatures. For bosons it approaches the ground state energy at low T. For fermions the chemical potential is always higher than in the Maxwell-Boltzmann case and approaches the Fermi energy for T=0.

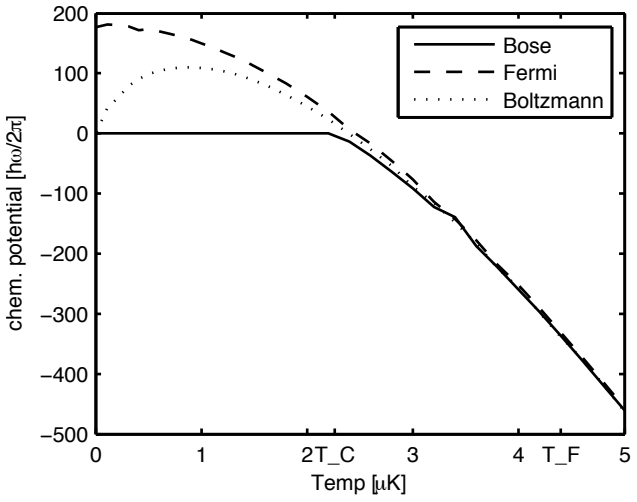

Figure 4.1: Chemical potential in units of $\hbar\bar{\omega}$ for 10^6 non-interacting atoms in a three-dimensional harmonic trapping potential with a mean trapping frequency of $\bar{\omega}$=2π·500 Hz. In the fermionic case the chemical potential approaches the Fermi energy at low temperatures. For bosons the chemical potential in the condensate phase is the ground state energy. On the temperature axis the critical temperature T_C of the BEC and the Fermi temperature T_F are given as reference.

4.1.1. Fermions

For fermions at $T = 0$, the distribution function (4.1) simplifies greatly: For energies ϵ larger than the chemical potential μ, the occupation of these levels vanishes. For energies below μ, all energy levels have the occupation one. In this case μ is identical with the Fermi energy E_F, defined as the energy up to which all levels have the occupation one.

As the occupation of the ground state is one, this state can be neglected and the number of atoms N can be identified with the number of atoms in excited states N_{ex}. Integration of equation (4.3) then leads to the relation:

$$N = \frac{E_F^3}{6(\hbar\bar{\omega})^3}.$$

This defines the Fermi energy, and the Fermi temperature T_F can be introduced via

$$E_F = k_B T_F = \hbar\bar{\omega}(6N)^{1/3}. \tag{4.4}$$

The result looks strikingly similar to the result for $k_B T_C$ that will be derived in the following section for bosons. However, other than in the bosonic case the Fermi temperature is not a critical temperature of a phase transition. It is only a crossover point characterizing the quantum nature of the system.

For typical trapping parameters in atom chip experiments with a mean trapping frequency $\bar{\omega} = 2\pi \cdot 500\,\mathrm{Hz}$ and $N = 10^6$ atoms, this transition temperature evaluates to $T_F = 4.4\,\mu\mathrm{K}$.

The definition of the Fermi temperature in equation (4.4) can be used to replace the number of particles in equation (4.3), and one arrives at a relation between the ratio T/T_F and the fugacity:

$$Li_3(-\mathfrak{z}) = -\frac{1}{6(T/T_F)^3}. \tag{4.5}$$

4.1.2. Bose-Einstein Condensation

The transition temperature to BEC is defined as temperature at which all particles can still be accommodated in the excited states. In the thermodynamic limit with $N \to \infty$, $\bar{\omega} \to 0$ and a constant density $N\bar{\omega}^3$, this transition temperature is well defined.

The critical temperature can be obtained by looking at the number of atoms in the excited states given in equation (4.3) in the limit that the chemical potential μ approaches the ground state energy of the system. In terms of the fugacity this is the limit $\mathfrak{z} \to 1$:

$$N_{ex} = \left(\frac{k_B T}{\hbar\bar{\omega}}\right)^3 Li_3(1) = \left(\frac{k_B T}{\hbar\bar{\omega}}\right)^3 \zeta(3). \tag{4.6}$$

By identifying the number of atoms in excited states N_{ex} with N, the critical temperature for the onset of condensation can be derived as

$$k_B T_C = \hbar\bar{\omega} \left(\frac{N}{\zeta(3)}\right)^{1/3}. \tag{4.7}$$

Inserting this result in equation (4.6), one arrives at a scaling relation for the number of condensed atoms in three dimensions as a function of the temperature:

$$\frac{N_0}{N} = 1 - \left(\frac{T}{T_C}\right)^3.$$

The condensation of bosons in typical chip traps is typically not in the thermodynamic limit of high atom numbers. The atom numbers reached are between $10^3 - 10^5$. Then the phase transitions is not sharp any more and is shifted to lower temperatures [89, 51]

$$\frac{\Delta T_C}{T_C} = \frac{\zeta(2)}{2[\zeta(3)]^{2/3}} \frac{\omega_1 + \omega_2 + \omega_3}{3\,\bar{\omega}} N^{-1/3} \approx -0.73 \frac{\omega_1 + \omega_2 + \omega_3}{3\bar{\omega}} N^{-1/3}. \tag{4.8}$$

The high aspect ratios of the cylindrical chip traps typically realized (around 100 to 1000), change the ratio of the average mean to the geometric mean in equation (4.8). This can enhance the temperature shift greatly for anisotropic trapping configurations.

In this section, only the case of a trapped gas in an anisotropic harmonic trap in three dimensions is considered. The situation is fundamentally different for lower dimensional systems in which the thermal energy $k_B T$ and the chemical potential are on the order of or smaller than the oscillator energies $\hbar\omega_i$ in one or two directions of the trapping potential. Whether BEC occurs, depends on the density of states in these systems. The situation for two dimensions will be discussed in more detail in section 4.4.

4.1.3. Interacting Bosons

Until now, no interactions between the particles were considered. This approximation is valid for a single component spin-polarized gas of fermions and a good approximation for thermal clouds. To evaluate the properties of the ground state of a bosonic system at low temperatures, it is not possible any more to neglect interactions. Interactions modify significantly the properties of the cold gas, for example the spatial shape and the expansion dynamics.

Assuming a properly symmetrized product state of single-particle wave functions, the fully condensed state can be expressed as the product of the same single-particle state $\phi(\mathbf{r})$. The wave function of the N-particle system then reads as

$$\Psi(\mathbf{r}_1, \ldots, \mathbf{r}_N) = \prod_{i=1}^{N} \phi(\mathbf{r}_i), \tag{4.9}$$

with the normalization of the single-particle wave function $\int d\mathbf{r}\, |\phi(\mathbf{r})|^2 = 1$.

At very low temperatures the exact shape of the interaction potential between two atoms is not important, as the thermal de Broglie wavelength $\lambda_T = \sqrt{2\pi\hbar^2/mk_BT}$ is much larger than the effective range of the interaction potential. The only relevant scattering amplitude is due to s-wave scattering and the interaction potential can be approximated by a delta like pseudo-potential $U(\mathbf{r}_i - \mathbf{r}_j) = g\delta(\mathbf{r}_i - \mathbf{r}_j)$. Therefore, the coupling strength g can be directly related to the s-wave scattering length a:

$$g = \frac{4\pi\hbar^2 a}{m}. \tag{4.10}$$

In spin-polarized bosonic quantum gases that are magnetically trapped in their maximally stretched state, the scattering length is dominated by the triplet channel. For ^{87}Rb this is $a_t = (98.98 \pm 0.04)\, a_0$ [90], a_0 being the Bohr radius $a_0 = 5.29 \cdot 10^{-11}$ m.

The approximation to neglect interactions in a single component Fermi gas is valid for sufficiently low temperatures. The first contribution to interspecies scattering processes is the the p-wave channel. Taking the typical size of a ^{40}K-^{40}K molecule orbital and the angular momentum of $\hbar$ that has to be transfered, a contribution of the p-wave channel can be estimated to play a role only for temperatures above 10 mK [91].

By using the effective interaction $U(\mathbf{r_i}-\mathbf{r}_j) = g\delta(\mathbf{r}_i-\mathbf{r}_j)$, the effective Hamiltonian including interaction is

$$H = \sum_{i=1}^{N}\left[\frac{\mathbf{p}^2}{2m} + V(\mathbf{r}_i)\right] + g\sum_{i<j}\delta(\mathbf{r}_i - \mathbf{r}_j).$$

$V(\mathbf{r})$ is the external potential. The energy of the fully condensed state of equation (4.9) is therefore given by [51]

$$E = N\int d\mathbf{r}\left[\frac{\hbar^2}{2m}|\boldsymbol{\nabla}\phi(\mathbf{r})|^2 + V(\mathbf{r})|\phi(\mathbf{r})|^2 + \frac{N-1}{2}g|\phi(\mathbf{r})|^4\right]. \tag{4.11}$$

Mean-Field Theory

When working with dilute atomic vapors, the interparticle spacing is still large compared to the scattering length a that describes the strength of interactions. With densities n where $a^3 n \ll 1$, the system can be described by a mean-field theory where all interactions between the atoms are summarized to the interaction of single particles with an effective potential [51].

Due to interaction the number of particles in the condensed state will not be N as assumed in equation (4.9), but lower. However, this depletion of the condensed state is at typical atomic densities very small and can be neglected in most cases.

The interaction term in equation (4.11) can be identified with the $N(N-1)/2$ different ways of producing pairs of bosons. In the limit of large N it can be set to$N^2/2$. By properly normalizing the wave function of the condensed state

$$\psi(\mathbf{r}) = N^{1/2}\phi(\mathbf{r}),$$

the density of particles can be identified by $n(\mathbf{r}) = |\psi(\mathbf{r})|^2$. Then the energy in equation (4.11) can be written as

$$E(\psi) = \int d\mathbf{r}\left[\frac{\hbar^2}{2m}|\nabla\psi(\mathbf{r})|^2 + V(\mathbf{r})|\psi(\mathbf{r})|^2 + \frac{1}{2}g|\psi(\mathbf{r})|^4\right]. \tag{4.12}$$

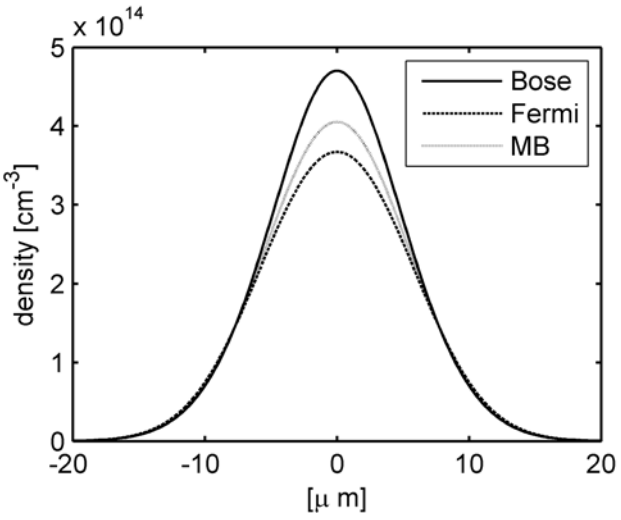

Figure 4.2: Cut through the three-dimensional in situ density distribution given by (4.15) for fermions, non-interacting bosons and an ideal gas of thermal atoms. Each at the same temperature $T = 0.7\,T_F = 1.4\,T_C$. Parameters used: 10^6 atoms, mass of ^{87}Rb and a harmonic trap with $\bar{\omega}$=$2\pi\cdot$500 Hz

Minimizing the energy in equation (4.12) by varying ψ under the constraint of a constant total number of particles results in the time-independent Gross-Pitaevskii equation [51]:

$$\left(-\frac{\hbar^2}{2m}\nabla^2 + V(\mathbf{r}) + g|\psi(\mathbf{r})|^2\right)\psi(\mathbf{r}) = \mu\psi(\mathbf{r}). \tag{4.13}$$

In the limit of weak interactions, $g \to 0$, the usual linear Schrödinger equation is recovered.

4.2. Density Distributions

For thermal atoms and for Fermi and Bose gases above their respective transition temperature, the phase-space density can be obtained by working in a semi-classical approach for the distribution function. This approach is valid, as long as the variations in the external potential are small on the length scale given by the de Broglie wavelength of the particles. Then every atom can be described by a wave packet with well defined momentum and position.

This description is not valid for the lowest energy states which have spatial variations on the length scales on which the potential changes [87]. The distribution function is then given by:

$$w = \frac{1}{\hbar^3}\frac{1}{\mathfrak{z}^{-1}\exp(\beta H(r,p)) + a}. \tag{4.14}$$

By integrating this distribution over the momentum degrees of freedom, the density distribution of the atomic ensemble in real space is obtained

$$n(\mathbf{r}) = -a\frac{1}{\lambda_T^3} Li_{3/2}\left(-a\xi e^{-\beta V(\mathbf{r})}\right) \tag{4.15}$$

with the thermal de Broglie wavelength $\lambda_T = \sqrt{2\pi\hbar^2/mk_BT}$.

In exactly the same manner, one can integrate over the spatial coordinates and arrives at the momentum distribution of the trapped cloud:

$$n(\mathbf{p}) = -a\frac{1}{\bar{\omega}}\left(\frac{1}{2\pi\beta\hbar^2 m}\right)^{3/2} Li_{3/2}\left(-a\xi e^{-\beta(\frac{\mathbf{p}^2}{2m})}\right). \tag{4.16}$$

Different to the spatial distribution, the momentum distribution does not reflect the anisotropy of the trap any more. The momentum distribution for non-condensed samples is due to the equipartition principle always isotropic and is, in the case of bosons, the main indicator for the existence or the non-existence of a condensate.

Equation (4.15) reduces in the limit of high temperatures to the density of a thermal gas trapped in a harmonic potential:

$$n(\mathbf{r}) = N\left(\frac{m\bar{\omega}^2}{2\pi k_B T}\right)^{3/2} e^{-\beta V(\mathbf{r})} = N\left(\frac{m\bar{\omega}^2}{2\pi k_B T}\right)^{3/2} e^{-\sum x_i^2/2\sigma_i^2}, \tag{4.17}$$

with the width $\sigma_i^2 = \frac{k_B T}{m\omega_i^2}$.

4.2.1. Fermions at T=0

For finite temperatures, the shape of the atomic cloud is given by equation (4.15). In the limit of T=0, the distribution can be easily calculated.

Fermions at $T = 0$ fill the potential landscape up to the Fermi energy E_F. The phase-space density is equal $1/h^3$ for all states with energies below E_F and zero above. By integrating the density of states over the momentum space one obtains the density distribution

$$n(\mathbf{r}) = \frac{(2m)^{3/2}}{6\pi^2\hbar^3}(E_F - V(\mathbf{r}))^{3/2} \text{ for } V(\mathbf{r}) < E_F. \tag{4.18}$$

At the same time, the momentum distribution of the cloud is, similar to the case of thermal atoms, isotropic as all momenta p with $p^2/2m < E_F$ are equally occupied.

For finite temperatures the edges of this distribution get washed out, similar to the typical behavior of the fermionic distribution function that is known from electrons in solid state systems.

In a harmonic trapping potential the extension of the cloud along the different axis of the trap is given by the Fermi radii

$$R_i = \sqrt{\frac{2\hbar\bar{\omega}}{m\omega_i^2}}(6N)^{1/6}.$$

4.2.2. Bosons at T=0

Thomas-Fermi approximation

Even in the limit of dilute atomic gases, the energy due to interactions dominates the kinetic energy, as long as the number of particles N is high and the interaction is sufficiently large.

In the Thomas-Fermi approximation, the kinetic term in the Gross-Pitaevskii equation (4.13) is neglected. The shape of the density distribution is therefore directly related to the shape of the confining potential, leading in the case of harmonic trapping to the shape of an inverted parabola:

$$n(\mathbf{r}) = |\psi(\mathbf{r})|^2 = \frac{\mu - V(\mathbf{r})}{g}. \tag{4.19}$$

The maximum density at the center of the trap is $n(0) = \frac{\mu}{g}$.

This approximation describes the condensate quite well in the central region of the trap, but fails to describe the density distribution of the cloud at the edges of the trap where the density vanishes.

The extension of the cloud is given by the condition that at the outermost points the potential equals the chemical potential μ, and the so-called Thomas-Fermi radii R_i of the spatial extension of the cloud evaluate to:

$$R_i = \sqrt{\frac{2\mu}{m\omega_i^2}}. \tag{4.20}$$

The chemical potential is fixed by the usual constraint that $N = \int dV\, n(\mathbf{r})$. For a harmonically trapped cloud the chemical potential is [51]

$$\mu = \frac{(15N\,a)^{2/5}}{2}\left(\frac{m\bar{\omega}}{\hbar}\right)^{1/5}\hbar\bar{\omega}. \tag{4.21}$$

4.3. Expansion & Thermometry

Due to the small size of an atomic cloud in the trap, most diagnostics rely on the free expansion of the atomic ensemble and successive absorption imaging. From cloud size measurements done at different expansion times, the momentum distribution of the atomic cloud can be reconstructed even if the exact shape of the potential is not known, leading to the temperature of the sample.

In the limit of long expansion times, in which the cloud expands to a size much larger than the initial in situ size, the density distribution of the thermal cloud is a direct measure of the momentum distribution in the trap, independent of the exact shape of the confining potential.

4.3.1. Thermal Atoms

As already mentioned in the previous section, for thermal atoms a semi-classical approach for the distribution function with well localized wave packets is applicable. Atoms originating from $\mathbf{x_0}$ can contribute to the density in $\mathbf{x}$ after a time of flight t only if their velocity is $\mathbf{v} = (\mathbf{x} - \mathbf{x_0})/t$. Integrating over all initial positions $\mathbf{x_0}$ or velocities $\mathbf{v}$ gives the density distribution as a function of the expansion time:

$$n(\mathbf{x}, t) = \int d\mathbf{v}\, p(\mathbf{v}) n_0(\mathbf{x_0}) \delta^3\left(\frac{\mathbf{x} - \mathbf{x_0}}{t} - \mathbf{v}\right)$$

with the probability $p(\mathbf{v})$ to find a particle with the corresponding velocity $\mathbf{v}$

$$p(\mathbf{v}) = \prod_{i=1}^{3} \sqrt{\frac{m}{2\pi k_B T}} \exp\left(-\frac{m v_i^2}{2k_B T}\right).$$

Assuming harmonic confinement and therefore a Gaussian distribution for the density as in equation (4.17), it can be shown through integration that the width σ_i of the cloud scales as

$$\sigma_i^2(t) = (1 + \omega_i^2 t^2)\sigma_i^2(0), \text{ with } \sigma_i^2(0) = \frac{k_B T}{m\omega_i^2}. \tag{4.22}$$

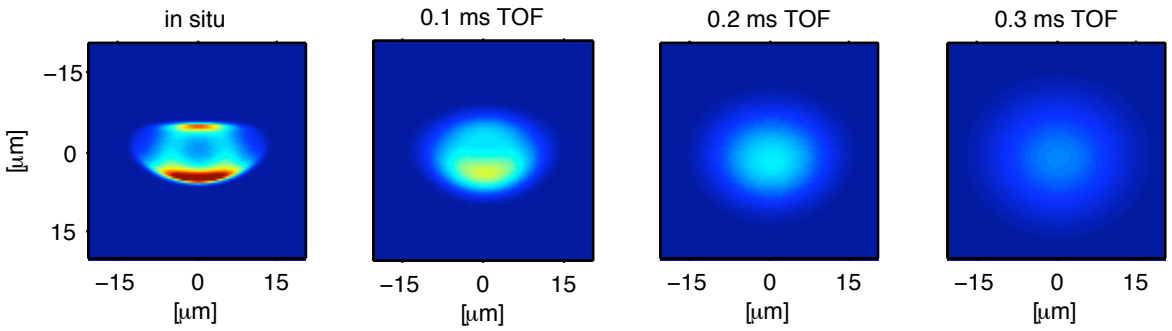

Figure 4.3.: Simulation of the expansion of a thermal cloud of atoms at $T = 5\,\mu\mathrm{K}$ from an rf trap, as considered in chapter 8. All pictures show the column density integrated along the trapping wire. For times longer than 0.2 ms the structure of the initial trap has vanished.

Arbitrary Shapes of the Trap

When the atoms are not confined in a harmonic potential, but are arbitrarily distributed within a volume d^3, extracting the temperature from the width of the expanding cloud is still possible. For a given temperature T a typical velocity is $v_0 = \sqrt{2k_BT/m}$. Considering again a semi-classical model, the atoms that are initially at $\mathbf{x_0}$ can during a time of flight t explore a sphere with radius $r_0 = v_0 t$. For

$$r_0 \gg d \quad \text{and therefore,} \quad t \gg t_0 = \frac{d}{v_0} = d\sqrt{\frac{m}{2k_BT}}$$

the initial inhomogeneities in the atomic distribution are washed out, as it is not possible to distinguish between particles originating from $\mathbf{x_0}$ and $\mathbf{x_0} + d$ any more, and the typical Gaussian shape of an expanding thermal cloud is recovered. For times longer than t_0, the width of the cloud as function of the expansion time is analog to equation (4.22) again a good measure of the temperature of the sample.

In the case of the adiabatic rf potentials, as considered in section 3.4, the typical lengthscale d is on the order of 10 µm. For temperatures in the µK range the time t_0 is fractions of a ms. A simulation of the expansion of thermal atoms from such a trap is visible in figure 4.3.

4.3.2. Fermions

For an ideal gas of harmonically trapped fermions, it can be shown that density distribution for an arbitrary time of flight can be obtained by scaling the width of the cloud with the identical relations as the ones obtained for a thermal sample in equation (4.22) [92].

$$\sigma_i^2(t) = \frac{k_BT}{m\omega_i^2}(1 + \omega_i^2 t^2)$$

The distribution of the expanded cloud can then be obtained by scaling the variables $x_i \to x_i/\sqrt{1+\omega_i^2 t^2}$ and adopting the prefactor for the normalization $\int n\,d\mathbf{r} = N$ accordingly. As a result the shape of the expanding cloud does not change as a function of the expansion time for harmonically trapped fermions.

$$n(\mathbf{r}) = -\left(\frac{1}{2\pi\beta^2\hbar^2\bar{\omega}^2}\right)^{3/2} \frac{1}{\sigma_1\sigma_2\sigma_3} Li_{3/2}\left(-\mathfrak{z}\exp\left[-\sum_{i=1}^{3}\frac{x_i^2}{2\sigma_i^2}\right]\right) \tag{4.23}$$

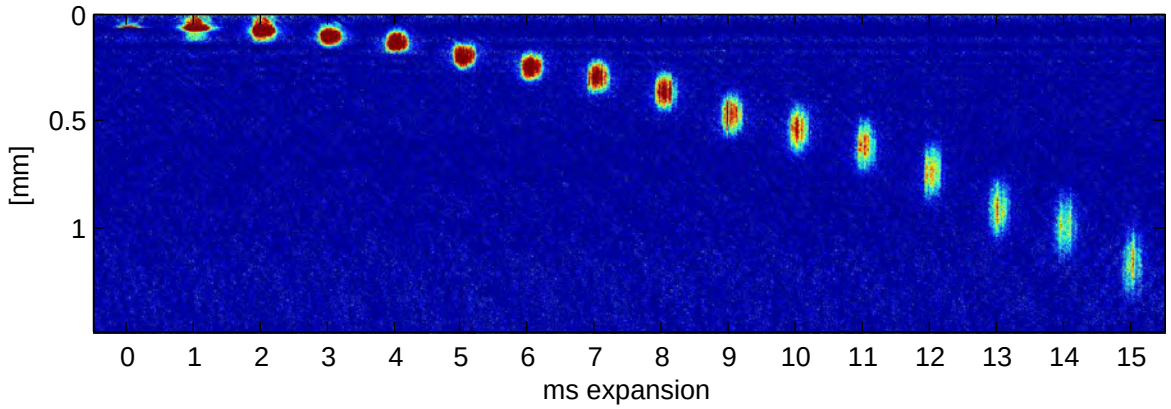

Figure 4.4.: Expansion of a quasi one-dimensional BEC, looking transversally on the cloud. The aspect ratio between the longitudinal and transversal size of the cloud is being inverted after some ms of expansion. The phase fluctuations that are due to the quasi one-dimensional nature of the condensate are visible as fringes. The parabola of the center of mass motion is one possible tool to determine the right scale for the axis of the imaging parallel to the direction of gravity.

In experiments one can usually not observe the three-dimensional density. By looking at the shadow of the cloud obtained by an absorption image, only the integrated column density is accessible. Integrating (4.23) along the z direction the column density in the x, y-plane evaluates to

$$n(x,y) = -\left(\frac{1}{2\pi\beta^2\hbar^2\bar{\omega}^2}\right)^{3/2}\frac{\sqrt{2\pi}}{\sigma_x\sigma_y}Li_2\left(-\mathfrak{z}\exp\left[-\frac{x^2}{2\sigma_x^2}-\frac{y^2}{2\sigma_y^2}\right]\right). \tag{4.24}$$

Expressing (4.24) in experimentally better accessible parameters leads to

$$n(x,y) = n_{max}Li_2\left(-\mathfrak{z}\exp\left[-\frac{x^2}{2\sigma_x^2}-\frac{y^2}{2\sigma_y^2}\right]\right)/Li_2\left(-\mathfrak{z}\right). \tag{4.25}$$

To obtain the temperature of the sample from expansion measurements, typical fit parameters on the measured spatial distributions are the fugacity $\mathfrak{z}$, the width of the cloud and the peak density n_{max} [93].

4.3.3. Bosons

To describe the dynamics of a BEC after the trap has been switched off instantaneously, the condensate can be described with hydrodynamic equations for the superfluid density. It is then possible to show that the Thomas-Fermi radii of the cloud during expansion scale with time dependent coefficients $b_i(t)$ [86]:

$$R_i(t) = R_i(0)\,b_i(t) = \sqrt{\frac{2\mu}{m\omega_i^2}}\,b_i(t). \tag{4.26}$$

The coefficients b_i are fixed by a set of coupled differential equations that can be solved for different trapping geometries. Assuming harmonic confinement with cylindrical symmetry

with $\omega_1 = \omega_2 = \omega_r$ and $\omega_3 = \lambda\omega_r$, the scaling coefficients can be solved analytically in the limit of low longitudinal trapping, $\gamma \ll 1$ [94]

$$\begin{aligned} b_\perp(t) &= \sqrt{1+\omega_r^2 t^2} \\ b_z(t) &= 1+\lambda^2[\omega_r t \arctan(\omega_r t) - \ln\sqrt{1+\omega_r^2 t^2}]. \end{aligned} \tag{4.27}$$

Therefore, a condensate expands highly anisotropic, and the aspect ratio between the two axis of the condensate is inverted after some expansion time. The aspect ratio is λ for $t = 0$ and reaches for long expansion times the limit $\lim_{t\to\infty} = 2/\pi\lambda$. Typical experimental pictures for an expanding condensate can be seen in figure 4.4.

4.4. Bosons in Two Dimensions

In this section, a little overview on the behavior of cold bosonic gases in a two-dimensional geometry is given. The influence of the reduced dimensionality on the exact nature of the phase transition at low temperatures has been studied theoretically in great detail [95, 96, 97, 30], and during the last years first experimental studies were possible [31, 98, 99]. A good introduction to the theory low-dimensional bosonic systems can be found in [25].

To reach a quasi two-dimensional situation, the condition has to be satisfied that the chemical potential μ is much smaller than the energy connected with the oscillation frequency ω_z of the tightly confined direction. Here and for the rest of this section, it is assumed that the high confinement is along the z-direction.

For $\mu \ll \hbar\omega_z$ the motion of the atoms is confined to zero point oscillations along this direction. Furthermore, the density of states is altered by the strong confinement. Going through the same formalism that was developed in the beginning of this chapter for the three-dimensional case, it can be shown that for a uniform gas, a BEC can only exist at T=0 [25].

The situation is a little different when the atoms are harmonically trapped in two dimensions. Then the occupation of the ground state becomes macroscopic below a critical temperature which depends on the number of particles and the trap frequencies. This is an ordinary BEC transition in which the transition temperature and the condensate fraction for an ideal gas are given by [100]:

$$k_B T_C = \hbar\bar{\omega}\left(\frac{N}{\zeta(2)}\right)^{1/2}, \quad \frac{N_0}{N} = 1 - \left(\frac{T}{T_C}\right)^2. \tag{4.28}$$

$\bar{\omega}$ is now the mean trapping frequency $\bar{\omega} = \sqrt{\omega_x\omega_y}$ in the two-dimensional plane.

At finite temperatures, phase fluctuations destroy the long-range order of the system. The condensate is then divided into blocks of constant phase, but the phases of these blocks are not correlated with each other. The system is then called a *quasicondensate*.

Interactions

The effect of interactions between the atoms in two dimensions can be expressed by an effective coupling constant. The interaction energy per particle in two dimensions is given

by averaging the three-dimensional interaction over the Gaussian density profile of the cloud along the confined, the z-direction [25].

$$E_{int} = n_{2D} g_{2D} = n_{2D} \frac{1}{l_0 \sqrt{2\pi}} g_{3D} = n_{2D} \frac{\sqrt{8\pi}\hbar^2}{m} \frac{a}{l_0}.$$

The effective coupling constant is therefore:

$$g_{2D} = \frac{\sqrt{8\pi}\hbar^2}{m} \frac{a}{l_0},$$

with $l_0 = \sqrt{\hbar/m\omega_0}$ the oscillator length along the confined direction. The criterion $n_{3D}a^3 \ll 1$ for weak interactions in three dimensions, reduces in the two-dimensional case to $a \ll l_0$. For a stronger confinement of the gas, the scattering length has to be corrected by a density dependent term [97].

Similar to the three-dimensional case, the Thomas-Fermi approximation can be applied for high atom numbers and a chemical potential that is much bigger than the level spacing in the two-dimensional trap. Then the density profile in the two-dimensional surface takes the usual parabolic shape

$$n_{2D} = \frac{1}{g_{2D}} \left(\mu - \frac{m}{2} \sum_{i=1,2} \omega_i^2 x_i^2 \right).$$

This leads with the half-radii $R_i = \sqrt{2\mu/m\omega_i^2}$ to a measure for the extend of the cloud in the trap. Integrating over the extend of the cloud gives a definition for the chemical potential in terms of the trapping frequencies and the total number of atoms:

$$\mu = \sqrt{\frac{N m g_{2D}}{\pi \hbar^2}} \hbar \bar{\omega}.$$

The transition to a two-dimensional situation takes place, when the number of atoms becomes smaller than the number of states that is available below the first excited state in the strongly confined direction. This is the situation when $\mu_{3D} = \hbar\omega_z$. The number of atoms for this crossover can be calculated at $T = 0$ using equation (4.21) to:

$$N_{2D} = \sqrt{\frac{32\hbar}{225ma^2}} \frac{\omega_z^{3/2}}{\bar{\omega}^2} \tag{4.29}$$

with $\bar{\omega}$ the mean of the trapping frequencies in the quasi-two-dimensional plane.

Below this atom number, the shape of the cloud along the confined direction will not be an inverted parabola any more, but assumes a constant Gaussian shape with $l_z = \sqrt{\hbar/m\omega_z}$ independent of the number of atoms.

After releasing the atoms from the trap, their expansion is dominated by the expansion along the direction of high confinement. Along this direction the width of the expanding cloud will scale as $\sqrt{2}\omega_z t$, whereas the expansion in the other two directions is negligible [101]. Therefore, the aspect ratio of an expanded cloud can be used as an experimental signature of the crossover from a three-dimensional to a two-dimensional situation [102]. In two dimensions, the release energy of the cloud is not proportional to N any more, as it was in the case of three dimensions, but saturates at the zero-point energy of the confined direction.

Berezinskii-Kosterlitz-Thouless Transition

Independent of the confining potential, the repulsive interaction induces a transition to a superfluid state at a critical temperature that is close to the critical temperature of BEC. This phase [95, 96] is associated with the formation of bound pairs of vortices. The nature of this phase transition was investigated experimentally by looking at fluctuations in the quasi-condensate phase and free vortices were observed [31].

4.4.1. Experimental Approaches

There are different experimental approaches to achieve strong trapping in one spatial direction whilst the two other axis of the trapping potential are kept much weaker:

- The first experimental realization of a BEC in two dimensions was in liquid helium experiments. There the condensation of spin-polarized hydrogen on a helium surface was observed in the late 1990s [103].
- A similar approach can be used with laser cooled atoms: It is possible to achieve a single two-dimensional system by combining the gravitational field with the evanescent light field that is created by total internal reflection of an repulsive blue detuned laser beam on the surface of a prism [99].
- Optical dipole traps are a good tool to confine atoms to a two-dimensional configuration. By using standing waves, usually a stack of pancake-like traps is obtained. In these far-detuned optical dipole traps, condensation in two dimensions can be reached either by lowering the atom number of a large number condensate in the trap [102], or by cooling the sample [104] in this geometry. In these experiments usually several potential minima are populated, leading in expansion to interference between the single realizations of a quasi two-dimensional gas. This allows to probe the coherence properties of the gas [105, 31].
- Single wells of such a standing wave can be selectively emptied by adding a magnetic gradient along the standing wave and then applying an rf field [105], resulting in a situation in which only one or a few traps are populated.
- A pancake-like trap can also be created by rotating a three-dimensional trap around one of the trapping axis [106]. This led to the observation of vortices and vortex lattices in two-dimensional systems.
- Within this thesis, a new approach for the implementation of a two-dimensional trap is suggested: In section 3.4, it was shown that by using a circular polarized rf field a rotational symmetric adiabatic trap can be created. By changing the detuning between the rf photon and the Zeeman splitting in the trap, a single cylindrical trap can be adiabatically be transformed into a toroidal shell structure. This shell forms a two-dimensional surface with periodic boundary conditions if variations in the trapping geometry are sufficiently suppressed. First experiments on the realization of such a system can be found in chapter 8.

5 Bose-Fermi Mixtures

The combination of a fermionic with a bosonic atomic sample gives rise to novel quantum phases. As an example, charge-density-waves and the screening of fermions by bosons are predicted in tight cigar-shaped traps [107]. In optical lattices, questions of impurity scattering and the localization of bosons were studied [22], and the proof of boson-induced superfluidity in a cloud of fermions [108] might lead to a better understanding of high-T_C superconductivity. Depending on the exact nature of the scattering potential between both species, the interaction can be described by a negative or attractive scattering length.

For several reasons that will be described in more detail in section 6.2, the mixture of ^{40}K with ^{87}Rb is used for the new mixture experiment. The interspecies scattering length for this mixture is large and negative, and the attractive interaction has different consequences:

On the one hand, the scattering between the two species makes it possible to use this mixture in sympathetic cooling experiments in which the fermions are cooled down to degeneracy via the thermal contact with the rubidium cloud. This situation is explained in more detail in section 5.1, where an estimate for the thermalization rate is given. The attractive interaction prevents at low temperatures a separation of the mixture into two phases, in contrast to the case of repulsive mixtures like ^{6}Li-^{7}Li. This guarantees that the sympathetic cooling process is working down to low temperatures, as there is always spatial overlap between the two components.

On the other hand, the attractive interaction can lead to a collapse of both components of the mixture, once a critical number or critical density of particles is exceeded. This behavior of mixtures with attractive interaction was predicted theoretically [109, 110] and was observed experimentally in ^{40}K-^{87}Rb [111, 18].

In section 5.2, the interactions between the two species will be treated in a mean-field model [112], and this model will subsequently be applied to the case of a split double-well potential in which the barrier height between the two clouds can be changed by the attractive interaction between the two species. Due to the exponential sensitivity of the tunneling dynamics of the double-well to the barrier, this might be a powerful tool to investigate the interaction between both components. This situation can experimentally be realized in the new K-Rb experiment using adiabatic rf traps as introduced in chapter 3.

5.1. Sympathetic Cooling

The suppression of the s-wave scattering between identical fermions, limits cooling by the usual evaporation method [113], as there is no rethermalization between the atoms through collisions at low temperatures possible any more.

A way to circumvent this obstacle, is to employ *sympathetic cooling*. For sympathetic cooling, the sample is brought in thermal contact with a second, colder, sample and the whole system rethermalizes via elastic collisions [114].

In the case of fermionic spin-polarized samples, two different hyperfine or Zeeman states of the same species can be used if both states can be trapped and if they are stable against spin changing collisions. This method, applied to ^{40}K, led in 1999 with the observation of a Fermi sea to the first quantum-degenerate Fermi gas [7].

A second possibility for sympathetic cooling is the usage of a different atomic species as a 'fridge'. This is typically a boson that is cooled down by evaporative cooling. A whole variety of Bose-Fermi mixtures is now routinely cooled in the lab. Examples of two component mixtures are: ^{6}Li-^{7}Li [115, 14], ^{6}Li-^{23}Na [116], ^{6}Li-^{87}Rb [62], and ^{40}K-^{87}Rb [117, 47].

Important for the sympathetic cooling process are elastic collisions in which the energy is redistributed between the two components. Inelastic collisions between the two species are to be avoided as they lead to trap losses.

5.1.1. Inelastic Collisions

The dominant mechanism for inelastic collisions in the absence of light are spin exchange collisions. For spin exchange collisions between two atoms with $|F1, m_{F1}\rangle$ and $|F2, m_{F2}\rangle$, the total projection of the angular momentum $m_{F1} + m_{F2}$ has to be conserved [51]. By choosing the states of the two atomic species carefully, mixtures can be created that are stable against spin exchange.

For example, the mixture of ^{87}Rb in $|2, 2\rangle$ and ^{40}K in $|9/2, 9/2\rangle$ is stable against these collisions, as there are no other spin combinations with a total $m_F = 13/2$. On the other hand, in the mixture of ^{87}Rb in $|1, -1\rangle$ and ^{40}K in $|9/2, 9/2\rangle$, different final states with a total $m_F = 7/2$ and with lower energy are possible. This leads to spin exchange collisions that drive the atoms into untrapped states.

Even when choosing states that form a stable mixture against spin exchange collisions, there is still a small loss channel due to dipolar interactions [118]. This dipolar relaxation allows two atoms entering in a s-wave channel to leave in a d-wave channel. Due to the high energy of the d-wave compared to the low energy of the atomic sample, these processes are strongly suppressed.

Nevertheless, these processes can pose a significant problem, as it was for example observed in an experiment cooling ^{6}Li with ^{87}Rb [62]. There, rubidium atoms that accumulated in the $|2, 1\rangle$ state due to dipolar relaxation, had to be removed selectively several times during the sympathetic cooling process, as they introduced a large inelastic scattering channel with the lithium atoms.

A different kind of inelastic processes can be observed in the light field of a MOT. There collisions between atoms in the ground state and atoms in the excited state are possible. Depending on the exact shape of the interatomic potential formed by the collision partners, this can lead to so-called radiative escape processes and fine structure changing collisions [119].

Depending on the kinetic energy that is transferred to the atoms during these processes, they might leave the trapping potential.

The inelastic processes in a MOT and the corresponding loss coefficient for the mixture ^{6}Li-^{87}Rb were measured in the framework of this thesis and are documented in more detail elsewhere [120, 121].

5.1.2. Elastic Collisions and Thermalization

The timescale for the thermalization between ^{40}K and ^{87}Rb can be estimated by looking at the rate of elastic collisions between the two species. If two gases with different initial temperatures are brought in contact, they will rethermalize to a common equilibrium temperature. Assuming no losses during this process, the final temperature is

$$T_{\text{fin}} = \frac{N_K T_K + N_{Rb} T_{Rb}}{N_K + N_{Rb}}.$$

The average energy transfered per elastic collision between ^{40}K and^{87}Rb is [122, 123]

$$\Delta E = k_B \, \Delta T \, \xi, \tag{5.1}$$

with the reduction factor ξ due to the unequal masses of the two species:

$$\xi = \frac{4 \, m_{Rb} \, m_K}{(m_{Rb} + m_K)^2} \approx 0.86.$$

The heat capacity for thermal gases that are harmonically trapped in three dimensions is $3 \, N \, k_B \, T$. Therefore, with equation (5.1) a number of $3/\xi = 3.5$ collisions for the thermalization of each ^{40}K atom are needed. This is assuming that the number of ^{87}Rb atom is much larger than the number of ^{40}K atoms.

The mean relative thermal velocity of the atoms is given by

$$\bar{v} = \left[\frac{8 k_B}{\pi} \left(\frac{T_K}{m_K} + \frac{T_{Rb}}{m_{Rb}} \right) \right]^{1/2}.$$

In the case of identical temperatures this reduces to $\bar{v}^2 = 8 k_B \, T / \pi m_{red}$ with m_{red} the reduced mass of the system.

The collision rate is given as the product of the spatial overlap of the two clouds, the relative velocity, and the scattering cross section σ_{KRb} between the two species:

$$\Gamma = \sigma_{\text{KRb}} \bar{v} \int dV \, n_{Rb}(x) n_K(x).$$

If both species are trapped in a three-dimensional harmonic trap as defined in equation (4.2) and experience the identical trapping potential, one arrives for the collision rate at

$$\Gamma = \sigma_{\text{KRb}} \bar{v} \left(\frac{m_{Rb}}{2\pi \, k_B \, (T_K + T_{Rb})} \right)^{3/2} \omega_x \omega_y \omega_z N_K N_{Rb},$$

with the trapping frequencies ω_i for ^{87}Rb. The thermalization rate is given by

$$\frac{1}{\tau} = -\frac{1}{\Delta T} \frac{d}{dt} \Delta T = \frac{\xi}{3} \frac{(N_K + N_{Rb})}{N_K N_{Rb}} \Gamma. \tag{5.2}$$

In the final stage close to T_{fin} it can be evaluated to [122, 123]:

$$\frac{1}{\tau} = \frac{1}{3\pi^2\sqrt{2}} \frac{\sigma_{\mathrm{KRb}}}{k_B T_{\mathrm{fin}}} \frac{m_{Rb}^2 \sqrt{m_K}}{(m_{Rb}+m_K)^{3/2}} \omega_x \omega_y \omega_z (N_{Rb}+N_K). \tag{5.3}$$

The thermalization rate of the mixture of ^{40}K-^{87}Rb was measured at different temperatures, and the cross section σ_{KRb} showed a change of one order of magnitude over a temperature range of 100 µK [124]. This can be explained by the Ramsauer-Townsend effect [125] in which the s-wave scattering cross section is greatly reduced for specific relative energies between the particles. At these energies, reflections at the molecular potential interfere destructively causing the scattering cross section to vanish.

This reduction of the scattering rate limits the maximum speed for the sympathetic cooling process in the range of temperatures above 50 µK. In an experiment with a comparable trapping geometry to the one that is realized on the new atom chip for the K-Rb experiment (see section 6.6 for details) a total cooling time of 6 s was reported [124].

5.1.3. Thermalization in the Degenerate Regime

Expressing the Fermi temperature (4.4) for ^{40}K in terms of the critical temperature (4.7) of ^{87}Rb, one arrives at

$$T_F = T_C \sqrt{87/40}\, [6\zeta(3) N_K/N_{Rb}]^{1/3}\,.$$

Therefore, both samples reach their degeneracy at almost the same temperature, assuming a ten times higher number N_{Rb} of rubidium atoms than of potassium atoms N_K.

In the degenerate regime the specific heat for a Bose gas in harmonic confinement [126] and for Fermi gases in the limit of temperatures below 0.5 T_F [87] can be calculated:

$$C_B \approx 10.8 k_B N_B \left(\frac{T}{T_C}\right)^3 \qquad C_F \approx \pi^2 k_B N_F \frac{T}{T_F}.$$

Using the results from section 4.1 for N_B and N_F and assuming perfect spatial overlap of the two clouds, the temperature T/T_F of the fermionic sample can be expressed in terms of the ratio of the two heat capacitances C_B and C_F and the trapping frequencies of both species. For an identical trapping potential for both species in the magnetic trap, the ratio of the trapping frequencies can be expressed as a ratio of the masses: $\omega_{Rb}/\omega_K = \sqrt{m_K/m_{Rb}}$, arriving at [127]:

$$\frac{T}{T_F} \approx 0.35 \left(\frac{\omega_{Rb}}{\omega_K}\right)^{3/2} \left(\frac{C_{Rb}}{C_K}\right)^{1/2} = 0.35 \left(\frac{m_K}{m_{Rb}}\right)^{3/4} \left(\frac{C_{Rb}}{C_K}\right)^{1/2}. \tag{5.4}$$

Equating the two heat capacitances, gives a good estimate for the temperature range when the thermalization between the two species becomes inefficient. For the above case of ^{40}K and ^{87}Rb this is at a temperature of $T/T_F \approx 0.2$. Lower temperatures can be reached if the bosons are at the end of the cooling ramp completely removed from the trap.

5.1.4. Influence of High Confinement

As visible from equation (5.3), increasing the trapping frequencies enhances the thermalization rate if one neglects for the moment issues like phase separation or mean-field collapse that arise at high densities.

The thermalization properties will change once the system is in a regime in which the chemical potential and the temperature are below the harmonic oscillator energy in one or two dimensions. The reduced dimensionality then alters the scattering properties between the atoms, provided that the ground state size of the system in the confined direction and the scattering length between the particles are similar [24].

Effects like confinement-induced resonances [24, 128, 129] and the fermionization of bosonic systems were predicted and experimentally realized [26]. Even bound states for particles with negative scattering length in a highly confined geometry have been demonstrated [27, 130].

The regime in which the ground state size $l_0 = (\hbar/m\omega)^{1/2}$ and the scattering length a are of the same order is not accessible in the magnetic traps of an atom chip, as there are no means to tune the interaction strength to large values using for example a Feshbach resonance.

5.2. Attractive Interaction

The effects of the attractive interaction on the single species potentials can be described in a zero-temperature mean-field model using the Thomas-Fermi approximation for every species [88]. Depending on the sign of the interspecies scattering length a_{FB}, both densities will enhance in the center of the trap or a phase separation between both species can occur.

For the bosonic part the Gross-Pitaevskii equation (4.13) is modified by a mean-field term proportional to the density of the fermions. Similarly, for the fermionic part the distribution function (4.18) is changed to incorporate a term proportional to the density of the bosons.

$$\left[-\frac{\hbar^2}{2m_B}\triangle + V_B(r) + g_{BB}n_B(r) + g_{BF}n_F(r)\right]\psi_B(r) = \mu_B\psi_B(r) \tag{5.5}$$

$$n_F(r) = \frac{(2m_F)^{3/2}}{6\pi^2\hbar^3}\max(\mu_F - V_F(r) - g_{BF}n_B(r), 0)^{3/2}. \tag{5.6}$$

The coupling constants g_{BB} and g_{BF} are defined through the corresponding scattering length a with: $g_{BB} = 4\pi\hbar^2 a_{BB}/m_B$ and $g_{BF} = 2\pi\hbar^2 a_{BF}/\mu_{BF}$. μ_{BF} is the reduced mass of the Bose-Fermi system.

Neglecting the kinetic energy term for the bosons and going over to the Thomas-Fermi approximation, equation (5.5) reduces to

$$n_B = \frac{1}{g_{BB}}\max(\mu_B - V_B(r) - g_{BF}n_F(r), 0). \tag{5.7}$$

This system of coupled equations can be solved iteratively with the condition that for both species the chemical potential is fixed by the requirement that the integral over the density equals the number of particles in the system.

$$N_i = \int_V d^3x\ n_i(r) \qquad i = \{B, F\}. \tag{5.8}$$

Following [131], a self-consistent solution of equations (5.7) and (5.6) can be found by going through the following procedure:

- First, the chemical potentials for the pure bosonic cloud and for the pure fermionic cloud are found by looking at the solution for both species in the Thomas-Fermi approximation without interaction from the different species.

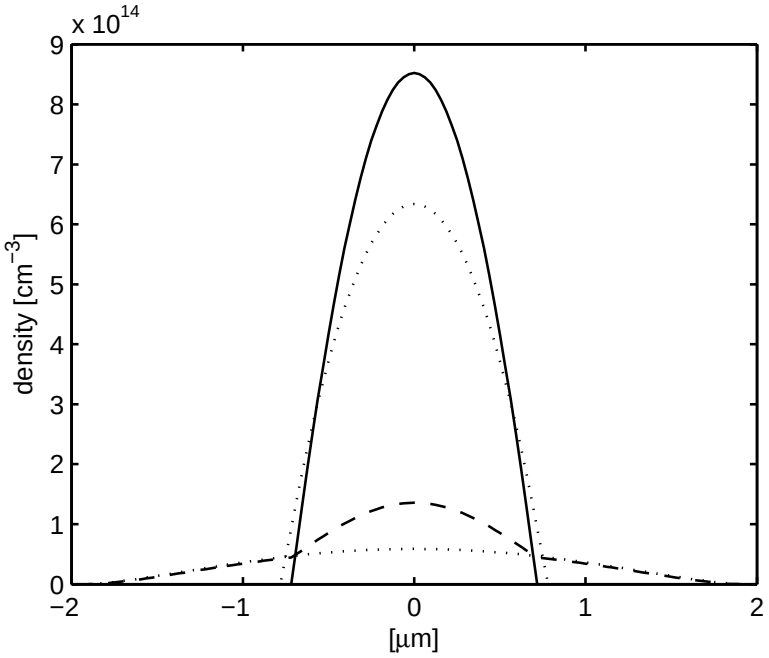

Figure 5.1.: Transversal density distributions for 10^5 ^{40}K and 10^5 ^{87}Rb atoms at T=0 in a cylindrical trap with trapping frequencies of $2\pi\cdot 2000$ kHz and $2\pi\cdot 10$ Hz. The dotted lines indicate the distributions without any interactions. The solid (dashed) line is the density distribution for ^{87}Rb(^{40}K) taking the attractive interspecies interaction into account.

- Then, the fermion distribution is injected in equation (5.7) and the chemical potential is adjusted such that the number of bosons is preserved.
- The obtained boson distribution is used in equation (5.6) and the chemical potential for the fermions is varied to obtain a constant number of fermions.
- The last two steps are repeated several times.

Depending on the number of fermions and bosons and for an attractive interaction between the species, there are two different cases that arise:

Either the system converges to constant chemical potentials μ_B and μ_F, or, in the case of high boson and fermion numbers, the peak density of the bosonic or fermionic cloud diverges. This corresponds to the case of a collapse of the system as observed in several experiments [111, 18]. An example for a stable solution obtained by simulations can be seen in figure 5.1, where the in situ density for an interacting mixture of potassium and rubidium is plotted.

For the case of repulsive interactions, a different situation can arise: The fermionic density goes to zero in the volume occupied by the bosons. This is the case of a total phase separation between the two components.

5.2.1. Collapse

Depending on the confinement of the system, the maximum number of bosons and fermions in the trap is limited. The atomic densities are increasing for higher confinements, and the

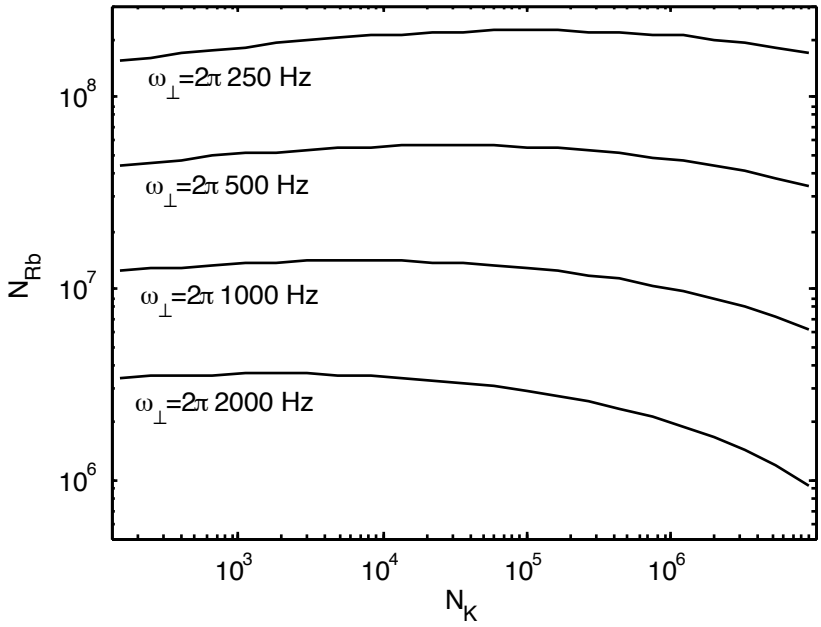

Figure 5.2.: Stability diagram for the mixture ^{40}K-^{87}Rb for different radial confinements in a cylindrical trap. Longitudinal trapping for all cases is $2\pi\cdot 10$ Hz. Below the corresponding lines the mixture is stable, above the line the mixture will collapse due to the attractive interaction between both species. Critical numbers were calculated in a T=0 model following [132].

number of atoms for a stable mixture is reduced. As visible in figure 5.2, this depends more crucial on the number of bosons than the number of fermions.

This can be understood in simple terms, as the BEC enhances the density of the fermions locally, whereas the mean-field contribution of the fermions to the bosonic cloud is spatially homogeneous as long as the fermionic cloud is bigger than that of the bosons.

In the case of collapse, the Pauli repulsion of the fermions and the repulsion between the bosons can not balance the attractive interaction between the species any more. The BEC is confined even more strongly through the interaction, which then will increase the local density of the fermions even stronger. This leads to a self-amplifying process, ultimately leading to a collapse of both components.

5.2.2. Modification of a Double-Well Potential

As seen in section 5.2, the attractive interaction between the bosonic and fermionic species leads to an change in the effective potential landscape compared to the case of non-interacting gases. By combining the species-selective nature of the rf traps that was introduced in section 3.6, with the attractive interaction between the atomic species, a situation can be created in the experiment, where the height of the barrier in a double-well can be tuned by the interaction with a the second species. The exponential dependence of the tunneling between the two wells on the barrier height, then delivers a very sensitive measurement tool on the exact atom number of the second species. The system can be tuned between the situation of a non-split cloud and a well-separated cloud just by varying the number of particles of the second species.

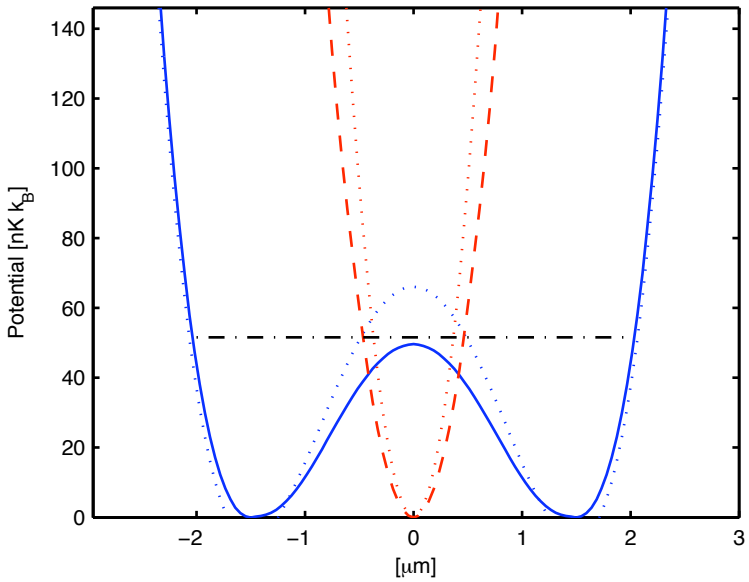

Figure 5.3.: The trapping potential of a double-well is changed by the attractive interaction between the two species. A rubidium cloud of 10^4 atoms (blue, solid) is transversally split in a double-well. Through the attractive interaction with a potassium cloud of 10^4 atoms (red, dashed), the height of the barrier between the two wells can be changed. The initial trapping potentials are given in dotted lines. For the rubidium cloud the chemical potential is given as a dash-dotted line. Without the second species present, the chemical potential is below the barrier, with potassium present, the chemical potential is higher than the interwell barrier.

The bosonic sample can be split in a double-well geometry by using an adiabatic rf potential. At the same time, the fermionic cloud can be confined to the static trap. Then, the fermionic cloud is located between the two bosonic clouds and can reduce the barrier height greatly. An example for such a situation is depicted in figure 5.3, where the fermions experience a trapping potential of $2\pi\cdot 2\,\mathrm{kHz}$ and $2\pi\cdot 10\,\mathrm{Hz}$ longitudinally, whereas the bosons are subject to a generic double-well potential with 6 μm splitting and a barrier height of $75\,\mathrm{nK}\cdot k_B$.

By tuning the atom number of the not-split atomic species, one tunes both the height of the barrier and the distance between the minima of the resulting potential. In figure 5.4 this situation is plotted for the same double-well potential than used in the previous example, now varying the number of fermions. For very low numbers of fermions, the density is too small to give a significant change to the double-well potential. At very high numbers of fermions the double-well structure vanishes altogether.

The opposite case, of modifying the double-well potential of a split fermionic cloud by a bosonic cloud that is located between the two wells of the fermions, is technically also possible. However, to split a fermionic cloud, a large barrier height in the order of the Fermi energy is necessary. This barrier is changed only slightly by the presence of the bosons.

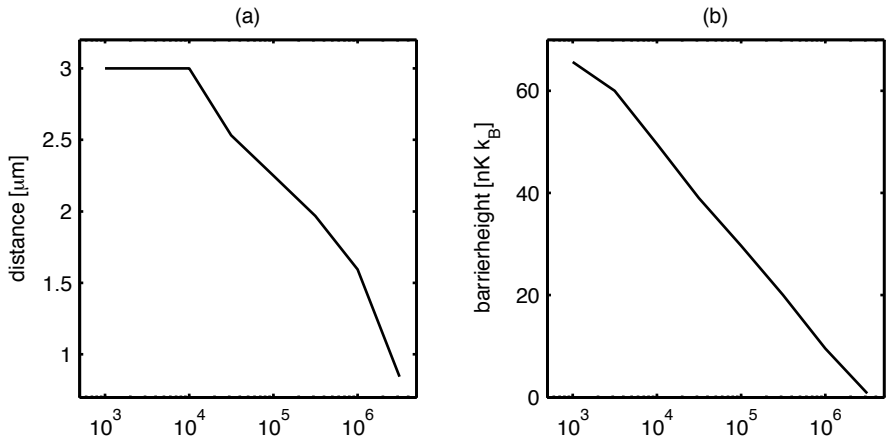

Figure 5.4.: Change in the resulting double-well potential for different numbers of fermions. The initial double-well potential and the trapping potential for the fermions are identical to the ones used in figure 5.3. (a) Distance of the two minima of the resulting double-well. (b) Height of the central barrier. The number of fermions allows to adjust the barrier of the double-well and therefore the tunneling dynamics in the double-well system over a wide range.

6 Setup for the New Mixture Experiment

This chapter represents the major part of this thesis work. Within the last years, an experimental apparatus for the preparation and study of quantum-degenerate Bose-Fermi mixtures was designed and built up. In the design and planning phase of the new experiment, many different chamber geometries, trapping geometries, layouts and experimental scenarios were envisioned, calculated or simulated. Once agreement on a layout of the new setup was reached, all the technical drawings had to be finalized to a level that workshops outside the institute were able to build all components according to the demands.

In the next step, the single components of the system had to be installed and integrated into the setup. Due to some technical obstacles on the way (mainly vacuum problems) this took longer than planned, and only first experiments characterizing the setup were possible. The work is now being continued by a new generation of PhD students.

In the first two sections of this chapter, the main design ideas and a piloting experiment on the mixture of Rb with Li will be presented. The subsequent sections are then devoted to the individual components of the new mixture experiment, starting with the laser system and the optical table in section 6.3. The vacuum chamber and the dual-MOT setup are explained in section 6.4. The mounting supports the 'heart' of the experiment structurally and incorporates all the copper structures that are used for the MOT and the large volume Ioffe trap. It is presented in section 6.5. Section 6.6 is devoted to the details of the atom chip and the considerations that led to the actual layout of the wires on the chip surface.

6.1. History

One-dimensional systems of fermions are a very promising field in physics, as they allow the direct comparison between exactly solvable models and experimental findings. Until 2006, there was no experimental realization of a quantum-degenerate Fermi gas in the miniaturized magnetic traps of an atom chip [124]. So the field of Bose-Fermi mixtures or fermions in low-dimensional traps was still open.

This motivated us about five years ago, to start thinking about an experiment with an ultracold gas of fermionic atoms on an atom chip. On such an atom chip one-dimensional trapping potentials with large aspect ratios were implemented previously [71]. Within the

group earlier work was carried out using lithium and rubidium, and a laser system for both species was readily available. Therefore, it was natural to choose the novel mixture of bosonic ^{87}Rb and fermionic ^{6}Li as a starting point for the realization of a ultracold fermionic system. At that time, there was no knowledge on the interspecies scattering properties of this mixture.

As a first step, the chamber of the former ^{7}Li experiment [133] was changed to incorporate rubidium as well, and the oven that was previously used with lithium in its natural abundance was changed to a ^{6}Li isotope-enriched version. The setup was always planned to be a temporary solution for a 'proof of concept'-experiment on the cooling of fermions. It was supposed to be replaced by a final setup in a new chamber as soon as more knowledge on the thermalization of the mixture was gained.

Therefore, the light assisted losses between ^{6}Li and ^{87}Rb were measured in a dual-species magneto-optical trap (MOT) [120], and subsequently the experiment was upgraded with an atom chip structure. At this point, magnetic trapping of both species was shown, but the short lifetime in the magnetic trap neither allowed the cooling of these species to degeneracy nor the observation of thermalization. The main reason for the short lifetime of 3.5 s were vacuum problems in the single chamber design [121].

A few months later, thermalization between ^{87}Rb and ^{6}Li was observed in a competing group in Tübingen [62]. At this point, it was clear that the move from Heidelberg to Vienna would be inevitable, and the decision was made that instead of moving the old vacuum chamber, we would start with a new experiment in a new lab.

6.2. Design Goals

After the experience gained from the Li-Rb mixture experiment, it was tried to implement as much of the acquired knowledge as possible in the new setup. The aim was a next-generation experiment that should be suitable for adiabatic rf trap experiments and for traps with very high aspect ratios. One of the first proposals for possible experiments was the investigation of the statistics and dynamics of a one-dimensional cloud. These clouds can have very low line densities in the range of 1 atom/μm. To have a chance to resolve such low atomic densities an optical resolution of a few μm is necessary.

In the planning phase a few goals were set that the new experiment should fulfill:

- A stable and robust laser system that on a daily basis does not need any attention.
- Good optical access to the chamber to be able to resolve structures in the μm range with an objective that has a high numerical aperture.
- Very low pressure at the experiment region to allow long lifetimes of the atomic samples.
- A short time for the sympathetic cooling stage to keep the overall length for each experimental cycle minimal.

Why ^{40}K-^{87}Rb?

As seen in section 5.1, a fast sympathetic cooling time can only be achieved if the elastic scattering rate between the two species is large. The triplet scattering length for ^{6}Li-^{87}Rb was experimentally shown to be relatively small $a_t = 20^{+9}_{-6}\, a_0$ [62]. In the corresponding experiment, the time to sympathetically cool the fermionic sample was more than 20 s. So,

for a new experiment in which this time was to be minimized, this mixture did not seem to be a very promising candidate.

Looking for alternative fermionic species, it was decided to switch to ^{40}K-^{87}Rb. This mixture has the advantage of having a very high interspecies scattering length. For several years there was a lively discussion over the exact value of this interspecies scattering length, but the measurement of several ^{40}K-^{87}Rb Feshbach resonances, together with a fit of an improved collisional model fixed the interspecies triplet s-wave scattering length to a value of $a_t = (-215 \pm 10)\, a_0$ [134]. Therefore, the absolute value of the scattering length is even bigger than the single species scattering length in ^{87}Rb, $a_t = (98.98 \pm 0.04)\, a_0$ [90], ensuring good thermalization rates between both samples.

Due to its low natural abundance of only 0.012%, ^{40}K was in the cold atom community somewhat neglected for several years, and magneto-optical trapping of ^{40}K was demonstrated considerably later than for the other alkali-metal atoms [135, 136].

The negative sign of the scattering length of this mixture allows the investigation of interesting physics questions. The attractive interaction leads to a collapse of the mixture at high atom numbers ([18], see section 5.2.1) and the formation of bright solitons might be observable [137].

The mixture of ^{40}K-^{87}Rb is currently investigated in many different labs, for example [138, 139, 62, 140, 141, 142], and one other group is using this combination in an atom chip experiment [47]. So a fair amount of technical details is published, one could follow in the build-up phase of the experiment. For example, on the fabrication of isotope-enriched potassium dispensers [143] that are necessary to allow high atom numbers for ^{40}K.

An experimental advantage of this mixture is the fact that the wavelengths of both species are very close together (767 nm and 780 nm). Therefore, the same set of optical components can be used, simplifying the layout of the optics greatly.

6.3. Optics

6.3.1. Lasers

To trap ^{87}Rb or ^{40}K in a MOT one needs, as for all alkali-metal atoms, light at two different frequencies. The cooling or cycling transition is neither for Rb nor for K perfectly closed. Repumping light at a second frequency is needed to bring the atoms back into the cooling cycle. The level schemes for both species and the corresponding transitions can be found in appendix A.2.

Rubidium

For rubidium the cooling light is provided by a Ti:Sapphire ring laser[1] that is pumped at 532 nm by a diode-pumped solid-state laser[2]. The pump laser runs at an output power of 10 W, as a higher pumping power might damage the crystal of the ring laser. With this setup, an output power of 1.6 W at the rubidium wavelength can be reached. The cavity of the ring laser is locked to the $F = 2 \rightarrow F' = 1, 3$ crossover in ^{87}Rb. Therefore, the light is detuned 212 MHz to the red with respect to the cooling transition. By using acousto-optical

[1] MBR110, Coherent
[2] Verdi V18, Coherent

modulators (AOMs) in double-pass configuration the light is shifted closer to the atomic transition.

To generate the rubidium repumping light, a combination of two lasers is used: a homebuilt external cavity diode laser in Littrow configuration (the master) seeds a second free running laser diode (the slave). The master laser is locked on the $F = 1 \rightarrow F' = 1, 2$ crossover, and therefore the light is shifted by 78 MHz relative to the repumping transition. The seeding of the slave laser is done through one of the 'wrong' ports of an optical isolator[3]. The seeded laser delivers enough power (40 mW) for the operation of two MOTs, as the loss channel in ^{87}Rb into the $F = 1$ ground state is approximately one part in 10^4.

Potassium

The situation is slightly different for ^{40}K. There the excited state hyperfine splitting is only seven natural line widths wide, necessitating a laser on the repumping transition that has almost the same strength than the cooler laser. In other experiments, an intensity ratio of 4:1 between cooling and repumping light has been found to be favorable for the operation of a MOT [91]. In addition, the repumper has to be detuned to the red of the transition for an optimal performance of the MOT.

To provide this light, two commercial diode lasers were bought[4]. These lasers combine a tapered amplifier chip with a tunable grating at the back facet. Each of the lasers delivers more than 400 mW of light at the specified wavelength.

The laser that is used to deliver the light at the repumping wavelength of ^{40}K, is locked on the ^{39}K repumping transition using a ^{39}K spectroscopy cell[5]. The isotope shift of 415 MHz between the repumping transitions in ^{39}K and the repumping transition in ^{40}K is bridged by an AOM in double pass configuration. It shifts the light going to the spectroscopy cell by $2\times$ 167.5 MHz. Effectively, the laser is running at 80 MHz blue to the repumping transition in ^{40}K. An additional AOM working at -110 MHz then ensures that the repumper is for the magneto-optical trap 30 MHz red detuned to the transition.

The second ^{40}K laser, the cooler, is frequency stabilized by a frequency offset lock relative to the repumping laser. This is done by beating the light of both lasers in a 3 m long optical fiber. The laser is then locked on the beat signal after this was mixed with a reference oscillator. This locking scheme guarantees a very good stability of the laser lock and gives a large flexibility when one wants to sweep the laser.

All diode lasers are mounted on an optical breadboard that is electrically isolated from the rest of the optical table. Additionally, a wooden box encloses all these lasers and the spectroscopy cells, to enhance the stability of the laser locks against acoustic noise and temperature changes. More details on the laser locking schemes, especially the beat lock can be found in [121].

For the alignment of the MOT beams, it is sometimes favorable to switch from ^{40}K to ^{39}K as trapped species. Even when using dispensers made from enriched ^{40}K, the number of trapped ^{39}K atoms is 20 times larger than the number of trapped ^{40}K atoms. Therefore, the fluorescence signal of the MOT is larger as well. There was no separate laser locking scheme developed for the transitions in this isotope, but by having the two lasers free running

[3] Linos, FI-780-5 SV

[4] DLX 110, Toptica

[5] all spectroscopy cells in our group were built by the glass blowing workshop at the Physikalische Institut in Heidelberg

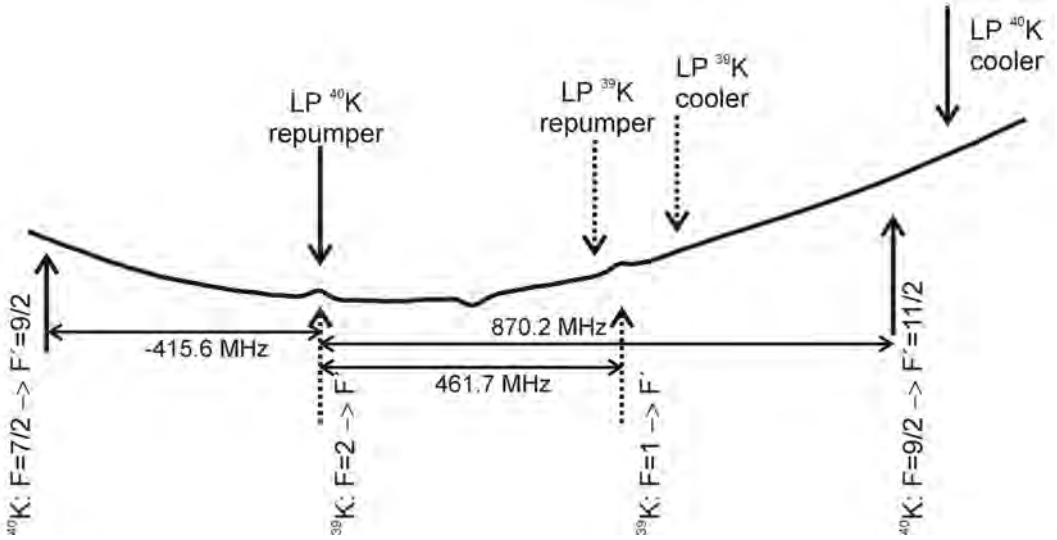

Figure 6.1.: A spectroscopy trace for ^{39}K and the relevant transitions for both isotopes. In spectroscopy the transitions of ^{40}K are not visible due to the low abundance. On the upper half of the picture, the lock point for the lasers are given for either running a ^{40}K-MOT or a ^{39}K-MOT.

at the two points of the spectroscopy signal marked in figure 6.1, a stable ^{39}K MOT can be realized in the experiment. If the experiment were to be change permanently to ^{39}K, only the frequency of the spectroscopy AOM and the frequency of the reference oscillator of the beat lock would have to be adapted.

6.3.2. Optical Table

To improve the stability of the whole setup, the optics and the vacuum chamber were separated and placed on two different optical tables. Above the tables, the air conditioning provides a laminar flow of air that is stabilized in temperature and humidity. The temperature deviations are kept below 0.1 K to ensure optimal conditions for a stable system.

To get the light from the optical table to the experiment, it is coupled into polarization maintaining optical fibers[6]. This splits the alignment of the optics on the table from the alignment of the optics next to the chamber, simplifying the work in the lab greatly. As the beam diameter and shape of the potassium and rubidium laser beams are similar but not identical, the focusing lens in the fiber incoupler and the divergence and diameter of the single beams being coupled have to be iteratively optimized . Only then an optimal coupling efficiency for both wavelengths can be reached. In each the two fibers going to the two separate MOTs, a total of four beams for the repumping and cooling light of the two species have to be coupled simultaneously.

The layout of the optics is visible in figure 6.2. On the table the light for the different purposes (MOT, imaging, push beam, optical pumping) is shifted to the right frequencies using a total of 11 AOMs. The frequency of each AOM is given in table 6.1.

As the diffraction efficiency of the AOMs depends strongly on the beam diameter, the beam size is reduced by a factor of four before any of the AOMs and after the AOM expanded again. For the double-pass AOMs a similar scheme with a Galilean telescope and a single refocusing

[6]Schäfter + Kirchhoff, `http://www.sukhamburg.de`

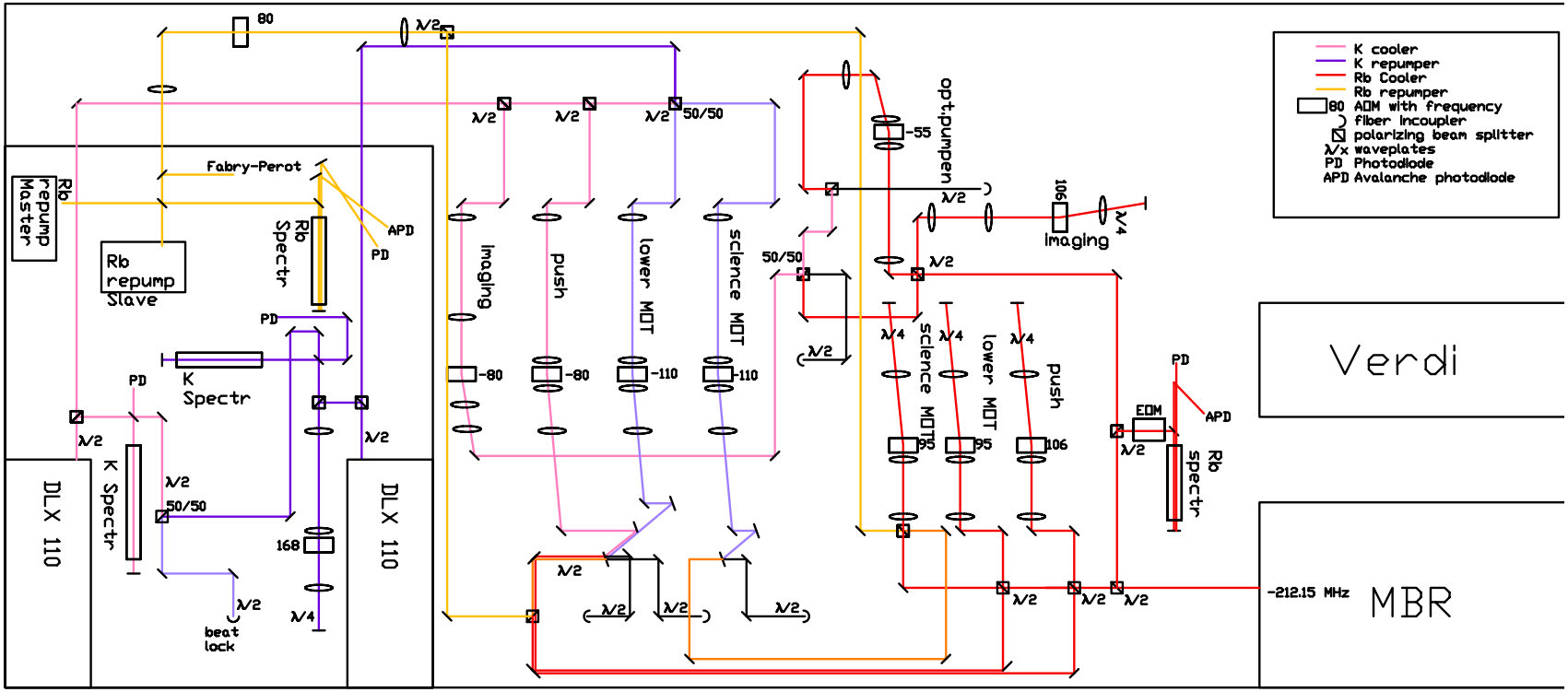

Figure 6.2.: Layout of the optical table. The different frequencies for the two MOTs, the push beam, the imaging and the optical pumping are created by AOMs for Rb and K separately. The light is then superimposed on unpolarized beam splitters (for the imaging an optical pumping) or superimposed on two specially coated mirrors before being coupled into five single-mode fibers that guide the light to the experiment.

AOM	Frequency [MHz]	resulting detuning to transition
^{40}K spectroscopy	167.5 DP	0 MHz to ^{39}K repumper
^{40}K MOT I/II	-110 SP	-30 MHz to ^{40}K cooler and repumper
^{40}K imaging	-80 SP	0 MHz to cooler ^{40}K
^{40}K push beam	-80 SP	0 MHz to cooler ^{40}K
^{87}Rb MOT I/II	+96 DP	-20 MHz to cooler ^{87}Rb
^{87}Rb imaging	+106 DP	0 MHz to cooler ^{87}Rb
^{87}Rb push beam	+106 DP	0 MHz to cooler ^{87}Rb
^{87}Rb optical pump	-55 SP	-267 MHz to cooler ^{87}Rb
^{87}Rb repumper	78 SP	0 MHZ to repumper ^{87}Rb

Table 6.1.: Frequencies and resulting detuning of the AOMs used in the K-Rb experiment. SP and DP label the single-pass or double-pass configurations. The different lasers are running at 80 MHz blue detuned to the ^{40}K repumper transition, 80 MHz blue detuned to the ^{40}K cooler transition, 212 MHz red detuned to the ^{87}Rb cooler transition and 78 MHz red detuned to the ^{87}Rb repumping transition.

lens is employed. This ensures a high coupling efficiency in the fiber even when the AOM is being detuned [144].

The number of AOMs could be reduced by using the same beam path for both, the collection MOT and the science MOT. However, from the experience of the previous double-MOT experiment in our group [145], the optimum detuning parameters for the operation of both MOTs are different as the magnetic field gradients differ. Therefore, the decision was made to separate the beam paths and to use individual AOMs.

On the output side of the fiber the same optics are used for both wavelengths 767 nm and 780 nm. This makes it necessary to combine the light from both species with identical polarization before coupling into the fibers. At beams paths where the absolute power of the beams is small (imaging beam and optical pumping beam), one output of a 50/50 non-polarizing beam splitter is used to couple light in the fiber and the light that leaves the other port of this cube is dumped.

To combine the light for the collection MOT, the science MOT and the push beam, two specially coated mirrors are used. The front of theses mirrors is coated such that they have a high reflectivity at 767 nm, whereas the backside of the substrate is coated in a way that rubidium light at 780 nm passes with minimal loss[7]. As there are only two of these mirrors available for the experiment, one of these mirrors is used to superimpose two beams of potassium light on two beams of rubidium light.

For the beams with only potassium light and for all beam paths after the combination of rubidium and potassium light, zero-order wave plates are used. They were fabricated for a central wavelength of 773.3 nm[8], right between 780 nm and 767.7 nm. This minimizes the problems that arise when working with polarization optics and two different wavelengths simultaneously.

[7] Laserzentrum Hannover `http://www.laser-zentrum-hannover.de/`
[8] Lens-Optics `http://www.lens-optics.de/`

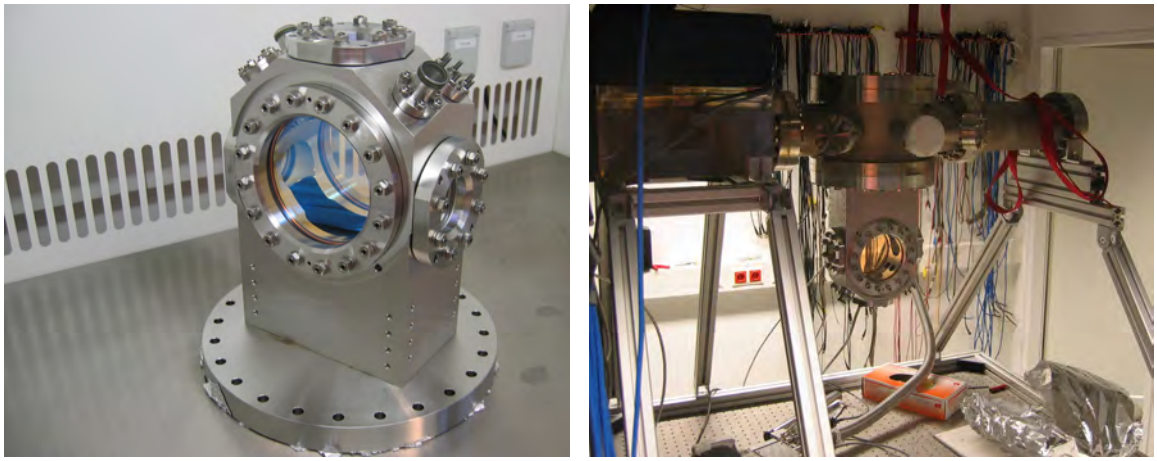

(a) (b)

Figure 6.3.: **(a)** Science Chamber after all windows were mounted. **(b)** The science chamber is attached to a star-like chamber that connects to a pipe with a TSP pump (right end) and an ion pump (left end). To evacuate this part of the setup a turbo pump can be connected at the star.

6.4. A New Vacuum Chamber

One of the goals of the new setup was to have good optical access to the experiment region. The natural choice was to look for a setup that incorporates a glass cell. Different groups combine glass cells with chip structures [40]. However, as there was only limited experience with glass cells in our group, a more conventional approach was chosen and a steel chamber was built that is somewhat similar to the one used in a previous experiment [66].

A first idea was to use a chamber that is welded together from standard vacuum components. When using standard of-the-shelf vacuum components there are some technical limits on the minimum size of vacuum chambers. Due to the rather unfortunate ratio between the free diameter of the windows and the outer diameter of the corresponding flange in standard ConFlat (CF) components, it is almost impossible to create chambers with a small distance between two opposite windows whilst keeping the optical access from any other direction acceptable.

Therefore, the decision was made to use a custom-made steel chamber and high-optical-quality anti-reflection-coated quartz substrates as windows. There is a well established sealing technique working with metal seals that have an internal spring. These seals allow to reach the necessary vacuum conditions of 10^{-12} mbar[9]. Nevertheless, sealing the vacuum chamber turned out to be the biggest obstacle in the build-up phase of the experiment (see section 6.4.1 for more details).

The minimal internal size of the chamber was given by the outer extensions of the mounting that holds the atom chip. The mounting has a cross section that is a little below 40 x 40 mm. The chamber was then planned with a minimal distance between the mounting and the windows that is around 1 mm.

In several iterations the position and size of the individual viewports were optimized, leading to a chamber with outer dimensions of 92 x 160 x 250 mm. It has two big viewports with a

[9] Helicoflex Δ-seals, `http://www.helicoflex.com`

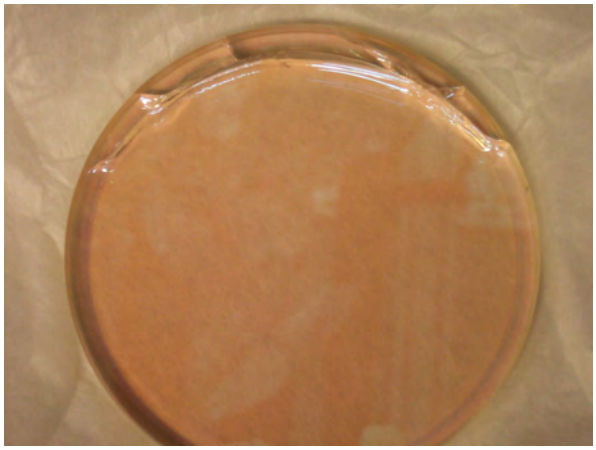

Figure 6.4: All three of the windows broke at about the same position at the uppermost position of the window during various stages of the baking process. The crack then propagates along the line where the seal puts pressure on the window.

free diameter of 100 mm for the transversal imaging of the cloud and the MOT beams that enter the chamber under 45°. Then, there are three identical viewports with a free diameter of 43 mm for the longitudinal imaging and the optical access from below. In addition, four small DN16CF ports are located in the four lower corners of the chamber. A picture of the chamber is visible in figure 6.3.

One of the DN16CF ports is used to connect to a second MOT chamber that serves as the atom source for ^{40}K and ^{87}Rb atoms, whereas the other ports are closed with non-magnetic windows or blanks. At a later point, one of these spare ports will allow the addition of a third atomic species to the experiment. More details on the science chamber and its design process can be found in [121].

The chamber was manufactured from a block of 316L steel by a company in Vienna and was welded into a DN200CF flange made from 316LN steel. Via this flange, the science chamber is attached to a star-like chamber. This star-like chamber connects to a tube that houses the titanium sublimation pump (TSP) and to the ion pump[10]. Additionally, an all-metal valve at the star allows the connection of a turbo pump to evacuate this section of the setup.

As visible in figure 6.3(b), the whole chamber is resting with this star-like chamber on a frame so that the lower window of the science chamber is about 46 cm above the optical table.

6.4.1. The Window Issue

The two big viewports of the chamber are designed to carry 10 mm AR-coated quartz glass substrates. During the bake-out of the chamber to around 100° C, there were three repeated incidents in which always the big window on the same side of the chamber broke at a similar position. There is no conclusive picture yet, but the most likely interpretation is that there might be some stress in the chamber due to the fabrication methods that were chosen. This stress then causes a local deformation of the chamber during the heating that breaks the window.

According to engineers working for companies that are specialized on the manufacturing of vacuum chambers[11], steel locally heats up either during milling or during welding. Therefore, stress can develop locally in the steel matrix. Especially the very elongated welding joint between the science chamber and the corresponding flange seems to be a very likely candidate

[10] Varian, VacIon Plus 150 StarCell
[11] for example Reuter, `http://www.reuter-technologie.de/`

to cause problems. The strategy used by these companies to avoid problems at metal-glass interfaces is, to do all the machining on the chamber, then anneal it to remove any stress from the metal and afterward redo the critical surfaces in a final machining step.

As a makeshift solution this window was after the third breakage replaced by an uncoated BK7 window that is 50% thicker than the ones previously chosen. This window was supposed to be on the side where the imaging beam leaves the chamber and the first lens of the imaging setup is located. As the optical performance degrades significantly when the first lens of the imaging setup has to move 5 mm away from the atomic cloud, the input and output side of the imaging beam were interchanged. Thankfully, this window survived now one bake-out cycle.

Possible Workarounds

As a backup solution for the case that this window breaks again, an adapter was designed and manufactured that will replace this big window with two standard CF-flanges, one DN40CF, the other one DN63CF. On these flanges coated windows will be used. This will limit the optical access from one side of the chamber, but will at least lead to a working solution that does not require that the whole chamber is taken apart and is remachined. A technical drawing of this adapter can be found in appendix C.

6.4.2. Double-MOT

To achieve in the experiment region a sufficiently low pressure, the collection MOT region and the science chamber were split into two separate chambers. The setup is visible in figure 6.5. A similar double-MOT setup that is connected by a differential pumping stage was used in one of the previous experiments of our group [66]. As one of the design constraints was optical access from directly below the chip, the connection between the two chambers has an angle of 37° towards the direction of gravity. An all-metal valve at this connection allows both chambers to be vented independently.

The collection MOT chamber is a three-way cross of DN40CF windows that has eight additional DN16CF flanges and is identical to the chamber used in [66]. Two of these DN16CF house the potassium and the rubidium dispensers, a third one is connected to a valve that itself then connects to the science chamber. The six bigger windows are used for a standard three-beam retro-reflected MOT layout. The quadrupole coils are wound directly on the chamber around the pipes of two of the DN40CF windows and have 90 windings each.

The lower MOT chamber is pumped separately from the rest of the setup and has a small ion pump[12] connected to a T-piece that is attached to one of the DN40CF flanges. Currently this pump does not seem to work properly and might need a replacement.

By restricting the geometry of the connection between the two chambers to a long small-diameter pipe, it is possible to maintain a pressure difference of several orders of magnitude between the two chambers. Two small diameter copper tubes were added to reduce the diameter. Going from the lower chamber to the science chamber the following diameters are present: for 45 mm ø 5 mm, 38 mm with ø 16 mm and then 90 mm ø 10 mm.

In the limit of molecular flow, the conductance for such tubes with a rather small length/diameter ratio can be determined [146]. For this setup, the values are 0.34 l/s, 11.25 l/s and 0.87 l/s. The conductance of the whole chain evaluates to 0.24 l/s. The ion pump has a pumping speed

[12] Varian, VacIon 20 StarCell

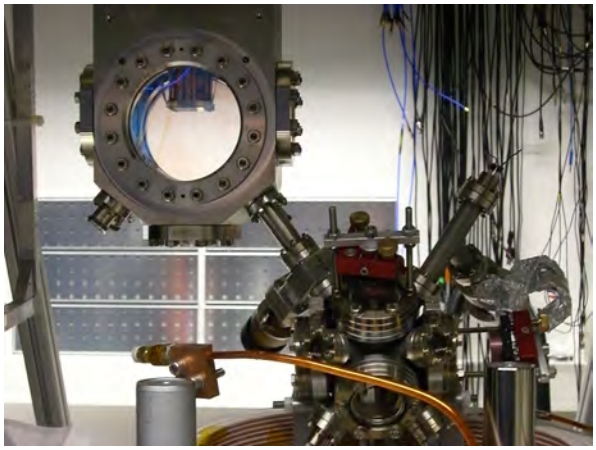

Figure 6.5: The lower collection MOT chamber and the science chamber before the coils were mounted. An all-metal valve allows to vent only the lower part of the vacuum setup or only the science chamber.

of 150 l/s. Below the atom chip the effective pumping speed is reduced due to the geometry of the science chamber where the mounting of the atom chip blocks most of the free diameter of the chamber. Even if the pumping speed is reduced by a factor of five to 30 l/s, the pressure in the science chamber will still be more than two orders of magnitude better than the pressure in the collection MOT chamber.

To get rubidium or potassium atoms in the science MOT, a push beam is used that points along the axis between both MOTs. A push beam is a beam of near resonant light that transfers momentum to the atoms and is therefore able to push the atoms from the collection MOT to the science MOT. To reduce the momentum spread during the transfer, typically no repumping light is used in the push beam. Then the atoms are pumped to a dark state after a few absorption-emission cycles. Currently, the optimal parameters for the transfer of both species have to be found to ensure high loading rates.

Dispensers

The atom sources in the collection MOT chamber are two commercial ^{87}Rb dispensers[13] and two homebuilt ^{40}K dispensers. The two dispensers for each species are mounted in parallel on a Macor piece inside one of the DN16CF flanges.

In theses dispensers, KCl is reduced by driving the reaction

$$2\mathrm{KCl} + \mathrm{Ca} \rightarrow 2\mathrm{K} + \mathrm{CaCl_2}.$$

The KCl powder is isotope-enriched to 5.5% ^{40}K[14] and mixed with Ca powder before being filled in little metal boats. The potassium dispensers release a sufficient amount of ^{40}K atoms once they are heated by a current of 3.5 A each.

Details on the manufacturing and the performance of these dispensers can be found in [121, 147]. Just recently, a company[15] started to sell dispensers for isotope enriched ^{40}K. If in the future it is necessary to break the vacuum of the lower chamber, these commercial dispensers will replace the homebuilt ones.

[13] SAES getters, `http://www.saesgetters.com`
[14] Strictly speaking the dispensers are therefore still ^{39}K dispensers
[15] alvatec, `http://www.alvatec.com`

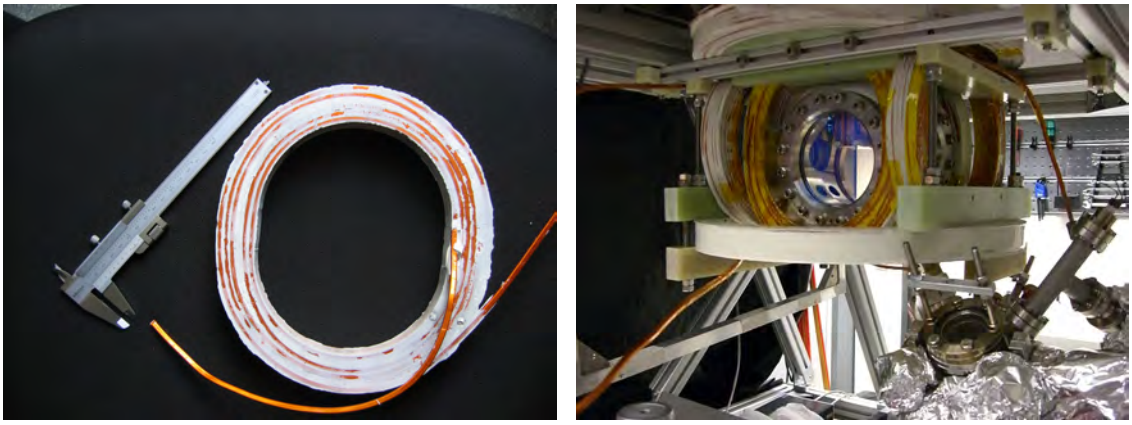

(a) (b)

Figure 6.6.: (a) One of the coils after manufacturing. The wire is held into place by epoxy glue. **(b)** All six coils mounted around the chamber. As the Kapton shield of the coils was damaged at several points, they were additionally isolated by Kapton tape. The coils are held into place by a structure of A4-grade steel rods and fiberglass-reinforced epoxy parts.

6.4.3. External Coils

In addition to have stable and very homogeneous fields, one of the design constraints was that the whole coil setup including all the mounting should be able to deal with temperatures of 150° C. Then, it is not necessary to remove the magnetic coils when performing a bake-out of the chamber, for example, after exchanging the chip. The coils were therefore made from Kapton®-isolated wire and are held together by heat-resistant epoxy glue.

The best configuration for homogeneous magnetic fields over large volumes is the Helmholtz configuration, in which both circular coils are a distance of one radius apart. In an expansion of the field around the central position, the first term after the constant field is then a quartic term. For smaller distances of the two coils than their radius, the curvature is negative, whereas with distances bigger than the radius the curvature is positive.

Due to other design considerations, such as optical access and the finite size of the coils, it is not possible to place all pairs of coils in the Helmholtz configuration. Optimizing the shape and size of the coils for optical access and minimal field curvature, the best design for the innermost coils were stadium-shaped coils that fit with their radius smoothly around the big windows of the science chamber. Due to their elongated shape along the axis of gravity the field maximum is not at the center of the window, but at the position of the atomic trap, a little below the chip. One of these coils can be seen in figure 6.6(a).

To keep the fabrication as simple as possible, the second pair of coils was built on the same mold and was just rotated by 90°, interchanging the two half axes. The third pair had to have a rather big diameter to fit over the DN200CF flange of the science chamber and was chosen to be circular. Details on the size and diameter of the coils can be found in table 6.2.

The coils are wound from a hollow square wire[16] that has a quadratic cross section of $4.4\,\mathrm{x}\,4.4\,\mathrm{mm}^2$, has a hole of 2 mm diameter and is isolated by Kapton tape. All coils were manufactured in-house on a lathe using a mold that was protected by teflon spray. The single

[16] S & W Wire Company,Cranberry Twp, PA 16066, United States `http://www.swwireco.com`

	Shape	Windings	Radii [cm]	Distance [cm]	Field Curvature between coils [G/cm^2]	Field Curvature transversal [G/cm^2]	Field Strength calculated [G/A]	Field Strength measured [G/A]	Resistance per coil [mΩ]	Inductance per coil [mH]
x-coil	elliptic	36	8.7/10.2	12.4	0.79	**0.58**/0.22	2.77	2.72	100	0.28
y-coil	circular	36	16.4	18.8	0.11	**0.06**	1.73	1.71	133	0.70
z-coil	elliptic	36	8.7/10.2	23.0	**0.82**	0.45/0.37	1.27	1.24	100	0.28

Table 6.2.: Parameters for the bias coils in the K-Rb experiment. All values were calculated for a uniform current density in an area of 2.8 x 2.8 cm around the central line given by the radius and the distance. Curvatures are given for a current of 50 A. Bold typeface indicates the parameters that are of greater importance in the experiment as those curvatures are along the weak trapping axis of the chip trap. Using Rb atoms those curvatures evaluate to maximum trapping frequencies close to $2\pi \cdot 1$ Hz.

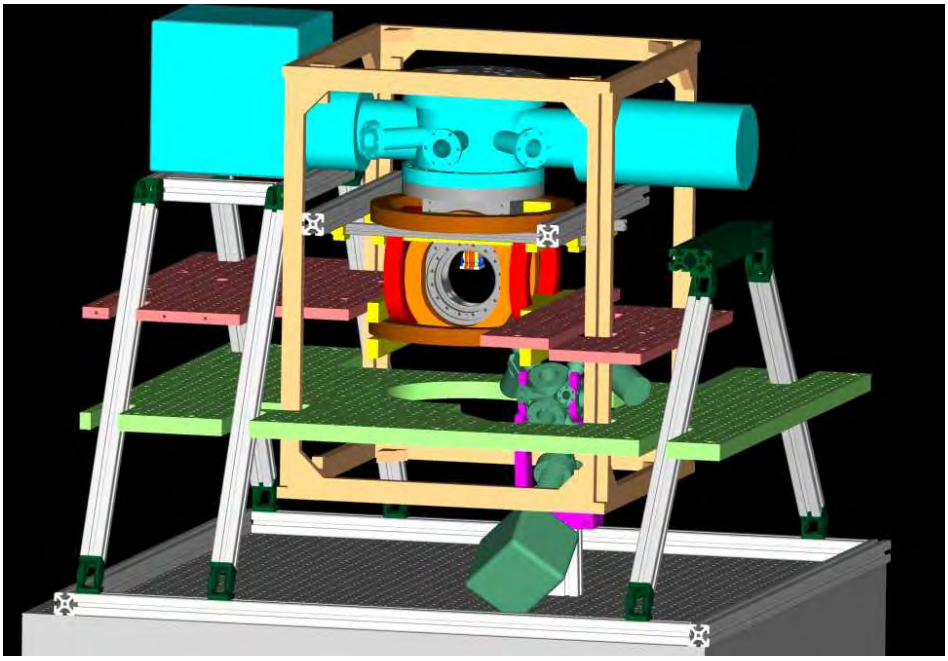

Figure 6.7.: CAD rendering of the whole setup. In addition to the vacuum parts the bias coils and the big compensation cage is visible. The optical components are mounted on three different height levels on optics boards and are omitted for clarity.

windings are held together by an epoxy glue[17] that can withstand the temperature of a mild bake-out of the chamber. Using clamps made from fiber-reinforced plastic parts, the coils are mounted around the science chamber as visible in figure 6.6(b).

Due to the compact design of the coils and the high currents that are flowing, the coils have to be cooled actively. A current of 60 A corresponds to a thermal load of 150 W per coil. As one coil with 36 windings has a total length of around 35 m, a pressure of around 2 bar is needed to push enough cooling water through the coils. For one pair of coils at a constant current of 45 A the temperature of the cooling water was measured to rise about 11 K between the inlet and outflow of the coil. All the necessary cooling water is provided by a chiller that is filled with distilled water.

In table 6.2, the various remaining curvatures of the fields created by these coils are given. They were calculated for a pair of coils supplied with 50 A, taking the spatial extension of 28 x 28 mm of each of the coils into account. The absolute values of the fields were measured using a hall probe mounted on a micrometer translation stage.

6.4.4. Compensation Coils

To compensate all ambient fields inside the science chamber, there is an additional set of compensation coils that was inherited from the former RbII experiment in our group [133]. These are six coils from thin copper wire wound on two quadratic (580 x 580 mm) and four rectangular (720 x 540 mm) frames. With a resistance close to 11 Ω per pair they deliver fields of 1.7 G/A in all three spacial directions. The power is supplied by a four-channel power supply

[17] Hysol 9492, Henkel, Austria

that is continuously running during the experimental cycle. The whole chamber including all the coils can be seen in a CAD rendering in figure 6.7.

6.5. Chip Mounting

To support the atom chip and the copper structures in the center of the vacuum chamber, a structure with more than 100 components had to be designed and built. The whole setup can be seen in figure 6.8. Everything has to be vacuum compatible in the 10^{-12} mbar range and has to be very rigid, as vibrations and movements of the chip with respect to the chamber were seen in previous experiments of our group. All manufacturing was done in the workshop of the Physikalische Institut in Heidelberg, even after the move to Vienna. The drawings of all major parts that were designed and commissioned by the author of this thesis can be found in appendix C.

To connect the chip and the copper structures to the outside world, several feedthroughs were welded in a DN200CF flange made from non-magnetic steel. It is equipped with six high-current feedthroughs[18] (five currently used for the copper structures, one spare), one 35-pin multicontact feedthrough[19] for the connections to the chip, two tubulated DN40CF flanges and four tubulated DN16CF flanges. Two of the DN16CF flanges were later equipped with SMA feedthroughs to connect to the rf foil. The flange serves as base plate for the whole rest of the mounting structure.

The structure of the mounting is as follows: The lowest part is a bulk piece of 316L steel which serves as base for a pillar made from copper. On top of this copper piece the so-called 'head' is screwed. This part can be seen in figure 6.8 (b)-(d) and is assembled separately. It can be exchanged as a whole if the chip is exchanged. Current is guided to the head using ø5 mm copper rods for currents up to 100 A. The single rods are clamped to the high-current feedthroughs by copper clamps and connected to the copper structures in the mounting head by screws. For the chip currents small Kapton-isolated wires are used that are clipped on small pins made from copper-beryllium. To feed the current to the rf foil on the back side of the chip, a vacuum-rated SMA-cable[20] is used which is soldered to the structures using silver solder[21].

6.5.1. Ceramic Structures

To support the atom chip and to keep the copper structures in place, a Shapal structure is used. This is machinable ceramic (aluminium nitride) has a 60 times better heat conductivity than Macor that was used previously ($100\,\mathrm{W\,m^{-1}\,K^{-1}}$ instead of $1.5\,\mathrm{W\,m^{-1}\,K^{-1}}$). The copper structures and the ceramic piece are made to fit, to ensure the biggest surface contact area possible. Unfortunately, the workshop had severe trouble machining the material and ended up with a working time of 62 hours on this ceramic structure. The top surface of the ceramic structure has different height levels to reduce the problem of enclosed air pockets once the chip is glued to the ceramic.

In the past, the problem was encountered that during the bonding process some of the pins moved slightly. Then, most of the power of the ultrasonic pulse is lost, leading to weak

[18] Caburn, MC5.150C
[19] Lesker, IFTAG355101
[20] Allectra, `http://www.allectra.com`
[21] Allectra, UHV Solder 315

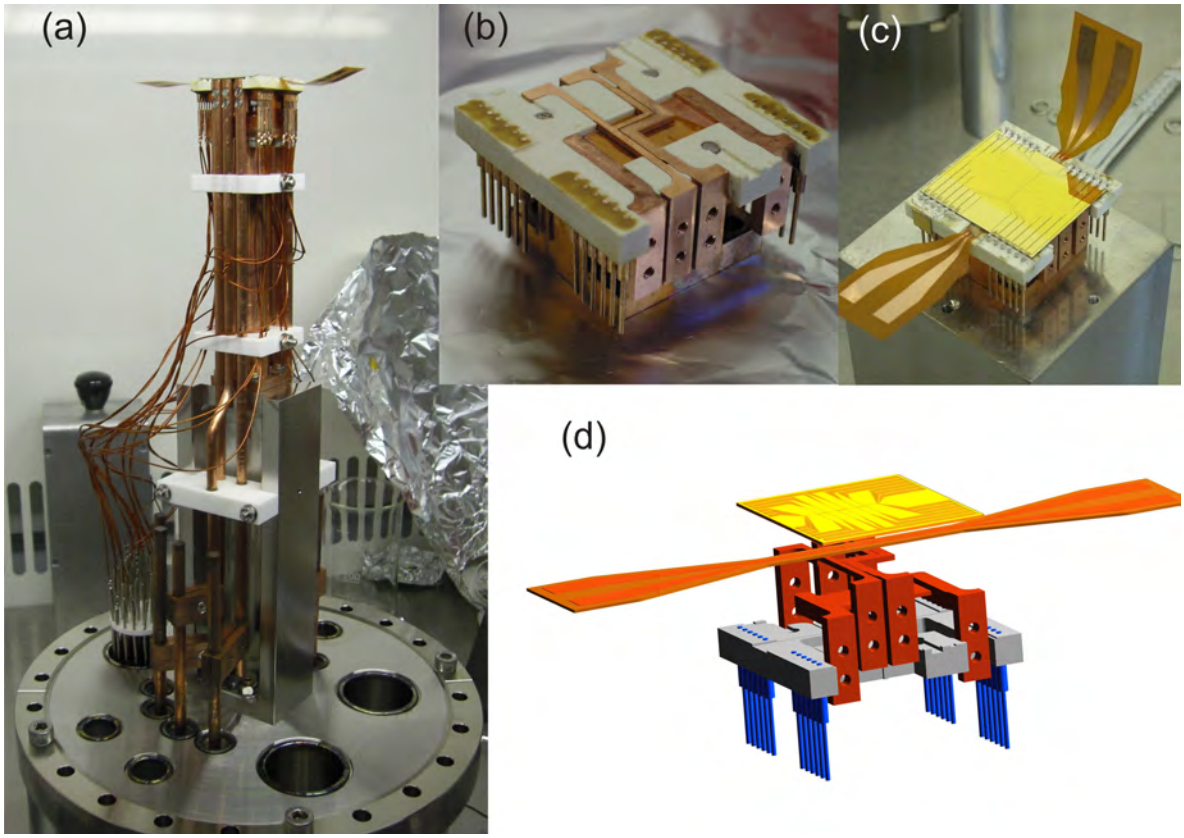

Figure 6.8.: **(a)** Overview of complete mounting. The height above the flange is around 31 cm. High currents are led through ø5 mm copper rods, low currents through Kapton isolated wires that are clipped on the pins. **(b)** The three copper structures embedded in the ceramic piece after gluing the pins. The distance between the structures is 100 µm and some Kapton foil is added for isolation. **(c)** Head with chip after gluing and bonding. Below the chip a 50 µm thick Kapton foil with printed copper structures that serve as additional rf wires is visible. On the chip surface a small change in reflectivity and color of the gold due to the SiO_2 layer is visible. **(d)** All components of the head in an explosion rendering.

bonds. To give the copper-beryllium pins more stability they were designed such that they barely reach above the ceramic surface. In addition, the chip was recessed that it is almost level with the ceramic. Finally, the pins were glued in the ceramic piece using UHV proof epoxy[22].

Nevertheless, the bonding of the chip was very slow. After several tedious days at the bonding machine each of the pins was connected to the corresponding pad with between 25 and 30 bonds. For the future it would be advisable to have someone looking in more detail into ways to improve the bonding process, as the long time under the bonding machine turns out to be currently the main source of dirt on the chip surface.

To stabilize the whole mounting and to make sure that neighboring copper rods are not touching each other, additional ceramic spacers made from Macor are added at two different height levels of the mounting.

6.5.2. Copper Structures

Similar to the RbI experiment [145] of our group, it was decided to use a wide U-structure for the magnetic field of the science MOT. Such a structure has the advantage of providing a rather big trapping volume, whilst offering the possibility of setting external quadrupole coils aside. An almost identical structure was investigated in our group in the past [148, 67]. The middle bar of the U is 10 mm wide and 0.7 mm thick. For typical parameters of 60 A current in the structure, 20 G bias field and an additional bias field of 5 A rotating the trap, the trap is a little less than 1 mm away from the chip surface with a gradient of 30 G/cm.

With such an integrated U-MOT, atoms can usually be cooled in the range of 100 µK. In principle these atoms could, after a short phase of molasses cooling, be loaded directly in a Ioffe trap formed by the microscopic wires on the chip. However, the small trapping volume of the chip trap limits the number of trapped atoms greatly.

In all our current experiments, atoms are, as an intermediate step, loaded into a Ioffe trap formed by macroscopic copper wires (1 mm x 1 mm cross section) that typically carry 50-60 A. In combination with an external bias field they allow rather big trapping volumes and, at the same time, a sufficient trap depth. For the new setup this scheme was improved by going over to two parallel Z-structures. One is 2 mm wide, the other one is 1 mm wide.

If both structures are supplied with the same current density, a trap right at the position of the MOT will form that has a considerably bigger trapping volume than in the current setups with a single Z-structure. This can been see in figure 6.9. A situation is created in which basically all atoms that were precooled in the MOT stage are trapped in the magnetic trap.

In the next step of the experimental sequence, the current in the wide Z is reduced and the trap moves closer to the chip and above the center of the small Z-structure. This compression reduces the trap volume and ensures a good mode matching with the chip trap. The position of this trap coincides with the position of the first trap on the chip surface that then will be ramped up.

The small Z-structure has an additional connecting lead and forms a structure that resembles the letter 'h'. By connecting the straight part of the h-structure, it can be used as a dimple wire that enhances the longitudinal confinement of the chip traps.

All three structures are made to fit to the ceramic structure. The distance between the

[22] EPO-TEK 920-FL, `http://www.epotek.com`

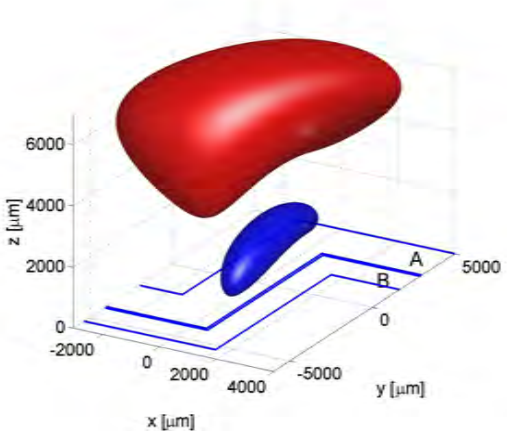

Figure 6.9: Red: Isosurface 20 G for 120 A in wire A and 60 A in wire B, blue Isosurface 20 G for 60 A in wire B. The direction of the biasfield (60 G) is always adjusted such that same trap depth is achieved. The red volume is 13.5 time the blue volume.

single structures is 100 µm. To avoid any contact between the structures in the case that one of the structures deforms slightly due to the heat, small pieces of Kapton foil are fit into the 100 µm gaps.

6.5.3. Thermal Management

In the planned future experimental sequence, the small copper Z-structure will carry 60 A for several seconds. As it has at the central region a cross section of only 1 mm x 1 mm, ohmic heating will be significant. To estimate the amount of heat that is dissipated, the structure was simulated using a combined electrostatic and heat conduction model in FEMLAB[23]. In figure 6.10, it is shown that the current density has local maxima at the points where the diameter of the wire changes abruptly and at the 90° edges. This leads to local resistive heating that then raises the temperature in the whole structure. After a few seconds a static situation is reached and the temperature is about 10 K higher than at the start.

In the real system, the surrounding ceramic structure and the big copper column below the ceramic act as a heat sink. Therefore, the temperature rise will be smaller. However, a probably bigger contribution to the heating of the structure is resistive heating at the surfaces where the rods are bolted to the copper structures (visible in figure 6.8(b)). These surfaces will have a non-zero resistance and even a low contact resistance of 1 mΩ leads, at a current of 60 A, to a heating power of 3.6 W that is locally dissipated. A typical experimental cycle will probably have a length close to 30 s. During this time both copper Z-structures will only be switched on for a short period of 5 to 10 s until the atoms are loaded into the chip structures. Therefore, there will be enough time for the structures to cool down and distribute the heat that is generated.

[23] `http://www.comsol.com`

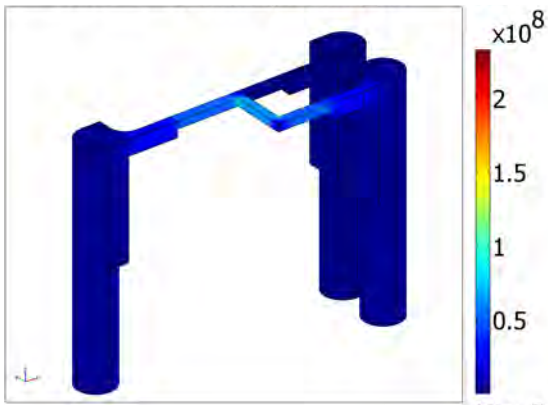

(a) Current density in A/m^3

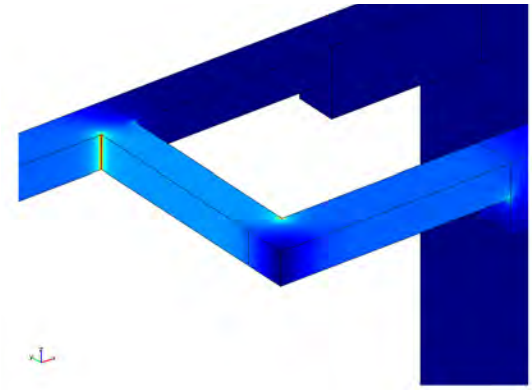

(b) Closeup on the central part of (a)

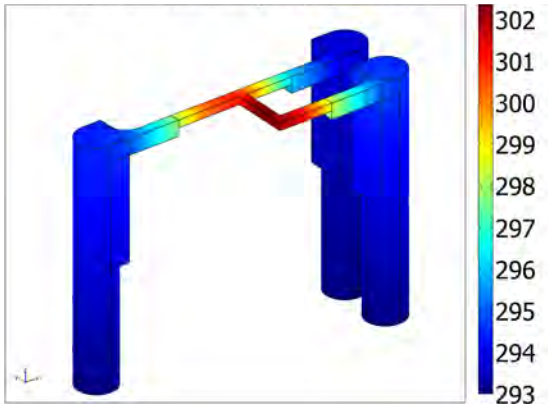

(c) Stationary temperature in K

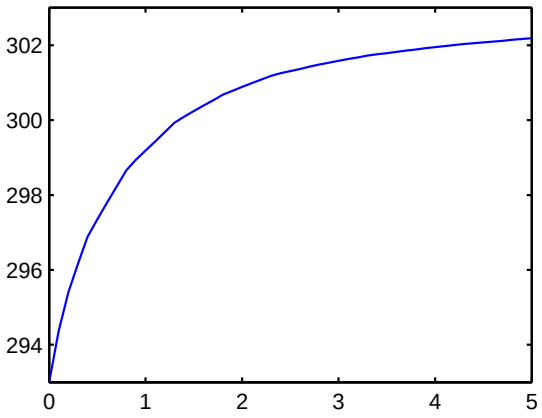

(d) Temporal evolution of temperature at hottest point in the first five seconds after switching on the current.

Figure 6.10.: FEMLAB simulation of temperature in small copper Z-structure. Parameters used: current of 60 A, temperature dependent conductivity and a surrounding temp 293 K. The lower ends of the three rods are kept at 293 K whilst heat is transferred to the environment only through radiation. In the real system, the main heating process are the imperfect connections of the copper structure to the rods and most of the heat is deposited in the ceramic structure and the rest of the structural support.

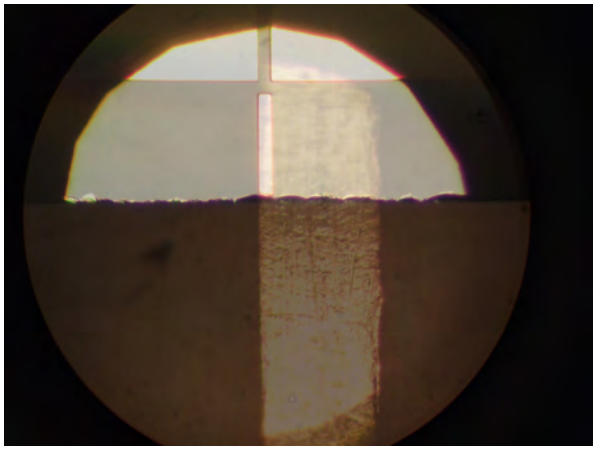

Figure 6.11: Superimposed pictures from the alignment process: the rf foil (lower half) and the chip (upper half) were aligned under the microscope to better than 10 µm. The size of the marker on the chip is 10 µm, the corresponding marker on the Kapton foil is 100 µm wide.

6.5.4. Foil for Additional RF Wires

In section 3.4.2, it was shown that for a toroidal trap a smaller variation in the trap bottom can be reached if additional rf wires are added that are further away than the two rf wires on the chip surface. To be able to use rather high currents in these wires, a flexible 50 µm thick Kapton foil is used, on which 35 µm thick copper wires are printed[24]. This foil is glued to the back side of the chip before the chip itself is glued to the ceramic piece. The relative position of the different rf wires is visible in figure 3.5.

To properly align the wires on the foil with the wire structures on the atom chip, small markers were incorporated on both. Using a translation stage below an optical microscope, both structures were aligned to better than 10 µm and glued with heat cured epoxy[25]. The process is visible in 6.11. In section 3.4.2, it was shown that even displacements ten times as big can still be compensated by adjusting the phase and power of the individual rf wires. The wires on the foil were tested outside of the vacuum chamber and can carry more than 5 A dc.

6.6. Atom Chip

The wire layout of the new chip for the K-Rb experiment was designed using the program *dw-2000*[26]. The new chip was fabricated by M. Trinker at the facilities of the Center for Micro- and Nanostructures (ZMNS) at the TU Vienna. It consists of a single layer of gold structures on a silicon substrate.

6.6.1. Fabrication

The gold structures are evaporated on a standard silicon substrate wafer (Si p-type, doped with Boron) with a nominal thickness of 525 µm. The dopant enhances the heat conductivity of the substrate that acts as a heat sink for the gold wires. Therefore, high currents in the gold wires are possible. To electrically isolate the gold structures from the wafer and to prevent

[24] ANDUS Electronic, `http://www.andus.de`
[25] EPO-TEK 920-FL, `http://www.epotek.com`
[26] design workshop technologies, `http://www.designw.com`

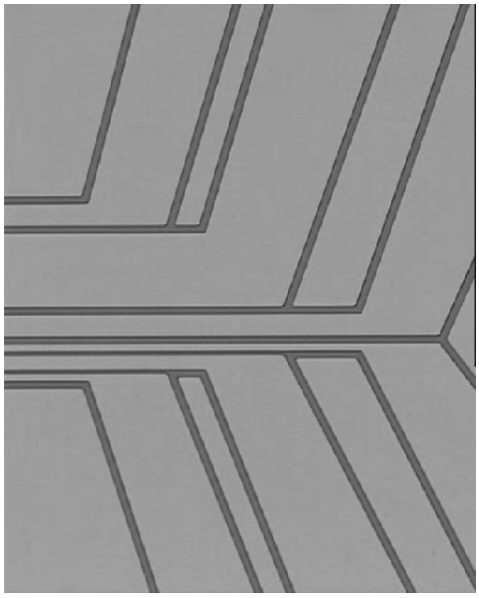

Figure 6.12: Actual chip under the microscope. The region is visible where the trapping wires coming from the left go over in funnel-like structures that lead to the pads. The regions between the wires are gold coated as well so that the whole chip serves as mirror for the reflection MOT. Almost all grooves between the structures are 10 µm wide, only the grooves between the three smallest wires are 5 µm.

shorts between the single wires, the wafer is covered on both sides by a 100 nm thick isolating layer of SiO_2.

As a first processing step, an intermediate 30 nm titanium adhesion layer is evaporated on the oxide layer as gold does not stick on Si or SiO_2. The wires are defined by using a standard lift-off process: The substrate is first covered with a photo resist, the mask is imaged on that resist using UV light, the degraded resist is removed in the exposed regions and subsequently gold is evaporated.

For our purposes, rather thick layers of gold are necessary. The thicker the wires are, the more current they can carry. The thickness of the gold layer is limited by the evaporation process and the thickness of the photo resist. It is 1.2 µm for the chip that is now built in the K-Rb experiment. After the evaporation of the gold, the remaining resist is removed in a chemical bath. The fabrication processes employed are described in great detail in [149]. A picture of a part of the chip under an optical microscope is visible in figure 6.12.

6.6.2. Coating

After the experience of one chip surface turning grayish/black after a few weeks in the Li-Rb chamber in Heidelberg and making it impossible to operate a mirror MOT with this setup, it was decided to additionally coat the central region of the chip with a transparent layer of 30 nm of SiO_2. The reflectivity is still above 95% and there was no measurable change in the polarization properties between reflection from an uncoated gold surface and reflection from a coated surface. The phase shift between the p- and s-components of the incoming light upon reflection under 45° at the coated substrate was measured to be $0.97\,\pi$. The region of the pads is not coated as the coating would make bonding to the chip impossible.

In the Li-Rb experiment there was a visible difference between coated and uncoated regions of the chip after a few weeks in the chamber. A slight darkening of the uncoated pad surfaces was observed while the coated part remained unchanged.

Analysis done by M. Lehto at the University of Uppsala, Sweden, measuring X-ray spectroscopy on one of the grey surfaces, revealed a high amount of titanium in the sample. But

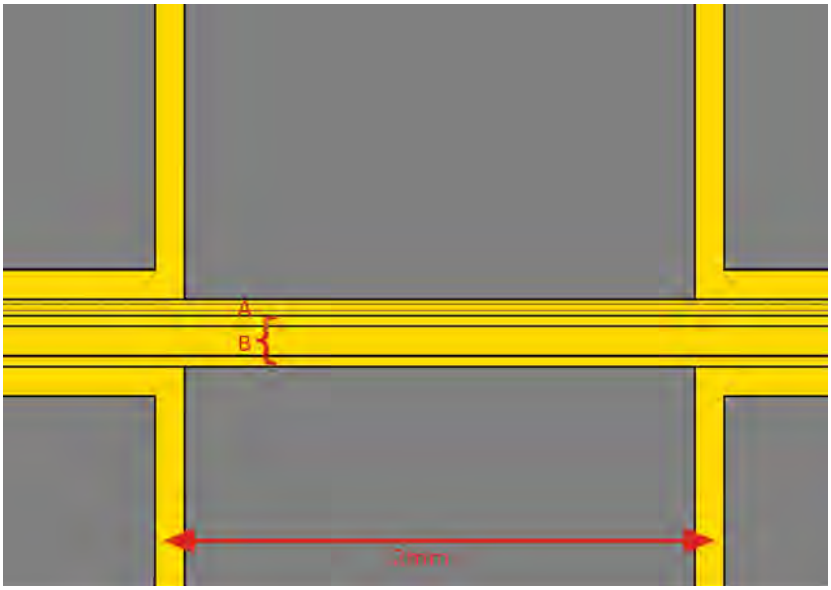

Figure 6.13.: Closeup on the trapping region. Two sets of three wires, labeled A and B, are present. Set A is a 20 µm trapping wire with one 10 µm wire on each side of it to apply rf potentials. Set B is a 100 µm wire enclosed by two 30 µm wires. The confinement along the wires is achieved through two pairs of U-shaped wires that can be seen at the right and left edge of the picture. The horizontal distance between the U-structures is 2 mm.

there was no conclusion reached how this amount of Ti could reach the chip surface during a bake-out cycle of the chamber or the daily operation of the chamber. Additionally, M. Letho's analysis showed that it was not a layered structure of titanium on top of gold, but more like a layer of gold on a 200 nm thick gold-titanium mixture; something that is not understood so far.

To allow a precise alignment of the chip to the ceramic and a precise alignment of the Kapton foil to the chip structures, small 10 µm wide alignment markers were incorporated at the edge of the chip that match alignment markers in the ceramic and on the rf foil. The alignment procedure of the foil is described in more detail in section 6.5.4. Additionally, the whole chip was enclosed by a line that served as guide during the cutting of the wafer with a diamond saw and defines the final size of the chip exactly so that it fits smoothly in the groove of the ceramic.

6.6.3. Layout

The chip used in the new K-Rb experiment was specially designed with the goal of having a cleaner realization of variable radio-frequency adiabatic potentials compared to the chip described in [150]. In addition, care was taken to have an improved optical access to the trapping region compared to previous experiments. The size of the chip was chosen that it allows at least the full reflection of a 1 inch diameter beam under an angle of 45° (29.7 x 35.7 mm). In the past experiments of the group, the chip was always smaller and reflected only parts of the MOT-beams, not giving the maximum possible volume for the four-beam mirror MOT.

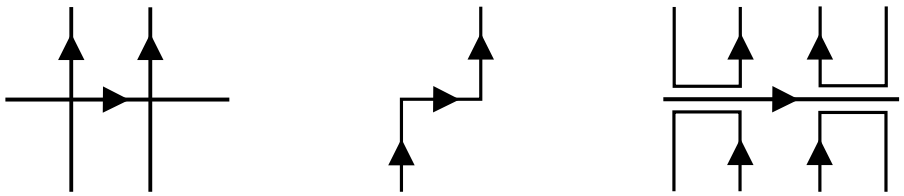

(a) Closing a trap by crossed wires

(b) Z-shaped trap

(c) Confinement by four U-shaped wires

Figure 6.14.: Different possibilities to close a wire trap along the horizontal direction. The arrows indicate the direction of current flow.

RF Wires

In section 3.2.2, it was shown, how different trapping geometries can be realized through the superposition of two orthogonal rf fields. For this purpose, two separate sets of three wires were incorporated on the K-Rb chip as can be seen in figure 6.13.

Set A consists of three wires: one 20 µm trapping wire and, on each side of this wire, a parallel 10 µm wire for the rf field. These three wires are separated by 5 µm grooves. Through this geometrical arrangement, the magnetic fields of the two smaller wires are perpendicular to each other at a height of 17.5 µm above the 20 µm wire.

Similarly, in set B one 100 µm trapping wire is symmetrically enclosed by two 30 µm rf wires that form orthogonal rf fields at a height of 75 µm above the wire. This second set allows for higher currents and is aligned to the copper structures on the back side of the chip. Additionally, the position of the trap formed by the 100 µm wire is aligned with the position of the final copper Z-trap to ensure an optimal transfer to the chip.

Trapping Along the Wire

The choice to go for straight trapping wires and straight rf wires, limits the possible realizations of trapping potentials along the wire. In figure 6.14, the different possibilities are sketched. The first idea is to cross the trapping wire with two straight wires. As there should be no contact between the crossing wires, this requires the fabrication of a chip with two layers stacked on top of each other like on the chip currently used in the RbII experiment of our group [151]. Unfortunately, nobody is currently able to build a similar double-layer chip at the facilities in Vienna, so this was not an option for the K-Rb experiment.

As the trapping and rf wires should be straight over the whole width of the chip, closing the trap in the usual Z-shape as seen in figure 6.14(b) is not possible. The next best choice is to close the trap along its longitudinal direction with four U-shaped wires. If the right direction of the currents in all five structures is chosen, the field configuration looks very similar to the case of the crossed wires in figure 6.14(a). The only difference is that the absolute trap depth is smaller for the case of the Us as a small piece of virtual wire is missing between the wires perpendicular to the trapping wire.

As there are six parallel wires (two trapping and four rf wires) going across the chip, the gap between opposite U-structures had to be 360 µm in the new layout. This lowers the trap depth for the atoms at theses points. Three-dimensional simulations of the trapping

geometry[27] show that this limits the trap depth to about 2 G. This trap depth will still be sufficient once atoms are cooled in the 10 µK range in the copper structures before loading them to the chip.

Along the chip wire there are three pairs of the identical U-shaped wires. All of these wires are 100 µm wide and are tested for currents up to 1 A. The distance between the pairs of Us is 3.5 mm, while the length of the central part of the each of the Us is 1.5 mm.

All three pairs can be addressed individually, therefore allowing the formation of a trap at three different positions along the wire. The trap can either be positioned at a position that coincides with the trap formed by the small copper Z-structure. This would be the natural choice for loading the atoms in the chip. A second trap can be formed above the dimple wire where the longitudinal trapping frequency can be enhanced greatly. Both possibilities are visible in figure 6.16.

As a third possibility, a trap with very low longitudinal trapping frequency can be realized by only using the outermost pairs of Us. Typical values from simulations of the new setup are collected in table 6.3.

Atoms are, due to their polarizability, also sensitive to electric fields, and differences in the electrical potential of neighboring structures on the chip can be used to trap atoms [152]. To avoid these trapping effects at the edges of the trapping wires, the chip surface around the wire can be set to a defined electric potential. There was no space for an additional connection pin in the layout of the ceramic structure. Therefore, two pads of neighboring U-structures were connected in the bonding process, and the additional pin that was now superficial is used to define the voltage at the chip surface. The connection of two of the U-structures does not reduce the versatility of the setup if floating current supplies are used to operate these two wires.

6.6.4. Imaging

A high resolution in the imaging of the atomic ensemble was one of the key goals of the new layout. Special care was taken to optimize the imaging performance in the direction perpendicular to the weak trapping axis. This transversal absorption image is typically taken at grazing incidence or at a small angle of the imaging beam to the chip, as sketched in figure 6.15. A slight angle of the imaging beam towards the reflecting surface of the chip results in two images of the cloud. One is a direct image of the cloud, and a second image is

[27] parameters used: bias field 24 G, 1 A in all wires, trap bottom 1 G

I_{wire} [A]	I_{U1} [A]	I_{U2} [A]	I_{U3} [A]	I_{dimp} [A]	B_B [G]	B_I [G]	trap bottom [G]	$\omega_\perp$ [2π kHz]	ω_L [2π Hz]	rotation [°]
1	1	-1	0	0	24	0.31	0.5	4.592	13.3	0.58
1	1	0	-1	0	24	0.48	0.5	4.600	1.9	0.07
1	1	-1	0	10	24	15.65	0.5	4.623	49.0	3.0

Table 6.3.: Typical trapping parameters for ^{87}Rb in $|2,2\rangle$ on the new chip. Given are the current in the central trapping wire, in the three pairs of U-structures and in the straight leg of the copper h-structure that works as a dimple wire. The rotation angle is the angle between the main axis of the trap and the current direction in the trapping wire. The height of the trap is 73 µm above the chip for all three cases.

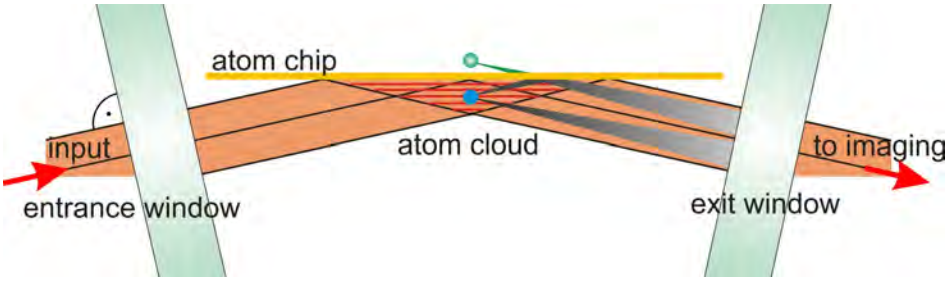

Figure 6.15.: Schematics of the transveral imaging. To improve the resolution of the transversal imaging, both windows of the chamber have been tilted in a way that they are perpendicular to the optical axis. Figure modified from [153].

reflected off the chip surface. Knowing the angle of the incoming light, a direct measurement of the height of the atoms above the surface is possible.

In all previous chamber designs of our group, the imaging beam always had to go through the windows of the chamber at this slight angle. Simulations of our setup using Zemax[28] show that a tilt between the optical axis and the exit window strongly changes the maximum possible resolution of the imaging system. If the optical axis is not perpendicular to the window, the window will, in addition to spherical aberrations, introduce a coma. The diffraction-limited imaging system with a spot size of 1.8 µm that is currently being built for the experiment degrades to a spot size of 6.4 µm if the window is tilted by 2°. To avoid this problem, the windows of the new chamber are tilted by these 2° to be perpendicular to the optical axes. More details on the calculations and characterization of the imaging system built in the experiment can be found in a recent diploma thesis [153].

There is a second effect, especially when working in close vicinity of the chip surface. Local corrugations of the mirror surface make it difficult to extract the precise density distribution of the cloud from absorption pictures [154]. In the new chip layout, care was taken to keep the regions on the chip surface that are right and left of the trapping region empty of any other wires. Especially if periodic wire structures are present, these act as diffraction gratings and make it difficult to reconstruct the wavefront. The empty regions are shaded in figure 6.16.

[28] `http://www.zemax.com`

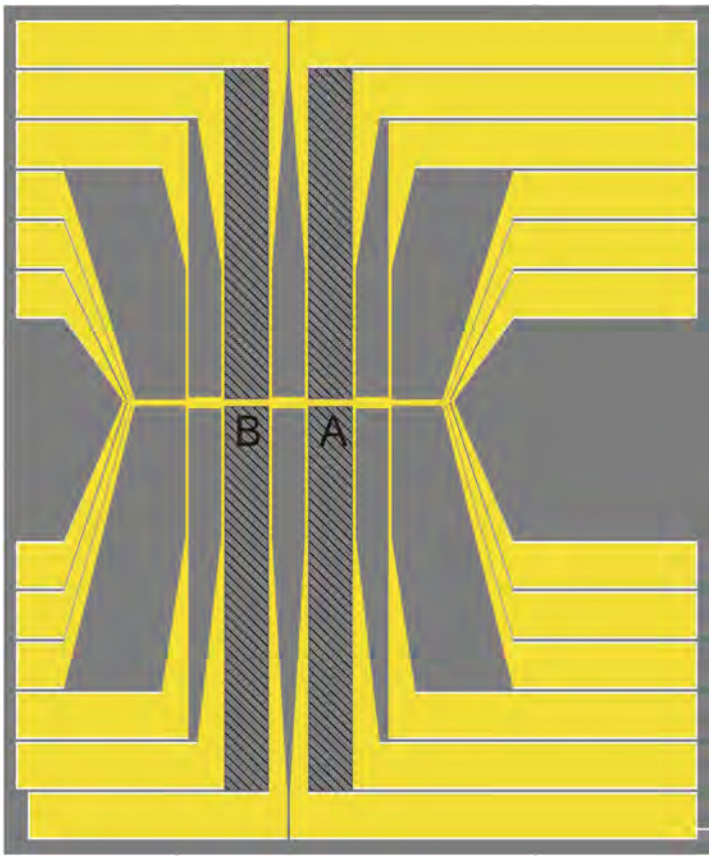

Figure 6.16.: Overview of the chip as seen from above. The overall dimensions are 29.8 x 35.8 mm. The trapping wires and the ground plane are shown in different colors for clarity. The trapping wires have a displacement of 1100 µm from the center of the chip in the vertical direction to match the trap position of the first chip trap A with the trap formed by the small copper Z below the chip. The position of the second trap B coincides with the position of the underlying copper wire that can form a dimple. The ground plane is interrupted in the lower right corner to avoid eddy currents and is connected to one of the pins in the lower left corner. For small angle absorption imaging, the large shaded rectangular areas are kept free from any structures. A closeup on the trapping wires can be found in figure 6.13.

7 First Measurements at the K-Rb Experiment

7.1. Optimization of the MOT Parameters

The maximum atom number captured in a magneto-optical trap depends on various parameters such as laser power, laser detuning, the magnetic field gradient and the intensity ratio between the repumping laser and the cooling laser. These parameters are not all independent of each other, and the optimal setting of trap parameters has to be found experimentally.

A good estimate for the atom number can be obtained by looking at the fluorescence signal emitted by the atomic cloud as the number of scattered photons is directly proportional to the number of atoms.

In a two-level system the occupation probability of the excited state can be calculated from the optical Bloch equations and is given by [155]:

$$\rho_{ee} = \frac{\Gamma}{2} \frac{I/I_{sat}}{1 + I/I_{sat} + 4\Delta^2/\Gamma^2} \tag{7.1}$$

with the natural linewidth Γ, the saturation intensity I_{sat} of the optical transition, I the intensity of the laser light and Δ the detuning of the light from the transition frequency.

In the experiment, the fluorescence signal is obtained by imaging the picture of the atomic cloud through a lens on a calibrated photodiode[1]. The low current signal of the photodiode is then amplified[2] and acquired through the analog input of the experiment control system[3]. To accurately calculate the number of atoms from the photodiode signal, two additional factors have to be taken into account: The lens collects light only from a solid angle Ω that is in the setup limited by the diameter of the DN16CF viewport. Additionally, the signal on the photodiode is reduced by a few percents due to the optical transmission of the imaging system.

Taking these factors into account, the number of atoms can be estimated from

$$N_{atom} = \frac{I_{PD}}{\eta g_{PD}\, \Omega\, \hbar\omega\, \rho_{ee}}, \tag{7.2}$$

[1] Thorlabs DET110
[2] Stanford Research Systems, SR570
[3] AdWinPro, Jäger GmbH

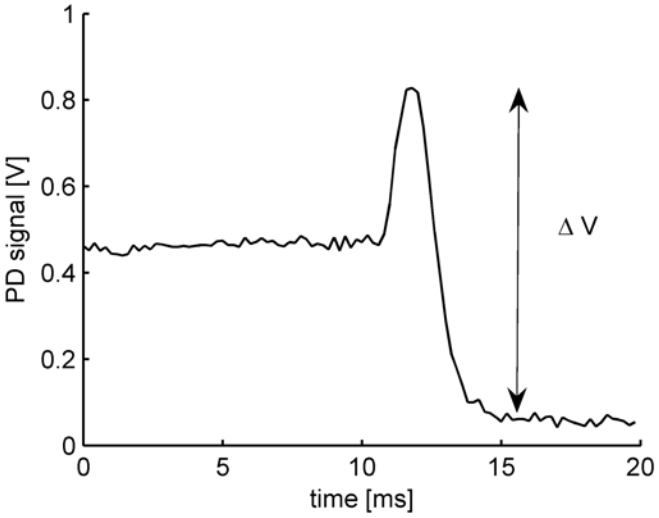

Figure 7.1: The number of atoms is determined by sweeping the cooling laser across resonance. The difference between the peak fluorescence signal on the photodiode and the background signal is a direct measure for the number of atoms in a MOT.

with I_{PD} the current signal from the photodiode, g_{PD} the conversion efficiency of the photodiode and η the transmittance of the window.

By sweeping the laser quickly from the detuning where the MOT is running across resonance, a fluorescence peak is obtained that corresponds to the scattering rate at $\Delta = 0$. Assuming that the intensity I is much larger than the saturation intensity, the scattering rate ρ_{ee} in equation (7.2) simplifies to $\Gamma/2$. A typical fluorescence peak is visible in figure 7.1.

After the frequency sweep, no atoms are left in the MOT and a photodiode signal is measured that corresponds to the background created by the light of the lasers. The difference between the peak signal on the photodiode and the background signal in the absence of atoms is then plugged into equation (7.2) to calculate the number of atoms. The settings for the collection MOT were optimized for both species. In figure 7.2, a two-dimensional plot for the atom number of ^{87}Rb as a function of the intensity and detuning of the ^{87}Rb cooler laser is shown.

To monitor the loading behavior of the MOT, the photodiode signal after the light has been switched on can be continuously monitored. The number of atoms in the trap then grows with $N \propto 1 - \exp(-t/\tau)$ and the loading time τ can be optimized by varying, for example, the detuning of the cooling laser or its intensity. A corresponding measurement can be found in figure 7.3.

In the final setup, the collection MOT will act as a source providing cold atoms that are transported to the science chamber by a push beam. Therefore, the main focus on the optimization procedure of the collection MOT is to enhance the (re)loading time of the trap in favor of a high total number of atoms. Comparing figure 7.2 with figure 7.3, it can be seen that the settings for the quickest loading of the trap do not necessarily coincide with the settings for the maximum atom number at this value of the cooling laser power.

7.1.1. Population of the Different ^{40}K-Levels

The method to detect atoms from their fluorescence signal works quite reliably for ^{87}Rb, but some care has to be taken when working with ^{40}K. As mentioned in section 6.3.1, when the laser system was introduced, the hyperfine splitting of the excited state of potassium is small

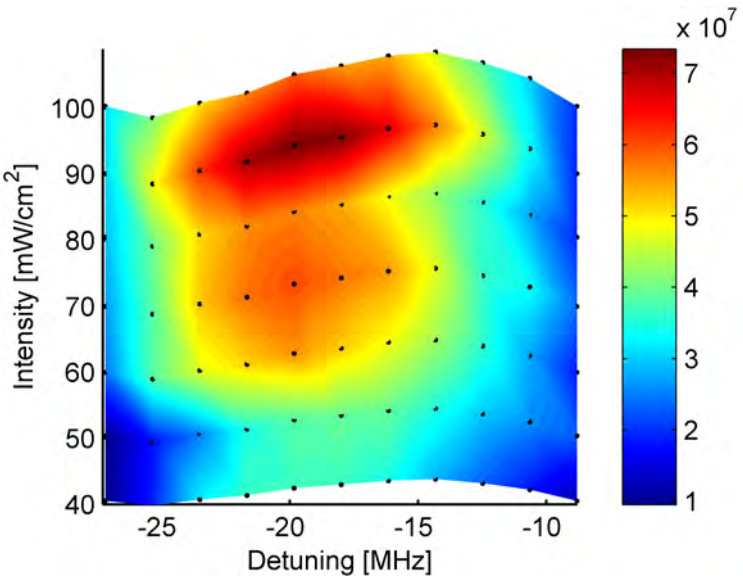

Figure 7.2.: Atom number for ^{87}Rb in the collection MOT for different detunings and intensities of the cooler laser. The field gradient along the strong axis of the quadrupole was 8.0±.4 G/cm and a repumping intensity of 15 mW/cm^2 was used. Data was taken at the black points. There is a clear optimum for the intensity and detuning of the cooler laser where the atom number in the MOT is maximized.

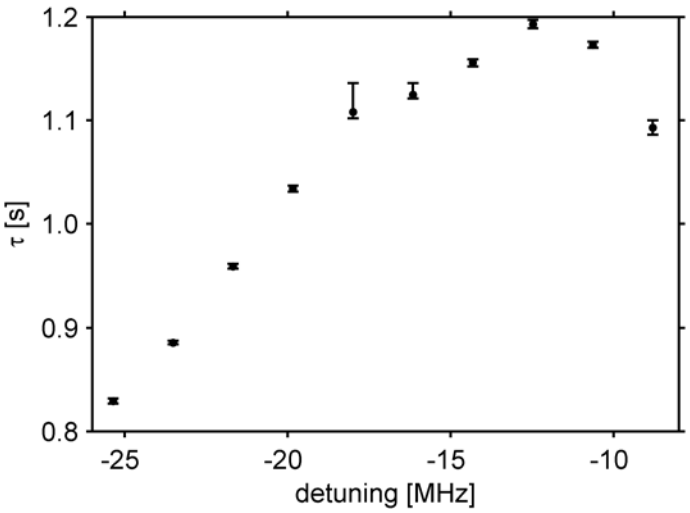

Figure 7.3: Loading time for the ^{87}RbMOT for different detunings of the cooling laser. The intensity of the cooling laser is approx. 60 mW/cm^2, other parameters as on previous figure. By comparing this figure to figure 7.2, it can be seen that a fast loading of the MOT does not have to coincide with a high total number in the trap.

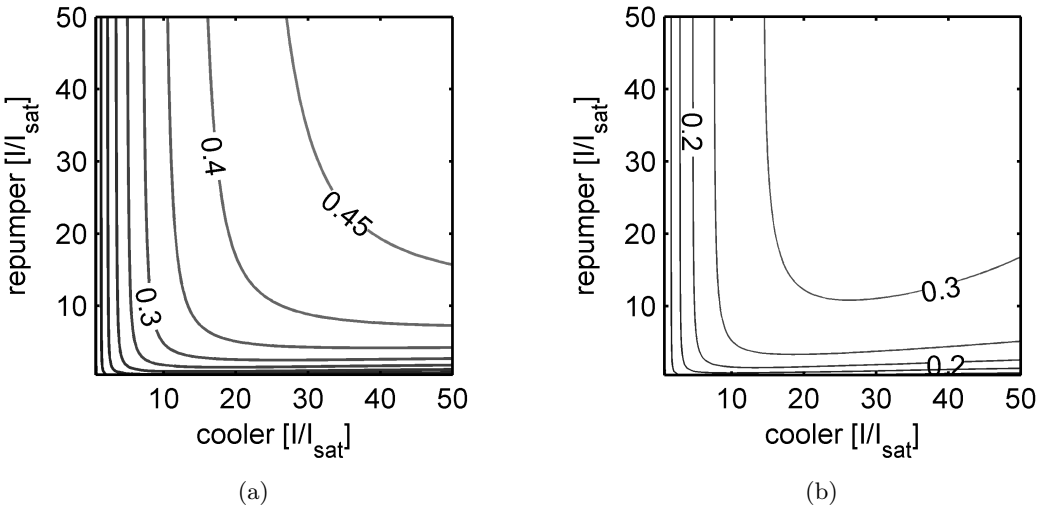

(a) (b)

Figure 7.4.: Simulation of the relative level population in ^{40}K using repumping light that is on resonance and cooling light that is 20 MHz red detuned to the transition. Intensities are given in units of the saturation intensity $I_{sat} = 1.796\,\mathrm{mW/cm^2}$. **(a)** Population of all excited levels. This can be related to the fluorescence measured in the experiment. **(b)** Relative population of the upper level $|11/2, 11/2\rangle$ of the cooling transition.

and a strong repumping laser is needed. The scattering rate cannot be modeled by using a two-level model any more, as in equation (7.2). However, it can be calculated by using the rate equation of a six-level model [136, 156, 157], taking both lasers and all contributing atomic levels into account.

Each of the excited levels can be populated by excitation from any of the two ground state levels. On the other hand, this level will decay to the two ground levels according to the branching ratio of the transition.

Taking the oscillator strengths of the different transitions into account (by averaging over the different Zeeman levels), the coupled equations [136] can be solved for various intensities. Figure 7.4 shows that to keep the atoms cycling on the cooling transition $|9/2, 9/2\rangle \rightarrow |11/2, 11/2\rangle$, the ratio of repumping laser power to cooling laser power should be somewhere between 1:4 and 1:2, and the maximum fraction of atoms being in the excited state of the cooling transition is limited to 30% in the intensity range considered here. This agrees well with optimal values for the intensity ratio reported in other ^{40}K experiments [158, 91].

7.2. Current Status & Next Steps

After being cooled in the collection MOT, atoms of both species have to be transferred through the differential pumping stage by a near-resonant beam. This beam has to be aligned and optimized in frequency and power such that the highest possible atom number in the science MOT is reached.

The push beam is operational for both species and transport of cold rubidium atoms from the lower to the upper chamber has been observed. Additionally, a mirror MOT in the science chamber was established for ^{87}Rb. However, a fair amount of optimization work has still to be done until competitive numbers of ^{40}K and ^{87}Rb atoms in the mirror MOT are reached.

For a better performance of the ^{40}K MOT it might be necessary to change the optics next to the chamber and to set up a dark SPOT as strong light-assisted losses were observed in similar experiments [158]. For a dark SPOT [159] (*dark SP*ontaneous force *O*ptical *T*rap) the beams for the repumping light are shaped such that there is no repumping light at the center of the MOT. At this central point, cold atoms accumulate in the hyperfine state that is now dark. There are significantly less inelastic collisions between ground and excited state atoms in the central region of the trap, and the radiation pressure pointing outwards is lower as there is less fluorescence. Therefore, the density in the MOT that can be obtained is higher.

This can be implemented in the experiment by using separate fibers for the cooler and repumper of potassium and combining both beams after they are expanded next to the science chamber. In the expanded beam of the repumper the central region has to be shaded to form the dark SPOT.

Next Steps

The next steps in the experiment that have to be established are the usual ones for a cold atom experiment: It is planned to first follow the route for ^{87}Rb to a BEC, before focusing on the cooling of the fermions. There are two reasons for this plan: first, the necessary experimental steps on the route to a BEC of ^{87}Rb atoms are well established within the group and, second, the cold bosons are a must for the sympathetic cooling mechanism with the fermions.

The steps for rubidium are the following: After a U-MOT loading phase in the science chamber, molasses cooling for the ^{87}Rb atoms has to be established. By a successive short optical pumping pulse, the sample is then prepared in the maximally stretched state $|2,2\rangle$. These atoms will then be trapped in a first magnetic trap formed by both copper structures running in parallel and then compressed in the small Z-structure. Subsequently, to transport the atoms to the chip, the chip wire is ramped up and the current in the small Z-structure is ramped down. During the magnetic trapping phase, the hottest atoms are always removed by performing evaporative cooling. In table 7.1, calculated trap parameters are given for each of these steps along the route to BEC.

structure	current	B_x	B_y	B_z	$\omega_\perp$	ω_l	height
U-MOT	60 A	20 G	2.5 G	0 G	gradient: 24 G/cm		850 µm
wide/small Z	60 A/30 A	65 G	0 G	11.2 G	$2\pi\cdot435$ Hz	$2\pi\cdot21$ Hz	850 µm
compr. small Z	60 A	80 G	0 G	3.9 G	$2\pi\cdot825$ Hz	$2\pi\cdot24$ Hz	215 µm
chip trap	1 A	24 G	0.81 G	0 G	$2\pi\cdot3.25$ kHz	$2\pi\cdot13$ Hz	73 µm

Table 7.1.: Typical trapping parameters for ^{87}Rb in $|2,2\rangle$ in several successive stages of the experiment. Given are the trapping frequencies perpendicular and longitudinal of the elongated trap and the height above the chip surface. For all Ioffe-type trapping configurations, a trap bottom of 1 G was selected. The corresponding trapping frequencies for ^{40}K in the maximally stretched state are a factor of $\sqrt{m_{Rb}/m_K} \approx 1.47$ bigger.

8 Two-Dimensional Toroidal Trap

Within the framework of this thesis, many different possible experiments were developed for the new K-Rb setup. However, the main focus was on a novel toroidal trapping geometry. This trap is formed by one static trapping wire and the rf fields of four additional wires. The layout of the four rf wires was investigated theoretically in section 3.4.2.

Unfortunately, at the beginning of the year 2008, the new mixture apparatus was not in a stage to perform any experiments with cold atoms in adiabatic traps. Therefore, piloting experiments on the properties of two-dimensional adiabatic rf traps were carried out at a different setup in our group. On the corresponding atom chip a two-wire layout for the realization of adiabatic trapping potentials is present, similar to the situation introduced in section 3.4.1. The experiments that were carried out at this setup were aimed at deepening the understanding of the properties of two-dimensional adiabatic rf traps and at shedding some light on the common pitfalls in the design of these potential landscapes.

In the first section 8.1, a short overview of the experimental apparatus that was utilized is given. Section 8.2 explains in detail the experimental methods that were employed to investigate the properties of the trapping potential. All these methods are well established, but this section might serve as a short introduction for a new generation of PhD students. In section 8.3, the results of several general characterization measurements of the experimental setup are presented. Section 8.4 is devoted to the results of the experimental implementation of a toroidal trap. The measured potential landscapes can be reproduced by simulations of the trapping potential using the formalism developed in section 3.1, and the transfer of a three-dimensional BEC into the two-dimensional geometry is possible. In section 8.4.5, the first results of the evaporative cooling of a thermal cloud in the two-dimensional trap will be presented.

8.1. Experimental Apparatus

The experimental setup at which the measurements presented in this chapter were carried out is the so-called RbII setup that is documented in several PhD theses [152, 67, 150]. The vacuum chamber was moved from Heidelberg to Vienna and reassembled there with some changes. The changes that were made to the setup can be found in [160, 161, 162].

The RbII chamber is, unlike the new K-Rb setup, a single chamber vacuum system. This requires a pulsed operation of the atomic sources and a high pumping speed of the pumps used. Then, the vacuum recovers quickly after the loading phase of the MOT, and long atomic lifetimes in the magnetic trap of the setup are possible.

Like in all experiments in our group, the 'heart' of the experiment consists of a pillar-like mounting that incorporates copper structures in U-shape and Z-shape and a chip structure that faces downwards towards gravity. The copper structures have almost identical dimensions to the dimensions of the copper structures introduced in chapter 6.2 for the new K-Rb experiment. However, in the RbII apparatus only one copper structure is used for the formation of the Ioffe trap.

The laser system for ^{87}Rb consists of two lasers. For all light on the cooling transition an amplified external cavity diode laser[1] is employed. An external cavity diode laser[2] delivers the light on the repumping transition.

8.1.1. Imaging

The experiment has two absorption imaging systems for the detection of the atomic cloud that are installed along two orthogonal directions in the horizontal plane.

One imaging system is set up along the weak axis of the cylindrical static trap and is therefore called *longitudinal imaging*. The CCD camera in this imaging system is from Princeton Instruments[3] and has a pixel size of 20 µm. Half of the CCD chip is covered along the vertical direction by a piece of cardboard to allow the usage of this camera in the frame transfer mode. This is necessary to be able to subsequently take two pictures, one with and one without atoms, within a short time (approx. 10 ms). The long axis of the asymmetric chip is oriented along the direction of the falling atomic cloud.

The second imaging system is directed transversely to the elongated cloud. Therefore, it is called *transverse imaging*. It uses a Princeton Instruments camera[4] as well. As the noise level of the CCD is still acceptable at a temperature of 15°C of the detector, it is possible to leave the fan of the camera switched off, leading to less fringes on the images.

A third detection possibility of the atomic cloud was developed after the move to Vienna. A light sheet detector is located 8 mm below the atom chip [160] and allows spatially resolved fluorescence detection of the expanded sample. Details of the optical elements used and the performance of all three imaging systems can be found in [160].

8.1.2. Double-Layer Chip

After the move of the experimental setup to Vienna, a novel double-layer chip was installed in the chamber. This chip consists of two layers. The direction of the wires in both layers is perpendicular to each other. To avoid electrical contact at the intersection points, an intermediate layer of polyimide was evaporated. Details on the fabrication and characterization of this chip are published in [151].

Unfortunately, the resistance between intersecting wires in both layers has finite values, and the current sources used had to be modified slightly. The current sources are designed in a way

[1] Toptica TA100
[2] Toptica DL 100
[3] NTE/CCD-1340/400
[4] MicroMax 1024 BFT

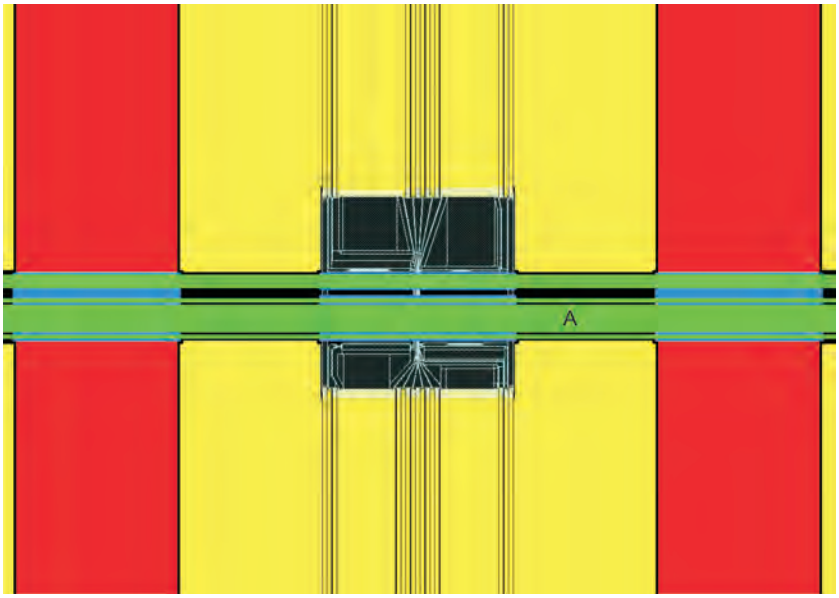

Figure 8.1.: Layout of the central region of the new double-layer chip. The green 80 µm wide wire labeled A is used for the static trapping. The pair of 10 µm wide wires that is located right and left of wire A is used for the rf fields. The 500 µm wide wires marked in red are in the lower layer and provide the longitudinal confinement. They are 2 mm apart (center-center-distance).

that they drive current towards a ground that is defined by the external voltage supplying the logic components[5]. As this voltage was common to several of the current supplies used, this led to unwanted current flow across the intersection point of crossing wires in the experiment. After small changes to the circuit, the sources are now supplied by a pair of batteries and are truly floating.

The central region of the chip layout can be seen in figure 8.1. For the experiments presented in this thesis, one 80 µm wide wire was used for the static trap with two intersecting 500 µm wide wires providing the confinement along the wire. Rf fields were applied via two 10 µm wide wires that are to the left and to the right of the static trapping wire. The gap between each of the small rf wires and the trapping wire is 10 µm.

Fragmentation

When the harmonic confinement along the longitudinal direction of the trap is lowered below approximately $2\pi \cdot 10\,\mathrm{Hz}$, the double-layer nature of the chip does get reflected in the density distribution of the atoms. The trapping wire has height variations, as it has to cross several wires that are located in the lower layer. In the central region of the longitudinal trapping potential three of these wires are crossed. They are each a distance of 300 µm apart. The height of the lower layer including the intermediate isolation layer is 0.9 µm. The height of the gold layer on top is 1.4 µm.

A pictorial representation of the height profile is given in figure 8.2. By evaporating the two layers on the crossing wires, the height profile of the lower layer is smeared out, but the absolute height variation of 0.9 µm is still present. Only taking the gravitational potential into

[5] more details on the layout of the electronics can be found in the appendix of [163]

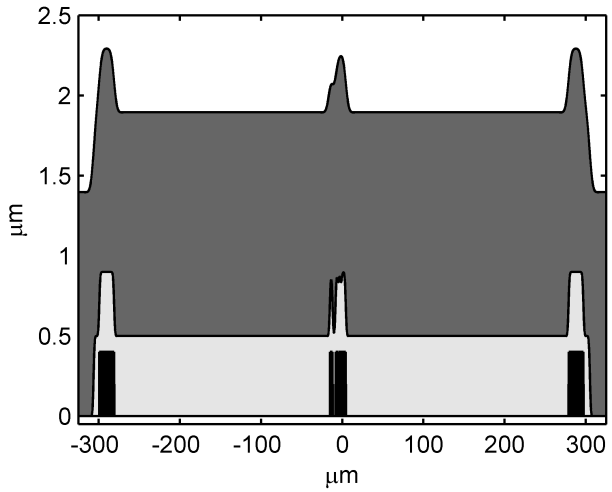

Figure 8.2.: Calculated variation in the height of the trapping wire in the central region of the chip. Black: wire cross sections for the wires in the lower plane; light gray: 500 nm insulation layer; dark gray: 1.4 µm thick trapping wire in the upper layer. The smearing out of the height variations due to the evaporation of the subsequent layers is modeled by convolving the height profile below with a Gaussian that has a width of twice the additional layer thickness.

account, these height variations correspond for ^{87}Rb to variations in the trapping potential of $h{\cdot}1.925\,\mathrm{kHz}$.

In the experiment, the three crossing structures are visible in the density distributions of static traps and in the density distributions of the adiabatic rf traps. An example of the density distribution of a thermal cloud in a static trap is given in figure 8.3.

More detailed simulations of of the magnetic field produced by a wire that follows a height profile like the one shown in figure 8.2, reveal that the two peak-like structures at $\pm 300\,\mu\mathrm{m}$ disappear almost completely at a height of 55 µm above the chip. This distance is the typical height for the static trap used in the experiments of this chapter. At this height the variations in the trapping wire lead to a 600 µm wide box-like variation of the trapping potential that has a slight dimple in the central region. The calculated variations in the longitudinal trapping potential are larger than the gravitational contribution and close to $h{\cdot}10\,\mathrm{kHz}$. This can be attributed to the magnetic field contributions of the current components that point perpendicular to the plane of the atom chip.

The longitudinal trapping potential experienced by the atoms can be reconstructed from the integrated density distribution by inverting equation (4.17). Under the assumption that the potential can be separated into a longitudinal part and a transversal part, the longitudinal part of the potential is characterized by the longitudinal density of the cloud $n(r)$ obtained by integration over the transversal direction of the trap:

$$n(r) = n_{max} \exp\left(-V_l(r)/k_B T\right) \quad \leftrightarrow \quad V_l(r) = -k_B T \log\left(n(r)/n_{max}\right) \tag{8.1}$$

Reconstructing the one-dimensional potential landscape from figure 8.3(b) gives variations in the harmonic potential that are visible in figure 8.3(c). Especially the left half of the reconstructed potential is in good agreement with the potential obtained from the simulations mentioned above.

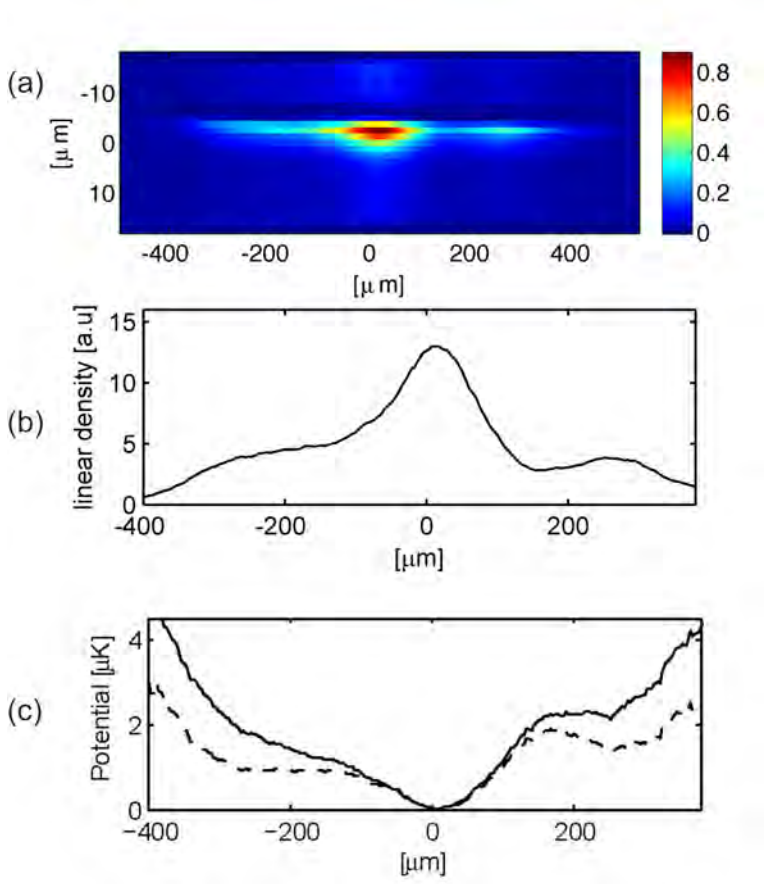

Figure 8.3.: **(a)** Absorption picture of a thermal cloud with T=1.4 µK in a static trap with a longitudinal trapping frequency of $2\pi \cdot 8$ Hz at a height of 55 µm above the chip (averaged over 20 pictures). **(b)** The integrated longitudinal density distribution shows the inhomogeneities in the trapping potential. **(c)** Solid: reconstructed longitudinal trapping potential using equation (8.1). Dashed: longitudinal potential after subtraction of a harmonic potential with $\omega = 2\pi \cdot 8$ Hz.

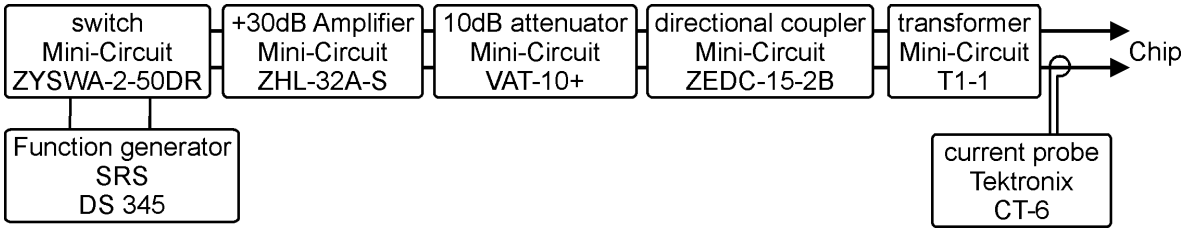

Figure 8.4.: RF setup supplying one of the rf wires on the chip

8.1.3. RF Setup

The rf field for the adiabatic potential is created by the fields of the two 10 µm wide wires on the surface of the atom chip that are visible in figure 8.1. They enclose the trapping wire symmetrically and are a center-to-center distance of 110 µm apart. At a height of 55 µm above the trapping wire this leads to a situation in which the two rf fields are orthogonal. This is not a requirement for the realization of the adiabatic potentials, but makes it easier to relate experiment to theory.

To supply the two small wires with rf currents, two identical chains of a function generator, a switch and an amplifier were set up. The components that are used are summarized in figure 8.4. The device directly connecting to the chip wire is a 1:1 rf transformer that separates the ground that is introduced by the amplifiers from the chip wire. To monitor the current and the relative phase between the two signals that are sent to the chip, a small AC current sensor[6] is used. It is installed on the chip side of the transformer. The directional coupler was used previously for the same purpose of observing the currents sent to the chip. To monitor the relative phase of the two rf wires, the signals of the current sensors of both chains are observed on the same oscilloscope. By changing the phase offset of one of the generators, the relative phase of the currents in the two wires can be adjusted to better than 0.01°.

The amplitude of the rf current is controlled by the analog input of the Stanford function generators that itself is operated by an analog output channel of the experimental control system[7]. To improve the long-term stability of the rf setup, both frequency generators are locked to the same 10 MHz reference oscillator.

Both rf wires including all connections inside the vacuum chamber were measured using a network analyzer to have an optimum control over the phase between the two signals on the chip. By introducing an ohmic resistor of 4 Ω in series with one of the wires, the impedance of both wires could be matched almost perfectly for frequencies below 5 MHz. A resonance is visible in the response of the wires between 500 and 600 kHz. However, this is of no concern as all experiments presented in this thesis were performed at a fixed rf frequency of 2.650 MHz.

To be able to still change the detuning between the rf frequency and the splitting of the Zeeman levels of the static trap, the trap bottom of the static trap has to be varied. This will be described in more detail in section 8.4.1, where the loading of the adiabatic trap is discussed. A direct frequency sweep of the rf sources is not possible, as it has the disadvantage that the function generators used, do not allow the full control of the relative phase between the two generators once they are used in a frequency sweeping mode.

Just recently, a new dual channel rf source was purchased[8]. It allows simultaneous fre-

[6] Tektronix CT-6
[7] AdWinPro, Jäger GmbH
[8] Tabor WW5062, `http://www.taborelec.com`

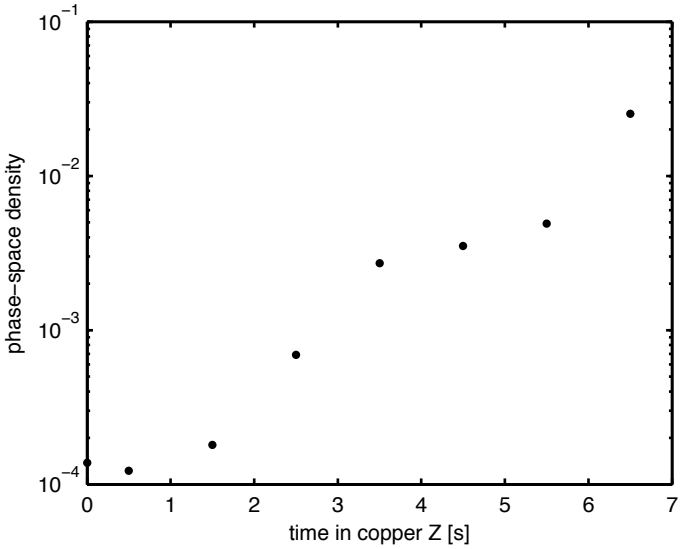

Figure 8.5.: Phase-space density during the rf cooling in the copper Z-structure. The first two seconds are dominated by a strong atom loss without much increase in phase-space density. This can be attributed to the moderate vacuum conditions shortly after the MOT phase.

quency sweeps on both channels with a fixed phase relation between the two output ports. Unfortunately, it does not allow a control of the output amplitudes at the same time. In the future it might replace the two Stanford function generators.

8.1.4. Experimental Cycle

As the experiment is relying on a single chamber, the atomic sources are used in a pulsed mode. The rubidium dispensers are supplied with current for a time of 17 s during the total length of the experimental cycle of 35 s. The released atomic vapor is captured in a MOT that is, after an initial loading phase, compressed towards the chip. The MOT phase is followed by a short stage of molasses cooling and optical pumping into the maximally stretched state $|2, 2\rangle$.

The sample is then evaporatively cooled in a magnetic trap formed by the copper Z-structure running at 60 A and a bias field of 30 G. During the evaporation ramp, the trap is compressed within 2 s to twice the bias field to enhance the trapping frequency and therefore the scattering and thermalization. Typically, a cloud of $2 \cdot 10^6$ atoms with a temperature of 10 µK is obtained after 6.5 s of evaporative cooling. This cold cloud is then loaded to the chip structure by first ramping up the chip trap and reducing the current in the copper structure in a successive step.

The phase-space density during the evaporative cooling in the copper structure is plotted in figure 8.5. In the first few seconds the cooling is not very efficient as the background pressure is still very high. Almost one order of magnitude of atoms is lost during the first three seconds with only a moderate increase in phase-space density.

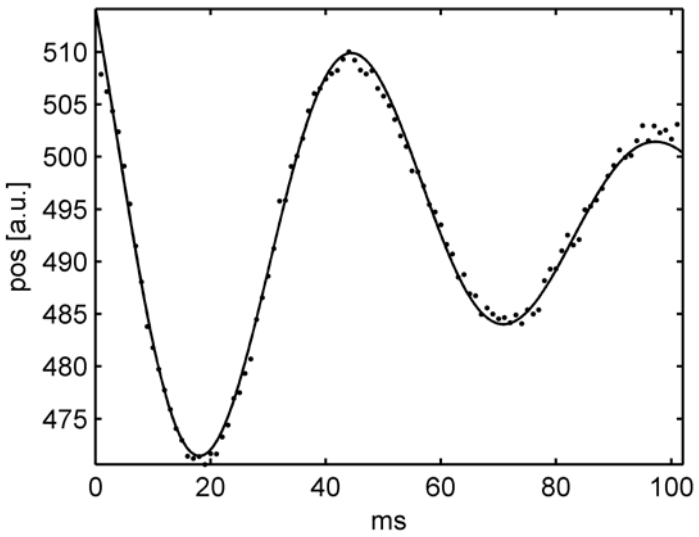

Figure 8.6.: Damped longitudinal oscillation of a cloud of thermal atoms. The center of mass position was fitted by a sine-function whose amplitude is damped exponentially. The trapping frequency is for this specific case $\omega = 2\,\pi \cdot (18.95 \pm 0.1)\,\mathrm{Hz}$

8.2. Experimental Methods

In this section, the different methods that were used to characterize the trap are introduced. A robust and stable operation of the experiment is only possible if all parameters of the trap are well known and controllable. In section 8.2.1, the techniques to obtain the different trapping frequencies of a harmonic trap will be explained, and in section 8.2.2, a method to measure the absolute field value at the trap bottom is presented.

8.2.1. Oscillations

To match the potentials obtained from calculations and the measured density distributions, an exact knowledge of the trapping frequencies is crucial. Depending on the frequency range of the oscillations, different experimental techniques can be used. The experimentally simplest possibility is to monitor the center-of-mass oscillation of a cloud of thermal atoms or a BEC in the corresponding potential. As the time resolution of the experiment control is 25 µs, the upper limit for oscillation frequencies measured with this technique is in the few kHz range. Higher trapping frequencies can be obtained by modulating the current in the trapping wire with the oscillation frequency, a method called *parametric heating*.

Center-of-Mass Oscillations

In figure 8.6, a typical example of the damped center-of-mass oscillation of a thermal cloud of atoms is visible. Typically not the in situ position of the cloud is monitored but instead the position of the cloud after some time of flight. Oscillations transversely to the imaging direction then translate to different horizontal positions of the cloud. Such an oscillation can be excited by displacing the minimum of the trap for a short time.

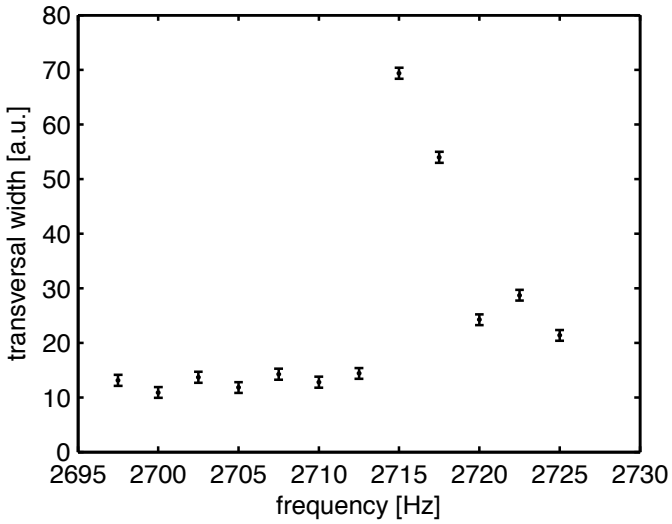

Figure 8.7.: Transversal cloud size for a fixed time of flight after modulating the current in the trapping wire with different frequencies. The cloud size is a good measure for the temperature of the atom cloud and therefore the heating in the trap. Resonance is observed at about $2\pi{\cdot}2.715\,\mathrm{kHz}$. Simulations of the trapping potential predict a value of $2\pi{\cdot}2.730\,\mathrm{kHz}$ for this set of parameters.

By fitting a damped oscillation

$$a(t) = a_0 \exp(-t/\tau) \sin(\omega t)$$

to the position of the center-of-mass of the cloud, the oscillation frequency ω can be extracted.

In the experiment, the displacement of the trap minimum along the longitudinal axis of the trap can be done in two different ways. Either a small 18 µm wire that crosses the trapping wire is ramped to a maximum current of 100 mA in 2 ms and then switched off. Or, as a second possibility, these oscillations can be excited by applying a magnetic field gradient along this direction of the trap.

Parametric Heating

Measuring the trapping frequency along the more confined direction of the trap by direct observation is difficult, as a high time resolution is required. By modulating the trap with a fixed frequency, heating and atom loss can be observed once the modulation frequency coincides with the trapping frequency or higher harmonics.

As the response of the bias coils in the frequency domain of kHz is small, it is experimentally favorable to modulate the current in the chip wire and not the bias field. This is done by adding the signal from a GPIB controlled frequency generator[9] to the amplitude signal that controls the current source for the trapping wire. The amplitude and duration of the modulation have to be adjusted carefully to avoid the problem of power broadening of the resonance. Typically, a modulation of -70 dB is sufficient. In figure 8.7, a frequency scan for atoms in a static trap is visible. The oscillation frequencies for static traps obtained with this method usually agree within a few percent with the values obtained from calculations of the trapping potential.

[9] Stanford DS 345

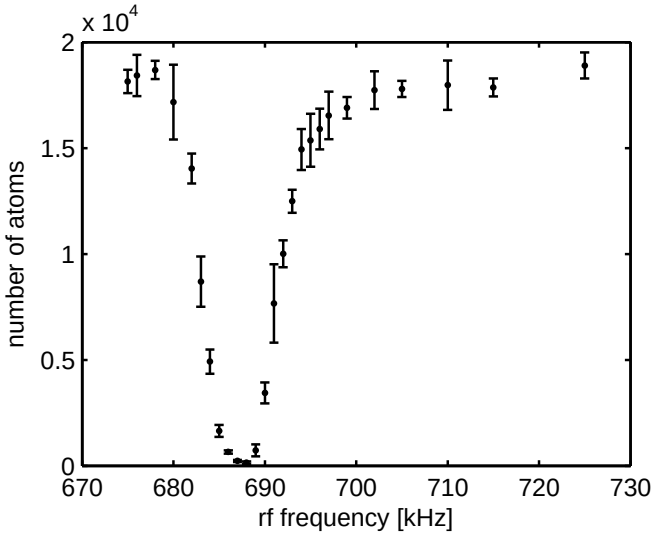

Figure 8.8.: RF spectroscopy on a BEC in a static trap. Depending on the frequency of the small amplitude rf field, atoms are lost from the trap. From the width of the left edge of the dip one can approximate the width of the rf trap bottom to 4.4 kHz. Each data point corresponds to five measurements.

8.2.2. RF Spectroscopy

To precisely determine the absolute magnetic field strength at the bottom of the trap, rf spectroscopy was performed on static and on adiabatic rf traps. This is done by adding for some 10 ms a weak rf field to the trap and monitoring the number of atoms as a function of the frequency of the rf field. If the energy of the rf photon $\hbar\omega$ matches the difference between the Zeeman levels in the trap at the position $\mathbf{r}$: $\hbar\omega = g_F \mu_B B(\mathbf{r})$, atoms are driven to untrapped states, which is similar to the situation of evaporative cooling. Different to the situation of the adiabatic traps described in chapter 3, the coupling strength of the rf field to the levels is now several orders of magnitude lower. By changing the frequency of the rf field, the population of the atoms in the trap can be mapped, and especially the trap bottom can be measured with great accuracy.

To minimize the power broadening of the transition, the power of the additional rf field was reduced so that the atoms were not completely removed from the trap at resonance. In figure 8.8, an example for such a scan with a BEC in a static trap is visible. The right edge of the dip, where the rf frequency is above the trap bottom, is a measurement of the distribution of the atoms in the trap, whereas the left edge of the dip is a measure of the stability of the trap bottom.

Fitting an error function to the left edge of the resonance in figure 8.8, a width of the trap bottom of 4.4±0.6 kHz·h can be extracted. The timescale of this variations has to be slower than the 50 ms that the spectroscopy field was on. The width of the trap bottom corresponds to shot-to-shot magnetic field variations of 6.3 mG. This value is two orders of magnitude bigger than previously measured at the same setup while it was still in Heidelberg [67]. This is related to the problem of noise in the system that will be described in more detail in section 8.4.6.

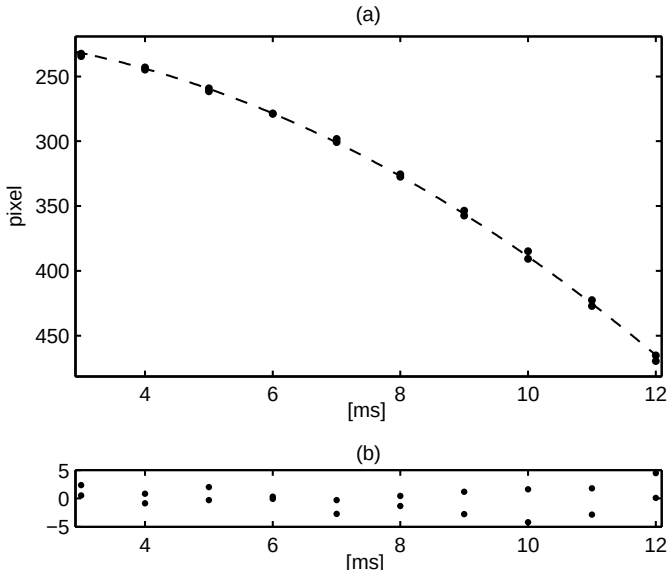

Figure 8.9.: (a) center of mass position of an expanding thermal cloud in the longitudinal imaging and parabolic fit (b) residuals of the fit. Comparing the curvature to the gravitational acceleration gives a magnification of 7.04±0.10 for the longitudinal imaging.

8.3. Characterization of the Setup

8.3.1. Magnification of the Imaging Systems

For temperature measurements and the determination of the atom number, a precise knowledge of the magnification of the imaging systems is necessary. To determine the magnification for both imaging systems and therefore the pixel size in the object plane, a BEC was released from a static trap. The center of mass position of the falling cloud was then fitted by a parabola, and the magnification was deduced from its curvature. Small momenta that are transferred to the atom in the switch-off process of the trap lead to constant velocities but do not contribute to the acceleration of the cloud.

For the longitudinal imaging, a magnification of 7.04±0.10 was obtained, leading to a pixel size in object space of 2.84±0.04 µm. This is visible in figure 8.9. The longitudinal camera is tilted by an angle of 20° in the horizontal plane away from the optical axis of the imaging system. This reduces etaloning artifacts on the images, but the pixel size in the horizontal direction has therefore to be corrected by a factor of $1/\cos(20°)$. As the radius of the Airy-disk for this imaging system was calculated to be close to 7 µm [160], image artifacts can be resolved with the CCD and are visible on pictures of the in situ density distribution.

The same time-of-flight measurement done with the transversal imaging system results in a magnification of 3.70±0.05. The real size of the pixels of the corresponding CCD are 13 µm, therefore the effective pixels size in the plane of the atoms is 3.51±0.05 µm.

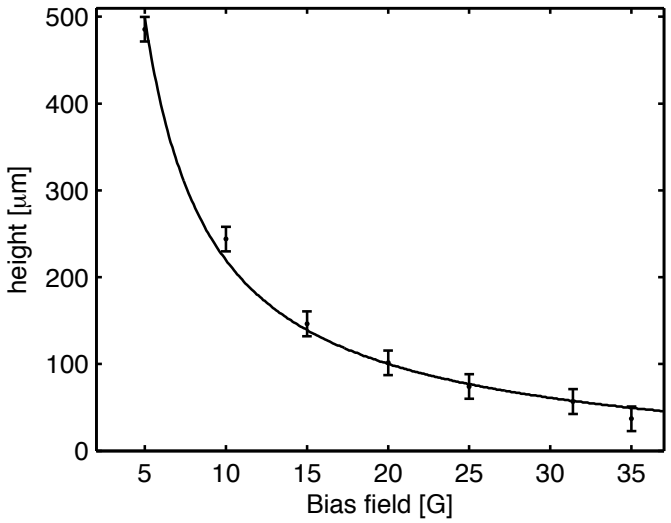

Figure 8.10.: To calibrate the absolute height and value of the bias field, the trap position of a static trap at different bias fields was measured in situ and extrapolated from expansion measurements. The solid line is a theory curve obtained from the formula for an 80 μm wide wire given in equation (B.2).

8.3.2. Height Calibration

To relate the adiabatic potentials obtained from simulations to the potentials measured in the experiment, it is important to know the absolute height of the atomic cloud above the chip. As was shown for an adiabatic trap in section 3.4.1, variations in the height of the static trap are directly related to changes in the phase between the two rf fields that are applied.

In the current setup of the longitudinal imaging system, the imaging beam does not get reflected by the surface of the chip. An absolute height calibration by looking at the image of the cloud and the mirror image that is reflected by the gold surface is not possible. Therefore, one has to rely on a comparison between the height of the static trap at different bias fields and theoretical predictions of the height of a static trap above a wide trapping wire. The drawback of this method is that it does not allow an independent calibration of the bias field and the height position, as both are closely related by equation (2.3). In figure 8.10, such a measurement and the corresponding fit are visible.

As trap frequency measurements of static traps like the one shown in figure 8.7 agree well with simulations, the error in the calibration of the bias field has to be in the few percent range. Assuming a perfect calibration of the magnitude of the bias field, the position of the chip surface, and therefore the absolute height of the cloud above the chip can be determined with an error bar of 1.5 pixels sizes or 4.3 μm.

8.3.3. Absolute RF Amplitude

As the measured impedance of the rf wires including the connecting wires had a non-zero reactance, the reading of the current sensors does not have to coincide with the actual current in the rf wire. Therefore, the trap bottom of the adiabatic trap was measured using rf spectroscopy for different amplitudes in the rf wires. An additional rf generator was used to probe the adiabatic potential as described in section 8.2.2.

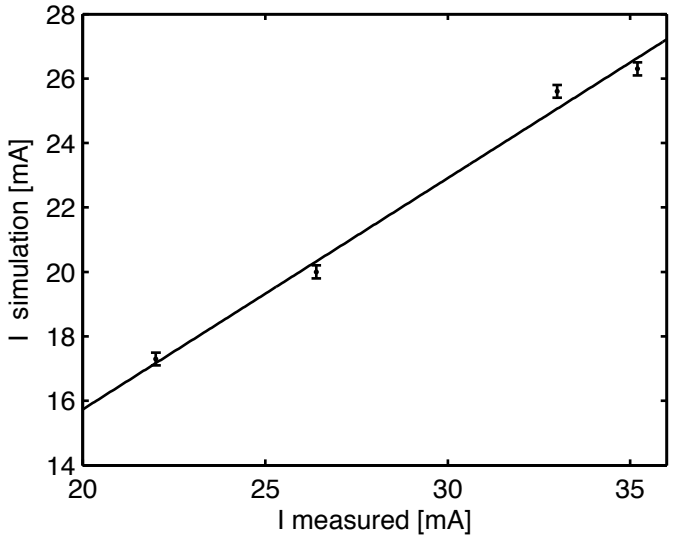

Figure 8.11.: To calibrate the amplitude in the rf wires, the trap bottom of the adiabatic trap is measured for different rf currents and compared to the trap bottom obtained from a two-dimensional simulation of the rf potential. The only fit parameter is a scaling factor for the amplitudes in the simulations. This global factor between the externally applied currents and the values obtained from simulations is 0.72. Parameters of the trap can be found in the text.

Measurements for the adiabatic trap were done for a negative detuning between the the rf frequency and the trap bottom of the static trap. This is the case depicted in figure 3.1(c). As described in more detail in section 3.2, the detuning term vanishes for this case at the minimum of the adiabatic trap, and the trap bottom is given by the absolute value of the coupling term: $\min(V_{ad}) = |\Omega|$.

The amplitude values obtained from the current probes are compared to simulations of the trap bottom of the adiabatic potential. The single fit parameter between the measurements and theory is a scaling factor between the measured amplitudes and the amplitudes in the simulations. The resulting graph is plotted in figure 8.11. The amplitude values obtained from simulations are 0.72 times the amplitude values directly obtained from the current probes. In the experiment, a static trap of 31.4 G bias field, a trapping wire current of 1 A, a trap bottom of 1 G and an rf frequency of 2.650 MHz were used.

In the next section 8.4, whenever experimental data is compared to theoretical calculations, the scaled amplitudes are used and not the values obtained directly from the current sensors.

One has to keep in mind that all theory introduced in chapter 3 and used for the simulations of the adiabatic potentials, assumes the validity of the rotating wave approximation (see section 3.1 for more details). In the case presented here, with a detuning almost as big as the rf frequency and a small static trap bottom, it is rather surprising that there is still a reasonable agreement between theory and experiment. Effects that go beyond the rotating wave approximation (RWA) can be derived from more elaborate calculations and show a slight change in the potential landscape and multi-photon transitions at large rf amplitudes [164].

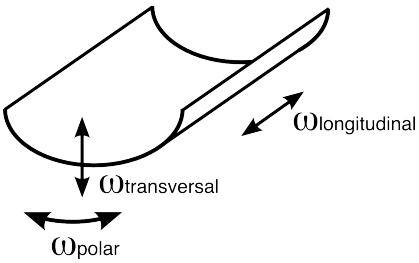

Figure 8.12: The toroidal trap is a bent two-dimensional trapping geometry that is characterized by three different oscillation frequencies: The longitudinal trapping frequency along the trapping wire, the transversal trapping frequency in the strongly confined direction and the polar trapping frequency along the circle in the plane perpendicular to the trapping wire.

8.4. Experimental Realization of a Toroidal Trap

In this section, the creation of a two-dimensional trapping geometry is shown for the case of two rf current carrying wires. This is a piloting experiment for the realization of a two-dimensional rf trap using four wires. In section 3.4.1, it was demonstrated that by varying the relative phase between two linearly polarized rf fields, a reduction of the polar trapping frequency of a toroidal trap can be achieved. Again, a toroidal trap is a bent two-dimensional trapping geometry, as visible in figure 8.12.

Using the parameters of the static trap that is present in the experiment, and the rf fields that are applied, such a trap should have a transversal frequency of $2\pi{\cdot}7.5\,\mathrm{kHz}$, a polar frequency of around $2\pi{\cdot}100\,\mathrm{Hz}$ and a radius of $9.8\,\mu\mathrm{m}$ in the plane perpendicular to the wire when a relative phase of 97° between the two rf fields is used.

Sensitivity of the Trapping Geometry on Experimental Parameters

Simulations of the adiabatic trapping geometry show that the polar oscillation frequency is more sensitive to changes of the different experimental parameters than the transversal frequency. The parameters that are experimentally accessible are on the one hand the settings of the static trap, and on the other hand the settings of the rf fields. Exploring the whole parameter space that is available, the following bounds can be set in which the polar oscillation frequency changes less than 10%:

The polar frequency is rather insensitive to the radius of the bent surface. Therefore, the absolute value of the rf frequency and the value for the Ioffe field can be off by 5%. More important are the two parameters that define the height of the static trap. They have to be within an interval of ±0,2%. In absolute values this is a deviation of 70 mG for the large bias field and of 2 mA for the current of the trapping wire. A similar effect than a change of the position of the static trap, is a change in the phase between the two rf fields. The phase between the two rf fields should not deviate more than ±0.2°. The amplitude of the rf fields can be varied by 10% without larger changes to the polar frequency. However, the relative amplitudes have to be equal to better than 0.2%. An imbalance has the same effect than an additional field pointing parallel to the direction of gravity. Both rotate the sickle away from the position the furthest away from the chip.

Experimentally the constraints are less strict, as non-perfect settings in the static trap can always be counteracted by changing the parameters of the rf field. The typical parameters to minimize the polar frequency are the relative amplitude of the two rf fields and their relative phase. Both processes will be shown in section 8.4.2 and section 8.4.3, respectively.

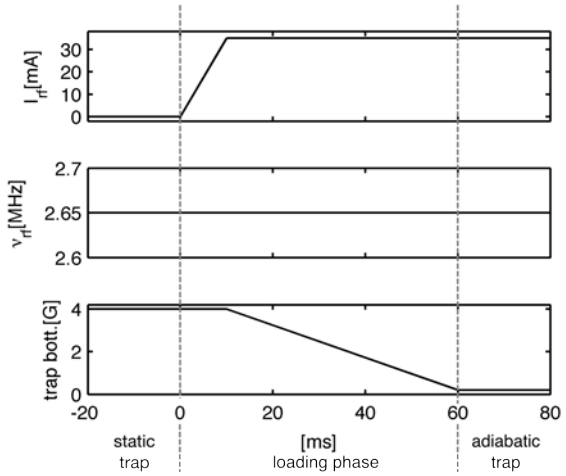

Figure 8.13: Experimental sequence to transform the static trap into the two-dimensional adiabatic rf trap. In a first step, the amplitude of the rf wires is ramped up, while the trap bottom is still above the rf frequency. In a second step, the detuning between the rf photon and the energy splitting in the static trap is changed by reducing the static Ioffe field to a small value. 2.65 MHz rf frequency corresponds to a trap bottom of 3.78 G. In the adiabatic trap the detuning is negative and close to the rf frequency.

Initial Static Trap

The starting point for all experiments in adiabatic rf potentials is a static trap formed by a current of 1 A in the 80 µm wide trapping wire and a bias field of 31.4 G. This trap is located at a height of 55 µm above the chip. There, the rf fields of both rf wires are perpendicular to each other, making it easier to relate the experimental findings to simulations of the potential landscape. The trap bottom of the static trap is at 3.85 G, resulting in measured trap frequencies of $2\pi\cdot19.0$ Hz longitudinally and $2\pi\cdot2.72$ kHz transversally.

Before the loading in the chip structures, cold samples of typically $2\cdot10^6$ atoms at 10 µK are prepared by evaporative cooling in the copper structures as described in section 8.1.4. These atoms are then transferred within 500 ms into an initial chip trap with 31.4 G bias field, 1 A current in the trapping wire and a trap bottom close to 3 G. In a first cooling step, the sample is evaporative cooled in this trap for 1 s by linearly sweeping the rf frequency from 4 MHz to 2.8 MHz.

In a next step, the trap bottom is increased to a value of 3.85 G. During this ramp of 350 ms, a constant rf knife with a frequency of 100 kHz above the final trap bottom is on, to cool the sample further. With a last linear rf cooling ramp of 100 ms duration that has a starting frequency of 2.8 MHz, the sample can be prepared at the desired temperature, either above or below the transition temperature to BEC. Pure BECs without detectable thermal background contain typically a few 10^4 atoms in this trap.

8.4.1. Adiabatic Loading of the RF Trap

As already mentioned, all rf potentials were realized with a fixed frequency of the rf generators. Therefore, the static trapping potential is deformed into the adiabatic potential by changing the Ioffe field of the static trap. Due to technical reasons a rf frequency of 2.650 MHz was chosen for most experiments.

To adiabatically transform the bare states into the new states, the trap bottom is in a first stage kept slightly above the transition frequency of the rf photon. The static trap is left unchanged, and the rf amplitude is ramped up, therefore coupling neighboring Zeeman levels. The splitting between the new dressed levels is, in the limit of weak rf amplitudes, given by the detuning of the rf photon to the energy splitting of the Zeeman levels in the static trap. An initial detuning of the rf frequency to the level spacing of 50 kHz is well above the limit where

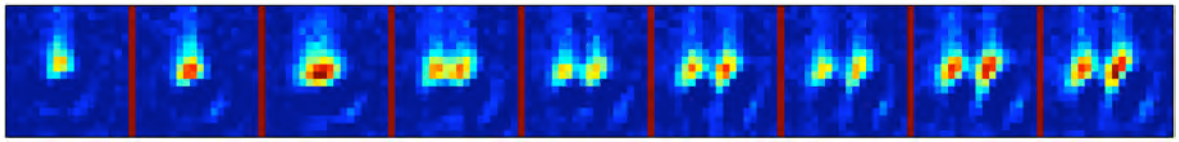

Figure 8.14.: Splitting of a static trap into a horizontal double-well by changing the Ioffe field of the static trap. Starting with 3 G at the picture far left, the external Ioffe field was decreased by 375 mG from left to right from picture to picture. The splitting in the picture far right is 18.5 µm.

Landau-Zener tunneling between the adjacent dressed levels plays a role on the timescale of the experiment. The final amplitude of the current in the single rf wires is typically 30 mA and therefore more than a factor two below the currents tested in DC operation of the wires.

Once the rf amplitudes are sufficiently large, the avoided crossing between the dressed states is given by the coupling of the rf field to the states. Therefore, it is possible to change the detuning to a negative value where the rf frequency is above the energy splitting in the static trap, without losing the atomic sample. This is done in a second step by reducing the static Ioffe field. A typical experimental sequence of the loading is visible in figure 8.13.

The deformation of the static trapping potential to the potential landscape of the adiabatic trap is illustrated in figure 8.14 for the formation of a horizontal double-well potential. There, several intermediate pictures of the in situ atomic density distribution are depicted during the ramp of the Ioffe field. The first picture was taken at 3 G external Ioffe field, the last one at 0 G. At a height of 55 µm above the chip surface, the trap bottom of the static trap is always by 0.2 G larger than the value of the external Ioffe field. This is a contribution of the two 500 µm wide wires, crossing the trapping wire, that generate the harmonic confinement along the longitudinal direction.

As the rf frequency was 2 Mhz for this measurement, the resonance condition of the trap bottom with the rf field is fulfilled at a trap bottom of 2.85 G. Around this value the confinement of the static trap is reduced along the horizontal direction, before, at lower fields, the barrier of a double-well emerges. As the detuning increases, the distance between the single wells grows. In exactly the same manner a two-dimensional trap can be loaded. The only difference is that now looking along the longitudinal direction not a double-well but a sickle-like shape emerges.

One can actually reverse the direction of the external Ioffe field and push the detuning between the rf frequency and the static field to even higher values. With an rf frequency of 2.65 MHz the external Ioffe field is experimentally limited to a maximum value of 1.2 G pointing in the 'wrong' direction. For a static trap without a rf dressing field, the trap bottom is at this value of the external Ioffe field already highly overcompensated, leading to a splitting of the Ioffe trap into two quadrupole traps.

At higher values of the external Ioffe field, the number of atoms in the adiabatic trap vanishes rather quickly within an interval of 0.1 G. We attribute this to the fact that at these field values the effective field at the position of the adiabatic trap minimum changes its direction, therefore abruptly changing the geometry of the trap.

In figure 8.14, imaging artifacts are visible on all pictures. This is due to the pixel size of the longitudinal imaging system being smaller than the radius of the (simulated) Airy disk.

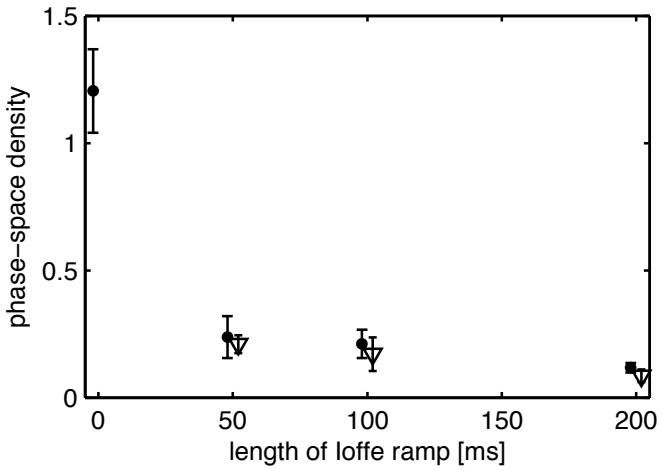

Figure 8.15.: To estimate heating and atom losses during the loading of the adiabatic rf trap, the static trap was deformed into the rf trap, and the rf trap was then symmetrically deformed back into the static situation. Closed circles: holding atoms for the same amount of time in static trap. Open triangles: sweeping to the adiabatic trap and back to the static trap. Error bars are given by the two different temperatures, measured transversally and longitudinally, of the cloud. For the closed circles the decay in phase-space density corresponds to a heating of 2.4 μK/s without any atom loss.

Transfer

To estimate heating and atom losses during the loading phase, both the Ioffe ramp and the amplitude ramp were reversed after the transfer in the adiabatic trap, as such bringing the atoms back into the static trapping configuration. The number and temperature of the sample was compared to the the situation where the sample was held in the static trap for the same amount of time. In figure 8.15, the resulting phase-space densities for a thermal cloud are visible for different loading times. There is no additional loss in phase-space density observable due to the transfer. The phase-space density decreases as much for the pure holding case as for the transfer case and is not connected to a loss in atom number. However, the decrease is due to a strong heating rate of close to 2.5 μK/ s of the sample. This will be discussed in more detail in section 8.4.6.

8.4.2. Balancing the RF Fields

One crucial point in the formation of a two-dimensional shell is the precise balancing between the two rf amplitudes. Only if they are balanced, a minimal polar trapping frequency can be reached.

Two different methods were used to balance the amplitudes:

- For low enough temperatures, the main expansion dynamics of the atomic sample is perpendicular to the direction of strongest confinement. If the two wires are not well balanced, the resulting potential is still sickle-shaped in the plane perpendicular to the trapping wire, but the sickle is rotated by a few degrees. Loading a BEC in such a trap and observing the density distribution after a short expansion time of around 2 ms, reveals the main expansion axis. By adjusting the amplitudes carefully, this direction can be matched to the direction of gravity.

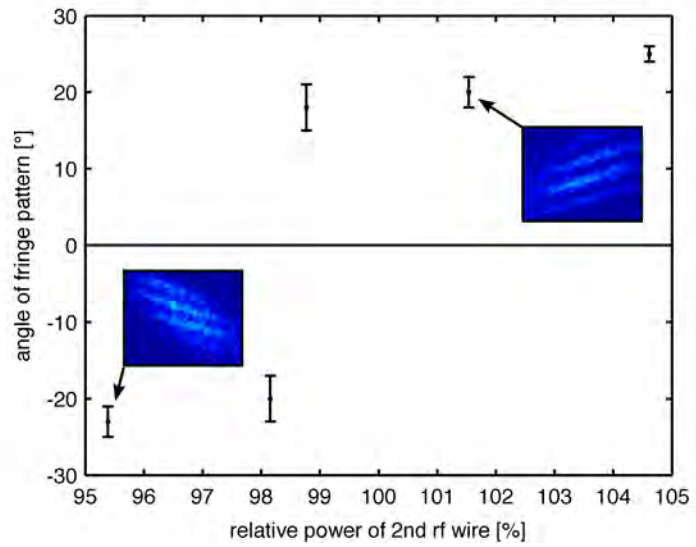

Figure 8.16.: If a BEC is released from a double-well potential, the emerging fringe pattern changes its orientation depending on the imbalance of the two rf amplitudes. This enables the calibration of the relative amplitudes to better than 0.5%.

Similarly the phase between the two rf fields can be changed by a few degrees to form a double-well potential. An imbalance in the amplitudes will lead to a tilt in the potential landscape, leading to a corresponding imbalance in the number of particles in both wells. Looking at expansion pictures with a short time of flight, where the expanded clouds of both wells do not overlap yet, the population of the two wells can be adjusted with great precision.

- The most sensitive approach is the observation of the interference of two BECs from a double-well. Therefore, the phase between the two rf fields was changed slightly from the optimal value for a two-dimensional shell (97°) to a value of 100°. This leads to a double-well with a barrier height of around 5 kHz between the two minima. The atomic sample is in the static trap cooled to BEC and then transfered into the adiabatic trapping geometry. If the amplitudes of the two rf wires is not perfectly equal, this leads to a tilt in the potential.

  In expansion, the interference between the two parts of the initial BEC leads to a fringe pattern. Depending on the imbalance of the potential, the orientation of the fringe pattern changes and can be optimized. As shown in figure 8.16, the calibration of the relative amplitudes of the two rf sources is possible to better than 0.5% using this method.

The amplitudes obtained from all methods agree to better than 1%. The small difference between the amplitudes of both wires that is visible in figure 8.16 is probably due to a small mismatch in the impedance of the two wires.

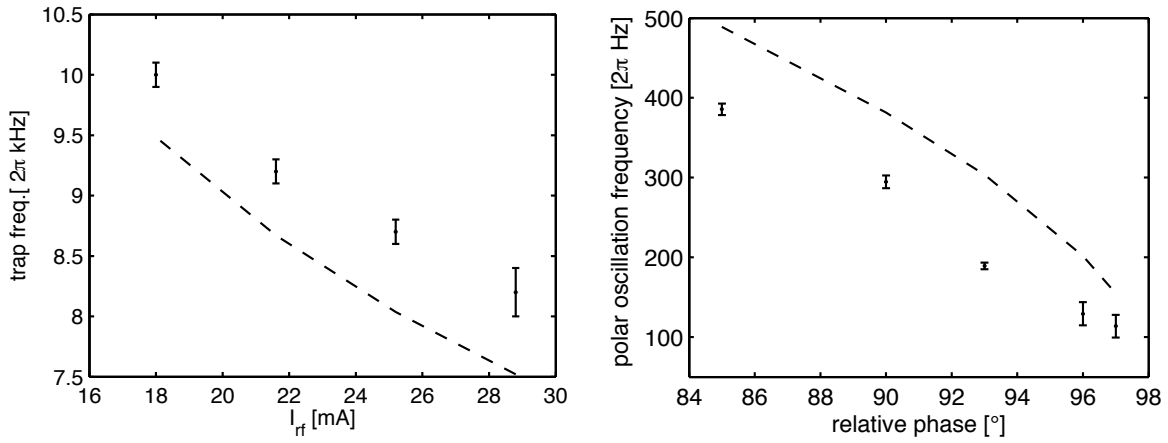

(a) (b)

Figure 8.17.: **(a)** Transversal oscillation frequency measured by parametric heating for different rf amplitudes. **(b)** Polar oscillation frequency of the toroidal trap for different relative phases between the two rf fields. The dashed line in both graphs corresponds to the values obtained from simulations. They reproduce the qualitative behavior, but fail to predict the exact value.

8.4.3. Oscillation Frequencies of the Toroidal Trap

With the methods introduced in section 8.2, the different trapping frequencies of the toroidal trap were measured in the experiment and compared to the values predicted from theory.

Transversal oscillations were determined for different amplitudes of the rf fields and a constant relative phase of 97° between the two rf fields. Polar oscillations were measured for different relative phases between the two wires at a constant rf amplitude of 29 mA. These oscillations were for a thermal cloud in the adiabatic trap excited by changing the current amplitude in one of the two rf wires abruptly.

Simulations of the potential overestimate the polar frequencies and underestimate the transversal frequencies. However, for both cases the qualitative behavior is reproduced. The discrepancy can again be attributed to the violation of the RWA approximation in the experiments presented.

At phase shifts larger than 97°, simulations predict an emerging double-well structure along the polar direction of the trap. This is visible in the experiment as a large damping of the polar oscillation for a relative phase of 98° between the rf fields. For even larger phase shifts the double-well is visible in the in situ density distributions and in pictures for small expansion times.

The longitudinal trapping frequency of the adiabatic trap does not correspond to the longitudinal oscillation frequency of the static trap any more, but is greatly reduced. Along the trapping wire at every point of the trap, the resonance condition between the rf field and the static trapping potential is fulfilled. Therefore, to first approximation, only gravity is the driving force that leads to the remaining curvature of the potential along this direction. In the experiment it was measured to $2\pi \cdot (5.8 \pm 0.4)$ Hz.

8.4.4. Crossover to Two Dimensions

The trap used in all experiments in the following sections was formed by a static trap of 31.4 G bias field, 1 A current in the trapping wire, 29 mA current in the rf wires, an rf frequency of 2.65 MHz and a trap bottom of the static trap of 0.2 G. As it was shown in the previous section, this leads to a trapping geometry with a longitudinal trapping frequency of $2\pi \cdot (5.8 \pm 0.4)$ Hz. The transversal oscillation frequency is $2\pi \cdot (8.15 \pm 0.20)$ kHz, and the polar frequency is $2\pi \cdot (113.7 \pm 14.2)$ Hz.

With this parameters this is a two-dimensional trapping geometry with a mean trapping frequency of $2\pi \cdot 25.7$ Hz in the two-dimensional plane and $2\pi \cdot 8.15$ kHz transversally. Therefore, the ratio between both energy-scales is larger than 1:300. This is much larger than in other realizations of two-dimensional trapping geometries that have a ratio of 1:82 [98], 1:92 [49] or 1:38 [105]. Our trap is unique, as its spatial shape is not flat like a pancake, but bent around an axis parallel to the trapping wire. For the parameters mentioned above, the radius of curvature is a little short of 10 µm. This complicates the understanding of the expansion dynamics slightly, as will be shown in the next section.

For $1{\cdot}10^4$ thermal atoms in this trap, the transition temperature to a three-dimensional BEC is 170 nK following equation (4.7). This value is below the temperature scale of 390 nK given by the transversal trapping frequency. For less than $1.5{\cdot}10^5$ atoms always an intermediate temperature range exists in which a thermal cloud shows a two-dimensional behavior before a phase transition to a two-dimensional BEC occurs. For an ideal gas of $1 \cdot 10^4$ atoms, the transition temperature to a two-dimensional BEC is 96 nK for this trap with a (two-dimensional) mean trapping frequency of $2\pi \cdot 25.7$ Hz. Experiments show [98] that interactions move the transition point of the ideal gas result to lower temperatures or equivalently to higher atom numbers.

When working with a three-dimensional BEC before going into the adiabatic trap, the crossover to two dimensions is characterized by the relation $\mu_{3D} < \hbar\omega_{trans}$. The number of atoms for which at T=0 this crossover occurs, evaluates according to equation (4.29) to $8.4{\cdot}10^5$ ^{87}Rb atoms. For less atoms in the BEC, the chemical potential is lower than the energy of the transverse confinement. Typical BECs in the static trap configuration used, contain an order of magnitude less atoms.

Temperature Measurements

At low temperatures, when $k_B T < \hbar\omega_{trans}$, the expansion dynamics of a thermal cloud changes. Due to the high confinement, the cloud adapts in transversal direction a Gaussian shape with width $l_0 = \sqrt{\hbar/m\omega_{trans}}$. Therefore, the expansion energy along this direction will not depend on the temperature or the number of particles any more, but will saturate to the kinetic zero-point energy along this direction $\hbar\omega_{trans}/4$ [32, 98, 102].

In our experimental situation, the interpretation of the expansion dynamics is a little more complicated, as the trap has a bent shape. The radius of the sickle in the plane perpendicular to the direction of the trapping wire is close to 10 µm. Assuming a release energy of $\hbar\omega_{trans}/4$ along the radial direction, the cloud spreads within 2.3 ms to a width as big as the radius. As this dynamic is transversal to the sickle-shaped potential, this leads to a focusing of the expanding cloud and makes it difficult to distinguish between the expansion dynamics perpendicular to the tight trapping direction and along the polar direction.

This effect is even more pronounced if a BEC is transferred to the two-dimensional potential. In figure 8.18, the density distribution for a BEC obtained from longitudinal images is given in situ and for different expansion times. To reproduce the density distributions, the adiabatic potential was calculated in the plane perpendicular to the trapping wire for this set of parameters. In a next step the Gross-Pitaevskii equation (4.13) was solved numerically in two dimensions for this potential to obtain the ground-state distribution and distributions for different time of flights. Simulations of the expansion of a BEC from this potential reproduce the qualitative features of the expansion dynamics well and show the same focusing behavior as observed in the experiment.

To mimic the finite resolution of the imaging system, the calculated density distributions were filtered in two dimensions with an Airy pattern of a radius of 6.8 µm. However, the size of the cloud in the experiment is always larger than predicted by simulations. This is probably due to a small angle between the direction of the imaging beam and the trap geometry. Such an angle increases the 'shadow' of the atomic density distribution visible in absorption images as they always integrate along the beam direction. A second effect is the much lower depth of field of the imaging system than the extension of the trap along the optical axis. This will again lead to larger images.

Regardless of the bent shape of the trapping potential, the pictures of the expanding sample were fitted along the horizontal and vertical direction of the image with Gaussians, and the temperature was extracted from the width of these Gaussians. Before the fitting, the images were always integrated over the perpendicular direction. The crossover to two dimensions can be seen by comparing the temperatures obtained from horizontal fits to the temperatures obtained from vertical fits.

In figure 8.19, the ratio of both temperature measurements is given as a function of the mean of both temperatures. For mean temperatures below 900 nK, a strong deviation of the ratio from unity is visible. This is 2.3 times higher than the temperature connected with $\hbar\omega_{trans}$ that is usually expected as a transition temperature. Nevertheless, it is a clear indication that the thermal gas is transversally confined to the ground state of the potential. In figure 8.19, the average ratio is 1.1 for mean temperature values above 1.5 µK, hinting at a systematic error in the determination of one of the temperatures. Most likely the angle at which the camera is tilted towards the optical axis was overestimated.

Generally, there is a slight disagreement between the temperatures obtained with different methods. In section 8.4.1, it was shown that the transfer into the adiabatic trap and back into the static trap can be done without any additional phase-space density loss. Therefore, assuming the same phase-space density at the beginning and at the end of the transfer ramp and knowing the initial temperature in the static trap, again a temperature of the sample in the two-dimensional trapping geometry can be obtained. By comparing this temperature to values acquired directly by expansion measurements, it can be seen that temperature values of the latter method are systematically between 15 and 20% higher than the values inferred from a constant phase-space density model.

To improve the temperature measurements in the two-dimensional trap, it was tried to sweep the frequency of the dressing field to higher values, shortly before the static field is switched off. This leads to an outward movement of the trap, as the resonance condition between the dressing field and the Zeeman levels of the static trap is fulfilled at larger and larger distances to the center of the trap. The geometry of the adiabatic trap is therefore magnified. If the velocity of this outward movement is larger than the expansion dynamics

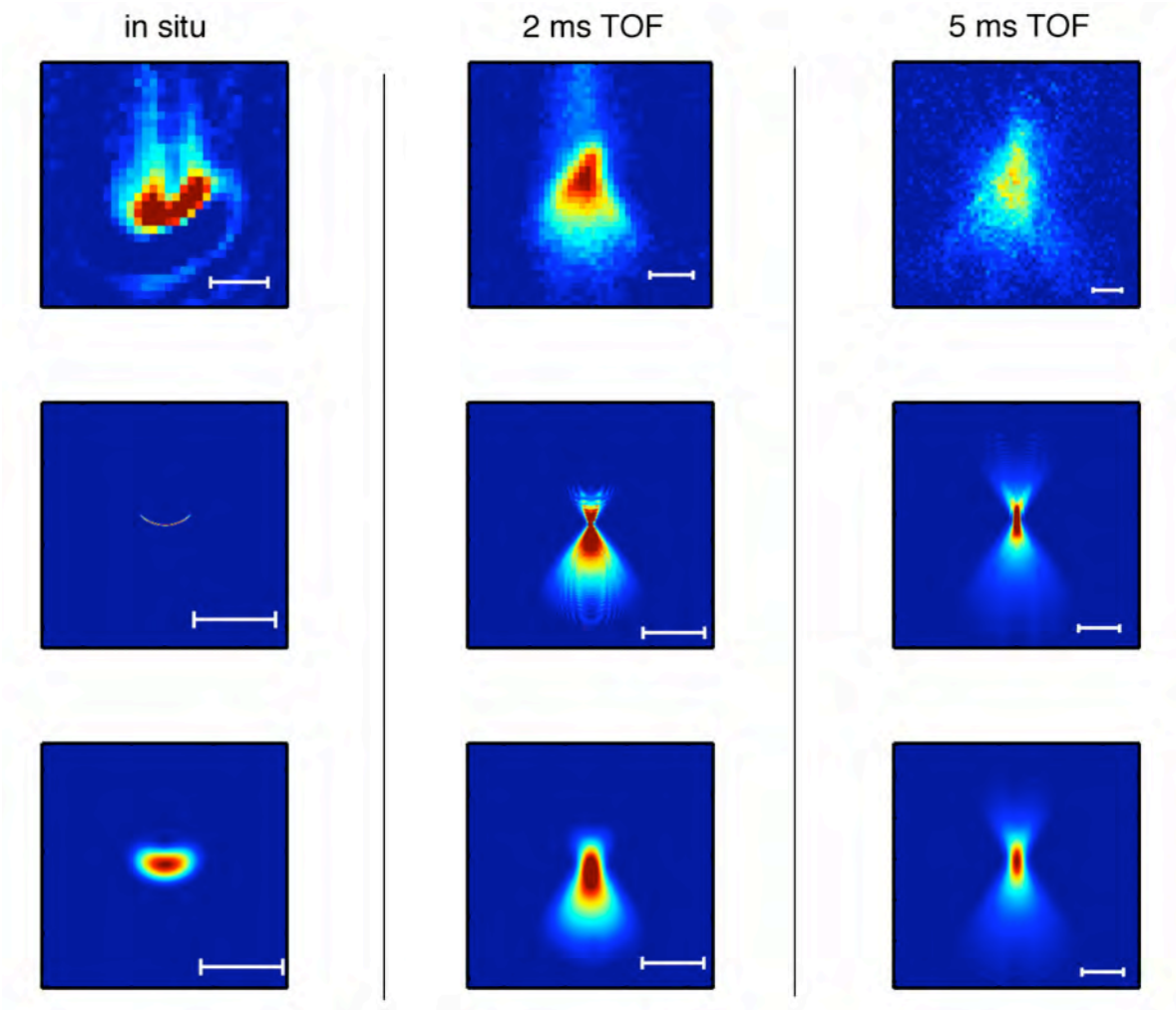

Figure 8.18.: Upper row: Density distributions integrated along the direction of the trapping wire for a BEC released from a two-dimensional adiabatic potential for different time of flights. **Middle row:** simulated expansion of a BEC from the corresponding calculated adiabatic potential for a chemical potential of $\mu = 5.5\,\mathrm{kHz}$. **Lowest row:** Simulated density distributions convoluted with an Airy pattern with radius 6.8 µm, therefore taking the performance of the imaging system into account. The white bar is in all pictures 20 µm long. Experiment and simulation show a focusing effect of the expanding cloud towards the center of the bent potential landscape. The measured density distributions are always slightly larger than the simulated ones. This could be due to a slight angle between the direction of the imaging beam and the trap geometry.

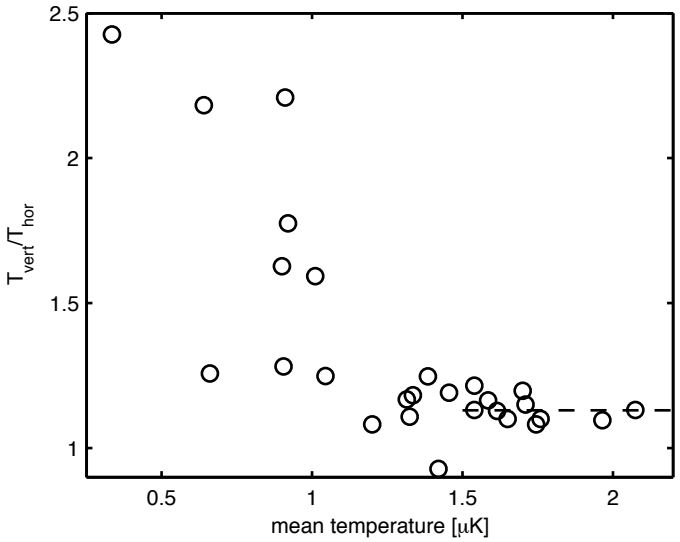

Figure 8.19.: Ratio of the temperature measured in vertical direction to the temperature measured in horizontal directions. At high temperatures, a systematic error between both measurements is visible, leading to a mean ratio of 1.1. At low temperatures, a clear deviation from this value shows that the expansion dynamics is dominated by the confinement of the atomic cloud to the transversal ground state size of the two-dimensional trap.

perpendicular to the sickle, the temperature transversal to the sickle can be extracted more easily, as the focusing effect of the sickle is compensated.

The initial expansion velocity of the cloud transversal to the sickle is close to 5 μm/ms with the above estimates for the kinetic energy along this direction. The gradient of the static trapping potential is according to simulations 4300 G/cm. Therefore, the gradient in the energy difference between the Zeeman levels is h·301 kHz/μm. To expand the sickle faster than the expansion dynamics, the rf frequency has to be increased at a rate faster than 1.5 MHz/ms. Experimentally the problem arises that at a rate of more than 2 MHz/ms the trap is not deformed adiabatically any more and the dressed state is projected to several of the bare states of the static potential. It was never possible to clearly separate the expansion dynamics from the focussing effect.

8.4.5. Cooling in the Adiabatic Trap

To see the transition to BEC in a two-dimensional trapping geometry, a cloud of thermal atoms was transferred into the adiabatic trap. Typically $5{\cdot}10^5$ ^{87}Rbatoms at a temperature of 1.5 μK were transfered within 50 ms in the two-dimensional trap. There an additional rf field allowed to perform evaporative cooling on the sample.

Following equation (4.28), the transition temperature for an ideal gas in two dimensions can be calculated for this trapping geometry and $5 \cdot 10^4$ atoms to be 215 nK; for $1 \cdot 10^4$ atoms it is 96 nK. To reach this regime, several different cooling ramps with different lengths and end frequencies were applied, but degeneracy was not accessible. The lowest temperatures reached were a little below 400 nK. However, with only $4 \cdot 10^3$ atoms remaining in the trap. The reason for not reaching the BEC regime in the adiabatic trap, is the large heating rate in the experimental setup that is equally present for static traps and for adiabatic traps. This

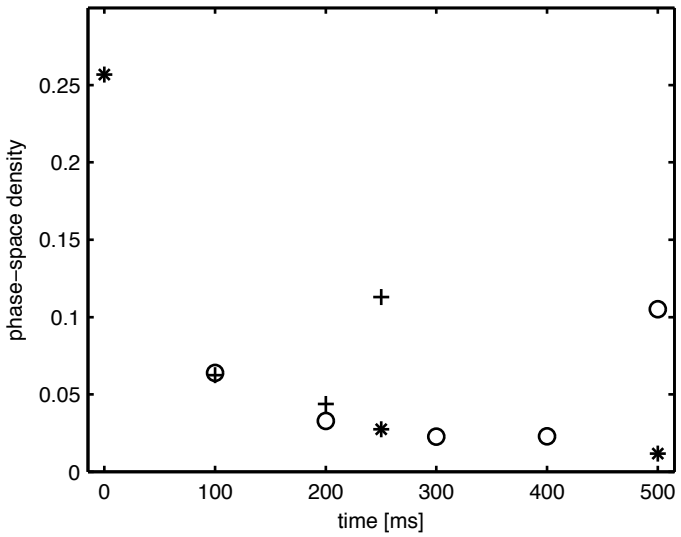

Figure 8.20.: Three-dimensional phase-space density for cooling ramps of different length, sweeping the rf from 400 kHz to 195 kHz in an adiabatic trap with a trap bottom of 190 kHz. The stars are values without any cooling, the crosses are values obtained for a cooling ramp of 250 ms length. The circles are values for a cooling ramp of 500 ms length. Only in the last steps of the cooling ramps, an increase of the phase-space density is visible. Dominant process for the decay of the phase-space density is the heating in the trap.

will be discussed in more detail in section 8.4.6.

Performing evaporative cooling, it is possible to counteract the loss in phase-space density that is caused by the heating, but an increase in phase-space density compared to the starting point of the cooling ramp is not achievable. In figure 8.20, the phase-space density is evaluated for two different cooling ramps with 250 ms and 500 ms length. An increase in phase-space density is only visible in the last steps of the respective cooling ramps, but an increase above the initial value of the cooling ramp is not possible. A similar example for different end frequencies of a cooling ramp with fixed length is given in figure 8.21.

In both figures, the absolute values for the phase-space density have to be taken with some caution, as the temperature measurement in this trapping geometry has its subtleties, as was shown in the previous subsection. For the evaluation of the phase-space density, always the temperature obtained from horizontal fits to the pictures was used. Regardless of the absolute values of the phase-space density, the qualitative message that the phase-space density can not be increased above the initial value is still valid.

8.4.6. Lifetime & Heating

In cold atom experiments heating processes are always a problematic issue. Neutral atoms have intrinsically a small coupling to the environment, besides the magnetic coupling to the confining potential. Still, any change in the trapping potential leads to excitations and loss from the trap, especially if the change occurs with one of the trapping frequencies or higher harmonics.

The lifetime in the static chip traps and in adiabatic traps was measured and has for both

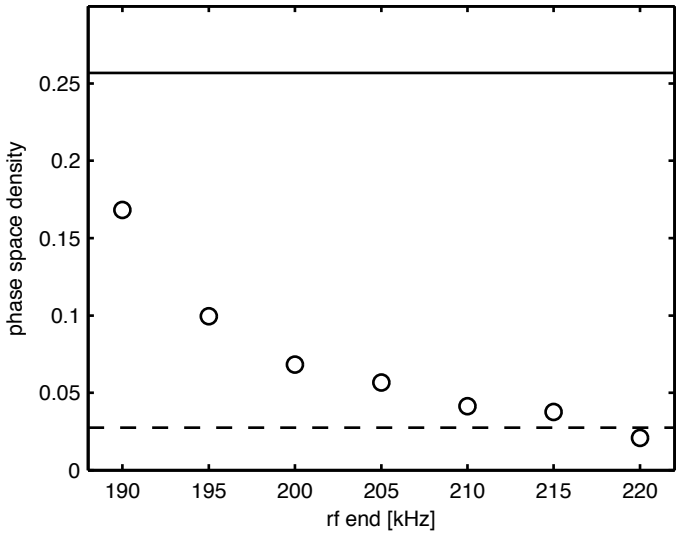

Figure 8.21.: Three-dimensional phase-space density for different end points of a 250 ms cooling ramp. The solid line corresponds to the initial phase-space density at the starting point of the ramp. The dashed line corresponds to the phase-space density for 250 ms holding time in the adiabatic trap without any cooling. The cooling ramp can reduce the phase-space loss that is due to heating, but does not increase the phase-space density above the initial value. The initial point corresponds to $4.9{\cdot}10^4$ atoms at 750 nK, the point at an rf frequency of 190 kHz to $4.5{\cdot}10^3$ atoms at 390 nK

traps a similar value of around 3.5 s. At the same time, a strong heating process is present. The measured heating rates are in both situations, the static trap and in the two-dimensional rf trap, between 2 and 2.5 μK/s. An example is visible in figure 8.22. At distances of 55 μm away from the trapping wire, this is not a surface effect, as in [152]. This heating rate is about a factor of ten larger than the values reported from the same setup when it was still in Heidelberg.

One source for the heating the atoms could be light, as any resonant photon heats the atom. However, due to the shallow potential of the chip trap, these atoms would be lost quickly. In the experiment, care is taken to keep the level of resonant light as low as possible during the magnetic trapping phase. In addition to AOMs in double-pass configuration, mechanical shutters are used, and the vacuum chamber is separated from the laser bench by several cardboard walls. As almost no atom loss is observed, this heating mechanism can be excluded.

Another source heating the sample, is noise in the current flow of the trapping wire or of the bias field. As the measured heating rate is large, it can not be attributed to thermal noise in the conductor but is of a technical nature. The current drivers of the chip can be ruled out as a possible noise source, as they are specially designed low-noise sources, identical to the ones already used in Heidelberg. Most likely the heating is caused by ambient electromagnetic noise radiated from sources inside or outside the lab.

Varying the parameters of the static trap did not change the heating rate significantly, leading to the conclusion that the noise source has to be broadband or $1/f$ in nature. If it were noise with a well defined frequency, it should show the same resonance behavior that was employed in the parametric heating measurements of section 8.2. The width of the trap bottom of 4.4 kHz as measured in section 8.2.2 hints to noise in the magnetic field with a

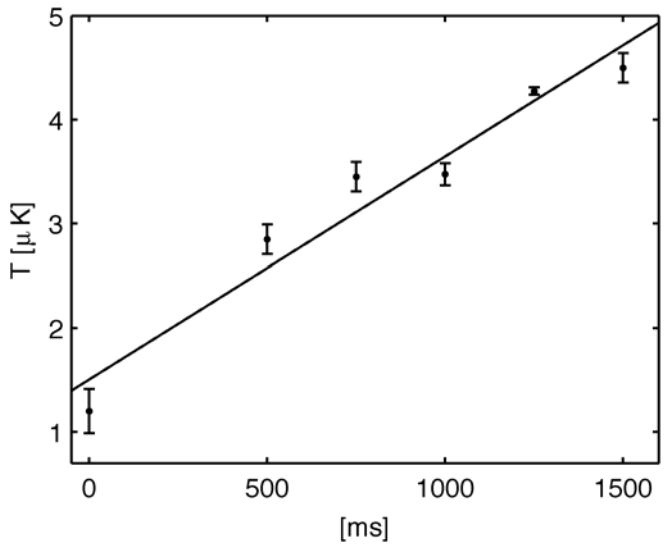

Figure 8.22.: Typical heating rate of 2.1 μK/s in a static trap of $2\pi \cdot 2.7$ kHz transversal confinement and $2\pi \cdot 18$ Hz longitudinal confinement.

rather large amplitude of 6.3 mG.

Over time, several noise sources in the lab were identified and removed, e.g. ground loops, a faulty ion pump controller, digital-to-analog converters and noisy uninterruptible power supplies. To remove the channel update frequency of the experiment control from the analog control lines, low pass filters were installed.

Nevertheless, none of these measures changed the heating rate drastically. There is still a significant amount of noise fed via the ground line to the lab. One of the next steps that will be taken, is the replacement of the noisy electrical ground of the building that is not well defined by a separate, cleaner one.

9 Summary & Outlook

In summary, the design and build-up phase of a new Bose-Fermi mixture experiment was described in this thesis. Since a large part of the effort which went into this thesis has been spent on designing and setting up the apparatus, first experiments characterizing the new setup were presented, showing promising results for future investigations. Several improvements were made to the apparatus compared to previous and existing atom chip experiments, leading to a next-generation setup that is optimized for maximum stability and a minimum duration of the experimental cycle. All experience gained with an initial mixture experiment of ^{6}Li and ^{87}Rb at the beginning of the time of my PhD, contributed to the design considerations of the new experiment. Once it is fully operational, it will be the second atom chip experiment worldwide working with ultracold Bose-Fermi mixtures.

In this new experiment, a double-chamber vacuum system combines high atom numbers with long lifetimes in the magnetic trap. Moreover, a stable laser system is operational, and the new science chamber offers a maximum of optical access that permits the incorporation of a high-performance optical imaging system. The atom chip that is currently inside the vacuum chamber has a wire geometry that is specialized for one-dimensional traps. These have very high aspect ratios that can be as large as 10^4. Additionally, a very neat realization of rf fields for adiabatic trapping potentials was implemented.

Together with the attractive interaction of the mixture ^{40}K-^{87}Rb, a whole variety of physical questions can be investigated. The combination of highly anisotropic traps with a Bose-Fermi mixture allows the study of the transport and of the statistics of bosons, fermions and mixtures in one-dimensional traps. Questions about the localization and impurity scattering of bosons at fermions were already addressed in three dimensions [22], but can now be investigated in one-dimensional systems. The attractive interaction between both species should also lead to the formation of bright solitons [137].

As was shown in this thesis, additional rf fields permit the creation of species-selective trapping geometries, beam splitters, and the realization of a smooth crossover from a one-dimensional trap to a two-dimensional geometry. For example, in a possible experiment in which the bosonic species is split in a double-well geometry, and in which the fermionic species extends over the whole volume of the double-well, the change in the coherence properties between the two bosonic clouds that is introduced by the fermions can be studied.

In this thesis, a similar trapping configuration was studied in more detail theoretically. There, the attractive mean-field interaction between both species changes the barrier in a double-well potential for the first species. Therefore, the tunneling dynamics between both wells depends strongly on the exact number of atoms of the second species.

As a new generation of PhD-students is currently taking over the experiment, it is not clear yet, which physical questions will be tackled first. Additionally, the experiment is still in an early stage, and several steps have to be mastered until a BEC and a ultracold gas of fermions is present in the chip trap.

Two-Dimensional Trap

Within this thesis, several experiments for the new setup were suggested with the main focus on the realization of a two-dimensional toroidal trap. This trapping geometry was studied theoretically for different wire geometries and was implemented experimentally in a two-wire setup.

Experimental results were obtained for different amplitudes and relative phases of the two rf fields, showing good qualitative agreement with numerical simulations of the potential landscape. It was shown that by using an elliptically polarized rf field, the minimal curvature of a two-dimensional toroidal trap can be reduced considerably, and variations below $2\pi\cdot 120\,\mathrm{Hz}$ are achievable. The ratio between the trapping frequency transversally to the bent surface and the mean trapping frequency in the surface is larger than 300:1 and therefore larger than in typical two-dimensional trapping geometries. By loading a thermal cloud in such a trap and subsequent evaporative cooling, the transition to a two-dimensional BEC could unfortunately not be observed. This is not a problem caused by the application of adiabatic rf potentials generating the trapping geometry, but due to the large heating rate that is equally present in the static trapping configuration.

Once the heating mechanism is fully understood and removed, nothing should prevent condensation in this trapping geometry. The RbII setup where these measurements took place has a unique fluorescence imaging system that is located several mm below the trapping region. If a method can be developed that counteracts the focusing effect of the expansion dynamics sufficiently, the direct observation of free vortices above the Berezinskii-Kosterlitz-Thouless transition of the two-dimensional gas is feasible.

The trap, as it was used in the experiments presented, allows the investigation of the properties of a two-dimensional BEC. However, the situation would get even more interesting if the atoms were to explore the whole surface of the torus, whilst being transversally in the ground state. Such a scenario was investigated theoretically in simulations of a four-wire geometry for the creation of the rf fields. These simulations led to very promising results. For specific values of the amplitudes and phases of the single wires, an almost flat two-dimensional trapping potential on a torus with $5\,\mu\mathrm{m}$ diameter is predicted that has variations in the trap bottom smaller than $h\cdot 250\,\mathrm{Hz}$. If the circumference of such a torus is smaller than the phase coherence length in the bent two-dimensional surface, the study of exciting new physics would be possible. As in the case of the transport experiments, the fact that bosons, fermions and mixtures can be investigated in the identical trapping geometry greatly increases the number of theoretical questions that can be addressed.

Exactly this optimized four-wire geometry for the rf fields was implemented in the new experimental setup for the K-Rb experiment and will allow the realization of this novel trapping configuration once cold samples are trapped in the wire traps of the new atom chip.

A Atomic Data for ^{87}Rb and ^{40}K

A.1. Atomic Parameters

		^{40}K		^{87}Rb	
number of protons	Z	19		37	
natural abundance	ν	0.012 %	[165]	27.83(2) %	[165]
atomic mass	m	39.96 u	[165]	86.91 u	[166]
nuclear lifetime	τ_n	$1.248\,10^9$ yrs	[167]	$4.88\,10^{10}$ yrs	[166]
nuclear spin	I	4		3/2	
cooling transition		$4^2S_{1/2} \rightarrow 4^2P_{3/2}$		$5^2S_{1/2} \rightarrow 5^2P_{3/2}$	
wavelength D_2(vacuum)	λ	766.701 nm	[165]	780.246 nm	[166]
wavelength D_2(air)	λ_{air}	766.491 nm	[165]	780.037 nm	[166]
D_2 sat. intens. (σ_+)	I_S	1.796 mW/cm^2	[168, 141]	1.669(2) mW/cm^2	[166]
excited state lifetime	τ	25.7 ns	[168]	26.24(4) ns	[166]
linewidth (FWHM)	Γ	2π·6.2 MHz	[168]	2π·6.065(9) MHz	[166]
recoil velocity	v_{rec}	13.02 mm/s	[168]	5.8845 mm/s	[166]
recoil temperature	T_{rec}	815 nK	[168]	361.95 nK	[166]

A.2. Level Schemes

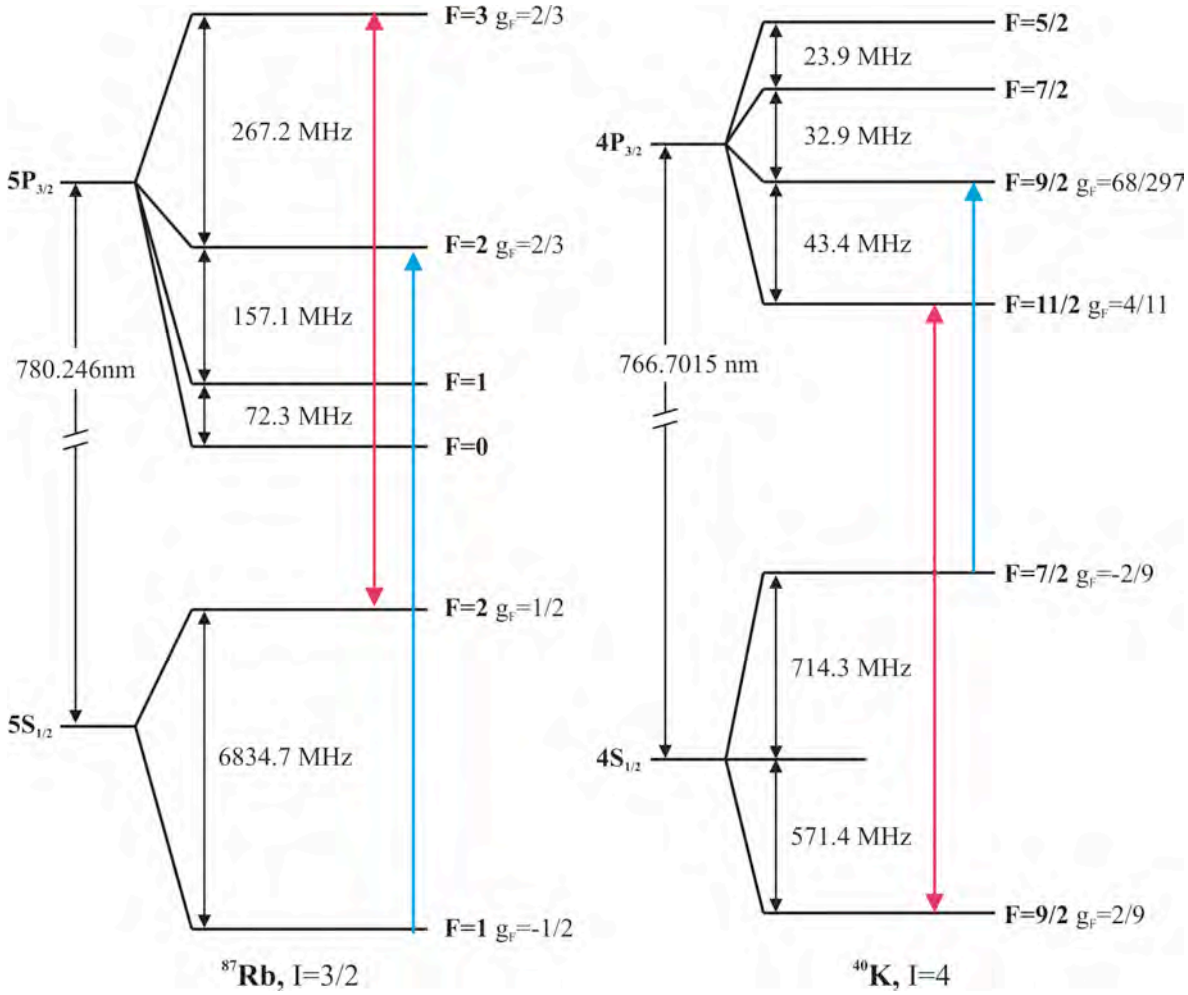

Figure A.1.: Level schemes for ^{87}Rb and ^{40}K. In ^{40}K the ground state and the excited state have both an inverted hyperfine splitting due to the large angular momentum of the nucleus. The cooling and repumping transitions are marked in red (cooling) and blue (repumping). The g_F factors given are the approximate Landé g-factors.

B Magnetic Fields of Extended Wires

The following equations are all given for a uniform current flow in $+y$-direction. The wires have their center of gravity at the point $(x = 0, y = 0, z = 0)$, and the magnetic field values are obtained by integrating Biot-Savart over the respective current distribution.

The following abbreviations are used where necessary

$$x_\pm = (x \pm w/2) \quad y_\pm = (y \pm l/2) \quad z_\pm = (z \pm h/2).$$

- B field for a flat wire of width w, infinitely long:

$$B(x,z) = \frac{\mu_0}{4\pi}\frac{I}{w}\sqrt{\left(\frac{x_+}{z\sqrt{z^2+x_+^2}} - \frac{x_-}{z\sqrt{z^2+x_-^2}}\right)^2 + \left(\frac{1}{\sqrt{z^2+x_+^2}} - \frac{1}{\sqrt{z^2+x_-^2}}\right)^2}$$

- B field for a wire of width w in x-direction and height h in z-direction, infinitely long:

$$\begin{aligned} B_x(x,z) &= \frac{\mu_0}{4\pi}\frac{I}{wh}\ln\left(\frac{(x_- + \sqrt{z_+^2+x_-^2})(x_+ + \sqrt{z_-^2+x_+^2})}{(x_+ + \sqrt{z_+^2+x_+^2})(x_- + \sqrt{z_-^2+x_-^2})}\right) \qquad \text{(B.1)} \\ B_z(x,z) &= \frac{\mu_0}{4\pi}\frac{I}{wh}\ln\left(\frac{(z_+ + \sqrt{z_+^2+x_+^2})(z_- + \sqrt{z_-^2+x_-^2})}{(z_+ + \sqrt{z_+^2+x_-^2})(z_- + \sqrt{z_-^2+x_+^2})}\right) \end{aligned}$$

Similar the fields for wires of finite length can be calculated.

- B field for a wire of length l, infinitely thin:

$$\begin{aligned} \frac{4\pi}{\mu_0}\frac{1}{I}B_x(x,y,z) &= \frac{y_+ z}{(x^2+z^2)\sqrt{x^2+y_+^2+z^2}} - \frac{y_- z}{(x^2+z^2)\sqrt{x^2+y_-^2+z^2}} \qquad \text{(B.2)} \\ \frac{4\pi}{\mu_0}\frac{1}{I}B_z(x,y,z) &= -\frac{y_+ x}{(x^2+z^2)\sqrt{x^2+y_+^2+z^2}} + \frac{y_- x}{(x^2+z^2)\sqrt{x^2+y_-^2+z^2}} \qquad \text{(B.3)} \end{aligned}$$

- B field for a flat wire of length l and width w:

$$\begin{aligned}\frac{4\pi}{\mu_0}\frac{w}{I}B_x(x,y,z) &= \arctan\frac{x_+y_+}{z\sqrt{x_+^2+y_+^2+z^2}} + \arctan\frac{x_-y_-}{z\sqrt{x_-^2+y_-^2+z^2}} \\ &- \arctan\frac{x_+y_-}{z\sqrt{x_+^2+y_-^2+z^2}} - \arctan\frac{x_-y_+}{z\sqrt{x_-^2+y_+^2+z^2}} \qquad \text{(B.4)}\end{aligned}$$

$$B_z(x,y,z) = \frac{\mu_0}{4\pi}\frac{I}{w}\ln\frac{(y_+ + \sqrt{x_+^2+y_+^2+z^2})(y_- + \sqrt{x_-^2+y_-^2+z^2})}{(y_- + \sqrt{x_+^2+y_-^2+z^2})(y_+ + \sqrt{x_-^2+y_+^2+z^2})} \qquad \text{(B.5)}$$

C Technical Drawings of the Mounting

All technical drawings were done using AutoCad[1]. The parts were manufactured by the mechanical workshop of the Physikalische Institut in Heidelberg. Detailed drawings of the science chamber can be found in [121].

[1] http://www.autodesk.de

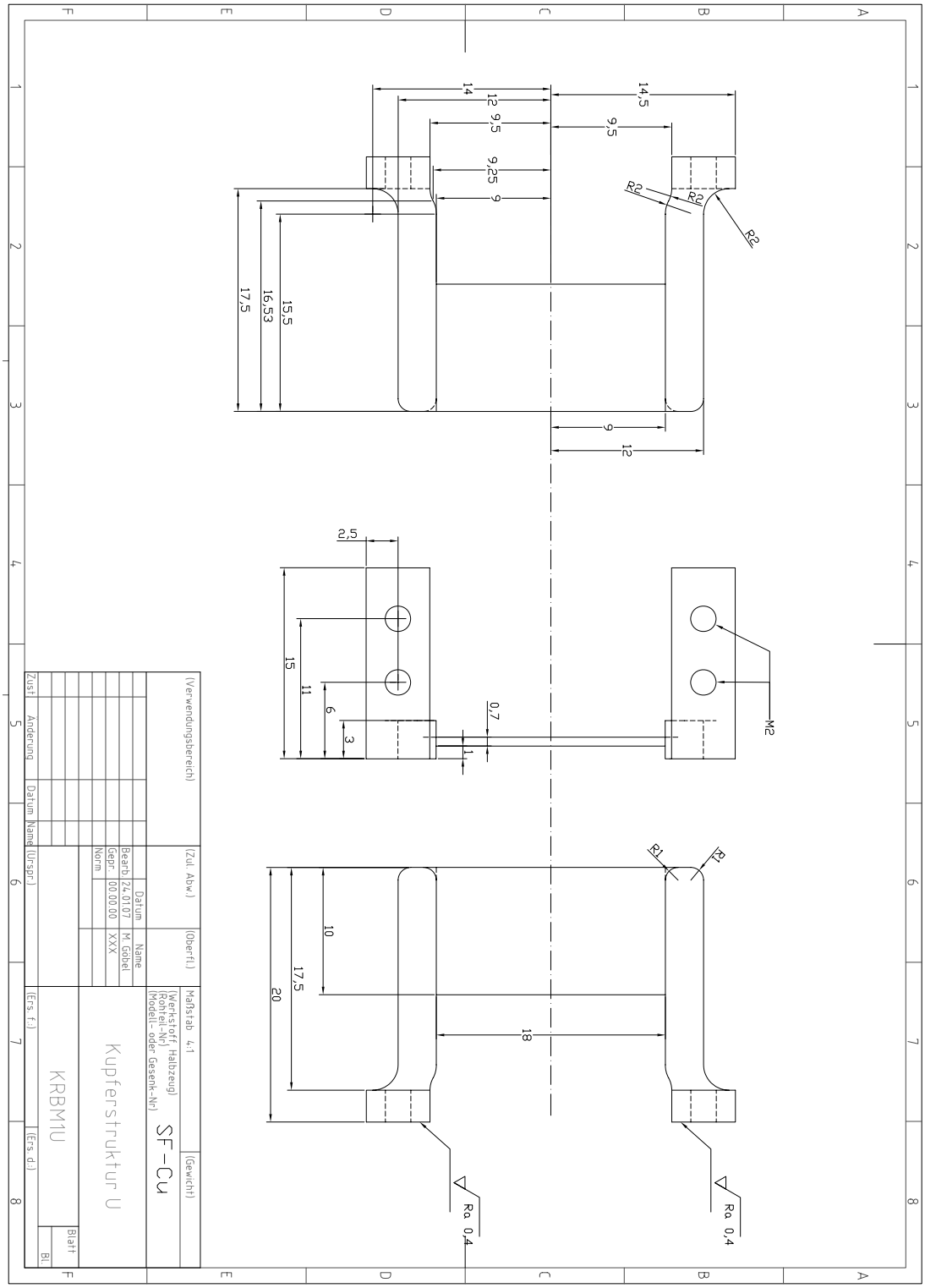

Figure C.1.: Copper U-structure used for the formation of the quadrupole field.

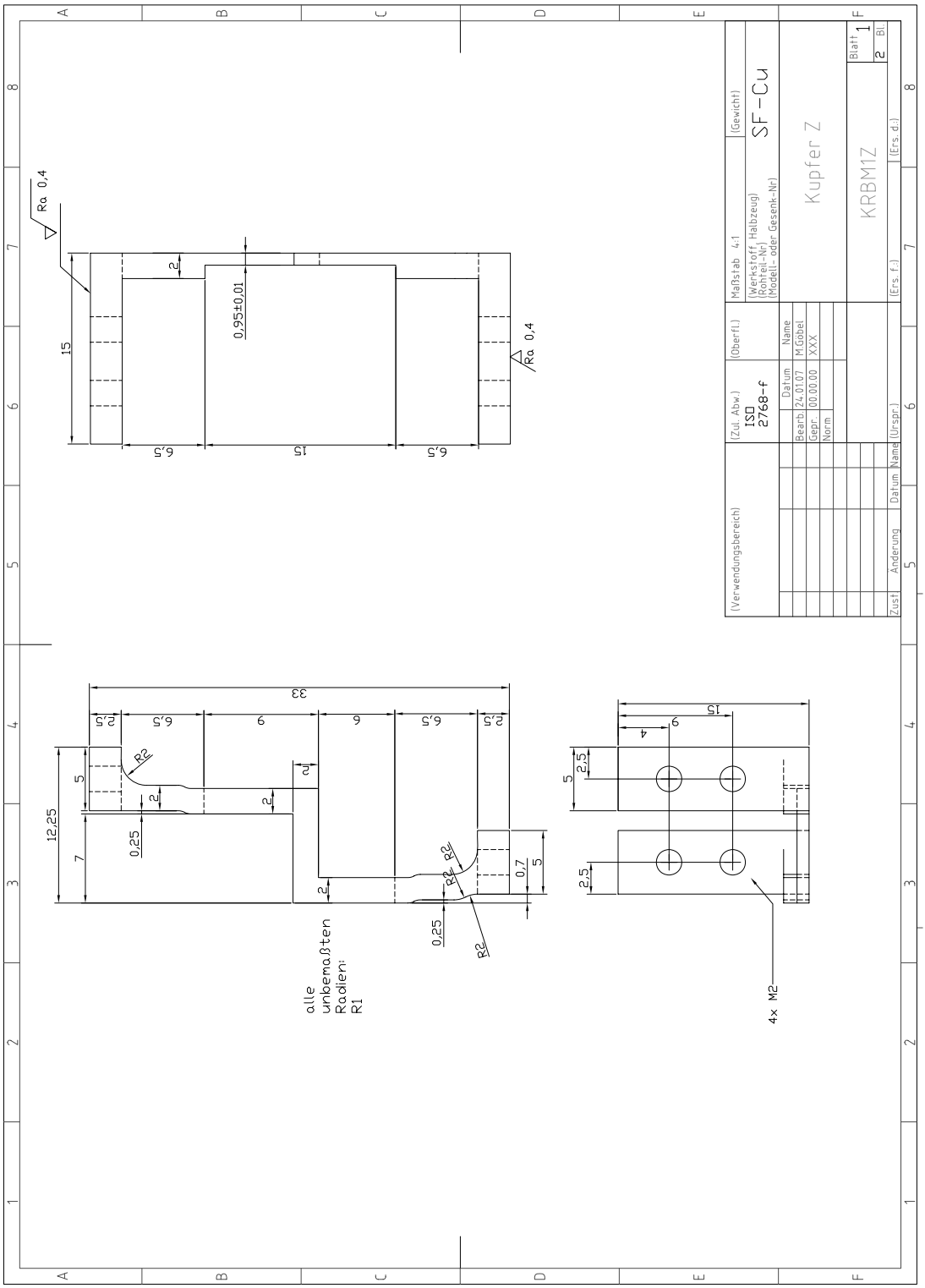

Figure C.2.: Wide Z-structure used together with the thin h-structure for the formation of the initial big volume Ioffe trap.

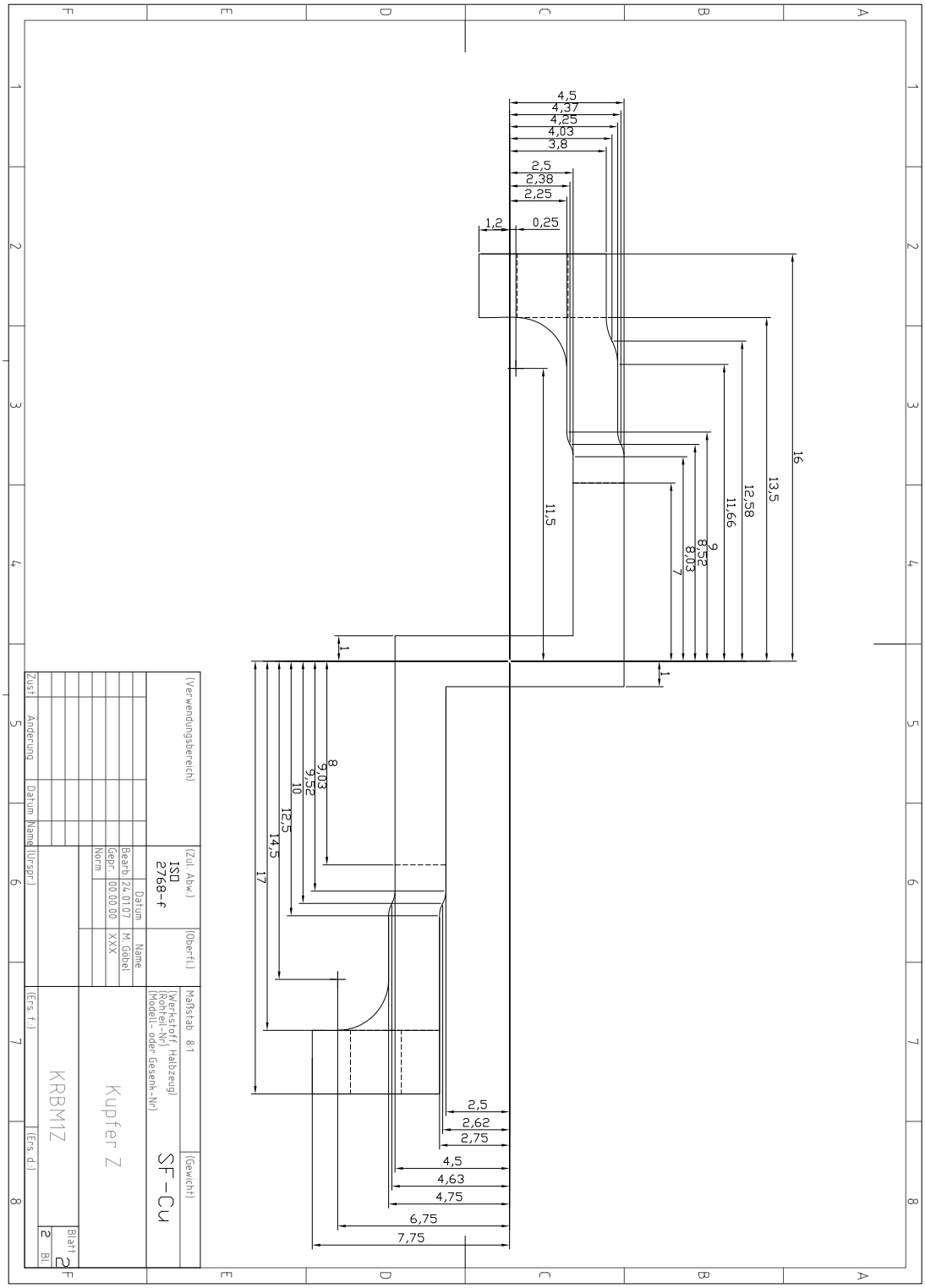

Figure C.3.: Details on the wide Z-structure.

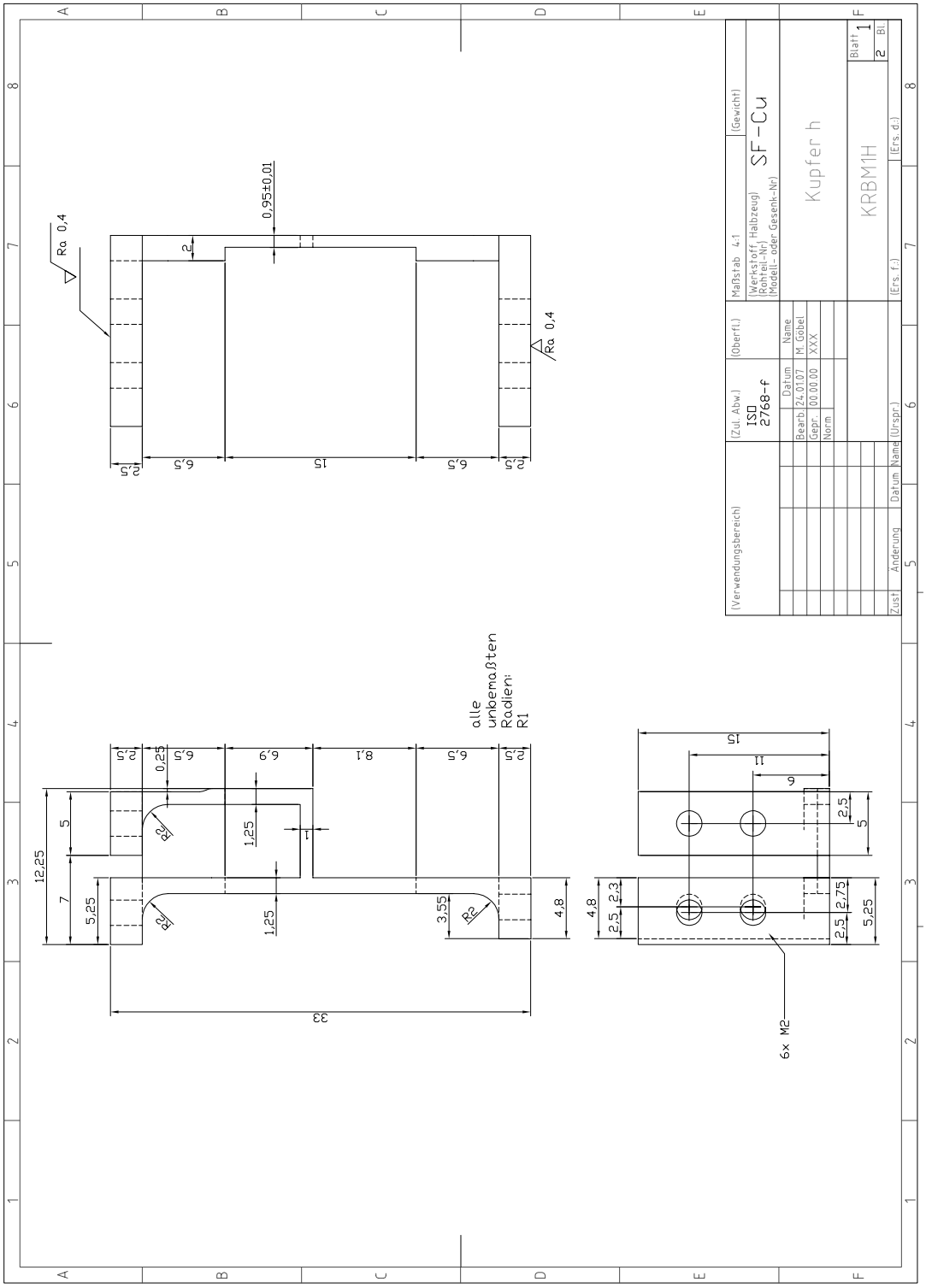

Figure C.4.: Thin h-structure used in Z-configuration as a Ioffe trap before the atoms are loaded on the chip. The straight copper leg perpendicular to the weak trapping axis of the chip allows the usage as an additional dimple wire.

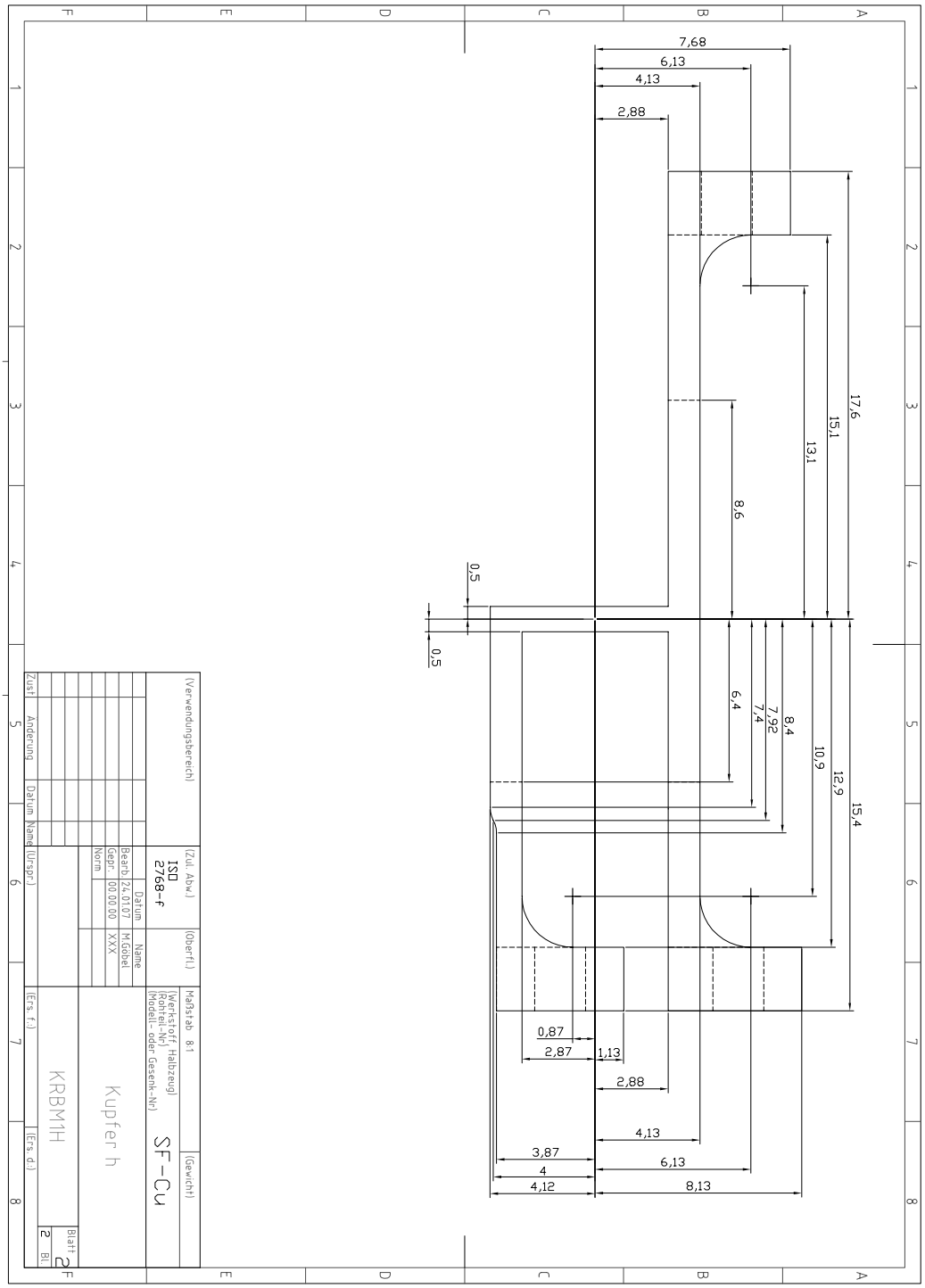

Figure C.5.: Details on the h-structure.

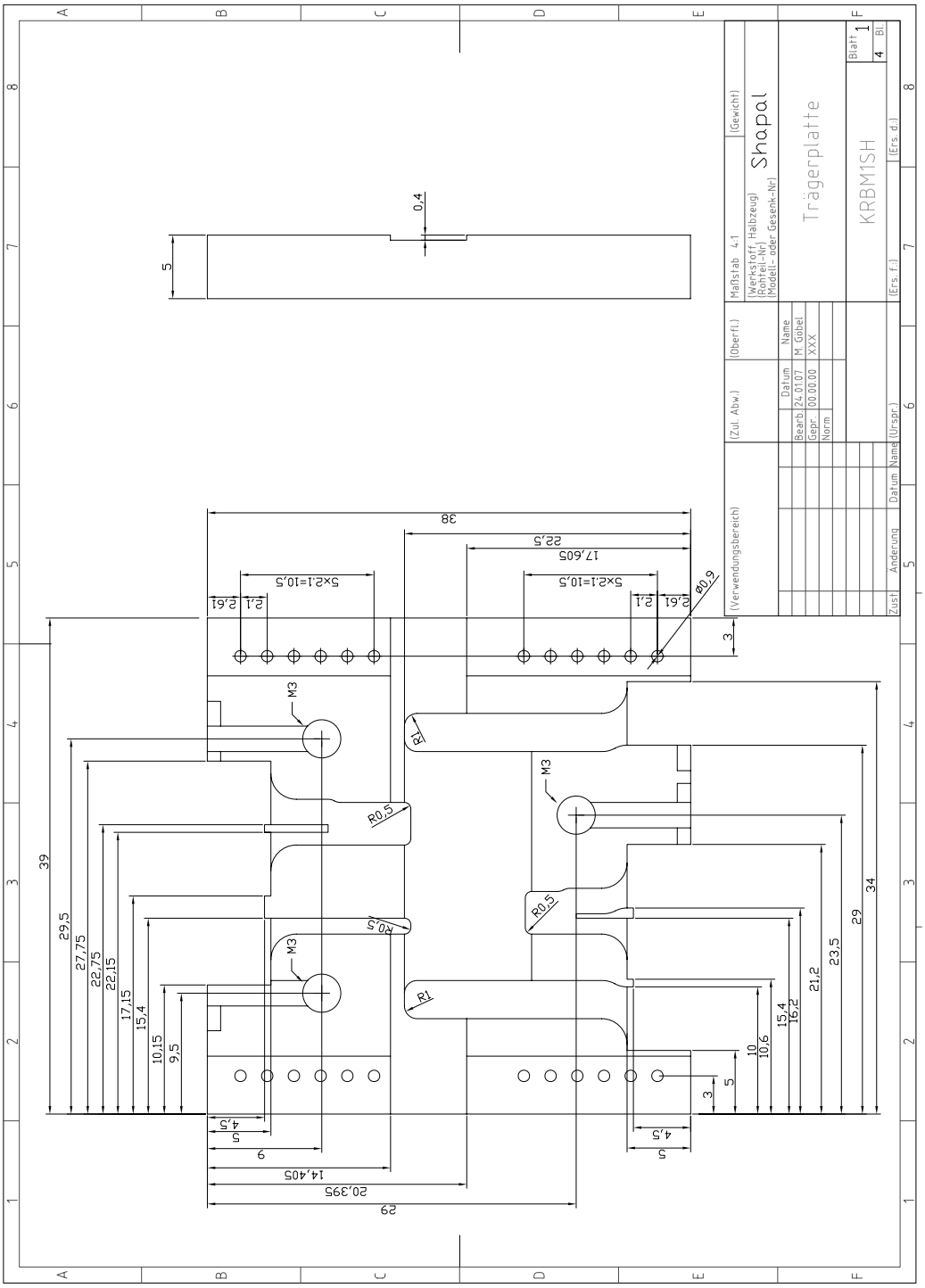

Figure C.6.: Support structure for the copper structures made from Shapal.

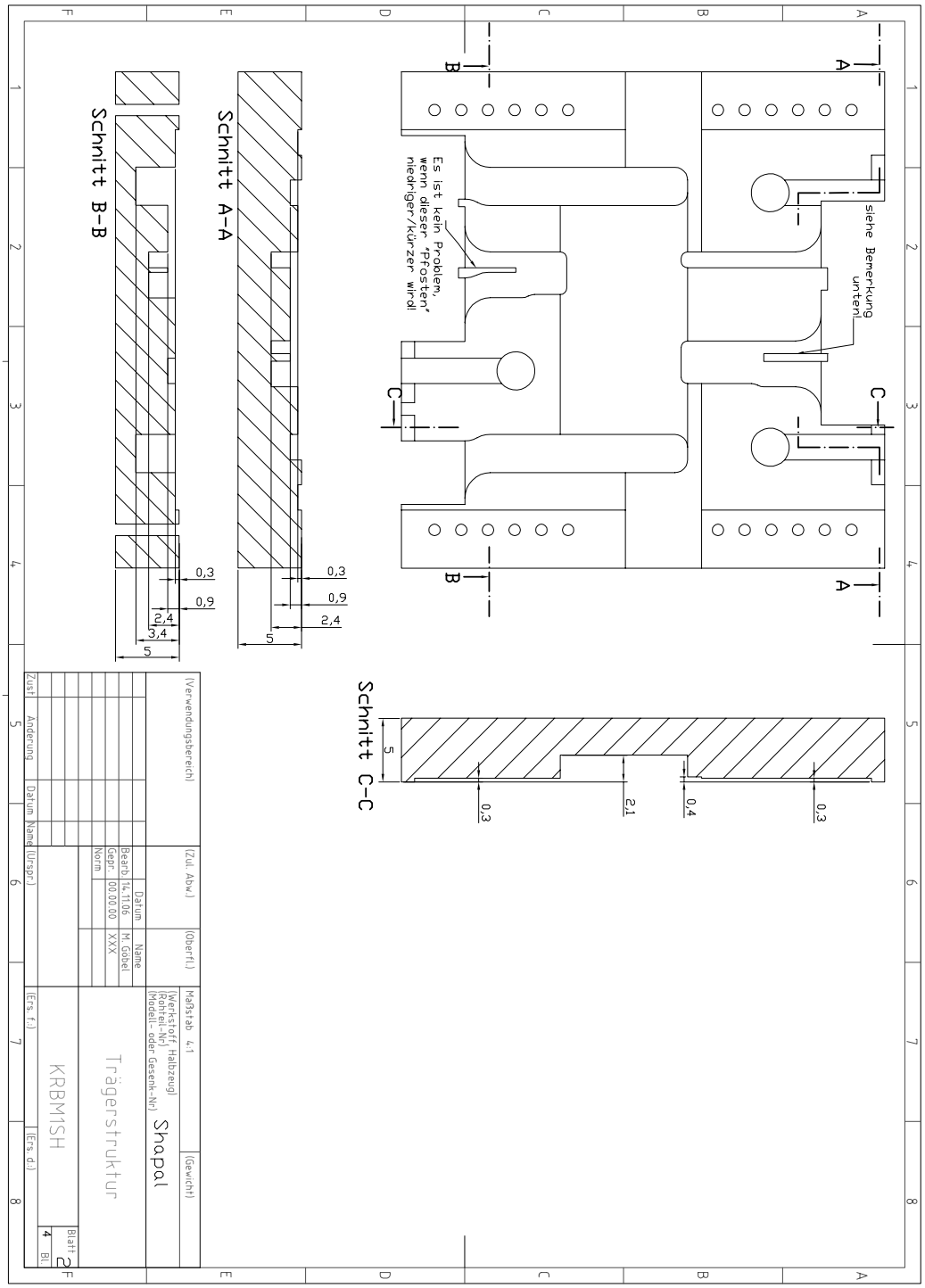

Figure C.7.: Details on the Shapal structure

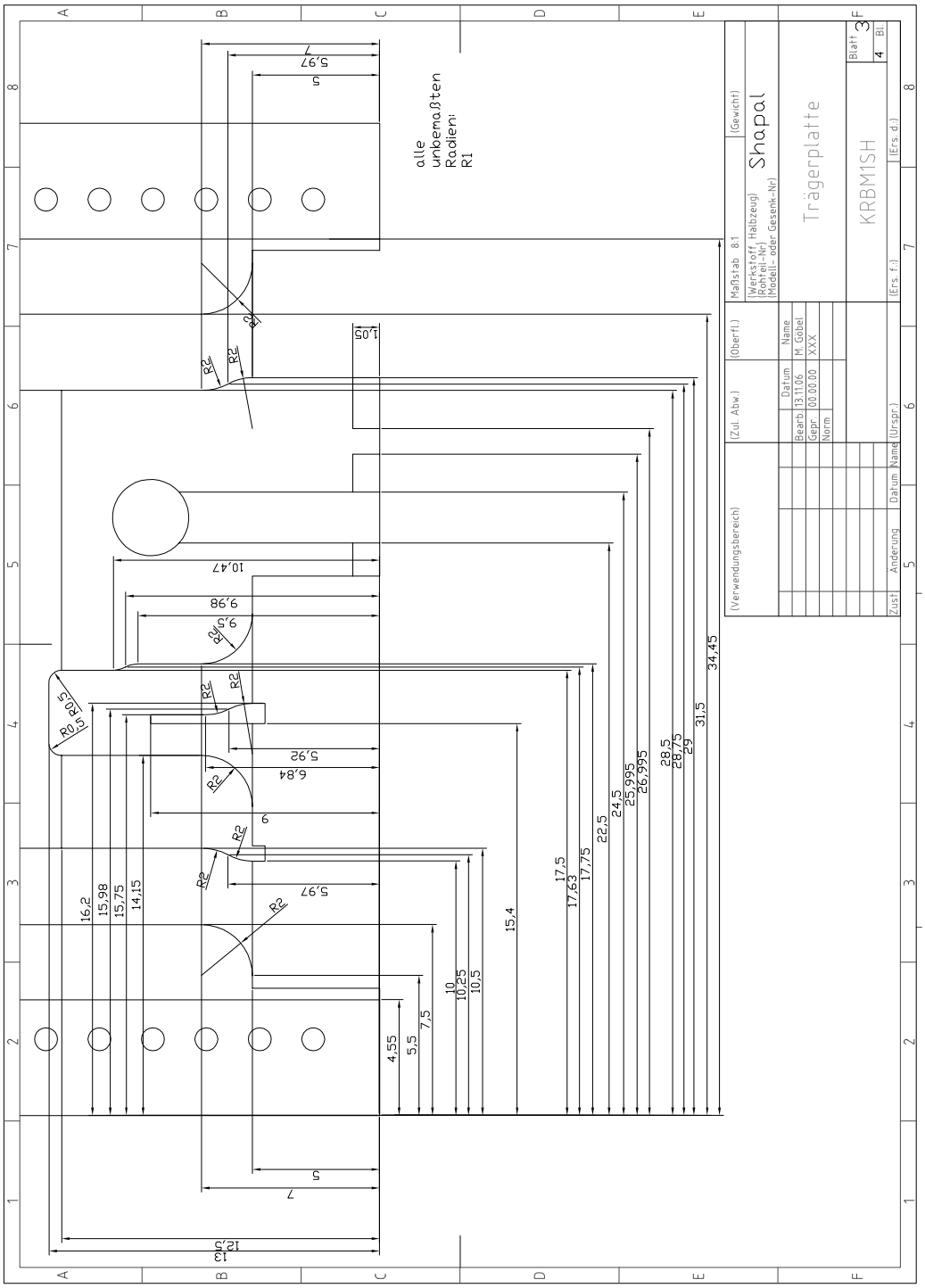

Figure C.8.: Details on the Shapal structure

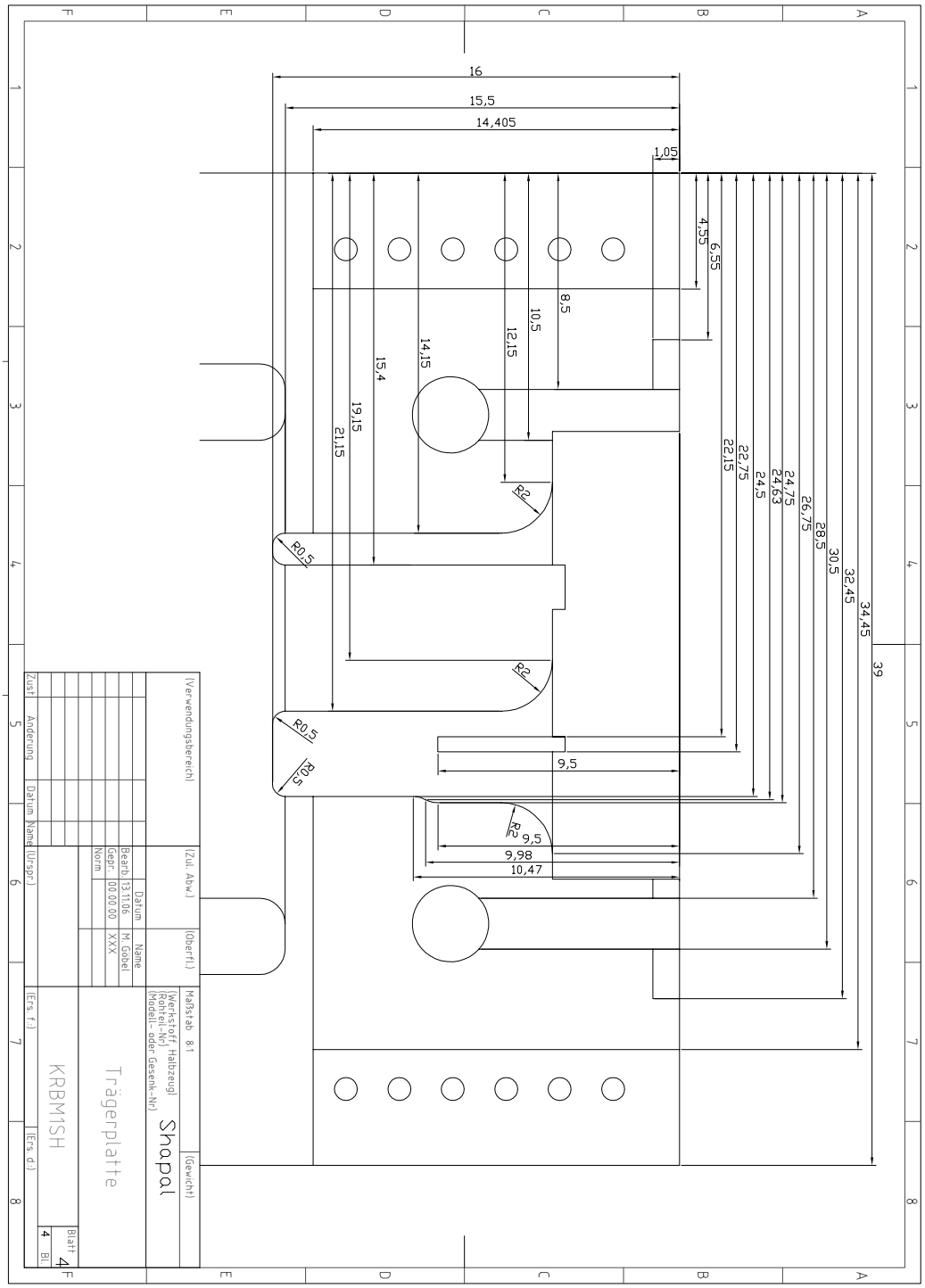

Figure C.9.: Details on the Shapal structure

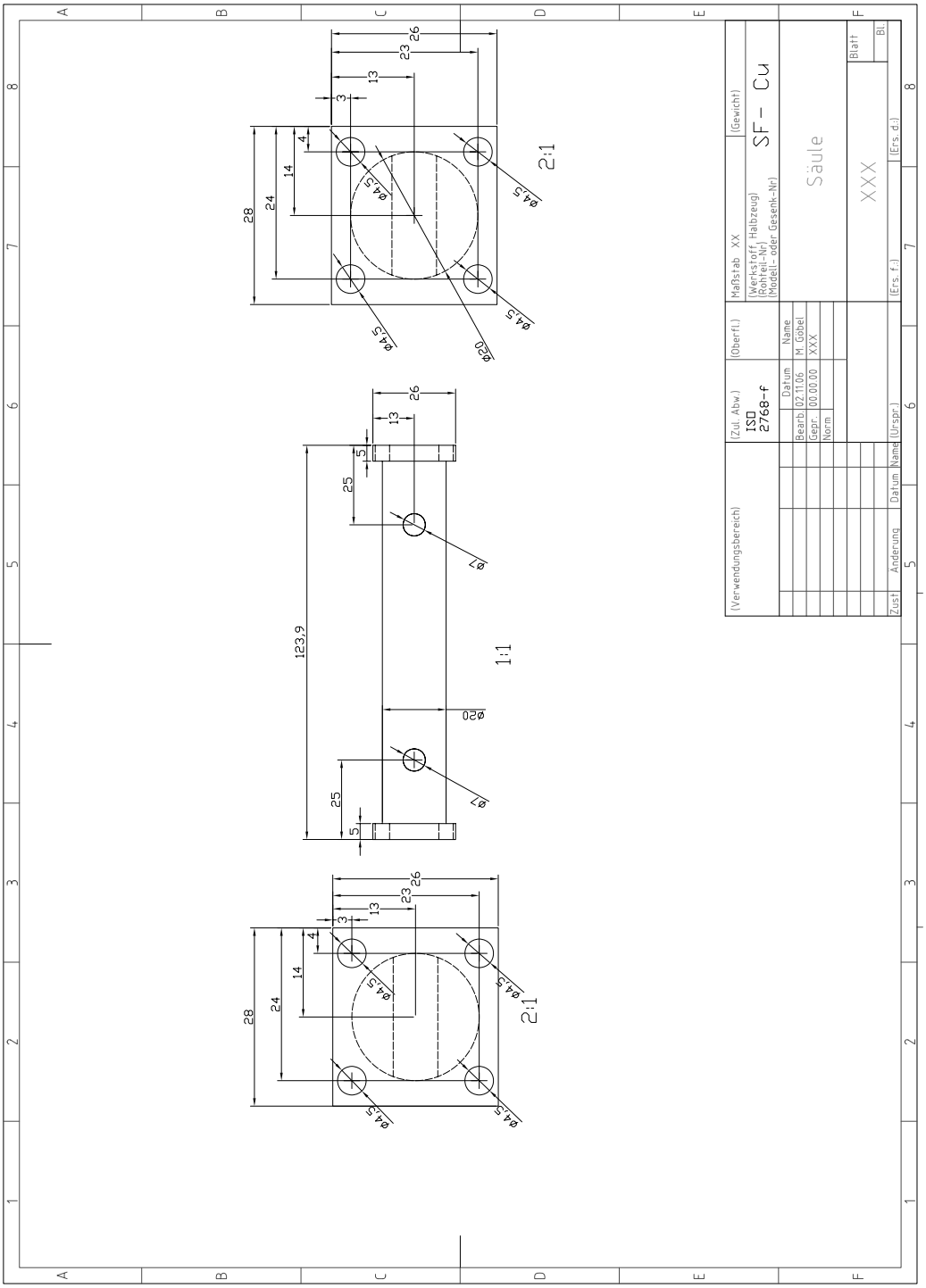

Figure C.10.: Upper part of the support structure

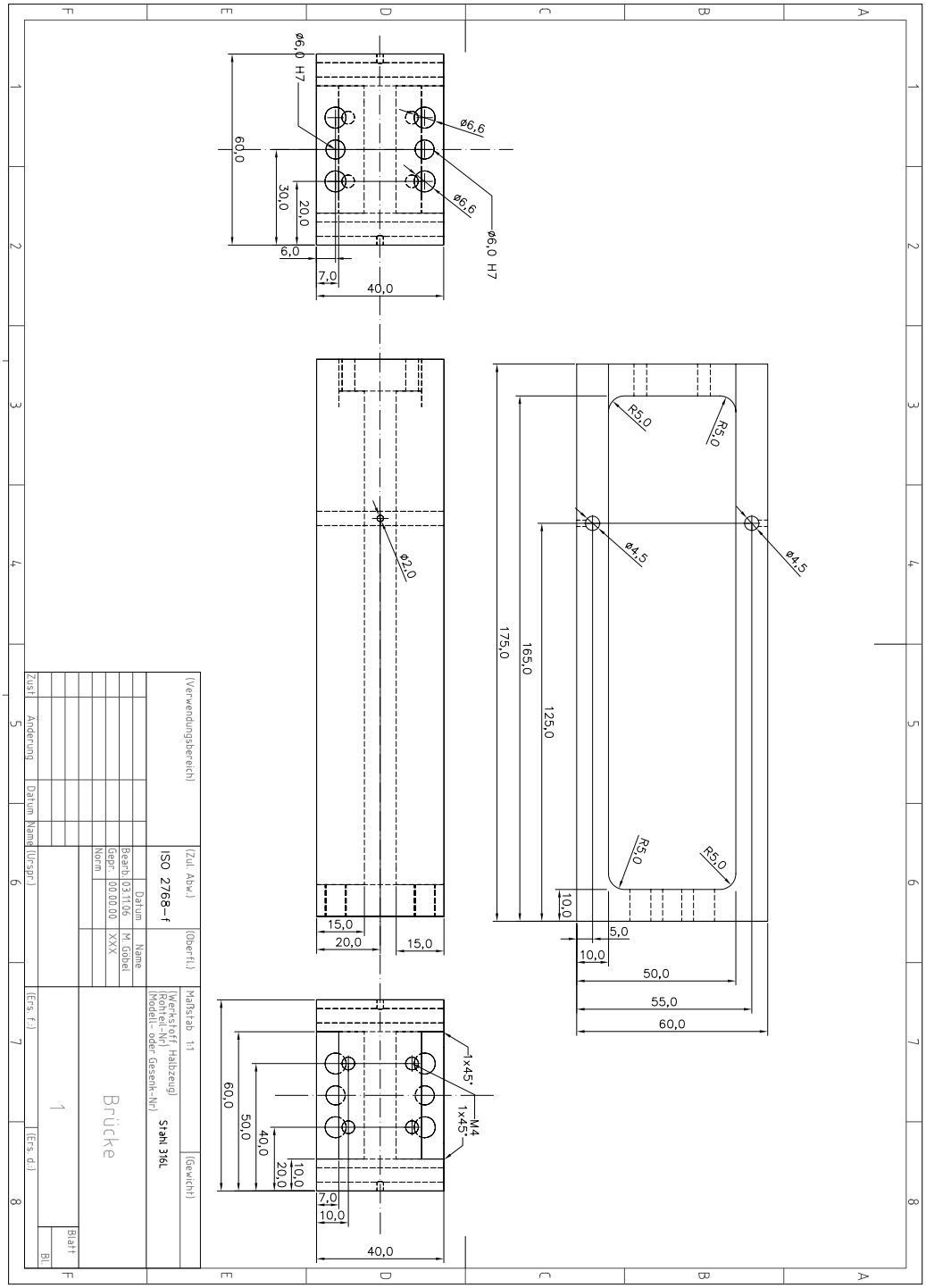

Figure C.11.: Lowest part of the support structure

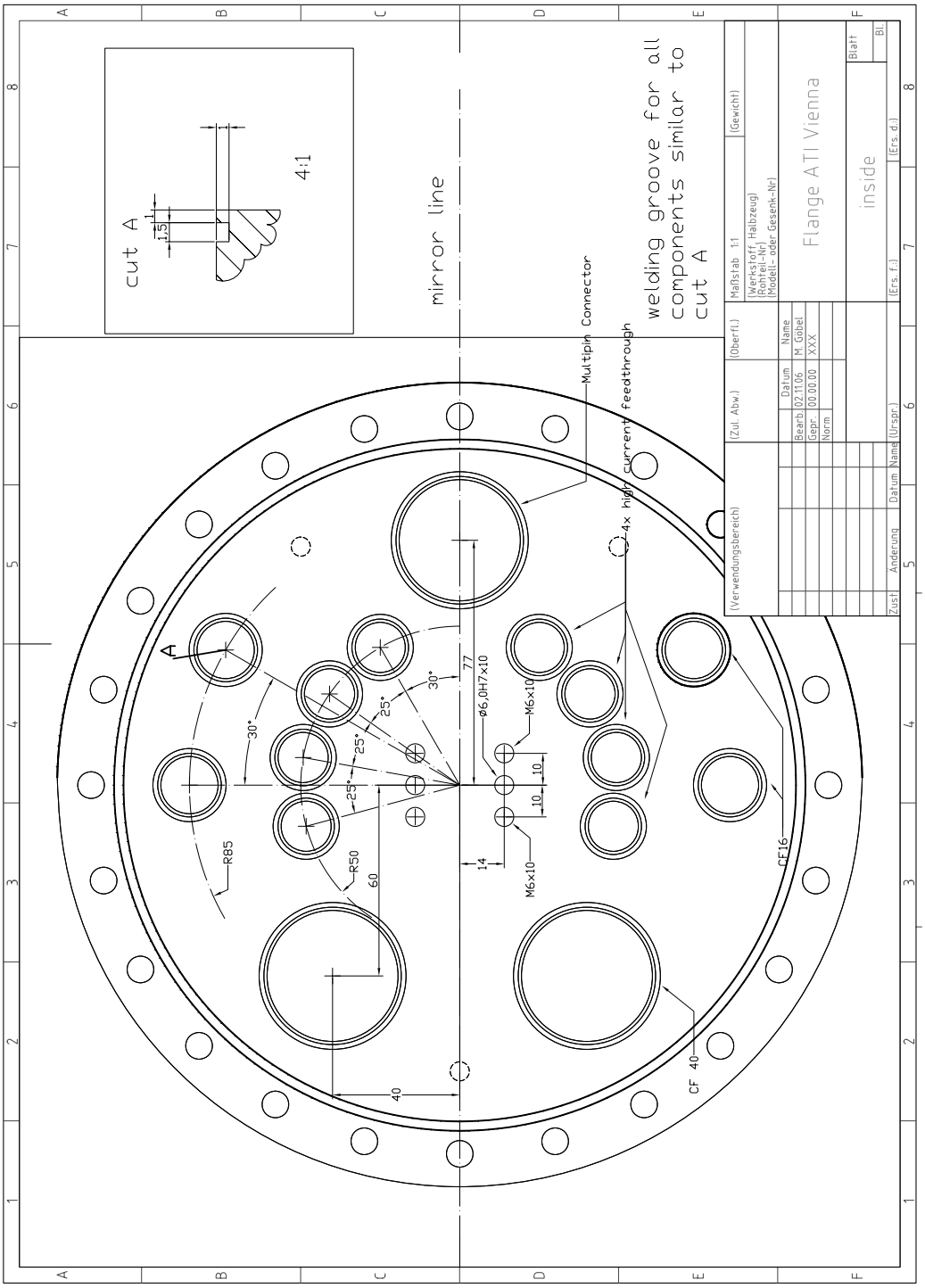

Figure C.12.: Flange with the position of all feedthroughs and connecting tubes.

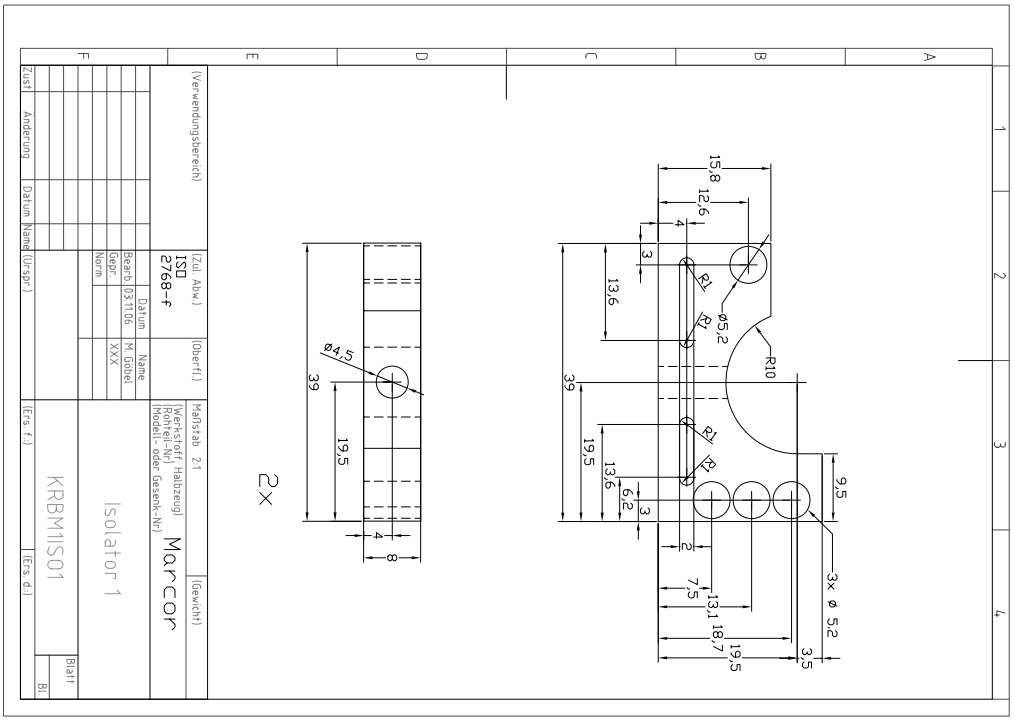

Figure C.13.: Small pieces from isolating Macor to stabilize the copper rods.

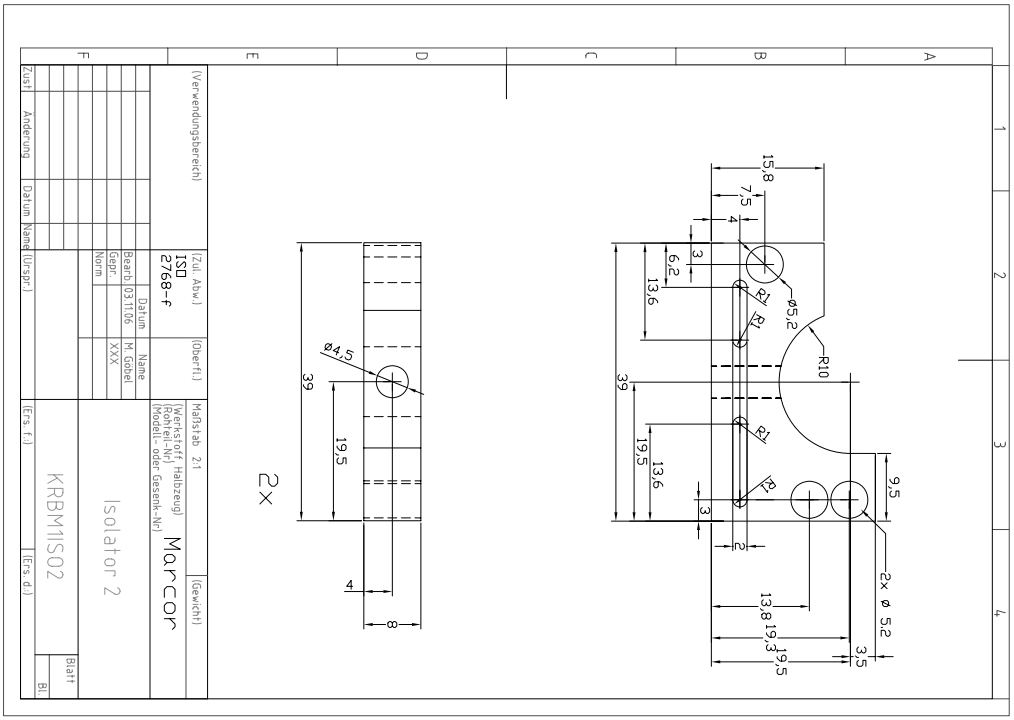

Figure C.14.: Small pieces from isolating Macor to stabilize the copper rods.

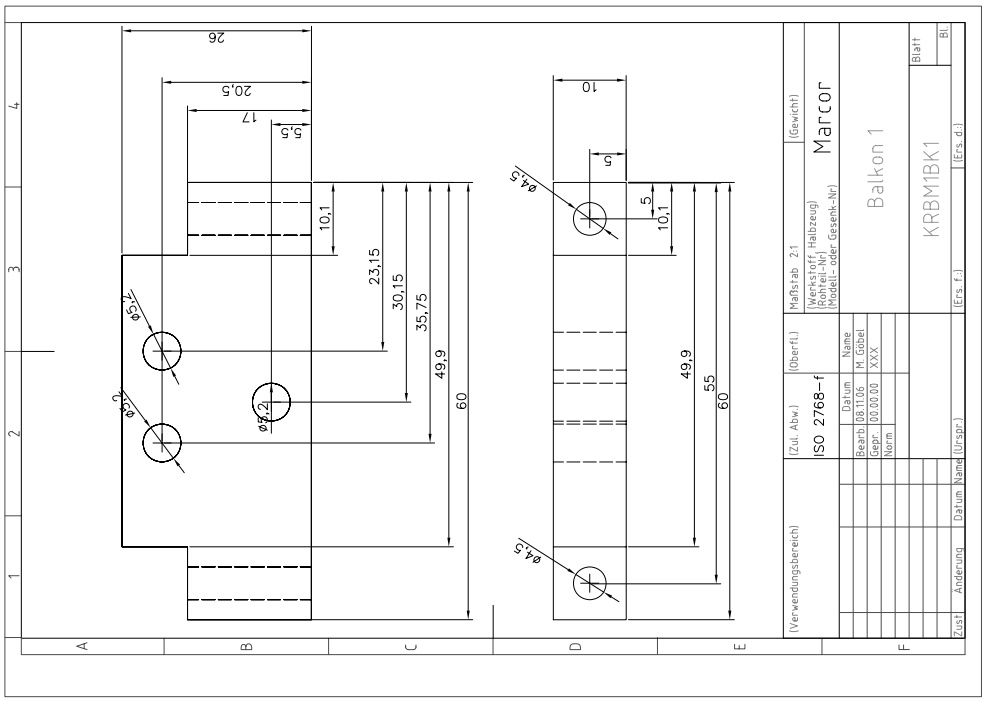

Figure C.15.: Small pieces from isolating Macor to stabilize the copper rods.

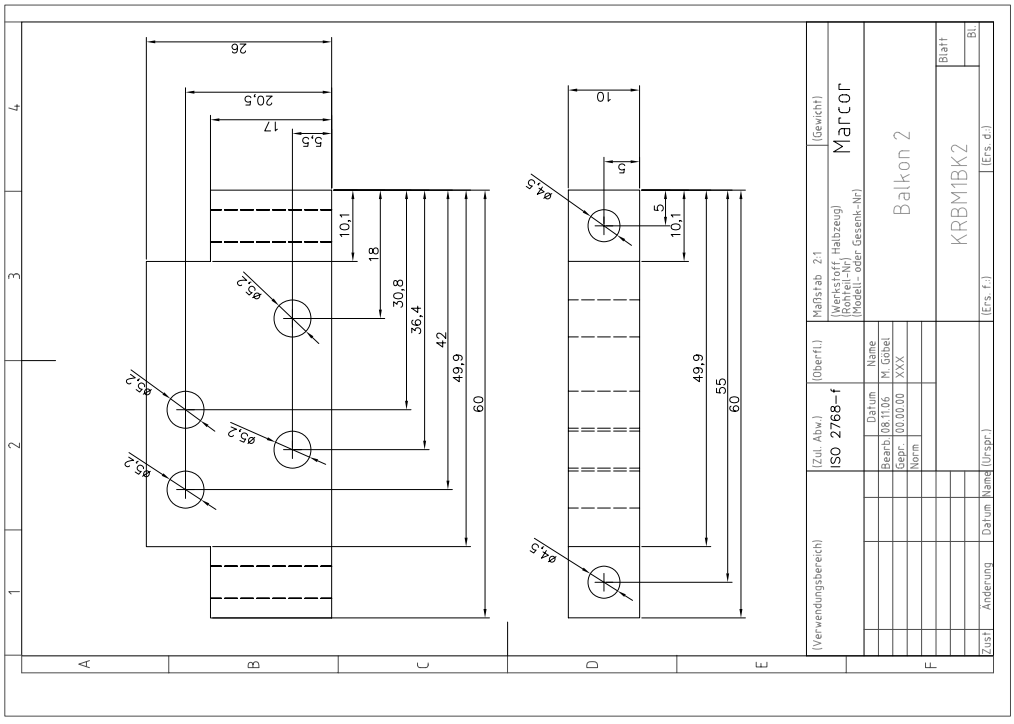

Figure C.16.: Small pieces from isolating Macor to stabilize the copper rods.

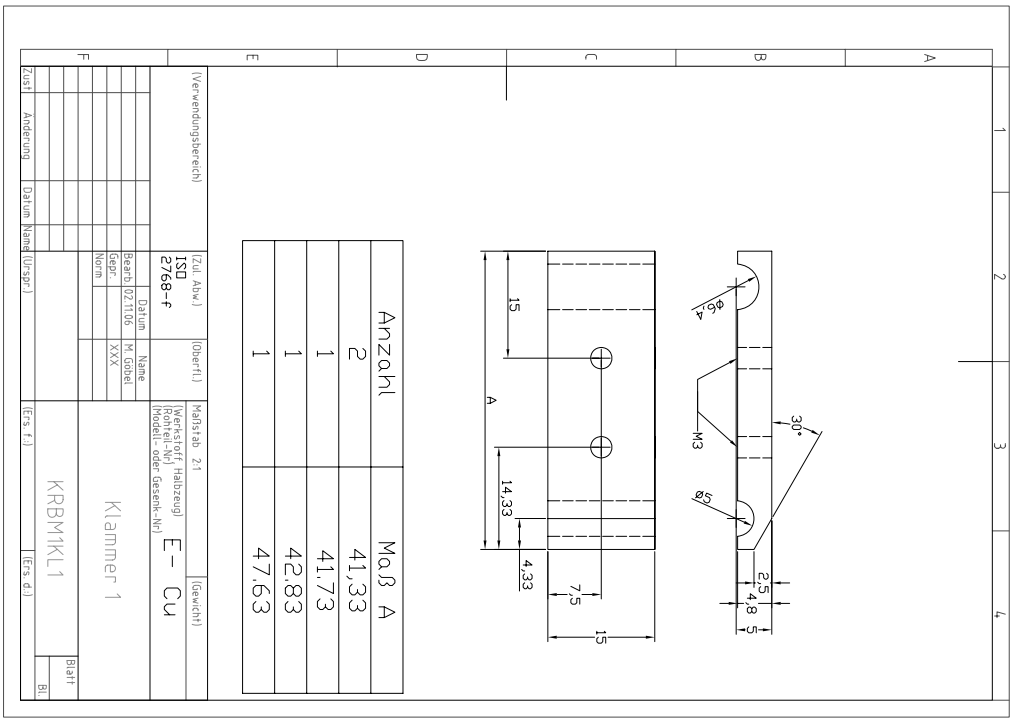

Figure C.17.: Copper clamps

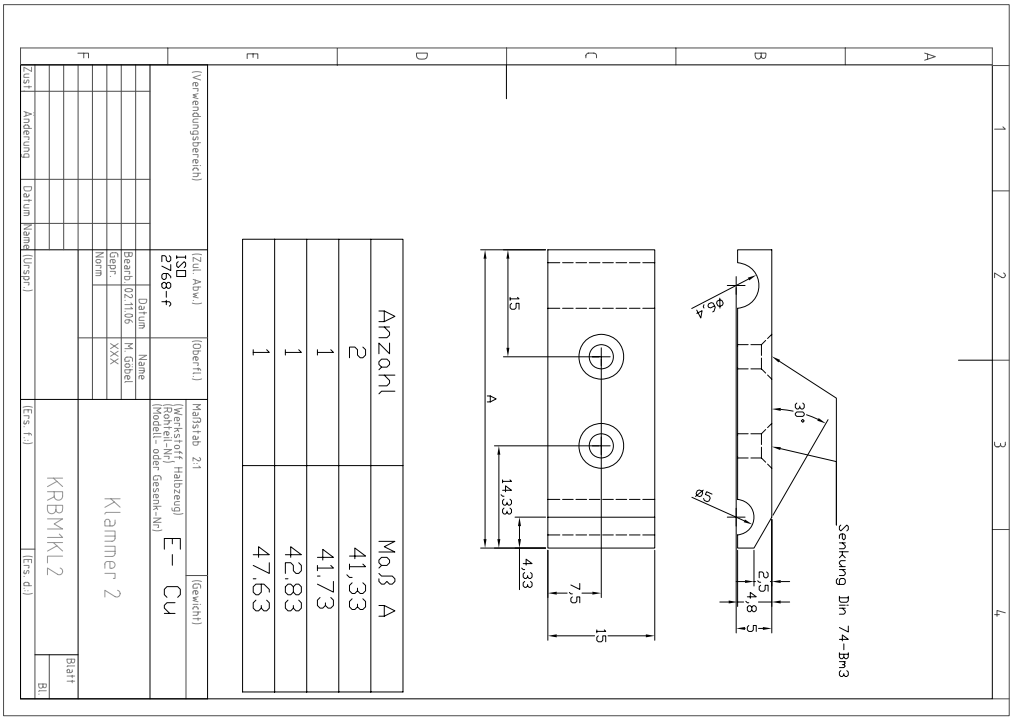

Figure C.18.: Copper clamps

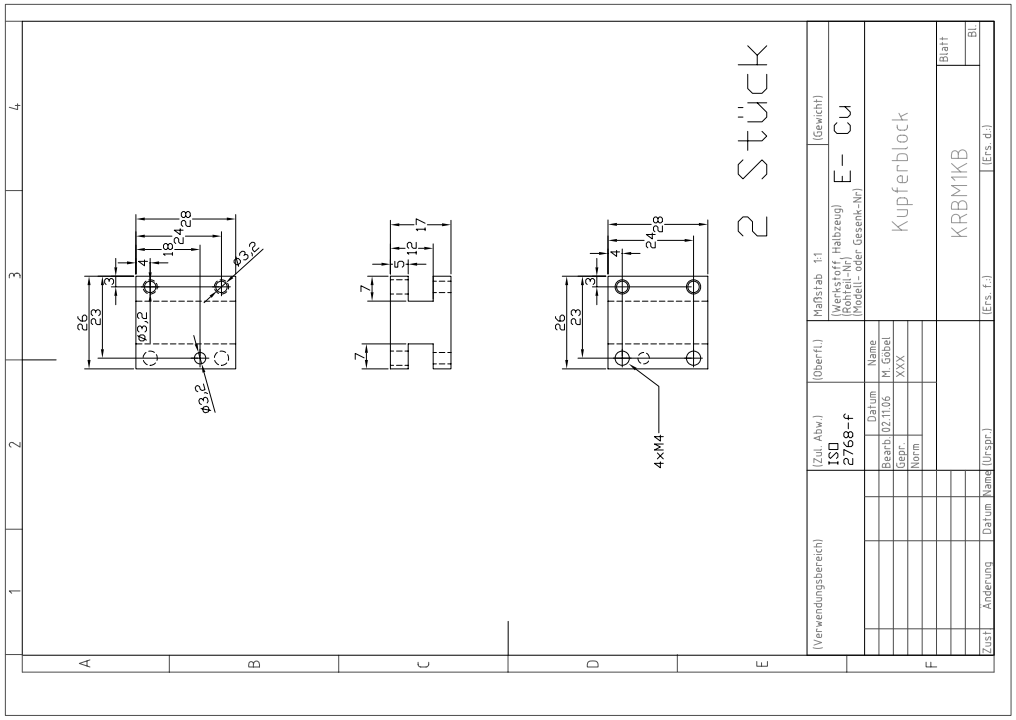

Figure C.19.: Small block of copper directly below the Shapal piece

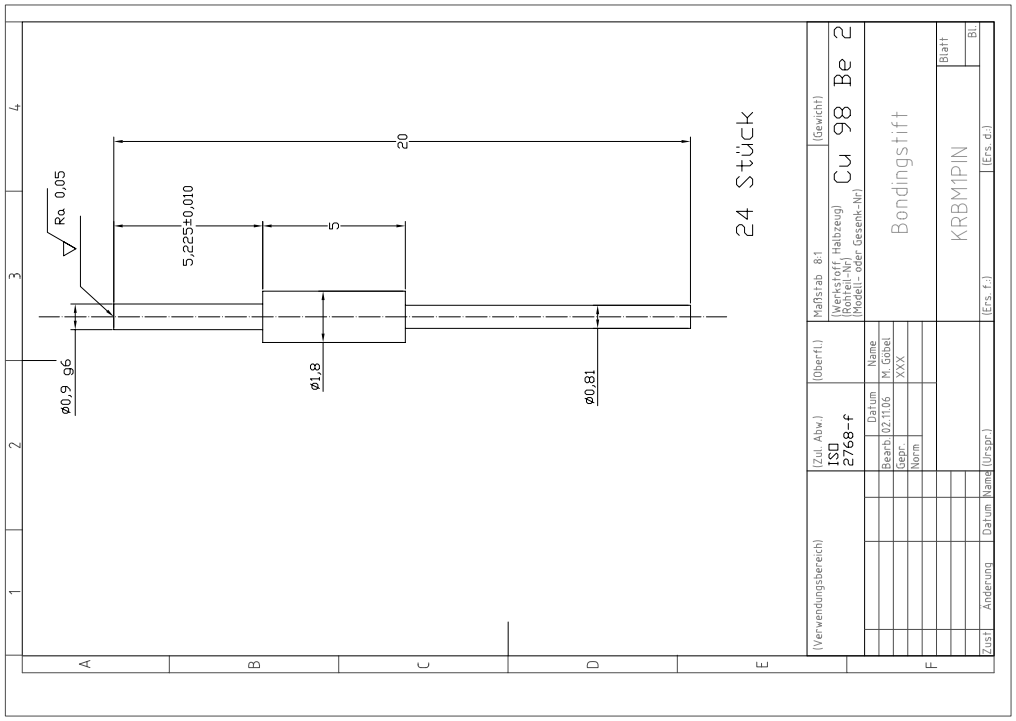

Figure C.20.: Copper-Berylium pins

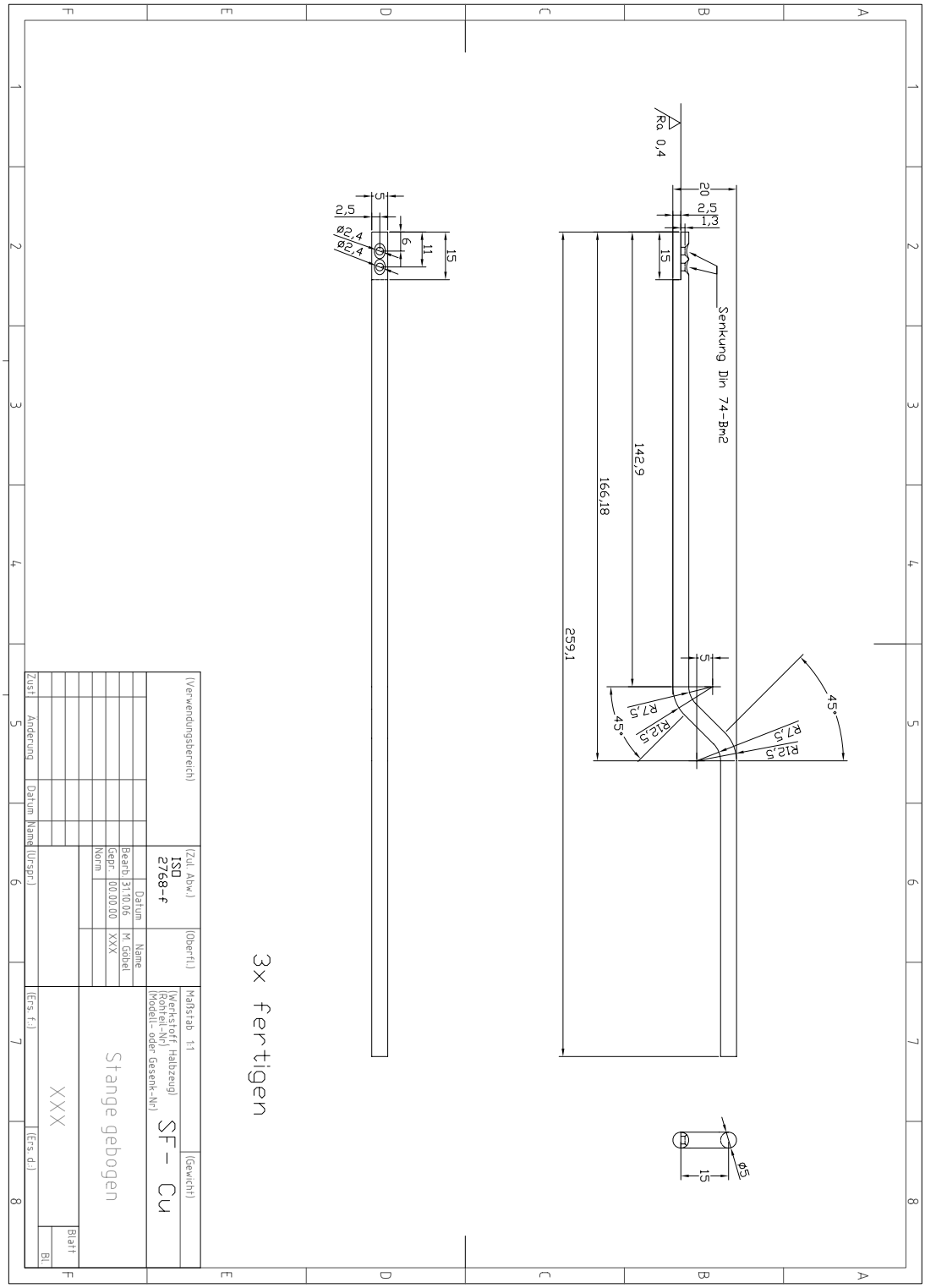

Figure C.21.: Rods connecting the copper structures

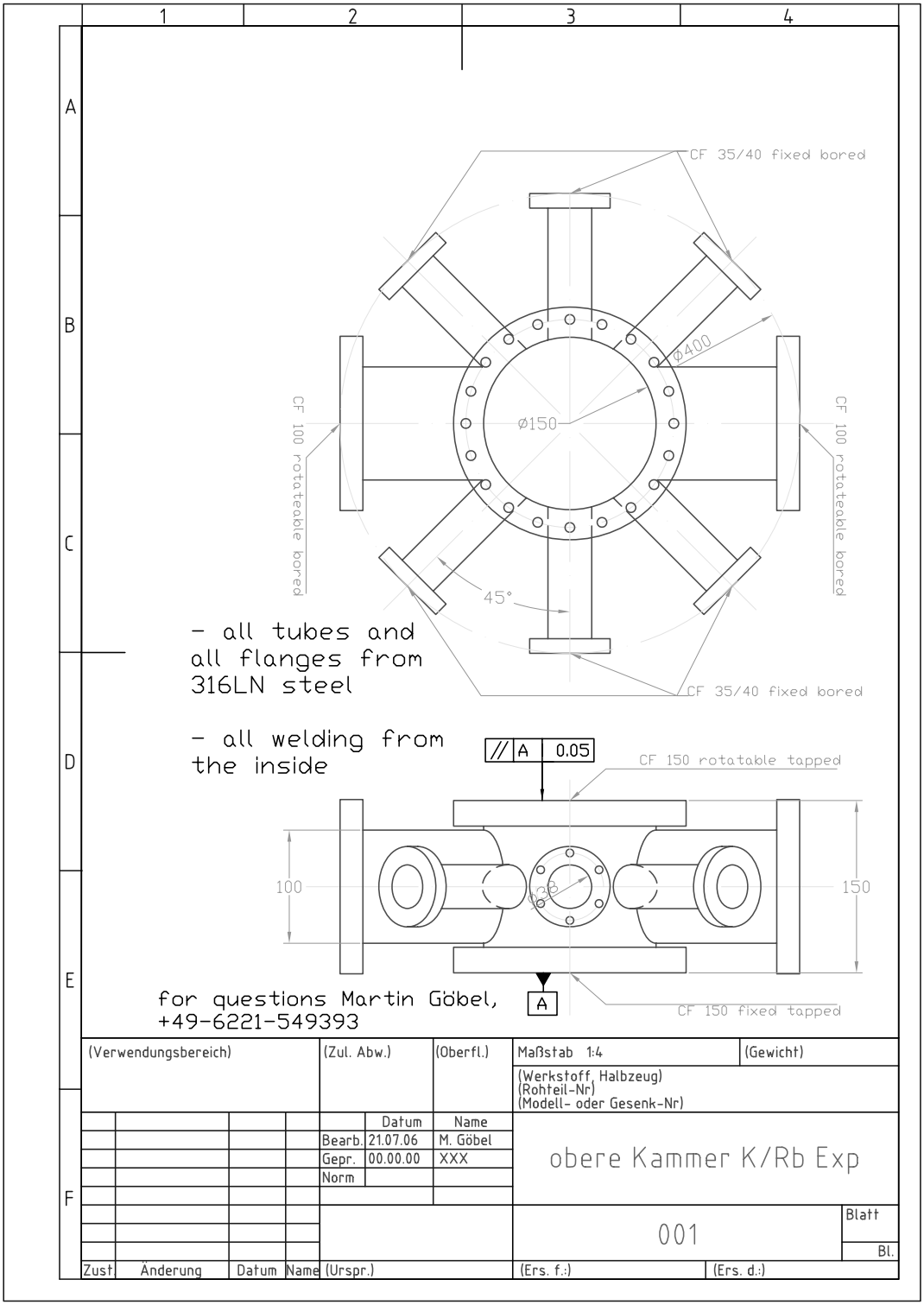

Figure C.22.: Upper chamber that connects the science chamber with its infrastructure like pumps and gauges.

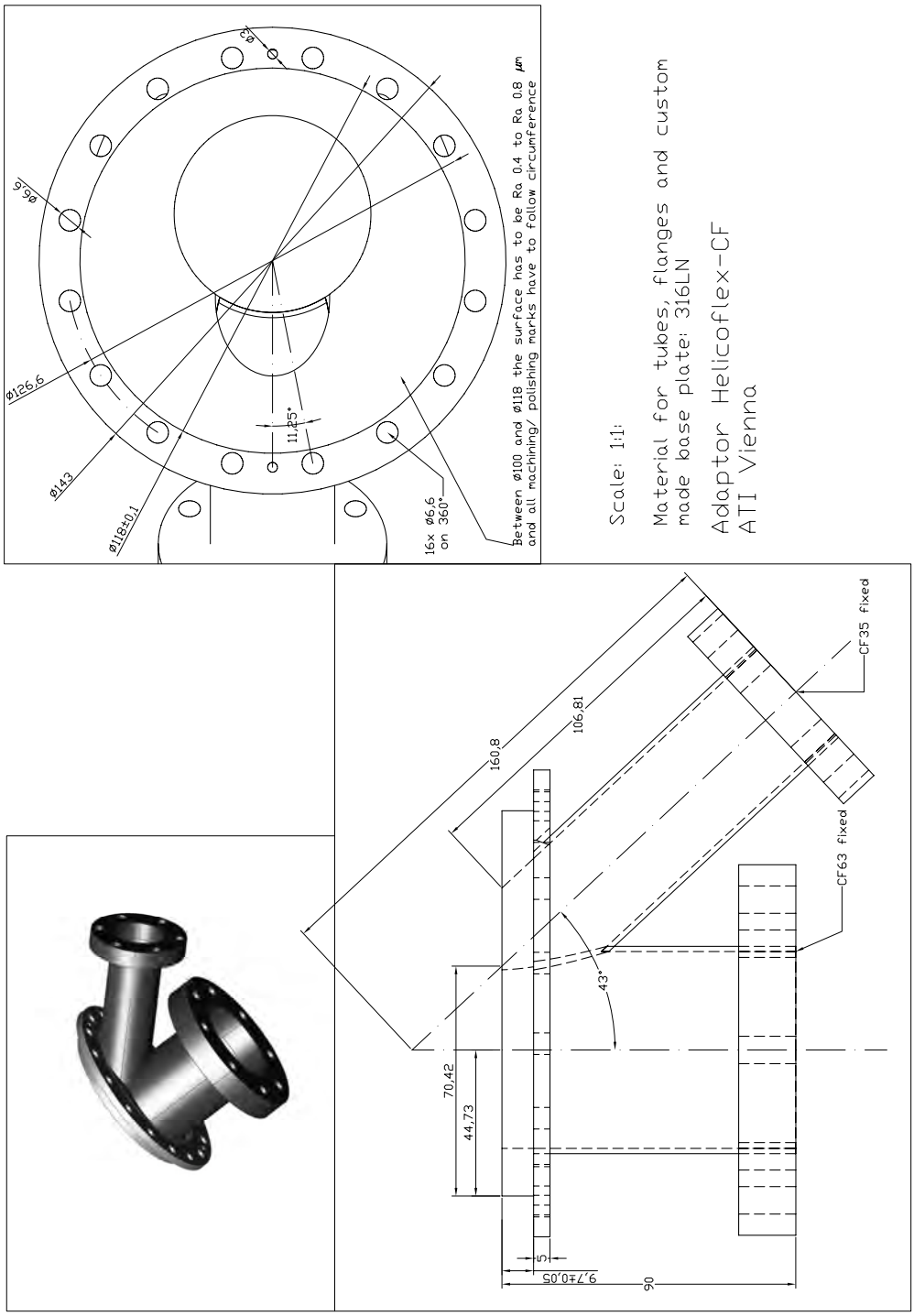

Figure C.23.: Drawing for the Helicoflex-CF adaptor that was build to replace one of the big windows on the science chamber with a DN63CF and a DN40CF window.

Acknowledgments

This thesis would not have been possible without the help and support from a long list of people that I would like to mention.
I would like to thank:

- First, my advisor Jörg Schmiedmayer, who offered me the opportunity to do research in such a well equipped group. He gave Christoph and me an amazing amount of freedom to develop our own project and to realize it in the lab.

- Christoph vom Hagen, master of the MBR, for being a reliable companion inside and outside of the lab. Especially in moments, when again another vacuum window broke, it was always reassuring to know that I was not the only one aboard the cursed ship of lost souls.

- Several post-docs (in chronological order) have to be mentioned:
  Stephan Schneider for the help in the early stages of the experiment in Heidelberg, for the organization of the move to Vienna and for the almost perfect construction work of the new labs.

  David Smith, who joined our team in experimentally tough times, jumped right in, and soon evolved to the driving force at the K-Rb setup. Thank you for all the support, especially in connection with my move to the lab next door!

  I am in great debt to Thorsten Schumm, who made it possible for me to work on the RbII machine and to realize some of my experimental plans. Thank you for all the physics discussions and all the work behind the scenes!

- The RbII team, namely Stephanie Manz, Thomas Betz, Aurélien Perrin, Thorsten Schumm, Christian Koller and Wolfgang Rohringer, who gave me a warm welcome in their lab, postponed parts of their own projects and offered me so much time to work at the setup. Good luck with the hunt of the mysterious noise source!

- The diploma students Christoph Hufnagel-san, Yong Zhao, Barbara Stix and Maximilian Kuhnert, who contributed at different stages to the progress of the experiments in Heidelberg and Vienna. Max and Michael: Good luck with the beast! You will tame it!

- Everybody of the group who contributed to the helpful, cooperative and pleasant working atmosphere. I always highly appreciated 'trash talk time' in the coffee corner. Especially my fellow office mates, Christian and Christoph, have to be mentioned separately, as they were always able to dig out just another bad joke.
- The staff at the mechanical workshop in Heidelberg, who worked for us delivering outstanding quality, even after our move to Vienna. Without their support, there would be probably no mounting in the vacuum chamber yet.
- The administrative staff at the Physikalische Institut in Heidelberg and at the Atominstitut in Vienna, who were always very helpful making impossible things happen.
- Everybody who helped with the proof-reading of this thesis and supplied helpful suggestions, as there were Christoph, David, Thorsten and Max.
- The Studienstiftung des Deutschen Volkes for the financial support during my years of study at university and during the first two years of this project.
- My family for their support and help not only during the last four years.
- And, of course, Uta for everything.

References

[1] M. H. Anderson, J. R. Ensher, M. R. Matthews, C. E. Wieman, and E. A. Cornell. Observation of Bose-Einstein Condensation in a Dilute Atomic Vapor. *Science*, 269(5221):198, 1995. doi:10.1126/science.269.5221.198.

[2] K. B. Davis, M. O. Mewes, M. R. Andrews, N. J. van Druten, D. S. Durfee, D. M. Kurn, and W. Ketterle. Bose-Einstein Condensation in a Gas of Sodium Atoms. *Phys. Rev. Lett.*, 75(22):3969, 1995. doi:10.1103/PhysRevLett.75.3969.

[3] C. C. Bradley, C. A. Sackett, J. J. Tollett, and R. G. Hulet. Evidence of Bose-Einstein Condensation in an Atomic Gas with Attractive Interactions. *Phys. Rev. Lett.*, 75(9):1687, 1995. doi:10.1103/PhysRevLett.75.1687.

[4] Ph. Courteille, R. S. Freeland, D. J. Heinzen, F. A. van Abeelen, and B. J. Verhaar. Observation of a Feshbach Resonance in Cold Atom Scattering. *Phys. Rev. Lett.*, 81(1):69, 1998. doi:10.1103/PhysRevLett.81.69.

[5] S. Inouye, M. R. Andrews, J. Stenger, H. J. Miesner, D. M. Stamper-Kurn, and W. Ketterle. Observation of Feshbach resonances in a Bose-Einstein condensate. *Nature*, 392(6672):151, 1998. doi:10.1038/32354.

[6] J. L. Roberts, N. R. Claussen, S. L. Cornish, and C. E. Wieman. Magnetic Field Dependence of Ultracold Inelastic Collisions near a Feshbach Resonance. *Phys. Rev. Lett.*, 85(4):728, 2000. doi:10.1103/PhysRevLett.85.728.

[7] B. DeMarco and D. S. Jin. Onset of Fermi Degeneracy in a Trapped Atomic Gas. *Science*, 285(5434):1703, 1999. doi:10.1126/science.285.5434.1703.

[8] J. Cubizolles, T. Bourdel, S. J. J. M. F. Kokkelmans, G. V. Shlyapnikov, and C. Salomon. Production of Long-Lived Ultracold Li_2 Molecules from a Fermi Gas. *Phys. Rev. Lett.*, 91(24):240401, 2003. doi:10.1103/PhysRevLett.91.240401.

[9] S. Jochim, M. Bartenstein, A. Altmeyer, G. Hendl, S. Riedl, C. Chin, J. Hecker Denschlag, and R. Grimm. Bose-Einstein Condensation of Molecules. *Science*, 302(5653):2101, 2003. doi:10.1126/science.1093280.

[10] M. Greiner, C. A. Regal, and D. S. Jin. Emergence of a molecular Bose-Einstein condensate from a Fermi gas. *Nature*, 426(6966):537, 2003. doi:10.1038/nature02199.

[11] M. Inguscio, W. Ketterle, and C. Salomon, editors. *Ultra-cold Fermi Gases*. Proceedings of the international school of physics "Enrico Fermi", Course CLXIV. IOS Press, Amsterdam, 2008.

[12] M. W. Zwierlein, J. R. Abo-Shaeer, A. Schirotzek, C. H. Schunck, and W. Ketterle. Vortices and superfluidity in a strongly interacting Fermi gas. *Nature*, 435(7045):1047, 2005. doi:10.1038/nature03858.

[13] M. Lewenstein, L. Santos, M. A. Baranov, and H. Fehrmann. Atomic Bose-Fermi Mixtures in an Optical Lattice. *Phys. Rev. Lett.*, 92(5):050401, 2004. doi:10.1103/PhysRevLett.92.050401.

[14] A. G. Truscott, K. E. Strecker, W. I. McAlexander, G. B. Partridge, and R. G. Hulet. Observation of Fermi Pressure in a Gas of Trapped Atoms. *Science*, 291(5513):2570, 2001. doi:10.1126/science.1059318.

[15] B. DeMarco. *Quantum Behavior of an Atomic Fermi Gas*. PhD thesis, University of Colorado, 2001.

[16] M. Modugno, F. Ferlaino, F. Riboli, G. Roati, G. Modugno, and M. Inguscio. Mean-field analysis of the stability of a K-Rb Fermi-Bose mixture. *Phys. Rev. A*, 68(4):043626, 2003. doi:10.1103/PhysRevA.68.043626.

[17] J. Goldwin, S. Inouye, M. L. Olsen, B. Newman, B. D. DePaola, and D. S. Jin. Measurement of the interaction strength in a Bose-Fermi mixture with ^{87}Rb and ^{40}K. *Phys. Rev. A*, 70(2):021601, 2004. doi:10.1103/PhysRevA.70.021601.

[18] C. Ospelkaus, S. Ospelkaus, K. Sengstock, and K. Bongs. Interaction-Driven Dynamics of ^{40}K–^{87}Rb Fermion-Boson Gas Mixtures in the Large-Particle-Number Limit. *Phys. Rev. Lett.*, 96(2):020401, 2006. doi:10.1103/PhysRevLett.96.020401.

[19] C. A. Stan, M. W. Zwierlein, C. H. Schunck, S. M. F. Raupach, and W. Ketterle. Observation of Feshbach Resonances between Two Different Atomic Species. *Phys. Rev. Lett.*, 93(14):143001, 2004. doi:10.1103/PhysRevLett.93.143001.

[20] S. Inouye, J. Goldwin, M. L. Olsen, C. Ticknor, J. L. Bohn, and D. S. Jin. Observation of Heteronuclear Feshbach Resonances in a Mixture of Bosons and Fermions. *Phys. Rev. Lett.*, 93(18):183201, 2004. doi:10.1103/PhysRevLett.93.183201.

[21] C. Ospelkaus, S. Ospelkaus, L. Humbert, P. Ernst, K. Sengstock, and K. Bongs. Ultracold Heteronuclear Molecules in a 3D Optical Lattice. *Phys. Rev. Lett.*, 97(12):120402, 2006. doi:10.1103/PhysRevLett.97.120402.

[22] S. Ospelkaus, C. Ospelkaus, O. Wille, M. Succo, P. Ernst, K. Sengstock, and K. Bongs. Localization of Bosonic Atoms by Fermionic Impurities in a Three-Dimensional Optical Lattice. *Phys. Rev. Lett.*, 96(18):180403, 2006. doi:10.1103/PhysRevLett.96.180403.

[23] H. Ott, E. de Mirandes, F. Ferlaino, G. Roati, G. Modugno, and M. Inguscio. Collisionally Induced Transport in Periodic Potentials. *Phys. Rev. Lett.*, 92(16):160601, 2004. doi:10.1103/PhysRevLett.92.160601.

[24] M. Olshanii. Atomic Scattering in the Presence of an External Confinement and a Gas of Impenetrable Bosons. *Phys. Rev. Lett.*, 81(5):938, 1998. doi:10.1103/PhysRevLett.81.938.

[25] D. Petrov, D. Gangardt, and G. Shlyapnikov. Low-dimensional trapped gases. In L. Pricoupenko, H. Perrin, and M. Olshanii, editors, *Quantum Gases in Low Dimensions*, volume 116, pages 5–44. QGLD 2003, Journal de Physique IV, 2004.

[26] T. Kinoshita, T. Wenger, and D. S. Weiss. Observation of a One-Dimensional Tonks-Girardeau Gas. *Science*, 305(5687):1125, 2004. doi:10.1126/science.1100700.

[27] B. Paredes, A. Widera, V. Murg, O. Mandel, S. Fölling, I. Cirac, G. V. Shlyapnikov, T. W. Hänsch, and I. Bloch. Tonks-Girardeau gas of ultracold atoms in an optical lattice. *Nature*, 429(6989):277, 2004. doi:10.1038/nature02530.

[28] S. Dettmer, D. Hellweg, P. Ryytty, J. J. Arlt, W. Ertmer, K. Sengstock, D. S. Petrov, G. V. Shlyapnikov, H. Kreutzmann, L. Santos, and M. Lewenstein. Observation of Phase Fluctuations in Elongated Bose-Einstein Condensates. *Phys. Rev. Lett.*, 87(16):160406, 2001. doi:10.1103/PhysRevLett.87.160406.

[29] S. Hofferberth, I. Lesanovsky, B. Fischer, T. Schumm, and J. Schmiedmayer. Non-equilibrium coherence dynamics in one-dimensional Bose gases. *Nature*, 449(7160):324, 2007. doi:10.1038/nature06149.

[30] T. P. Simula, M. D. Lee, and D. A. W. Hutchinson. Transition from the Bose-Einstein condensate to the Berezinskii-Kosterlitz-Thouless phase. *Philosophical Magazine Letters*, 85(8):395, 2005. doi:10.1080/09500830500256587.

[31] Z. Hadzibabic, P. Krüger, M. Cheneau, B. Battelier, and J. Dalibard. Berezinskii-Kosterlitz-Thouless crossover in a trapped atomic gas. *Nature*, 441(7097):1118, 2006. doi:10.1038/nature04851.

[32] K. K. Das. Highly anisotropic Bose-Einstein condensates: Crossover to lower dimensionality. *Phys. Rev. A*, 66(5):053612, 2002. doi:10.1103/PhysRevA.66.053612.

[33] F. Gerbier. Quasi-1D Bose-Einstein condensates in the dimensional crossover regime. *Europhysics Letters*, 66(6):771, 2004. doi:10.1209/epl/i2004-10035-7.

[34] R. Folman, P. Krüger, J. Schmiedmayer, J. Denschlag, and C. Henkel. Microscopic atom optics: from wires to an atom chip. *Adv. At. Mol. Opt. Phys.*, 48:263, 2002.

[35] J. Fortágh and C. Zimmermann. Magnetic microtraps for ultracold atoms. *Rev. Mod. Phys.*, 79(1):235, 2007. doi:10.1103/RevModPhys.79.235.

[36] M. Wilzbach, D. Heine, S. Groth, X. Liu, B. Hessmo, and J. Schmiedmayer. A simple integrated single-atom detector. arXiv:0801.3255v1.

[37] S. Wildermuth, S. Hofferberth, I. Lesanovsky, E. Haller, L. M. Andersson, S. Groth, I. Bar-Joseph, P. Krüger, and J. Schmiedmayer. Bose-Einstein condensates: Microscopic magnetic-field imaging. *Nature*, 435:440, 2005. doi:10.1038/435440a.

[38] S. Aigner, L. D. Pietra, Y. Japha, O. Entin-Wohlman, T. David, R. Salem, R. Folman, and J. Schmiedmayer. Long-Range Order in Electronic Transport Through Disordered Metal Films. *Science*, 319(5867):1226, 2008. doi:10.1126/science.1152458.

[39] J. Schmiedmayer, R. Folman, and T. Calarco. Quantum information processing with neutral atoms on an atom chip. *Journal of Modern Optics*, 49:1375, 2002. doi:10.1080/09500340110111077.

[40] S. Du, M. B. Squires, Y. Imai, L. Czaia, R. A. Saravanan, V. Bright, J. Reichel, T. W. Hänsch, and D. Z. Anderson. Atom-chip Bose-Einstein condensation in a portable vacuum cell. *Phys. Rev. A*, 70(5):053606, 2004. doi:10.1103/PhysRevA.70.053606.

[41] O. Zobay and B. M. Garraway. Two-Dimensional Atom Trapping in Field-Induced Adiabatic Potentials. *Phys. Rev. Lett.*, 86(7):1195, 2001. doi:10.1103/PhysRevLett.86.1195.

[42] T. Schumm, S. Hofferberth, L. M. Andersson, S. Wildermuth, S. Groth, I. Bar-Joseph, J. Schmiedmayer, and P. Krüger. Matter-wave interferometry in a double well on an atom chip. *Nature Physics*, 1(1):57, 2005. doi:10.1038/nphys125.

[43] I. Lesanovsky, T. Schumm, S. Hofferberth, L. M. Andersson, P. Krüger, and J. Schmiedmayer. Adiabatic radio-frequency potentials for the coherent manipulation of matter waves. *Phys. Rev. A*, 73(3):033619, 2006. doi:10.1103/PhysRevA.73.033619.

[44] G.-B. Jo, Y. Shin, S. Will, T. A. Pasquini, M. Saba, W. Ketterle, D. E. Pritchard, M. Vengalattore, and M. Prentiss. Long Phase Coherence Time and Number Squeezing of Two Bose-Einstein Condensates on an Atom Chip. *Phys. Rev. Lett.*, 98(3):030407, 2007. doi:10.1103/PhysRevLett.98.030407.

[45] J. J. P. van Es, S. Whitlock, T. Fernholz, A. H. van Amerongen, and N. J. van Druten. Longitudinal character of atom-chip-based rf-dressed potentials. *Phys. Rev. A*, 77(6):063623, 2008. doi:10.1103/PhysRevA.77.063623.

[46] R. J. Sewell, J. Dingjan, S. Eriksson, and E. A. Hinds. Single and Double Well Potentials on an Atom Chip. Poster at QuAMP 2007, London.

[47] M. H. T. Extavour, L. J. LeBlanc, T. Schumm, B. Cieslak, S. Myrskog, A. Stummer, S. Aubin, and J. H. Thywissen. Dual-Species Quantum Degeneracy of ^{40}K and ^{87}Rb on an Atom Chip. In Ch. Roos, H. Häffner, and R. Blatt, editors, *ATOMIC PHYSICS 20: XX International Conference on Atomic Physics - ICAP 2006*, volume 869, page 241. AIP, 2006. doi:10.1063/1.2400654.

[48] J. H. Thywissen, R. M. Westervelt, and M. Prentiss. Quantum Point Contacts for Neutral Atoms. *Phys. Rev. Lett.*, 83(19):3762, 1999. doi:10.1103/PhysRevLett.83.3762.

[49] Y. Colombe, E. Knyazchyan, O. Morizot, B. Mercier, V. Lorent, and H. Perrin. Ultracold atoms confined in rf-induced two-dimensional trapping potentials. *Europhysics Letters*, 67(4):593, 2004. doi:10.1209/epl/i2004-10095-7.

[50] A. L. Migdall, J. V. Prodan, W. D. Phillips, T. H. Bergeman, and H. J. Metcalf. First Observation of Magnetically Trapped Neutral Atoms. *Phys. Rev. Lett.*, 54(24):2596, 1985. doi:10.1103/PhysRevLett.54.2596.

[51] C. J. Pethick and H. Smith. *Bose-Einstein Condensation in Dilute Gases*. Cambridge University Press, 2002.

[52] E. A. Hinds and I. G. Hughes. Magnetic atom optics: mirrors, guides, traps, and chips for atoms. *Journal of Physics D*, 32(18):R119, 1999. doi:10.1088/0022-3727/32/18/201.

[53] S. Earnshaw. On the nature of the molecular forces which regulate the constitution of the luminiferous ether. *Trans. Camb. Phil. Soc.*, 7:97, 1842.

[54] H. J. Metcalf and P. V. der Straten. *Laser Cooling and Trapping*. Springer, 1999.

[55] E. L. Raab, M. Prentiss, A. Cable, S. Chu, and D. E. Pritchard. Trapping of Neutral Sodium Atoms with Radiation Pressure. *Phys. Rev. Lett.*, 59(23):2631, 1987. doi:10.1103/PhysRevLett.59.2631.

[56] E. Majorana. Atomi orientati in campo magnetico variabile. *Nuovo Cimento*, 9:43, 1932.

[57] W. Petrich, M. H. Anderson, J. R. Ensher, and E. A. Cornell. Stable, Tightly Confining Magnetic Trap for Evaporative Cooling of Neutral Atoms. *Phys. Rev. Lett.*, 74(17):3352, 1995. doi:10.1103/PhysRevLett.74.3352.

[58] Y. V. Gott, M. S. Ioffe, and V. Tel'kovskii. Some new results on confinement in magnetic traps. *Nucl. Fusion*, Part 3:1045, 1962 Supplement.

[59] D. E. Pritchard. Cooling Neutral Atoms in a Magnetic Trap for Precision Spectroscopy. *Phys. Rev. Lett.*, 51(15):1336, 1983. doi:10.1103/PhysRevLett.51.1336.

[60] C. V. Sukumar and D. M. Brink. Spin-flip transitions in a magnetic trap. *Phys. Rev. A*, 56(3):2451, 1997. doi:10.1103/PhysRevA.56.2451.

[61] S. Gov, S. Shtrikman, and H. Thomas. Magnetic trapping of neutral particles: Classical and quantum-mechanical study of a Ioffe–Pritchard type trap. *Journal of Applied Physics*, 87(8):3989, 2000. doi:10.1063/1.372444.

[62] C. Silber, S. Günther, C. Marzok, B. Deh, Ph. W. Courteille, and C. Zimmermann. Quantum-Degenerate Mixture of Fermionic Lithium and Bosonic Rubidium Gases. *Phys. Rev. Lett.*, 95(17):170408, 2005. doi:10.1103/PhysRevLett.95.170408.

[63] E. W. Streed, A. P. Chikkatur, T. L. Gustavson, M. Boyd, Y. Torii, D. Schneble, G. K. Campbell, D. E. Pritchard, and W. Ketterle. Large atom number Bose-Einstein condensate machines. *Review of Scientific Instruments*, 77(2):023106, 2006. doi:10.1063/1.2163977.

[64] T. Esslinger, I. Bloch, and T. W. Hänsch. Bose-Einstein condensation in a quadrupole-Ioffe-configuration trap. *Phys. Rev. A*, 58(4):R2664, 1998. doi:10.1103/PhysRevA.58.R2664.

[65] J. Denschlag, D. Cassettari, and J. Schmiedmayer. Guiding Neutral Atoms with a Wire. *Phys. Rev. Lett.*, 82(10):2014, 1999. doi:10.1103/PhysRevLett.82.2014.

[66] S. Schneider. *Bose-Einstein Kondensation in einer magnetischen Z-Falle*. PhD thesis, Universität Heidelberg, 2003.

[67] S. Wildermuth. *One-dimensional Bose-Einstein condensates in micro-traps*. PhD thesis, Universität Heidelberg, 2005.

[68] J. D. Jackson. *Classical Electrodynamics*. John Wiley & Sons, New York, 1999.

[69] J. Fortágh, A. Grossmann, C. Zimmermann, and T. W. Hänsch. Miniaturized Wire Trap for Neutral Atoms. *Phys. Rev. Lett.*, 81(24):5310, 1998. doi:10.1103/PhysRevLett.81.5310.

[70] J. Reichel, W. Hänsel, and T. W. Hänsch. Atomic Micromanipulation with Magnetic Surface Traps. *Phys. Rev. Lett.*, 83(17):3398, 1999. doi:10.1103/PhysRevLett.83.3398.

[71] R. Folman, P. Krüger, D. Cassettari, B. Hessmo, T. Maier, and J. Schmiedmayer. Controlling Cold Atoms using Nanofabricated Surfaces: Atom Chips. *Phys. Rev. Lett.*, 84(20):4749, 2000. doi:10.1103/PhysRevLett.84.4749.

[72] N. H. Dekker, C. S. Lee, V. Lorent, J. H. Thywissen, S. P. Smith, M. Drndić, R. M. Westervelt, and M. Prentiss. Guiding Neutral Atoms on a Chip. *Phys. Rev. Lett.*, 84(6):1124, 2000. doi:10.1103/PhysRevLett.84.1124.

[73] X. Luo, P. Krüger, K. Brugger, S. Wildermuth, H. Gimpel, M. W. Klein, S. Groth, R. Folman, I. Bar-Joseph, and J. Schmiedmayer. Atom fiber for omnidirectional guiding of cold neutral atoms. *Opt. Lett.*, 29(18):2145, 2004. doi:10.1364/OL.29.002145.

[74] D. Müller, E. A. Cornell, M. Prevedelli, P. D. D. Schwindt, A. Zozulya, and D. Z. Anderson. Waveguide atom beam splitter for laser-cooled neutral atoms. *Opt. Lett.*, 25(18):1382, 2000. doi:10.1364/OL.25.001382.

[75] W. Hänsel, P. Hommelhoff, T. W. Hänsch, and J. Reichel. Bose-Einstein condensation on a microelectronic chip. *Nature*, 413(6855):498, 2001. doi:10.1038/35097032.

[76] P. Hommelhoff, W. Hänsel, T. Steinmetz, T. W. Hänsch, and J. Reichel. Transporting, splitting and merging of atomic ensembles in a chip trap. *New Journal of Physics*, 7:3, 2005. doi:10.1088/1367-2630/7/1/003.

[77] R. Long, T. Rom, W. Hänsel, T. W. Hänsch, and J. Reichel. Long distance magnetic conveyor for precise positioning of ultracold atoms. *The European Physical Journal D*, 35(1):125, 2005. doi:10.1140/epjd/e2005-00177-6.

[78] A. Günther, M. Kemmler, S. Kraft, C. J. Vale, C. Zimmermann, and J. Fortágh. Combined chips for atom optics. *Phys. Rev. A*, 71(6):063619, 2005. doi:10.1103/PhysRevA.71.063619.

[79] A. Haase, B. Hessmo, and J. Schmiedmayer. Detecting magnetically guided atoms with an optical cavity. *Opt. Lett.*, 31(2):268, 2006. doi:10.1364/OL.31.000268.

[80] Y. Colombe, T. Steinmetz, G. Dubois, F. Linke, D. Hunger, and J. Reichel. Strong atom-field coupling for Bose-Einstein condensates in an optical cavity on a chip. *Nature*, 450:272, 2007. doi:10.1038/nature06331.

[81] P. Krüger, X. Luo, M. W. Klein, K. Brugger, A. Haase, S. Wildermuth, S. Groth, I. Bar-Joseph, R. Folman, and J. Schmiedmayer. Trapping and Manipulating Neutral Atoms with Electrostatic Fields. *Phys. Rev. Lett.*, 91(23):233201, 2003. doi:10.1103/PhysRevLett.91.233201.

[82] Ph. Treutlein, P. Hommelhoff, T. Steinmetz, T. W. Hänsch, and J. Reichel. Coherence in Microchip Traps. *Phys. Rev. Lett.*, 92(20):203005, 2004. doi:10.1103/PhysRevLett.92.203005.

[83] S. Hofferberth, I. Lesanovsky, B. Fischer, J. Verdu, and J. Schmiedmayer. Radiofrequency-dressed-state potentials for neutral atoms. *Nature Physics*, 2(10):710, 2006. doi:10.1038/nphys420.

[84] J. Reichel. Microchip traps and Bose-Einstein condensation. *Applied Physics B*, 74(6):469, 2002. doi:10.1007/s003400200861.

[85] I. Lesanovsky, S. Hofferberth, J. Schmiedmayer, and P. Schmelcher. Manipulation of ultracold atoms in dressed adiabatic radio-frequency potentials. *Phys. Rev. A*, 74(3):033619, 2006. doi:10.1103/PhysRevA.74.033619.

[86] F. Dalfovo, S. Giorgini, L. P. Pitaevskii, and S. Stringari. Theory of Bose-Einstein condensation in trapped gases. *Rev. Mod. Phys.*, 71(3):463, 1999. doi:10.1103/RevModPhys.71.463.

[87] D. A. Butts and D. S. Rokhsar. Trapped Fermi gases. *Phys. Rev. A*, 55(6):4346, 1997. doi:10.1103/PhysRevA.55.4346.

[88] K. Mølmer. Bose Condensates and Fermi Gases at Zero Temperature. *Phys. Rev. Lett.*, 80(9):1804, 1998. doi:10.1103/PhysRevLett.80.1804.

[89] W. Ketterle and N. J. van Druten. Bose-Einstein condensation of a finite number of particles trapped in one or three dimensions. *Phys. Rev. A*, 54(1):656, 1996. doi:10.1103/PhysRevA.54.656.

[90] E. G. M. van Kempen, S. J. J. M. F. Kokkelmans, D. J. Heinzen, and B. J. Verhaar. Interisotope Determination of Ultracold Rubidium Interactions from Three High-Precision Experiments. *Phys. Rev. Lett.*, 88(9):093201, 2002. doi:10.1103/PhysRevLett.88.093201.

[91] C. Klempt. *Wechselwirkung in Bose-Fermi-Quantengasen.* PhD thesis, Universität Hannover, 2008.

[92] G. M. Bruun and C. W. Clark. Ideal gases in time-dependent traps. *Phys. Rev. A*, 61(6):061601, 2000. doi:10.1103/PhysRevA.61.061601.

[93] D. S. Jin and C. A. Regal. Fermi gas experiments. In M. Inguscio, W. Ketterle, and C. Salomon, editors, *Ultra-cold Fermi Gases*, Proceedings of the international school of physics "Enrico Fermi", Course CLXIV, page 1. IOS Press, Amsterdam, 2008.

[94] Y. Castin and R. Dum. Bose-Einstein Condensates in Time Dependent Traps. *Phys. Rev. Lett.*, 77(27):5315, 1996. doi:10.1103/PhysRevLett.77.5315.

[95] V. L. Berezinskii. Destruction of long-range order in one-dimensional and two-dimensional systems possessing a continuous symmetry group. II. Quantum systems. *Sov. Phys. JETP*, 34:610, 1972.

[96] J. M. Kosterlitz and D. J. Thouless. Ordering, metastability and phase transitions in two-dimensional systems. *Journal of Physics C*, 6(7):1181, 1973. doi:10.1088/0022-3719/6/7/010.

[97] D. S. Petrov, M. Holzmann, and G. V. Shlyapnikov. Bose-Einstein Condensation in Quasi-2D Trapped Gases. *Phys. Rev. Lett.*, 84(12):2551, 2000. doi:10.1103/PhysRevLett.84.2551.

[98] P. Krüger, Z. Hadzibabic, and J. Dalibard. Critical Point of an Interacting Two-Dimensional Atomic Bose Gas. *Phys. Rev. Lett.*, 99(4):040402, 2007. doi:10.1103/PhysRevLett.99.040402.

[99] D. Rychtarik, B. Engeser, H.-C. Nägerl, and R. Grimm. Two-Dimensional Bose-Einstein Condensate in an Optical Surface Trap. *Phys. Rev. Lett.*, 92(17):173003, 2004. doi:10.1103/PhysRevLett.92.173003.

[100] V. Bagnato and D. Kleppner. Bose-Einstein condensation in low-dimensional traps. *Phys. Rev. A*, 44(11):7439, 1991. doi:10.1103/PhysRevA.44.7439.

[101] D. S. Petrov. *Bose-Einstein Condensation in Low-Dimensional Trapped Gases*. PhD thesis, FOM Institute for Atomic and Molecular Physics, Amsterdam, 2003.

[102] A. Görlitz, J. M. Vogels, A. E. Leanhardt, C. Raman, T. L. Gustavson, J. R. Abo-Shaeer, A. P. Chikkatur, S. Gupta, S. Inouye, T. Rosenband, and W. Ketterle. Realization of Bose-Einstein Condensates in Lower Dimensions. *Phys. Rev. Lett.*, 87(13):130402, 2001. doi:10.1103/PhysRevLett.87.130402.

[103] A. I. Safonov, S. A. Vasilyev, I. S. Yasnikov, I. I. Lukashevich, and S. Jaakkola. Observation of Quasicondensate in Two-Dimensional Atomic Hydrogen. *Phys. Rev. Lett.*, 81(21):4545, 1998. doi:10.1103/PhysRevLett.81.4545.

[104] I. Bouchoule, M. Morinaga, C. Salomon, and D. S. Petrov. Cesium gas strongly confined in one dimension: Sideband cooling and collisional properties. *Phys. Rev. A*, 65(3):033402, 2002. doi:10.1103/PhysRevA.65.033402.

[105] S. Stock, Z. Hadzibabic, B. Battelier, M. Cheneau, and J. Dalibard. Observation of Phase Defects in Quasi-Two-Dimensional Bose-Einstein Condensates. *Phys. Rev. Lett.*, 95(19):190403, 2005. doi:10.1103/PhysRevLett.95.190403.

[106] V. Schweikhard, I. Coddington, P. Engels, V. P. Mogendorff, and E. A. Cornell. Rapidly Rotating Bose-Einstein Condensates in and near the Lowest Landau Level. *Phys. Rev. Lett.*, 92(4):040404, 2004. doi:10.1103/PhysRevLett.92.040404.

[107] L. Mathey, D.-W. Wang, W. Hofstetter, M. D. Lukin, and E. Demler. Luttinger Liquid of Polarons in One-Dimensional Boson-Fermion Mixtures. *Phys. Rev. Lett.*, 93(12):120404, 2004. doi:10.1103/PhysRevLett.93.120404.

[108] D.-W. Wang, M. D. Lukin, and E. Demler. Engineering superfluidity in Bose-Fermi mixtures of ultracold atoms. *Phys. Rev. A*, 72(5):051604, 2005. doi:10.1103/PhysRevA.72.051604.

[109] R. Roth and H. Feldmeier. Mean-field instability of trapped dilute boson-fermion mixtures. *Phys. Rev. A*, 65(2):021603, 2002. doi:10.1103/PhysRevA.65.021603.

[110] R. Roth. Structure and stability of trapped atomic boson-fermion mixtures. *Phys. Rev. A*, 66(1):013614, 2002. doi:10.1103/PhysRevA.66.013614.

[111] G. Modugno, G. Roati, F. Riboli, F. Ferlaino, R. J. Brecha, and M. Inguscio. Collapse of a Degenerate Fermi Gas. *Science*, 297(5590):2240, 2002. doi:10.1126/science.1077386.

[112] N. Nygaard and K. Mølmer. Component separation in harmonically trapped boson-fermion mixtures. *Phys. Rev. A*, 59(4):2974, 1999. doi:10.1103/PhysRevA.59.2974.

[113] W. Ketterle and N. J. van Druten. Evaporative Cooling. *Adv. At. Mol. Opt. Phys.*, 37:181, 1996.

[114] C. J. Myatt, E. A. Burt, R. W. Ghrist, E. A. Cornell, and C. E. Wieman. Production of Two Overlapping Bose-Einstein Condensates by Sympathetic Cooling. *Phys. Rev. Lett.*, 78(4):586, 1997. doi:10.1103/PhysRevLett.78.586.

[115] F. Schreck, G. Ferrari, K. L. Corwin, J. Cubizolles, L. Khaykovich, M.-O. Mewes, and C. Salomon. Sympathetic cooling of bosonic and fermionic lithium gases towards quantum degeneracy. *Phys. Rev. A*, 64(1):011402, 2001. doi:10.1103/PhysRevA.64.011402.

[116] Z. Hadzibabic, C. A. Stan, K. Dieckmann, S. Gupta, M. W. Zwierlein, A. Görlitz, and W. Ketterle. Two-Species Mixture of Quantum Degenerate Bose and Fermi Gases. *Phys. Rev. Lett.*, 88(16):160401, 2002. doi:10.1103/PhysRevLett.88.160401.

[117] G. Roati, F. Riboli, G. Modugno, and M. Inguscio. Fermi-Bose Quantum Degenerate ^{40}K-^{87}Rb Mixture with Attractive Interaction. *Phys. Rev. Lett.*, 89(15):150403, 2002. doi:10.1103/PhysRevLett.89.150403.

[118] F. Mies, C. Williams, P. Julienne, and M. Krauss. Estimating Bounds on Collisional Relaxation Rates of Spin-Polarized ^{87}Rb Atoms at Ultracold Temperatures. *J. Res. NIST*, 101:521, 1996.

[119] J. Weiner. *Cold and Ultracold Collisions in Quantum Microscopic and Mesoscopic Systems*. Cambridge University Press, 2003.

[120] Ch. Hufnagel. Cold Collisions between ^{6}Li and ^{87}Rb in a Two-Species Magneto-Optical Trap. Master's thesis, Universität Heidelberg, 2005.

[121] Ch. vom Hagen. *Towards a low-dimensional degenerate Fermi-Fermi-Bose mixture.* PhD thesis, Universität Heidelberg, 2008.

[122] A. Mosk, S. Kraft, M. Mudrich, K. Singer, W. Wohlleben, R. Grimm, and M. Weidemüller. Mixture of ultracold lithium and cesium atoms in an optical dipole trap. *Applied Physics B*, 73(8):791, 2001. doi:10.1007/s003400100743.

[123] M. Mudrich, S. Kraft, K. Singer, R. Grimm, A. Mosk, and M. Weidemüller. Sympathetic Cooling with Two Atomic Species in an Optical Trap. *Phys. Rev. Lett.*, 88(25):253001, 2002. doi:10.1103/PhysRevLett.88.253001.

[124] S. Aubin, S. Myrskog, M. H. T. Extavour, L. J. LeBlanc, D. McKay, A. Stummer, and J. H. Thywissen. Rapid sympathetic cooling to Fermi degeneracy on a chip. *Nature Physics*, 2(6):384, 2006. doi:10.1038/nphys309.

[125] C. Ramsauer. Über den Wirkungsquerschnitt der Gasmoleküle gegenüber langsamen Elektronen. *Annalen der Physik*, 369:513, 1921. doi:10.1002/andp.19213690603.

[126] V. Bagnato, D. E. Pritchard, and D. Kleppner. Bose-Einstein condensation in an external potential. *Phys. Rev. A*, 35(10):4354, 1987. doi:10.1103/PhysRevA.35.4354.

[127] M. Brown-Hayes and R. Onofrio. Optimal cooling strategies for magnetically trapped atomic Fermi-Bose mixtures. *Phys. Rev. A*, 70(6):063614, 2004. doi:10.1103/PhysRevA.70.063614.

[128] V. Peano, M. Thorwart, C. Mora, and R. Egger. Confinement-induced resonances for a two-component ultracold atom gas in arbitrary quasi-one-dimensional traps. *New Journal of Physics*, 7:192, 2005. doi:10.1088/1367-2630/7/1/192.

[129] J. I. Kim, V. S. Melezhik, and P. Schmelcher. Suppression of Quantum Scattering in Strongly Confined Systems. *Phys. Rev. Lett.*, 97(19):193203, 2006. doi:10.1103/PhysRevLett.97.193203.

[130] H. Moritz, T. Stöferle, K. Günter, M. Köhl, and T. Esslinger. Confinement Induced Molecules in a 1D Fermi Gas. *Phys. Rev. Lett.*, 94(21):210401, 2005. doi:10.1103/PhysRevLett.94.210401.

[131] C. Ospelkaus. *Fermi-Bose mixtures: From mean-field interactions to ultracold chemistry.* PhD thesis, Universität Hamburg, 2006.

[132] S. Chui, V. Ryzhov, and E. Tareyeva. Stability of the Bose system in Bose-Fermi mixture with attraction between bosons and fermions. *JETP Letters*, 80(4):274, 2004. doi:10.1134/1.1813686.

[133] K. Brugger. *Experimente mit mikroskopischen atomoptischen Elementen.* PhD thesis, Universität Heidelberg, 2004.

[134] F. Ferlaino, C. D'Errico, G. Roati, M. Zaccanti, M. Inguscio, G. Modugno, and A. Simoni. Erratum: Feshbach spectroscopy of a K-Rb atomic mixture [Phys. Rev. A 73, 040702 (2006)]. *Phys. Rev. A*, 74(3):039903, 2006. doi:10.1103/PhysRevA.74.039903.

[135] F. S. Cataliotti, E. A. Cornell, C. Fort, M. Inguscio, F. Marin, M. Prevedelli, L. Ricci, and G. M. Tino. Magneto-optical trapping of Fermionic potassium atoms. *Phys. Rev. A*, 57(2):1136, 1998. doi:10.1103/PhysRevA.57.1136.

[136] R. S. Williamson. *Magneto-Optical Trapping of Potassium Isotopes*. PhD thesis, University of Wisconsin - Madison, 1997.

[137] T. Karpiuk, M. Brewczyk, S. Ospelkaus-Schwarzer, K. Bongs, M. Gajda, and K. Rzążewski. Soliton Trains in Bose-Fermi Mixtures. *Phys. Rev. Lett.*, 93(10):100401, 2004. doi:10.1103/PhysRevLett.93.100401.

[138] L. G. Marcassa, G. D. Telles, S. R. Muniz, and V. S. Bagnato. Collisional losses in a K-Rb cold mixture. *Phys. Rev. A*, 63(1):013413, 2000. doi:10.1103/PhysRevA.63.013413.

[139] A. Simoni, F. Ferlaino, G. Roati, G. Modugno, and M. Inguscio. Magnetic Control of the Interaction in Ultracold K-Rb Mixtures. *Phys. Rev. Lett.*, 90(16):163202, 2003. doi:10.1103/PhysRevLett.90.163202.

[140] M. Köhl, H. Moritz, T. Stöferle, K. Günter, and T. Esslinger. Fermionic Atoms in a Three Dimensional Optical Lattice: Observing Fermi Surfaces, Dynamics, and Interactions. *Phys. Rev. Lett.*, 94(8):080403, 2005. doi:10.1103/PhysRevLett.94.080403.

[141] M. Taglieber, A.-C. Voigt, F. Henkel, S. Fray, T. W. Hänsch, and K. Dieckmann. Simultaneous magneto-optical trapping of three atomic species. *Phys. Rev. A*, 73:011402, 2006. doi:10.1103/PhysRevA.73.011402.

[142] S. Ospelkaus, C. Ospelkaus, L. Humbert, K. Sengstock, and K. Bongs. Tuning of Heteronuclear Interactions in a Degenerate Fermi-Bose Mixture. *Phys. Rev. Lett.*, 97(12):120403, 2006. doi:10.1103/PhysRevLett.97.120403.

[143] B. DeMarco, H. Rohner, and D. S. Jin. An enriched ^{40}K source for fermionic atom studies. *Review of Scientific Instruments*, 70(4):1967, 1999. doi:10.1063/1.1149695.

[144] E. A. Donley, T. P. Heavner, F. Levi, M. O. Tataw, and S. R. Jefferts. Double-pass acousto-optic modulator system. *Review of Scientific Instruments*, 76(6):063112, 2005. doi:10.1063/1.1930095.

[145] L. Della Pietra. *Coherent micromanipulation of 1-d BEC in designed potentials*. PhD thesis, Universität Heidelberg, 2007.

[146] W. Umrath. Grundlagen der Vakuumtechnik. Technical report, Oerlikon Leybold Vacuum GmbH, 1997.

[147] M. Kuhnert. A Dual-Species Two-MOT Setup for Preparing a Bose-Fermi Mixture on an Atom Chip. Master's thesis, Technische Universität Wien, 2008.

[148] S. Wildermuth, P. Krüger, C. Becker, M. Brajdic, S. Haupt, A. Kasper, R. Folman, and J. Schmiedmayer. Optimized magneto-optical trap for experiments with ultracold atoms near surfaces. *Phys. Rev. A*, 69(3):030901, 2004. doi:10.1103/PhysRevA.69.030901.

[149] S. Groth. *Development, Fabrication and Characterisation of Atom Chips*. PhD thesis, Universität Heidelberg, 2007.

[150] S. Hofferberth. *Coherent manipulation of Bose-Einstein condensates with rf adiabatic potentials*. PhD thesis, Universität Heidelberg, 2007.

[151] M. Trinker, S. Groth, S. Haslinger, S. Manz, T. Betz, S. Schneider, I. Bar-Joseph, T. Schumm, and J. Schmiedmayer. Multilayer atom chips for versatile atom micromanipulation. *Applied Physics Letters*, 92(25):254102, 2008. doi:10.1063/1.2945893.

[152] P. Krüger. *Coherent matter waves near surfaces*. PhD thesis, Universität Heidelberg, 2004.

[153] B. Stix. A New Imaging System For Dual-Species Atomchip Experiments. Master's thesis, Technische Universität Wien, 2008.

[154] S. Aigner. *Magnetic Field Microscopy using ultracold Atoms*. PhD thesis, Universität Heidelberg, 2007.

[155] C. Cohen-Tannoudji, J. Dupont-Roc, and G. Grynberg. *Atom-Photon Interactions*. Wiley-VCH, 1998.

[156] K. Lindquist, M. Stephens, and C. Wieman. Experimental and theoretical study of the vapor-cell Zeeman optical trap. *Phys. Rev. A*, 46(7):4082, 1992. doi:10.1103/PhysRevA.46.4082.

[157] K. E. Gibble, S. Kasapi, and S. Chu. Improved magneto-optic trapping in a vapor cell. *Opt. Lett.*, 17:526, 1992.

[158] S. Ospelkaus-Schwarzer. *Quantum Degenerate Fermi-Bose Mixtures of ^{40}K and ^{87}Rb in 3D Optical Lattices*. PhD thesis, Universität Hamburg, 2006.

[159] W. Ketterle, K. B. Davis, M. A. Joffe, A. Martin, and D. E. Pritchard. High densities of cold atoms in a dark spontaneous-force optical trap. *Phys. Rev. Lett.*, 70(15):2253, 1993. doi:10.1103/PhysRevLett.70.2253.

[160] R. Bücker. Fluorescence Imaging of Ultracold Atoms. Master's thesis, Universität Heidelberg, 2008.

[161] S. Manz. *to be published*. PhD thesis, Technische Universität Wien.

[162] T. Betz. *to be published*. PhD thesis, Technische Universität Wien.

[163] A. Kasper. *Bose-Einstein condensation in a robust microtrap – the combination of wire traps and atom chips*. PhD thesis, Universität Heidelberg, 2003.

[164] S. Hofferberth, B. Fischer, T. Schumm, J. Schmiedmayer, and I. Lesanovsky. Ultracold atoms in radio-frequency dressed potentials beyond the rotating-wave approximation. *Phys. Rev. A*, 76(1):013401, 2007. doi:10.1103/PhysRevA.76.013401.

[165] Y. Ralchenko, A. Kramida, J. Reader, and NIST ASD Team. NIST Atomic Spectra Database Lines Data (version 3.1.5). [Online], June 2008. Available from: http://physics.nist.gov/asd3.

[166] D. A. Steck. Rubidium 87 D Line Data, 2001. Los Alamos National Laboratory. Available from: `http://steck.us/alkalidata/`.

[167] Evaluated Nuclear Structure Data File (ENSDF) Database version of May 30, 2008. Available from: `http://www.nndc.bnl.gov/ensdf/`.

[168] F. Henkel. Fermionisches Kalium in der Dreikomponentigen Magnetooptischen Falle. Master's thesis, Ludwig-Maximilians-Universiät München, 2005.